Electrostatic extraction of buffer-gas-cooled beams for studying ion-molecule chemistry at low temperatures

Kathryn S. Twyman

Merton College
University of Oxford

A thesis submitted for the degree of Doctor of Philosophy

Trinity 2013

Electrostatic extraction of buffer-gas-cooled beams for studying ion-molecule chemistry at low temperatures

Kathryn S. Twyman, Merton College

A thesis submitted in partial fulfilment of the requirements
for the degree of Doctor of Philosophy of the University of Oxford

Trinity Term, 2013

Abstract

This thesis describes the design, construction, operation, and characterisation of an experimental apparatus that produces a source of internally cold, slow molecules that can be used for studying ion-molecule reactions at low temperatures. The apparatus combines buffer-gas cooling with a bent quadrupole velocity selector to cool both the translational and rotational degrees of freedom of the molecules.

A cold cell (6 K) is filled with a buffer gas, such as helium, that exhibits sufficiently high vapour pressure for cryogenic applications. Hot molecules (150 to 300 K) enter the cell and thermalise with the buffer gas through collisions. Molecules are subsequently loaded into an electrostatic quadrupole guide, which acts as a velocity filter; only translationally cold polar molecules are guided around the bend. Using a buffer-gas-cooled source of molecules for electrostatic velocity selection, rather than a 300 K effusive source, yields a rotationally cold sample, with $J \leq 3$. This rotational selectivity will enable the dependence of reaction cross sections on the reactant rotational state to be examined.

Mass spectrometry is used to characterise cold molecular beams of ND_3 and CH_3F, while (2+1) REMPI spectra are recorded for the ammonia isotopologues. The peak velocity of guided ND_3 is 75.86(0.70) ms^{-1} for standard conditions in a 6 K helium buffer gas cell (1.0 sccm ND_3 flow rate, 0.6 mbar helium inlet pressure, ± 5 kV voltage). This corresponds to a peak kinetic energy of 6.92(0.13) K. (2+1) REMPI spectroscopy of the $\tilde{\mathrm{B}}^1\mathrm{E}''(\nu_2' = 5) \leftarrow \tilde{\mathrm{X}}(1)$ transition enabled the rotational state distribution of guided ammonia molecules to be established. PGOPHER simulations of the experimental spectra suggest a rotational temperature of 10 K for ND_3 molecules (from a 6 K helium buffer gas cell).

The extent of translational and rotational cooling can be controlled by varying the molecular and buffer gas densities within the cell, by changing the temperature of the buffer gas cell (we can operate at 6 K or 17 K), or by changing the buffer gas. The translational temperature of guided ND_3 is similar in a 6 K helium and 17 K neon buffer gas cell (peak kinetic energies of 6.92(0.13) K and 5.90(0.01) K, respectively) because the heavier neon gas has a slightly lower thermal velocity at 17 K than helium does at 6 K. Despite similar translational temperatures, the rotational temperature of guided ND_3 is lower for molecules exiting the 6 K helium cell compared to the 17 K neon buffer gas cell (10 K and 15 K, respectively).

The 6 K helium and 17 K neon buffer gas cells provide an excellent opportunity to investigate the effect of rotational cooling on branching ratios and reaction rates in low temperature ion-molecule reactions. The buffer gas cell and velocity guide described in this work will be combined with a linear Paul ion trap, to facilitate the study of cold ion-molecule reactions.

Acknowledgements

There are several people I would like to acknowledge who, in various ways, have helped me during my D.Phil. I am thankful for the useful discussions, suggestions, and guidance provided by my supervisor, Prof. Tim Softley, and his willingness to work with my unusual schedule. Furthermore, I am very grateful for the extraordinary amount of freedom I was given to build the experiment. It was the equivalent of a blank cheque in terms of ideas, design, and assembly of the apparatus, if not quite from a purchasing point of view.

I feel incredibly fortunate to have spent so many hours working with Dr. Martin Bell. His wealth of experience in the group was invaluable, not only in providing practical advice while I was building the experiment and teaching me about experimental work, but also in knowing what bits of unused equipment could be found in the back cupboards and corners of the lab. A special thanks is in order for the hours we spent bending electrode rods until the prefect fit was achieved, and other such tasks, which were made much more enjoyable by his jokes, logic puzzles, and interesting questions. I was sad to see him leave the group, both as a colleague and a friend.

I am appreciative of the advice and suggestions provided by Dr. Brianna Heazlewood, both in the laboratory and while writing my thesis. Her fresh perspective on the experiment was helpful, and I learnt a great deal about lasers under her guidance. I am thankful for the time she spent reading the many drafts of my thesis, her critical appraisal of the work, the useful discussions, and her encouragement throughout the process.

I am indebted to the members of the mechanical and electronics workshops of the Physical and Theoretical Chemistry Laboratory, whose technical assistance was essential in building the experimental apparatus. I am particularly thankful to Andy Green for teaching me the basics of CAD and for discussions about the design of the experiment; to Howard Lambourne for the construction of the multitude of parts for the apparatus; to Charlie Jones for his introduction to the student workshop and help with subsequent projects; and Neville Baker for the electrical components necessary for the quadrupole guide and the ion detection set-up.

I was fortunate to have overlapped with so many friendly and interesting individuals during my time in the Softley group, including Elin, Alex, Eric, Sashi, Mark (postdoc), Will, James, Nabanita, Lee, (German) Mark, Chris, Laura, Katrin, Jess, Ed, Jemma, Mike, and Kasra. It was a pleasure to work alongside these individuals, and made for enjoyable lunches and afternoon tea. Finally, I would like to acknowledge the funding and support I received from Rhodes House during my time in Oxford on a Rhodes Scholarship.

Contents

Symbols

Notation	Description
A	cross-sectional area
A	rotational constant
A_1	area of the enclosed cold surface
A_2	area of the outer warm surface
a	amplitude
a_1	initial asymptote
a_2	final asymptote
B	rotational constant
B	second electronic excited state
C	gas conversion factor
C	rotational constant
$C_{3\mathrm{v}}$	point group representation
c_p	specific heat
$D_{3\mathrm{h}}$	point group representation
E	energy
E	factor between 0 and 1 depending on surface emissivity
E_{kin}	kinetic energy
$\mathrm{E_T}$	translational energy
e	control error in PID algorithm
f	gas flow rate
g	degeneracy factor
h	Planck's constant
I	nuclear spin
I_{x}	moment of inertia about axis x
J	rotational quantum number for total angular momentum
K	proportional gain in PID algorithm
K	rotational quantum number for projection of total angular momentum on the molecular axis
k	growth coefficient (Gompertz function)
k	rate coefficient
k	spherical tensor rank
k_{B}	Boltzmann's constant
L	length

Notation	Description
M	molecular species
m	mass
N	number of molecules
n	temperature dependence of the thermal rate coefficient
n	number density
$\mathbb{N}$	interger number
$\mathbb{N}_0$	interger number including zero
$\mathcal{N}$	number of collisions
$\hat{O}$	multiphoton transition operator
p	linear momentum
p	power (logistic function)
q	electric charge
q	spherical tensor component
$\dot{q}_{\mathrm{cond}}$	rate of conductive heat flow
$\dot{q}_{\mathrm{rad}}$	rate of radiant heat flow
R_{f}	reflectivity
S	signal
T	spherical tensor
T	temperature
T_{d}	derivative time in PID algorithm
T_{i}	integral time in PID algorithm
t	arrival time
t_{c}	sigmoidal function centre
u	control signal in PID algorithm
u	supersonic flow velocity
v	velocity
$\bar{v}$	mean thermal velocity
X	ground electronic state
Z	partition function
α	collision energy dependence of the reaction cross section
α	temperature coefficient of linear expansion
δ	diffusion constant
ϵ	surface emissivity
κ	fractional energy loss per elastic collision
λ	mean free path
λ	thermal conductivity
λ	wavelength
ρ	density
σ	reaction cross section
σ	Stefan-Boltzmann constant
ν_2	excitation frequency

Abbreviations

Notation	Description
AISI	American Iron and Steel Institute
AWG	American Wire Gauge
bcc	body-centred-cubic
CF	Conflat flange
COM	centre-of-mass
CRESU	Cinétique de Réaction en Ecoulement Supersonic Uniforme (reaction kinetics in a uniform supersonic flow)
CW	continuous wave
DC	direct current
DCM	4-dicyanomethylene-2-methyl-6-p-dimethylaminostyryl-4H-pyran
fcc	face-centred-cubic
FCF	Franck-Condon factor
FORT	far-off resonance optical trap
FWHM	full-width at half-maximum
FS	full span
hcp	hexagonal-close-packed
HFS	high field seekers
HV	high vacuum
HV	high voltage
ID	inner diameter
ISO	International Standards Organisation
KF	Klein flange
LFS	low field seekers
LIAD	laser-induced atomic desorption
MCP	microchannel plate
ME	metal
MOT	magneto-optical trap
MS	mass spectrometry
NW	nominal flange bore size

Notation	Description
OD	outer diameter
OFHC	oxygen-free copper
PA	Photoassociation
PES	potential energy surface
PID	proportional-integral-derivative
PT	platinum resistance thermometer
QMS	quadrupole mass spectrometer
REMPI	resonance enhanced multi-photon ionisation
RMS	root mean square
RRR	residual resistivity ratio
RT	room temperature
sccm	standard cubic centimetres per minute
SD	silicon diode temperature sensor
SS	stainless steel
TOF	time-of-flight
UHV	ultrahigh vacuum
X	halogen

List of Figures

List of Tables

Chapter 1

Introduction

1.1 Historical overview

Cold molecules and low temperature chemistry are amongst the new frontiers of physical chemistry. The research field is rapidly expanding, and the discoveries are likely to shape many new technologies that will emerge in the future. The production of cold atoms by the development of laser cooling revolutionised the field of atomic, molecular, and optical physics. The production of cold molecules is expected to have a similar impact on the field of physical chemistry.

In 1975, the theoretical possibility of using laser beams to slow down neutral atoms was independently outlined by both Hänsch and Schawlow, and by Wineland and Dehmelt [1, 2]. It was not until 1984, however, that laser cooling of neutral atoms was demonstrated experimentally by Chu and co-workers. The radiation pressure of counter-propagating laser beams, tuned to an atomic resonance, was used to slow a beam of sodium atoms to approximately 60 cm/sec, which corresponds to a temperature of 240 μK [3]. This experimental technique was originally termed 'optical molasses' and later Doppler cooling, but now it is more common to simply refer to it as laser cooling. A detailed description of laser cooling can be found in Section 1.4.2

or [4]. The enormous impact of laser cooling and trapping atoms on the field of atomic, molecular, and optical physics was recognised in 1997 when Chu, Cohen-Tannoudji and Phillips were jointly awarded the Nobel Prize in Physics for their work on this technique.

The extension of laser cooling to molecules would seem like a logical progression. However, laser cooling requires the atom or molecule to undergo many cycles of photon absorption-emission to reach temperatures in the millikelvin range. The rotational and vibrational degrees of freedom in molecules lead to more complicated energy level structures compared to atoms, increasing the likelihood of unwanted decay to levels other than the initial state, and making it difficult to find a closed cycling transition. In 2010, twenty-six years after laser cooling was first realised experimentally for atoms, DeMille and co-workers were finally able to demonstrate direct laser cooling of the diatomic molecule strontium monofluoride (SrF) [5]. By carefully selecting the correct molecule and transition, and with a couple of repumping lasers to pump back those lost by off-diagonal vibrational transitions, DeMille was able to eliminate most of the rotational and vibrational branching that limits the optical cycling in other molecules. While direct laser cooling of molecules is a significant achievement, it is limited to a select number of molecules with very specific characteristics, and not generally applicable to most molecules (see Section 1.4.2 for more details on laser cooling molecules).

Due to the difficulty of laser cooling molecules, many of the first attempts at generating cold molecules were instead focused on assembling a molecule from laser cooled alkali-metal atoms. In 1998, photoassociation of laser cooled Cs atoms produced the first translationally cold Cs_2 molecules at a temperature of 300 μK [6]. Later that same year, calcium monohydride (CaH) was cooled via thermalising elastic collisions with a cryogenically cold buffer gas of helium to 400 ± 50 mK and loaded into a magnetic trap. This was the first time that neutral polar molecules were magnetically trapped [7].

Prior to 1998, there were no known techniques to produce cold molecules (as defined in Section 1.2), and indeed very few research groups were even studying cold molecules. By 2005, less than a decade later, there were nine different techniques to generate cold molecules, and more have been developed since then. Details of the commonly used methods to produce cold and ultracold molecules can be found in Section 1.4. Recently, many prominent journals have published special thematic issues on cold molecules, including the New Journal of Physics in 2009 [8], a Faraday Discussion topic later that year [9], Physical Chemistry Chemical Physics in 2011 [10], and most recently Chemical Reviews in 2012 [11].

Clearly, there has been a rapid expansion and development of the field of cold molecules in the past fifteen years. Much of the research involves improving existing techniques and developing new ones to obtain greater densities of colder molecules. However, the interest does not lie so much in simply attaining colder temperatures, but rather in the fascinating applications of cold molecules. For example, cold molecules provide a unique access to many quantum phenomena because their de Broglie wavelengths are comparable to the size and separation of the molecules. The interesting properties of cold molecules and their applications are described in the following section (Section 1.2).

1.2 Cold molecules

1.2.1 Molecular properties in the cold and ultracold regime

The current convention in the field of cold matter is to define ‘cold’ as the temperature regime below approximately 10 K, while ‘ultracold’ corresponds to temperatures below 1 mK. One problem with using temperature to describe a system is that quite often the system is not actually in thermodynamic equilibrium. It then becomes more appropriate to use temperature T as a description of the mean kinetic energy E_{kin} of the ensemble of molecules through the relationship $E_{\text{kin}} = k_{\text{B}}T$, where k_{B} is the Boltzmann constant [12]. Maxwell's relationship between the temperature of a gas and a particular velocity distribution of the atoms or molecules further emphasises the idea that 'cold' refers to slow moving molecules. Furthermore, a molecule has translational, vibrational, and rotational degrees of freedom, each of which can be assigned a separate temperature (vibrational and rotational temperatures are normally defined with respect to a Boltzmann distribution). For example, collisions between translationally cold molecules can still result in the release of large amounts of internal energy if the collision partners are vibrationally or rotationally hot.

While we typically think of molecules as 'particles' at room temperature, their de Broglie wavelength becomes much larger in the cold and ultracold regime, leading to many interesting quantum phenomena. The wave-particle duality of nature was formalised by de Broglie in 1924 when he recognised that the relationship $\lambda = h/p$, which was already known for light, also applied to matter [13]. Here, p is the momentum of the particle, λ is the wavelength of the particle, and h is Planck's constant. Substituting the mass m and velocity v for the momentum gives the relationship $\lambda = h/(mv)$. It is easy to see that at room temperature, when molecules are moving at high speeds, their de Broglie wavelength will be quite small. For example, the molecule ND_3 has a mean speed of 564 ms^{-1} at 300 K, which corresponds to a de Broglie wavelength of only 0.354 Å. When ND_3 is brought into the cold (T < 10 K) or ultracold (T < 1 mK) regime, its mean speed drops dramatically, while its de Broglie wavelength increases to 1.94 and 194 Å, respectively. Table 1.1 summarises the speed and de Broglie wavelength of ND_3 for various temperatures. Chemical bond lengths are typically less than 5 Å, while long range potentials of intermolecular forces operate over distances of around 50 Å [11]. It is clear that the wave-like nature of molecules becomes incredibly important in the ultracold regime, where quantum mechanical effects dominate many of the molecular interactions.

Table 1.1: The mean speed and de Broglie wavelength of ND_3 calculated for various temperatures. Cold and ultracold typically refer to temperatures below approximately 10 K and 1 mK, respectively.

Temperature / K	Mean speed / ms^{-1}	Wavelength / Å
300	564	0.354
10	103	1.94
1	32.5	6.13
1×10^{-3}	1.03	194

In addition to translation, a molecule posseses electronic, vibrational, rotational, and spin degrees of freedom, which can all be described with suitable quantum numbers. At room temperature, not only is the translational temperature of a molecule very high, but a large number of the internal rotational and vibrational quantum states will also be populated. Rate constants or cross sections for elastic, inelastic, or reactive collisions that are obtained at room temperature will result from averaging over these internal quantum states. Furthermore, the relative rotational motion of the reactants and products are described by 'partial wave' quantum numbers. Up to hundreds of partial waves may contribute to the collision rate constants at room temperature.

At ultracold temperatures, however, only the lowest one or two internal quantum states are populated, so rate constants can be obtained for a single internal quantum state. Additionally, the wide range of possible impact parameters or angular momentum states is now highly restricted, collapsing to pure s-wave (bosonic species) or p-wave (fermionic species) collisions in the limiting case [11]. Long-range intermolecular forces between reactants often dominate in chemical reactions involving cold molecules, providing information about the intermolecular potential energy surface [14, 15]. Cold, slow moving molecules can be manipulated with external electric, magnetic, or optical fields. The external fields are used to finely control molecular collisions or to trap the molecules and thereby extend the observation times for chemical reactions [16, 17].

1.2.2 Applications

The large amount of interest in cold molecular sources from many different branches of physics and chemistry stems from the extensive and varied applications of cold molecules. High-resolution spectroscopy [18] and precision measurements, such as determining the small energy differences between enantiomers of chiral molecules [19, 20, 21, 22], clearly benefit from the longer interaction times possible in cold, slow molecular beams. Experiments to determine the permanent electric dipole moment of electrons [23] and the time variation of fundamental constants [24, 25, 26, 27] usually involve cold polar molecules.

New quantum phases may arise from long range interactions of ultracold molecules, and lead to the observation of quantum phenomena on the macroscopic scale [28]. Ultracold molecules have been proposed for use as qubits in the physical realisation of a quantum computer and will be important in the development of quantum information processing [29]. The development and advancement of cold and ultracold molecular sources is critical to many of these applications.

One of the applications gathering a lot of interest at the moment is the use of cold molecules to study low temperature chemistry, ranging from controlled chemical reactions and collision dynamics to astrochemistry. Collision dynamics and studies of inelastic and reactive scattering are now being conducted in the cold and ultracold regimes, providing unique insight into reactive pathways and barriers for many chemical reactions [10]. A significant advantage of low temperature chemistry is the extreme amount of control that can be exerted over the chemical reaction. For example, the vibrational, rotational, electronic and nuclear spin, orientation, and translational degrees of freedom of colliding species can be controlled and quantised when observing chemical reactions at 200 nK, something which is impossible at room temperature [30, 31]. Studying cold chemical reactions - with unprecedented control - makes it possible to test and improve theoretical models. It also unveils details on the underlying potential energy surfaces (PESs) hidden by thermal averaging at higher temperatures.

At low temperatures, it is easier to manipulate and control chemical reactions with external fields [32], and effects such as quantum tunnelling and quantum resonances can play a large role in chemical reactivity [33, 34, 35, 36]. The interstellar medium is the only region where temperatures below 10 K are found naturally, so the study of cold chemical reactions is particularly relevant to astrochemistry.

1.3 Astrochemistry

1.3.1 Overview

The lowest natural temperature ever recorded on the surface of the earth was 184 K at the Vostok research station in Antarctica in 1983 [37]. Temperatures drop to between 100 to 200 K in Earth's upper atmosphere, and are significantly lower in the interstellar medium, explaining the large amount of interest in cold chemical reactions from the field of astrochemistry. Around 10% of the matter in the Milky Way galaxy is found in giant interstellar clouds of dust particles and gas. The diffuse regions of the clouds have temperatures of 50 to 100 K and number densities of approximately 10^2 to 10^3 molecules per cm^{-3}. The number density rises to 10^4 molecules per cm^{-3} in the cold dense core of the clouds where temperatures may be as low as 5 to 10 K [38]. The cosmic microwave background has a temperature of 2.728 K. This is the lowest naturally occurring temperature region with the exception of the Boomerang nebula, whose unusually large rate of mass-loss for a dying star drives an extremely fast adiabatic expansion of gas and leads to temperatures as low as 1 K [39].

The first molecule to be detected in space was the methylidyne radical CH in 1937 [40]. More than 150 molecules (200 including isotopologues) have been detected in space since then, ranging in size from diatomics to polycyclic aromatic hydrocarbons [41]. Despite the low density of molecules in space, cold ion-molecule reactions are very important in the formation of interstellar molecules, the chemical evolution of interstellar clouds and the birth of stars [42].

Photochemical models of the interstellar medium and planetary atmospheres have been developed that require rate coefficients and branching ratios for the relevant chemical reactions [43, 44]. To date, however, only a small fraction of the processes have been studied over a temperature range comparable to those found in space or the planetary atmospheres. In the absence of experimental data, room temperature values are often extrapolated to 10 K or trajectory-scaling formulae are used to approximate the low temperature rate coefficients [45]. The temperature dependence of the rate coefficient for four neutral-neutral reactions is shown in Figure 1.1. A general trend clearly does not exist for all rate coefficients, and extrapolation from room temperature values down to 10 K could lead to an error in the predicted value by several orders of magnitude. Therefore, it is essential to measure these rate coefficients experimentally at low temperatures in order to create a more robust and accurate astronomical database for use in modelling the cold chemistry that occurs in the interstellar medium [46].

1.3.2 Experimental techniques

Several experimental techniques have been developed to study cold chemical reactions. Ion-neutral reactions are particularly important to astrochemistry, and the main techniques used to study this type of reaction are described in this section. The charged species are easily manipulated and stored by electromagnetic fields. Reactions with

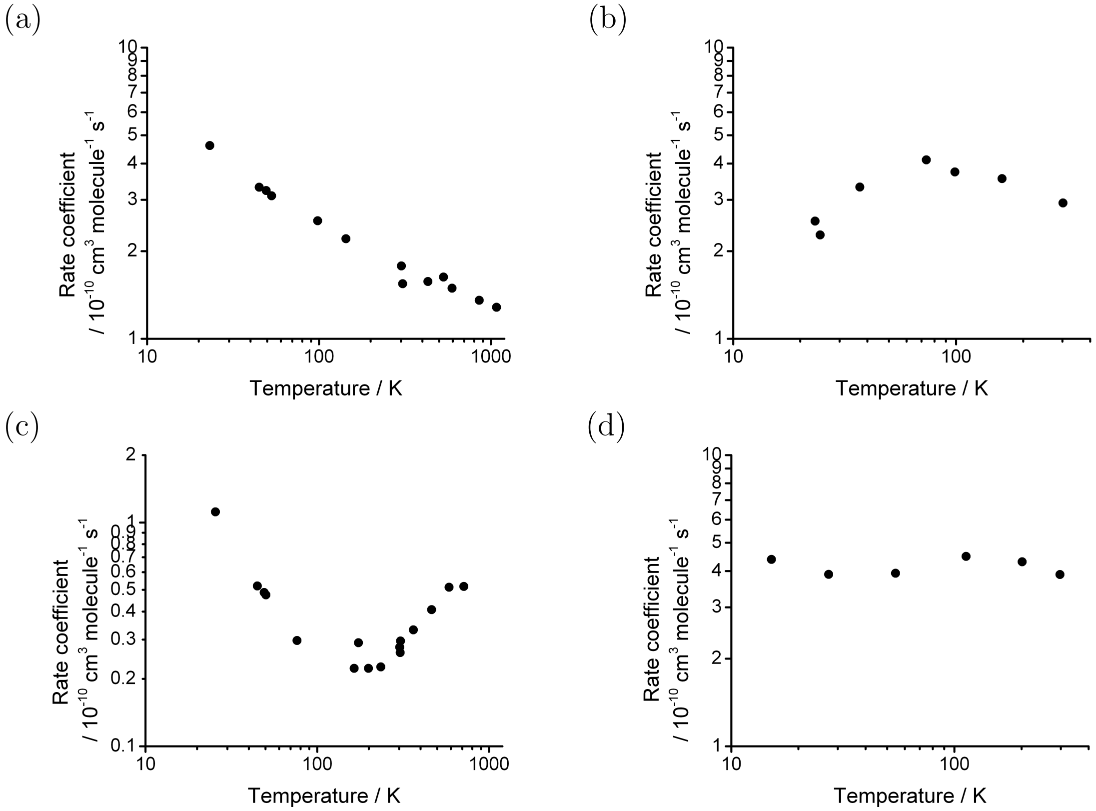

Figure 1.1: Experimentally determined rate coefficients over a wide range of temperatures for four different reactions: (a) Al + O_2 (b) B + C_2H_2 (c) CN + C_2H_6 and (d) CN + $CH_2=C=CH_2$. Data provided from [46].

neutral species, however, are more difficult to study at low temperatures due to condensation or sublimation of the neutral polar gases [47].

Cryogenic cooling

Cryogenic cooling is a simple, but limited technique that involves using a cryogenic fluid to cool the walls of a cell and then introducing a gas mixture into the cell. In order to prevent neutral gas species from condensing on the walls, the reagents must be kept at a partial pressure well below their vapour pressure at the temperature of the wall. This concentration is too low to conduct kinetics experiments for most species. Higher concentrations of ionic species can be used by keeping the particles away from the cell walls with electric or magnetic fields.

Reactions can only be studied at temperatures down to about 80 K when using liquid nitrogen as the coolant [48]. To achieve lower temperatures it is necessary to use a liquid helium cooled drift tube [49]. Another limitation of the technique is that the ions are not in thermodynamic equilibrium with the apparatus, and thus do not have a Maxwell-Boltzmann distribution of velocities. However, cryogenically cooled ion traps lead to long interaction times (up to several milliseconds) and make it possible to study both fast and slow bimolecular reactions (typically $k \sim 10^{-15}$ - 10^{-13} cm^3 molecule^{-1} s^{-1}) [50], and slow radiative association processes [51].

Supersonic expansion

Low-temperature chemical reactions of neutral molecules are most commonly studied using molecular beams generated through supersonic expansion of a non-condensible gas. Conservation of energy dictates that the sum of the specific enthalpy and kinetic energy must remain constant during the adiabatic expansion of a gas, causing the gas to cool as it expands. This is shown in Equation 1.1, where c_p is the specific heat capacity of the gas (which is constant for a perfect gas), T_0 and T are the temperatures of the gas prior to and after expansion, respectively, and u is the supersonic flow velocity [46].

$$c_pT_0 = c_pT + \frac{u^2}{2} \tag{1.1}$$

Free jet expansion occurs when gas in a high pressure reservoir escapes through a small orifice into a low pressure chamber. Although the gas may be cooled to around 100 mK, conditions and flow within the molecular beam are inhomogeneous and the molecules do not exhibit a thermodynamic equilibrium (Fig. 1.2(a)). A molecular beam with a well defined velocity may be produced by inserting a ‘skimmer’ into the supersonic zone of the free jet (Fig. 1.2(b)) [52].

Ion-molecule reactions can be studied using a pulsed supersonic free-jet expansion

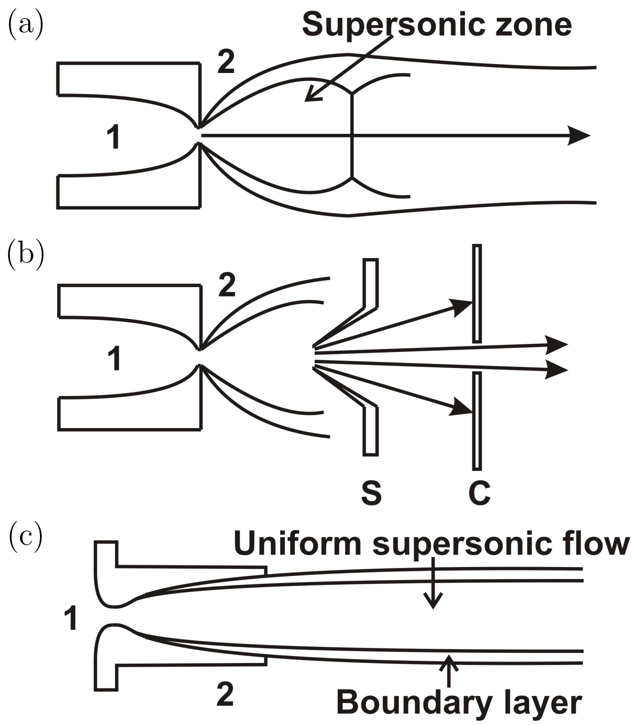

Figure 1.2: Three different types of supersonic expansions are illustrated here, where region 1 is the high pressure reservoir of gas and region 2 is the low pressure chamber. (a) The free jet expansion is simple, but only the supersonic zone is usable; the rest of the beam is inhomogeneous and exhibits complex thermodynamic conditions. (b) A molecular beam with a well defined velocity can be generated by placing a skimmer (S) into the supersonic zone, and directionality achieved by placing a collimator (C) after the skimmer. (c) The convergent-divergent shape of the Laval nozzle allows the gas to expand isentropically, thereby generating a collimated, uniform supersonic flow. Using the Laval nozzle to study low temperature reactions has become known as the CRESU technique (see Section 1.3.2 for more details).

of a mixture of reactant gas, an ion precursor, and a suitable buffer gas [53]. Various ionisation techniques can be used to produce a packet of ions which then flow downstream in the expanding jet beam. Techniques such as electron impact produce several different ion species from the gas mixture, whereas resonance enhanced multiphoton ionisation (REMPI) is a highly selective technique that typically produces only one ionic species. Pulsed-field ionisation techniques can also be used, as was first demonstrated by Mackenzie-Softley [54] and subsequently used by Hsu-Ng [55].

The ions collide with neighbouring neutral species at very low energies as they flow downstream. An electric field applied perpendicular to the axis of the molecular beam is used to eject the ions from the jet in order to be analysed with a time-of-flight (TOF) mass analyser. Using a movable mass spectrometer to detect the parent and product ions allows the temporal progression of chemicals reactions to be studied by varying the distance, and therefore time delay, between the ion production and detection.

Rate coefficients measured for ion-molecule reactions within a free jet expansion can still be associated with an average kinetic temperature despite the lack of thermodynamic equilibrium within the jet (which has a non Maxwell-Boltzmann velocity distribution). The rotational temperature can differ dramatically from the kinetic temperature, however, and is more difficult to model; in some cases lack of data on rotational relaxation at low energies makes the modelling impossible [56].

Crossed molecular beams

Reactive cross sections can also be measured by crossing two molecular beams, making it possible to study neutral-neutral reactions. The reactive cross sections can be determined for very low relative translational energies when the collision angle is very small. A collisional energy of 0.35 kJ/mol, corresponding to a temperature of approximately 30 K, has been achieved by reducing the intersection angle to 22° [57]. Even lower collisional energies (0.066 kJ/mol or $\sim$ 5 K) can be achieved by using a cryocooled pulsed valve to generate the molecular beams [58]. Crossed molecular beams have the additional benefit of a greater collisional frequency compared to studying ion-molecule reactions within a single supersonic beam.

A collisional angle of zero can actually be obtained in merged beam experiments between a supersonic molecular beam and a guided ion beam [59, 60]. Cryogenically cooled traps are used to produce a slow, intense beam of ions, which are then merged with a supersonic beam of neutral molecules at the same terminal velocity as the ion beam, leading to translational collision energies as low as 0.096 kJ/mol ($\sim$ 10 K).

Recently, merged beam experiments have also been demonstrated for neutral-neutral molecules [61].

CRESU

Collimated, uniform supersonic flows can be generated by using a specially designed Laval nozzle which has a convergent-divergent shape (Fig. 1.2(c)) rather than the standard orifice. A local thermodynamic equilibrium exists within the uniform flow of these molecular beams, making them ideally suited to studying low temperature chemical reactions. This has become known as the CRESU technique (Cinétique de Réaction en Ecoulement Supersonic Uniforme / Reaction Kinetics in a Uniform Supersonic Flow), and can be used to study ion-molecule reactions [62] and neutral-neutral reactions in a continuous [63] or pulsed flow version [64]. Similar to the supersonic free jet expansion, ions can be generated by electron impact, REMPI, or other methods and then monitored using a movable mass spectrometer. In this manner, rate coefficients can be measured for temperatures as low as 8 K [65].

One limitation of the CRESU technique is that the Laval nozzle is much larger than the small orifice used in standard supersonic jet expansions, leading to high gas consumption and the need for large pumping capacities. The gas consumption can be reduced by operating with a pulsed rather than a continuous beam. A pulsed valve is placed upstream of the Laval nozzle, or a rotating disk is used to 'chop' the gas in the divergent part of the Laval nozzle [46]. Another limitation of studying chemical reactions using supersonic beams is that only fast rate coefficients can be measured (typically $> 5 \times 10^{-13}$ cm^3 molecule^{-1} s^{-1}) because of the high laboratory velocity associated with the molecular beams.

Summary

The field of astrochemistry relies heavily on the techniques that have been described in this section, most involving molecular beams, to study low temperature reactions. However, the energy resolution is limited by the velocity spread in the beams, the high laboratory velocity of the beams prevents the measurement of rate constants for slow reactions, and the lowest temperatures achieved by these methods are around 10 K. Although thermal equilibrium should be achieved using the CRESU technique, most of the techniques focus on obtaining low translational energies with little control over rotational or vibrational state distribution. In order to study chemical reactions at temperatures significantly lower than 10 K and to gain greater control over the internal degrees of freedom of the reactants, several methods have been developed to produce cold and ultracold molecules in the laboratory. These are detailed in the next section (Section 1.4).

1.4 Methods to produce cold and ultracold molecules

Since the production of the first cold molecule in 1998 using photoassociation [6], many different experimental techniques have been developed to produce cold and ultracold molecules. These techniques can be divided into two main categories: indirect and direct cooling methods. Indirect methods generate cold molecules by combining laser cooled atoms, while direct methods involve cooling pre-existing molecules. A brief description of the theory and technical aspects of the main methods is provided, including some advantages and limitations of each technique.

1.4.1 Indirect methods

Photoassociation

Photoassociation (PA) is a resonant process that occurs when two colliding atoms absorb a photon (γ) and form a bound, electronically excited molecule (Reaction 1.2). The excited molecule then emits a photon and decays to either two free atoms (Reaction 1.3) or to a bound, ground electronic state of the molecule (Reaction 1.4).

$$A + B + \gamma \rightarrow (AB)^* \tag{1.2}$$

$$(AB)^* \rightarrow A + B + \gamma_d \tag{1.3}$$

$$(AB)^* \rightarrow AB + \gamma_d \tag{1.4}$$

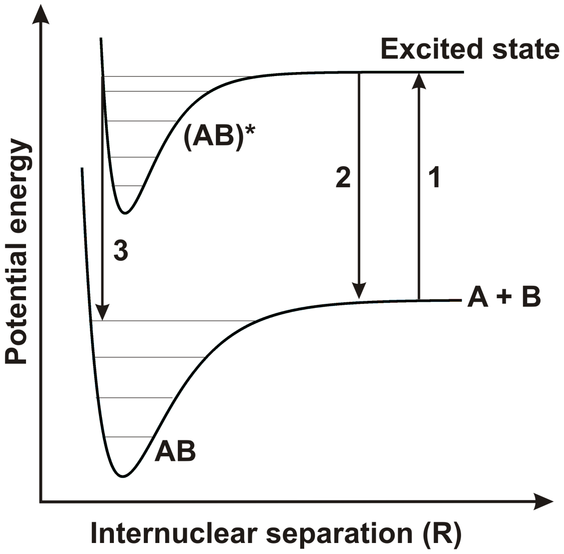

Figure 1.3: Two ultracold, colliding atoms can resonantly absorb a photon to form a bound, excited electronic state by a process called photoassociation (process 1). Spontaneous decay or induced emission of a photon may lead to either two free atoms (process 2) or a bound, ground electronic state of the molecule (process 3).

When the spread in the initial kinetic energy of the colliding atoms is small, then the spread in photon frequencies needed to drive the resonant photoassociation process is also small. This leads to sharply defined resonances for the free → bound photoassociation transitions. Temperatures of 0.5 mK or less are usually required for the two colliding atoms, easily achievable by laser cooling for many atomic species [66].

The two colliding atoms are first laser cooled and held in an atom trap, such as a magneto-optical trap (MOT) or a far-off resonance optical trap (FORT) [67]. A narrow-frequency continuous-wave laser then drives the photoassociation process. Most of the excited molecules decay quickly through spontaneous emission into the separate atoms. Through spontaneous emission or induced emission with a second laser, some molecules can be transferred from the rovibronic level n' of the electronically excited state into a bound level n of the electronic ground state or a low-lying triplet state (Fig. 1.3) [68]. Recent advances have produced a significant number of vibrational ground-state molecules, for example Cs_2 [69] and LiCs molecules [70].

Photoassociation and magneto-association (discussed shortly) are the only currently demonstrated methods to produce ultracold molecules (T $<$ 1 mK). Photoassociation has been used to explore the long-range regions of molecular potential curves and provides information on low energy atomic collision parameters such as scattering length. However, only a small fraction of the cold atoms in the trap are actually photoassociated and spontaneously decay to the bound molecule in the electronic ground state. Those that do are usually in a highly excited vibrational state, despite having a very low translational temperature. This technique is also limited to the production of predominately alkali-metal diatomic molecules. Refer to [71, 72, 73] for further reading on photoassociation.

Feshbach resonances

The coldest molecules that have been produced to date, in the nanokelvin temperature range, are generated through the use of Feshbach resonances in the magneto-association of ultracold atoms. A Feshbach resonance occurs when the energy of a pair of atoms in a non-bound state is identical to the energy of the bound dimer state (associated with a slightly higher energy dissociation asymptote). An external magnetic field can change the molecular interaction potential when the interacting species are paramagnetic, so ramping an external magnetic field across a Feshbach resonance can be used to form Feshbach molecules [74].

For example, if a Feshbach resonance occurs at a magnetic field strength $B = B_0$, the atomic gas is initially prepared in a field $B > B_0$ where the atoms are in a non-bound state. The magnetic field is ramped to a final $B < B_0$, and the non-bound pair of atoms are adiabatically converted into the bound molecular state as the magnetic field passes through the Feshbach resonance (Fig. 1.4). Oscillatory magnetic fields and three-body recombination can also be used to resonantly couple the scattering state to the molecular state and transform the atom pairs into molecules, although the application of a time-varying magnetic field is the more commonly used method [75].

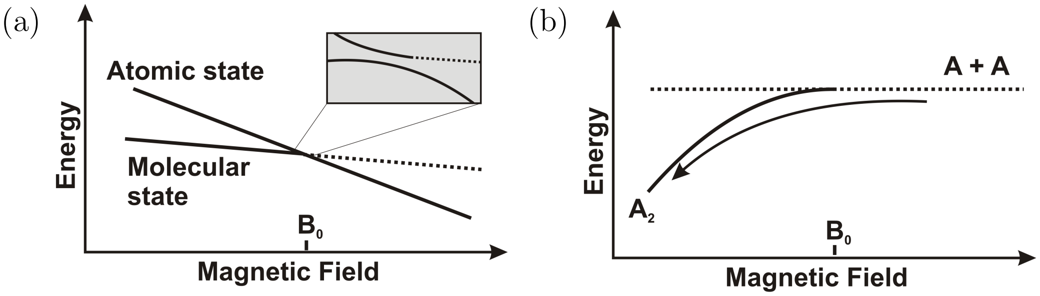

Figure 1.4: (a) The Zeeman energy of the atomic and molecular states can vary with external magnetic field strength for paramagnetic species. In this example, the states cross at B_0, and result in an avoided crossing when the states are coupled. (b) A Feshbach resonance occurs at B_0, where the energy of the two individual atoms (A + A) is identical to the energy of the dimer A_2. Sweeping the external magnetic field across the Feshbach resonance converts the atomic pair (dotted line) into the weakly bound dimer state (solid line).

Feshbach molecules are generally rotationally and translationally cold because the magnetic field is spatially homogeneous and the process does not affect the centre of mass of the atom pairs [76]. The binding energy of the molecule, however, is very low. Stimulated Raman adiabatic passage (STIRAP) employs a two-photon Raman transition that can transfer the Feshbach molecules to more deeply bound states [77, 78, 79]. Similar to photoassociation, the range of molecules that can be formed using Feshbach resonances is limited to diatomic molecules assembled from laser cooled atoms.

1.4.2 Direct methods

Laser cooling

The principle of laser cooling is to use the radiation pressure of light to slow down an atomic beam. A laser beam is tuned slightly below an atomic resonance and focused on an atomic beam. Lasers are tuned slightly below an electronic transition ('red' detuned) in order to exploit the Doppler effect, which selectively enhances photon absorption in atoms moving toward the light source. Photons that hit an atom travelling toward the laser beam will be absorbed, and the atom will slow down due to the momentum imparted by the photon in the collision. The excited atom will spontaneously emit a photon, gaining a 'kick' of momentum equal to the original photon, but this time in a random direction. The net result of the absorption-emission cycle is a reduction in the speed of the atom in the direction of motion. Often, the atomic beam is initially slowed using a 'pre-cooling' laser and then allowed to drift into the intersection region of six pairs of counter-propagating lasers to undergo further cooling [80, 4].

Laser cooling relies on a closed cycle optical transition in order to be effective. After each photon absorption, the atom must return to its initial state through spontaneous decay. Usually one or two 'repump' lasers are necessary to ensure that a sufficient number of atoms remain in the main optical cycle, addressing any population that spontaneously decays to unwanted states [81]. The additional vibrational and rotational degrees of freedom in molecules give rise to a multitude of additional energy levels (which are absent in atomic species). This complexity hinders the creation of a closed cooling cycle. The high probability of decay into (undesirable) levels outside the main cooling cycle means that direct cooling schemes - where they could be devised - would require an impractical number of ‘repumping’ lasers.

In 2010, however, DeMille and co-workers demonstrated direct laser cooling of the diatomic molecule strontium monofluoride (SrF) [5]. By carefully selecting the correct molecule and transition, they were able to eliminate most of the rotational and vibrational branching that limits the optical cycling in other molecules.

The FranckCondon principle is a rule in spectroscopy and quantum chemistry that explains the intensity of vibronic transitions. Vibronic transitions are the simultaneous changes in electronic and vibrational energy levels of a molecule due to the absorption or emission of a photon of the appropriate energy. The principle states that during an electronic transition, a change from one vibrational energy level to another will be more likely to happen if the two vibrational wave functions overlap more significantly.

Franck-Condon factors (FCFs) quantify the overlap between the vibrational wavefunctions of different electronic states and are indicative of the branching ratios to different vibrational levels when a molecule decays from an excited electronic state [82]. When there is little overlap between the two vibrational wavefunctions, as in the case for highly diagonal FCFs, the vibrational energy level is not likely to change during an electronic transition. Highly diagonal FCFs thus prevent vibrational branching in the $X^2\sum_{1/2}^{+} \rightarrow A^2\Pi_{1/2}$ electronic transition of SrF used by DeMille. Selecting the P branch $N = 1 \rightarrow N' = 0$ type rotational transition prevents rotational branching. Population loss to the dark Zeeman sublevels of the ground state is avoided by applying a magnetic field that remixes the dark states back into bright states [83]. Finally, use of an electro-optic modulator means that all four hyperfine structure levels of the $X(N = 1)$ state of SrF can be pumped with the same laser [81]. Directly laser cooling molecules is a remarkable achievement. However, it is limited to a select number of molecules with very specific characteristics, such as highly diagonal Franck-Condon factors, and is thus not generally applicable to most molecules.

Evaporative cooling is often employed after laser cooling to obtain even colder atoms. A cloud of laser-cooled atoms are prepared in a magnetic trap. The atoms are in thermal equilibrium, and consequently display a Boltzmann distribution of energies. The trap depth is lowered slightly so that only the hottest atoms ‘escape’ from the trap. Collisions between atoms remaining in the trap lead to a new thermal equilibrium at a lower temperature, and repeating the process many times leads to further cooling. Although in practise the trap depth is continuously ramped down without allowing rethermalisation to occur, the hottest atoms are still selectively lost from the trap [4].

Theoretically, it should be possible to evaporatively cool molecules with elastic and inelastic collision cross-sections comparable to atoms at low temperatures. Recently, progress has been made toward demonstrating this experimentally. A Stark-decelerated beam of neutral hydroxyl molecules (OH) is loaded into a high-gradient magnetic quadrupole trap. Microwave-forced evaporative cooling (using a radio frequency knife edge) reduces the temperature of the trapped molecules from 45 mK to 5.1 mK, while simultaneously increasing the phase space density [84]. Further progress in the evaporative cooling of molecules has the potential to lead to many fascinating discoveries in the future.

Collisional methods

Buffer-gas cooling

In stark contrast to the limited range of molecules for which laser cooling is applicable, buffer-gas cooling is a versatile method of direct cooling that can be applied to many different atoms and molecules. Molecules are introduced into a buffer gas cell containing cold helium gas, where they thermalise with the helium buffer gas through elastic collisions. Any molecules that collide with the cell wall freeze and are lost from the cooling process. Depending on the experimental set-up, temperatures as low as a few hundred millikelvin can be obtained [85].

One of the main experimental challenges of this technique is the introduction of the molecules into the buffer gas cell. This is usually the limiting factor in the number of molecules that can be cooled and trapped. Laser ablation, capillary filling, and the use of a molecular beam are the main methods used to deliver molecules to the buffer gas cell. Laser ablation is favoured for studies involving unstable species because the molecules are actually produced within the cell. Yield and molecular variety tend to be limited, however [86, 87]. Capillary filling is well suited to molecules that remain gaseous at low temperatures, while the most general technique is to use a molecular beam from a room temperature source to load molecules into the buffer gas cell [88].

The other technical difficulty is actually studying or using the cold molecules generated by this technique without interference from the buffer gas. One solution is to surround the buffer gas cell with a pair of superconducting coils in an anti-Helmholtz configuration. Once the molecules have been buffer-gas-cooled, the magnetic field is able to trap the paramagnetic species of interest inside the cell while the buffer gas is pumped away [89]. A second solution is to allow the molecular species to diffuse out of the cell through an exit aperture and then move the molecular species away from the buffer gas cell through a magnetic guide [90], or for polar molecules, an electrostatic guide (used in our experimental set-up) [91]. Further details on the theory of buffer-gas cooling and the experimental apparatus used in this work can be found in Section 2.1 and Section 3.5, respectively.

Crossed beam

The second collisional method that can be used to produce cold molecules is based on billiard ball-like, single collision events in crossed or opposing molecular beams. The cancellation of the laboratory velocity of the scattered molecules can occur when the laboratory velocity of the centre-of-mass (COM) of the colliding partners is equal in magnitude but opposite in direction to the centre-of-mass recoil velocity of the scattered molecules. The kinematic collapse of the laboratory velocity only occurs when the molecule recoils opposite to the direction of the COM motion. Molecules that recoil in all other directions experience increased laboratory velocities. The molecules with enhanced laboratory velocities quickly leave the scattering centre while the slowed molecules remain behind. Although only a small fraction (10^{-5}) of the collisions between a pulsed molecular beam of nitric oxide (NO) and a beam of argon satisfy the necessary conditions for the cancellation of the laboratory velocity for NO, for example, it is still possible to produce approximately 10^5 molecules of slow NO per pulse [92].

Using this method, Elioff and co-workers have produced translationally cold NO molecules with a velocity distribution centred about zero and an upper limit root mean square (RMS) velocity of 15 ±1 ms^{-1}, equivalent to a temperature of 406 ±23 mK. The inelastic collisions between the pulsed beam of NO and a beam of argon produced 10^8 to 10^9 molecules per cubic centimetre of NO in a single quantum state ($^2\Pi_{1/2}$, $\nu = 0$, $j' = 15/2$) [93]. The ability to prepare molecules in a single, selectable ro-vibronic quantum state is ideally suited for subsequently trapping the molecule.

In principle, this is an incredibly general technique because it depends only on the energy and momenta of the colliding partners rather than on their physical properties. Elastic collisions will also generate slow molecules for collision partners with identical mass. Another advantage is that the experimental equipment and conditions needed for crossed atomic and molecular beam experiments are relatively simple and accessible [92].

A modification of this method involves using an exothermic reaction between counter-propagating atomic and molecular beams to produce translationally cold molecules. A large difference in mass of the products and highly specific initial beam velocities are required. Liu and Loesch used counter-propagating beams of potassium atoms and HBr molecules to generate, through reactive collisions, a translationally cold beam of

KBr molecules with a velocity distribution peaking at 42.5 m/s, corresponding to a temperature of 13 K. To date, this method has only been used to generate metal-halogen molecules from the reactive collision of type Me + HX → MeX + H [94].

In the centre-of-mass (COM) frame of the collision, the speed of the product molecule MeX is proportional to the ratio of the mass of the products ($m_H/(m_H + m_{MeH})$), and is also dependent on the total energy available to the products. The total energy depends on the relative kinetic energy of the reagents, the internal rovibrational energy of the HX molecule, and the energy released by the process. The extremely small mass ratio is the dominating factor in producing slow MeX product molecules. Additionally, some of the total energy is transferred into the internal degrees of freedom of MeX rather than into translational energy, leading to even slower product molecules [95].

The velocity of the MeX molecule in the laboratory frame of reference, however, is the sum of its velocity in the COM frame and the speed of the COM frame itself (relative to the lab frame). In order to produce slow MeX molecules in the laboratory frame, the collision kinematics of the reagents are carefully selected such that the velocity of the COM frame approaches zero. This is the case when the counter-propagating reagent beams fulfil the relation $m_{HX}v_{HX} = -m_{Me}v_{Me}$ [95].

Decelerating beams

Molecular beams are created by allowing gas to escape from a high pressure source through an aperture and into vacuum. The supersonic expansion of the gas creates a beam of rotationally cold molecules with a very narrow velocity distribution. Molecular densities of 10^{13} molecules/cm^3 are typically produced in a pulsed molecular beam. However, the vibrational degrees of freedom are not efficiently cooled, and although translational temperatures of approximately 1 K are achieved in the moving beam frame, the absolute velocity of the molecules in the laboratory frame is very high [96, 97]. Three main techniques have been developed that use external fields to slow the laboratory velocity of a packet of molecules within the pulsed molecular beam: Stark deceleration, Zeeman deceleration, and optical deceleration.

Stark deceleration

Inhomogeneous electric fields are used to slow the longitudinal velocity of a beam of polar molecules in Stark deceleration. The interaction between polar molecules and an external electric field is described by the Stark effect. Molecules with a positive Stark effect gain potential energy with increasing electric field strength, and are termed 'low-field-seeking' molecules. 'High-field-seeking' molecules exhibit a negative Stark effect and lose potential energy with increasing electric field strength. The sign and strength of the Stark effect is quantum-state specific [98]. Further details are provided in Section 2.2.1.

Some recent alternative designs include a chip-based decelerator [99], a ring-electrode decelerator [100], and a Rydberg-Stark decelerator [101]. In its original design, a Stark decelerator is composed of many stages of electrode pairs held at opposite polarity, as shown in Figure 1.5(a). The electrode pairs generate a series of electric fields along the axis of the decelerator which is aligned to the molecular beam axis. A low-field seeking molecule will lose kinetic energy as it travels along the molecular beam axis until it reaches an electric field maximum, located between the electrodes. At this point, the molecule has climbed to the top of the potential hill and lost the maximum kinetic energy possible.

The molecule will re-gain the same amount of kinetic energy if it is allowed to travel down the opposite side of the potential hill. Instead, the electrode polarity is abruptly switched when the molecule reaches the region of high electric field, so that the molecule suddenly finds itself at the foot of another potential hill (Fig. 1.5(b)). Kinetic energy is removed continually from the molecules by using time-varying inhomogeneous electric fields. The process must be repeated many times in order to significantly decelerate the molecular beam, so a typical Stark decelerator consists of around 100 electrode pairs [102].

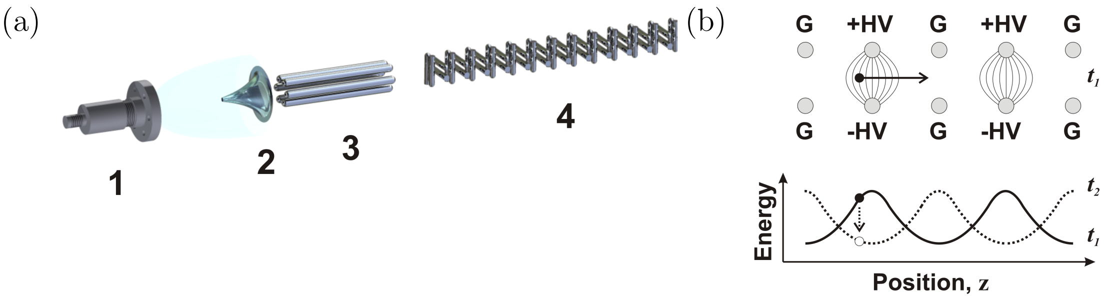

Figure 1.5: (a) Design of a typical Stark decelerator. The molecular beam emerges from the pulsed nozzle (1), passes through a skimmer (2), and enters an electrostatic hexapole (3) that focuses the low-field seeking molecules into the decelerator stages (4). (b) The low-field seeking molecules lose energy as they approach a pair of high voltage electrodes and are forced to climb up the Stark potential energy curve at time t_1. Just before a molecular packet reaches the top, the high voltages are switched to the adjacent pair of electrodes to give the potential curved at time t_2 (dashed line). The molecular packet gradually loses energy and is slowed by repeating the process many times along the length of the decelerator.

The amount of kinetic energy removed from a molecule at each stage depends on its Stark effect, its position when the fields are switched, and the strength of the external field. Therefore, only a small packet of molecules in the same quantum state and with positions and velocities within the acceptance range are simultaneously decelerated during the operation of a Stark decelerator. The compact molecular packet is confined transversely for low-field seeking states because there is always an electric field minimum on the molecular beam axis relative to the electrodes, and exits the decelerator with a reduced laboratory velocity [68].

Stark deceleration produces molecules in a single quantum state with a tunable velocity. However, the range of molecules that can be decelerated is limited to polar molecules that exhibit a strong Stark effect. Additionally, the cold molecules are produced in packets, typically with a density of around 10^6 molecules/cm^3, rather than as continuous source.

Zeeman deceleration

Following the success of Stark deceleration, a magnetic analogue was proposed in order to extend molecular beam deceleration to a broader range of molecules, specifically paramagnetic species. It was only in 2007, however, that Zeeman deceleration (the Zeeman effect describes the interaction between a molecule and an external magnetic field) was demonstrated experimentally with hydrogen and deuterium atoms in the ground state [103]. Metastable neon atoms [104] and O_2 molecules [105] have now also been decelerated down to 50 $\mathrm{ms^{-1}}$ by increasing the number of deceleration stages from six to sixty-four.

The rapid switching of high magnetic fields posed the biggest experimental challenge. The solution was to create the magnetic deceleration stages from insulated copper wire coiled into solenoids. The solenoid axis is aligned to the molecular beam axis in order to create a transversely confining force. Magnetic fields of about 2 T are generated at the solenoid centre when pulsed currents of up to 300 A are applied to the coils, with rise and fall times as short as 5 ms. Rapidly switching the current on and off generates a large amount of heat that must be safely dissipated to prevent over-heating, so water-cooled ceramic pieces are thermally connected to the solenoids.

Optical deceleration

In addition to directly laser cooling atoms and molecules, lasers can be used to decelerate molecules through a kind of optical tweezer effect. Whereas Stark (Zeeman) deceleration can only be applied to polar (paramagnetic) molecules, optical deceleration can be applied to a wide range of neutral molecules that can be polarised using an intense optical field [106]. The force exerted by the optical field of a single laser beam is sufficient to decelerate neutral, polarisable molecules a small amount [107].

A more effective method is to use two opposing laser beams whose interference forms an optical lattice. Each lattice site represents a potential minimum that, by adjusting the frequency difference of the two lasers, moves at the same velocity as the molecular beam. The molecules are then decelerated by gradually reducing the lattice velocity [108]. Thus, the potential minimum actually moves along the beam axis with the molecules in optical deceleration. Recently, a moving potential has been applied to Stark and Zeeman deceleration as well [100, 109].

Velocity filters

A sample of gas from an effusive source exhibits a Maxwell-Boltzmann distribution of velocities, so even at room temperature there is a small fraction of molecules with very low translational energy. Electrostatic velocity selection separates molecules in the low-velocity tail of the distribution from the rest of the molecules in the effusive source. A voltage is applied to the guide electrodes, typically in a quadrupole or hexapole arrangement, to create an electric field minimum along the guide axis that transversely confines the low velocity molecules. Longitudinal velocity selection is achieved by curving the electrostatic guide so that only the slowest molecules are successfully guided around the bend [110].

Molecules with translational temperatures of a few Kelvin can be obtained with this method. However, the rotational degrees of freedom are not cooled by this method, and the internal temperature of the molecules are known to resemble that of the source. The translationally cold molecules can then be used for various applications such as the study of ion-molecule reactions with laser cooled and trapped ions [111].

Translationally cold polar molecules are selected using electrostatic velocity filters, but an equivalent method can be employed to select cold paramagnetic molecules using magnetic octapole filters [112, 113]. An electrostatic quadrupole guide is used in this work; further details on the theory of electrostatic velocity filtering and the experimental apparatus can be found in Section 2.3 and Section 3.6, respectively.

Other methods

Sisyphus cooling

Recently, an optoelectrical cooling scheme based on a Sisyphus-type cooling cycle has been demonstrated for polar molecules [114]. Standard laser cooling methods rely on closed cycle transitions in order to achieve significant photon momentum transfer. Although more common in atoms, closed cycle transitions are not generally present in molecules. Laboratory electric fields, however, can produce significant energy level shifts in polar molecules. The proposed Sisyphus cooling relies on the electric-field interaction energy rather than photon recoil to remove energy from the molecules (Fig. 1.6).

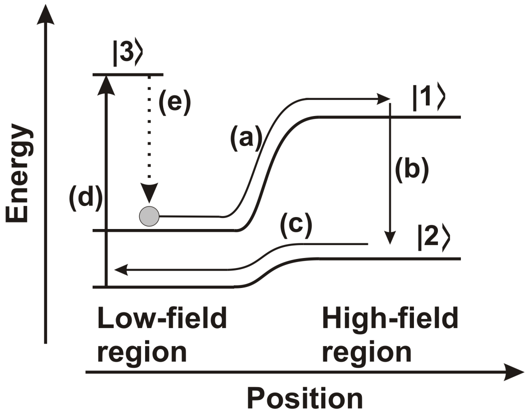

Figure 1.6: Schematic illustrating a cycle of Sisyphus cooling. (a) Diffusion of the molecule in a strong, LFS state |1⟩ from a low-field region to a high-field region. (b) Transfer of the molecule from a strong, LFS state |1⟩ to a weak, LFS state |2⟩. (c) The molecule moves back to the low-field region. (d) Transfer of the molecule to an excited state |3⟩. (e) Spontaneous decay of the molecule back to the original state |1⟩ (irreversible). Modified from [115].

An electrostatic trap consisting of a low-field and high-field region is used to produce a potential step for the trapped molecules as they move between the two regions. The Stark state of the molecule determines its effective dipole moment with respect to the electric field, and therefore the potential energy difference between the two electric field regions. When moved between regions with different electric field strengths, a molecule exhibiting a strong Stark shift will experience a larger change in potential energy compared to a molecule in a weak Stark state. The first step in the cooling process is to transfer a molecule in a strong, low-field seeking (LFS) Stark state $|1\rangle$ (Fig. 1.6) from a low-field to a high-field region through diffusion. The molecule is driven into a weak, low-field seeking state $|2\rangle$ before moving back to the low-field region. Finally, the molecule is driven from the weak state to an excited state $|3\rangle$, before spontaneously decaying back to the original strong Stark state $|1\rangle$. The spontaneous emission of the photon removes kinetic energy from the molecule, equivalent to the energy difference between the potential step for the strong and weak Stark states of the molecule. Repeated cycles leads to overall cooling of the molecule, as demonstrated in [115].

Helium nanodroplets

Most of the techniques described thus far have been for generating isolated, neutral cold molecules. Helium nanodroplets, on the other hand, are ideally suited to studying highly reactive, transient species, such as radicals. The reactive particles are immersed directly into the helium nanodroplet, where they thermalise with the cold helium. This technique has also significantly enhanced molecular spectroscopy [116, 117].

The nanodroplets are produced by supersonic expansion of a low temperature (5 - 25 K) and high pressure (5 - 45 bar) source of helium, and are further cooled through evaporation to temperatures of a few hundred millikelvin. The nanodroplets typically contain thousands of helium atoms, and are passed through a vapour ‘pickup cell’ in order to incorporate atoms or molecules into the droplet.

All degrees of freedom of the introduced species are cooled through thermalisation in the cryogenic nanodroplet [118]. Cold molecules may also be produced within the nanodroplet when a droplet accepts two or more particles that recombine to form a cold molecule. Although many of the studies reported to date have employed heteronuclear alkali dimers such as NaK, LiCs, and NaCs [119, 120], even large oligomers may form through this method [121]. A recently proposed extension of this technique is to ionise the nanodroplets by electron impact, apply a stopping potential to the droplet, and then photo-desorb the cold molecules and confine them within an electrostatic trap [120].

Mechanical methods

In 1978, Moon and co-workers used ultra-high-speed rotors to accelerate molecular beams to velocities greater than 2000 ms^{-1}. The rotor tip is coupled to the molecular beam by depositing an evaporable solid on the rotor, and then increasing the vapour pressure of the beam material by heating the rotor. The rotor tip velocity is added to the normal Maxwellian thermal velocity (for a given temperature) to yield the net velocity of the molecules leaving the rotor surface [122]. It was not until 1999 that Herschbach used the same principle, but in reverse, to generate cold molecules. By mounting a molecular beam source to a backward rotating high-speed rotor, the rotor velocity effectively cancels the flow velocity of the gas and leads to a molecular beam travelling at significantly reduced laboratory velocities. Velocities of less than 70 ms^{-1}, corresponding to a kinetic energy below 10 K, were achieved for molecular beams of O_2 [123, 124]. This is a versatile and relatively simple technique to generate cold molecules, and addresses the main limitation of supersonic beams, namely their high laboratory velocity. However, the technique is limited by a low beam intensity and large background pressure resulting from the continuous 360 ° spray of gas exiting from the rotor tip.

A closely related technique was used to slow a beam of helium atoms with a backward-rotating silicon paddle. An atomic mirror, rather than the molecular beam source, is mounted to the tip of a spinning rotor. The mean velocity of the supersonic beam is reduced by elastic reflection from the receding atomic mirror, a Si-H crystal in this case. It is necessary to use a rotating rather than a linearly receding mirror in order to achieve sufficiently high mirror velocities to cool the beam. The helium atoms were slowed from 511 ± 9 ms^{-1} to 265 ms^{-1} and exhibit a temperature of less than 250 mK in the co-moving frame of the rotating atomic mirror [97].

Recently, a mechanical filter has been successfully implemented to obtain slow macromolecules (masses up to 6000 amu) from an effusive source. The rotating helical velocity selector only transmits molecules of a specific velocity through the twisting vertical grooves in the outer rim of the selector. The angular velocity of the rotor determines the mean velocity of the transmitted molecules while the aspect ratio (width/length) of the milled grooves dictates the velocity spread [125].

A similar concept has been proposed [126] and implemented [127] that uses a rotating, spiral electrostatic guide to decelerate molecules by forcing them to climb a centrifugal potential hill. The molecules enter the guide at the outer edge and are guided along the spiral trajectory to the centre of the rotation, losing kinetic energy as it is converted to centrifugal potential energy. Only molecules with a specific range of velocities are successfully guided for a given frequency of rotation of the guide. Therefore, it is possible to tune the centrifuge decelerator to a specific rotational speed that will accept a small range of input velocities for molecules that are then decelerated to the desired range of output velocities. The rotating spiral guide was technically difficult to build, and was finally achieved by using four disks with specially grooved edges to form the electrodes of the guide [127].

1.4.3 Summary of methods

There currently exists a wide range of experimental techniques that can be used to produce cold and ultracold molecules. A summary of the main techniques is provided in Table 1.2. This has been a relatively recent and rapid progression, considering it was only in 1998 that the first cold molecule was produced in the laboratory using photoassociation [6]. The main challenges for experimental techniques are to produce samples of greater density at even colder temperatures, and to increase the chemical variety of the cold molecules [10]. Currently, the only methods that can produce ultracold molecules are the indirect methods of photoassociation and magnetoassociation. The wide array of direct methods have only been able to achieve temperatures in the millikelvin range. Although the types of molecules that can be cooled is no longer limited to bi-alkali dimers and small molecules, further expanding the variety of molecules that can be cooled, especially to include large polyatomic molecules, will lead to many interesting developments and discoveries in the field of cold chemistry.

1.5 Outline of this thesis

This thesis describes the design, construction, operation, and characterisation of an experimental apparatus that provides a source of cold molecules for studying ion-molecule reactions at low temperatures. Two different experimental techniques for producing cold molecules, buffer-gas cooling and electrostatic velocity filtering, are combined in order to generate a rotationally and translationally cold molecular beam. A detailed description of the buffer-gas cooling process, an overview of the interaction of polar molecules with external electric fields, and Monte Carlo simulations of the electrostatic guiding are provided in Chapter 2. The Monte Carlo simulations were used to develop the design and geometry of the experimental apparatus.

Chapter 3 details the design and construction of the experimental apparatus. An

Table 1.2: The main experimental techniques used to produce cold molecules are listed along with the species that have been successfully cooled using that method, modified from [68]. If the molecules were trapped after cooling, then the temperature T of the sample is given, otherwise the final velocity v of the decelerated molecules is provided instead. Also listed is the number of molecules N typically obtained using that method of cooling.

Method	Molecule	T or ν	N
Photoassociation	Rb_2, Cs_2, He_2^*, H_2, Li_2, Na_2, K_2, Ca_2, KRb, RbCs, NaCs, LiCs, LiRb	30 μK	2×10^5
Feshbach resonances	Li_2, K_2, Cs_2, Rb_2, Na_2, Cs_3, KRb	50 nK	$> 10^5$
Laser cooling	SrF	50 mK	no data
Buffer-gas cooling	CaH, CaF, VO, PbO, NH, ND, CrH, MnH	400 mK	$> 10^8$
Velocity filters	H_2CO, ND_3, CH_3F, D_2O	1 K	10^9 molecules/s
Stark deceleration and trapping	$^{14}NH_3$, $^{15}NH_3$, $^{14}ND_3$, $^{15}ND_3$, CO^*, OH, OD, NH^*, SO_2, YbF, H_2CO, C_7H_5N	5 mK	10^6
Rydberg deceleration	H_2	-10% E_{kin}	no data
Zeeman deceleration	O_2	50 ms^{-1}	no data
Optical deceleration	C_6H_6, NO	295 or 242 ms^{-1}	no data
Collisions/reactions	NO/KBr	400 mK/15 ms^{-1}	no data
Mechanical methods	O_2, CH_3F, perfluorinated C_60	70 or 11 ms^{-1}	no data

introduction to experimental techniques in the cryogenic regime is provided, including some basic principles of pulse-tube cryocoolers, cryogenic materials, and specialised temperature sensors. Heat transfer is an incredibly important aspect of the experimental design. Heat shields are constructed to reduce the thermal radiation and heat load placed on the cryocooler. The buffer gas line is thermally connected to the cryocooler stages in order to deliver cold buffer gas molecules to the buffer gas cell. Conversely, the molecular gas line must be thermally disconnected from the cryogenic environment to prevent the molecular gas from freezing. Details of the electrostatic guide are provided, including descriptions of the electrodes, insulators, and operation of the guide.

The electrostatic guide is loaded with the buffer-gas-cooled molecules in the main cryogenic chamber, and delivers a continuous beam of rotationally and translationally cold molecules to the detection chamber. Chapter 4 describes the characterisation of the cold molecular beam using mass spectrometry. Experimental results are provided showing the effect of changing the buffer gas and molecular gas densities on the molecular flux. Experiments conducted to determine the velocity distributions of the guided molecular beam are also detailed here. From these experiments, it was possible to determine the 'optimal' operating conditions for the buffer gas cell for each molecule of interest. One of the advantages of this source of cold molecules is its applicability to a large range of neutral polar molecules. Although detailed characterisations are only provided for ND_3 and CH_3F, extension to other molecules should be trivial.

In a later modification of the experimental apparatus and detection chamber, (2+1) REMPI was used to analyse the cold molecular beam (in place of mass spectrometry). The modified REMPI apparatus and subsequent experimental results are described in Chapter 5. PGOPHER simulations are used to help analyse the (2+1) REMPI spectra and determine the rotational state distribution in the ND_3 molecular beam. Details are provided showing how the molecular gas density, buffer gas density, and temperature of the buffer gas cell influences the rotational state distribution of ND_3. A brief description of the (2+1) REMPI spectra of the ammonia isotopologues is also provided.

Chapter 6 highlights the main results of this thesis, which describes the construction and operation of an experimental apparatus that produces a beam of translationally and rotationally cold molecules. It also provides details about using this buffer-gas-cooled source of molecules for studying low temperature chemical reactions. At the time of writing, the apparatus will shortly be combined with a linear Paul trap in order to study reactions between the cold molecular beam and Coulomb crystals formed from laser cooled ions within the trap. A brief description of linear Paul traps and Coulomb crystals is provided. This is followed by a description of the experimental apparatus that combines the cold molecular source with the ion trap. The chapter concludes with a short disscussion of the first target reactions that will be studied with this new experimental apparatus, such as $CH_3F + Ca^+ \rightarrow CH_3 + CaF^+$.

Chapter 2

Theoretical calculations and simulations of buffer gas cooling and electrostatic guiding

In this work, a cold, slow molecular beam source has been constructed to facilitate the study of cold ion-molecule reactions. This has been achieved through the combination of two direct cooling techniques: buffer gas cooling and electrostatic velocity selection (Figure 2.1). A more detailed description of the theory behind these two techniques is provided in this chapter; refer to Section 2.1 for buffer gas cooling and Section 2.3 for electrostatic velocity selection.

The manipulation of polar molecules with electric fields is critical for electrostatic velocity selection. As such, a detailed examination of the molecular Stark effect is presented in Section 2.2.1 and Appendix A. Section 2.4 outlines the Monte Carlo simulations that were performed to guide the design of the apparatus, to provide information about the cooling process, and to aid data analysis.

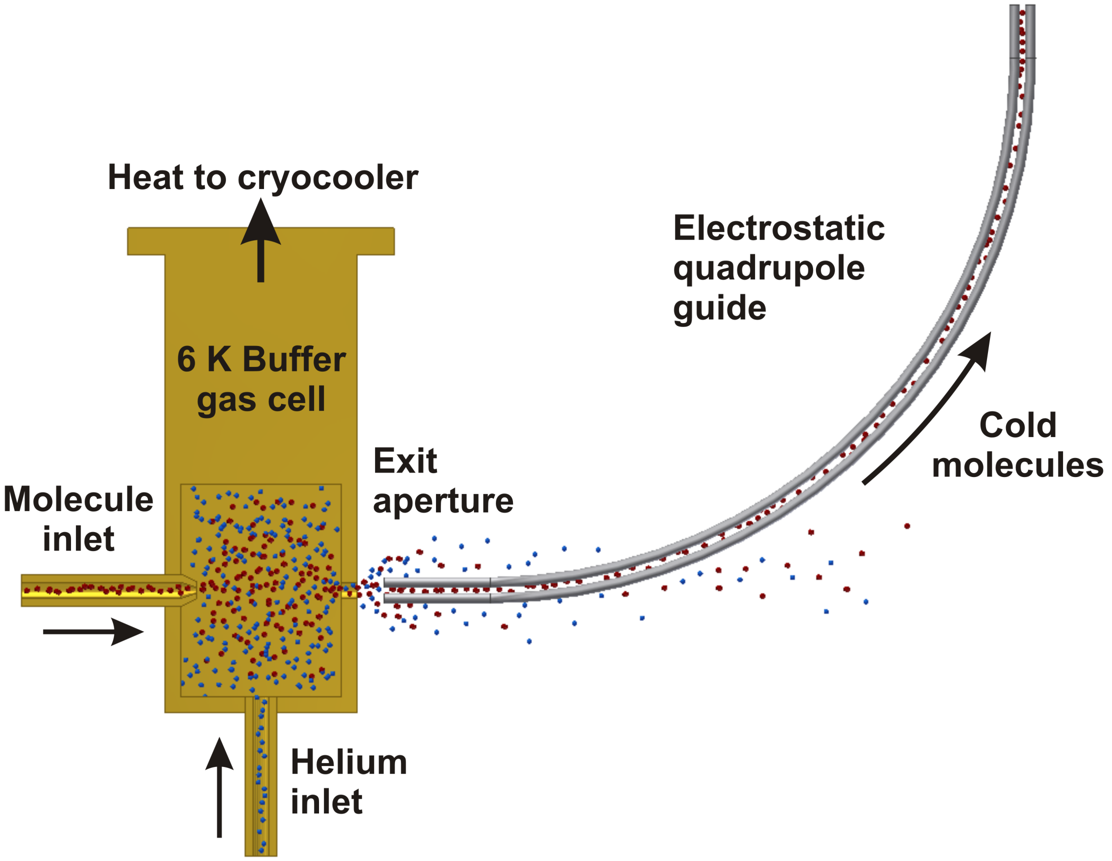

Figure 2.1: Cross sectional view of the cryogenic buffer gas cell that provides a source of internally cold molecules for loading into the electrostatic quadrupole guide velocity selector.

2.1 Theory of buffer gas cooling

Whilst molecular beams generated from supersonic expansion have been an important tool in the study of low temperature chemistry, the main disadvantages of the technique are the high laboratory velocity and the low flux of the molecular beam. Buffer-gas-cooled molecular beams overcome both of these limitations, producing higher fluxes of molecules that are slow moving in the laboratory frame.

The basic principle of buffer gas cooling is to fill a cold cell (2 - 20 K, achieved with a cryogenic refrigerator) with a buffer gas that exhibits sufficiently high vapour pressure at low temperatures, such as helium. Hot molecules (150 to 10,000 K) are introduced to the cell and thermalise with the buffer gas through elastic and inelastic collisions. Inelastic collisions change the rotational state of the molecules, and are therefore important for rotational cooling. The buffer-gas-cooled molecular beam is generated by letting the molecules escape from the cold cell through a small aperture into a high vacuum region (Figure 2.2); this may be effusively or with hydrodynamic enhancement, depending on the cell parameters.

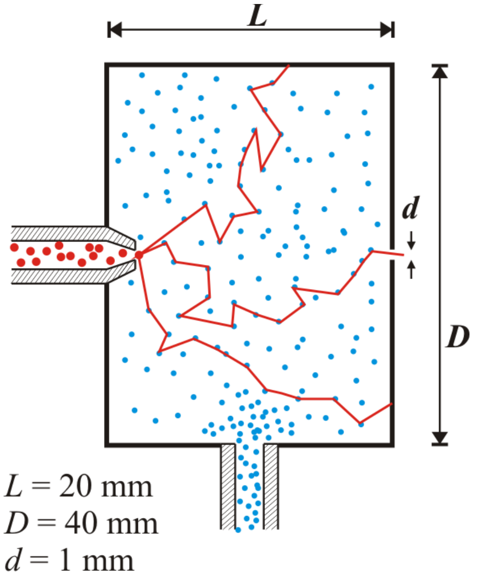

Figure 2.2: Schematic illustrating buffer gas cooling. Molecules (red) enter the cold cell where they thermalise with the cold buffer gas (blue), such as helium, through elastic collisions. Molecules exit the buffer gas cell through random diffusion to the exit aperture; those that hit the cell wall become frozen to the wall. For high buffer gas flows, the molecules are carried out of the cell by the buffer gas via hydrodynamic effects. Dimensions for the buffer gas cell used in this work are also provided.

Compared to supersonic expansion, a relatively low density of buffer gas is needed to achieve sufficient cooling of the molecules. This means buffer-gas-cooled beams can be operated in a continuous rather than pulsed mode without excessive consumption of gas. In addition to the lower gas output, the cryogenic surfaces help to produce a good vacuum within the chamber without the need for powerful external pumps. Since this direct method of cooling is independent of internal molecular structure, it is generally applicable to a wide range of molecules and cools both the translational and rotational (but not vibrational) motions of the molecules [136].

A description of the various stages of buffer gas cooling is provided in this section, including the introduction of molecules into the cell (Section 2.1.1), thermalisation with the buffer gas (Section 2.1.2), and extraction of the molecules (Section 2.1.3). The properties of the buffer-gas-cooled beams are also described, such as typical forward velocity and angular spread of the molecular beam (Section 2.1.4). In some sections, quantitative descriptions of the processes are included, which depend on cell geometry, molecular and buffer gas species, and other conditions within the cell. Most of the physical parameters used in example calculations are based on the buffer gas cell constructed in this work. These parameters are within standard ranges and represent a reasonable description of the processes within most buffer gas cells. Refer to Section 3.5 for technical details of the buffer gas cell used in this work.

2.1.1 Methods of introducing molecules to the cell

Several different techniques can be used to introduce the species of interest into the buffer gas cell, such as laser ablation, laser-induced atomic desorption (LIAD), beam injection, capillary filling, and discharge etching [137]. The number density of the molecular species is usually less than 1% of the density of the buffer gas for all of the standard techniques used to load the cell. One of the reasons for this is to ensure that molecule-molecule collisions can be neglected. The following description will be limited to the two most common techniques - capillary filling and laser ablation.

Capillary filling

Capillary filling is theoretically the simplest method for introducing the species of interest into the buffer gas cell - the molecules simply enter the cell through a gas fill line. However, the method is limited to molecules with an appreciable vapour pressure at temperatures around 150 to 300 K, and presents several technical challenges in the construction of the cell. The fill line must be thermally isolated from the cell and kept at a sufficiently high temperature so the molecules do not freeze at any point in the line, even when they enter the cell. The method can still be used for molecules which only have appreciable vapour pressure at temperatures above room temperature (up to about 600 K) by using an oven to produce the vapour. However, a complex, multi-stage cell is required to prevent the cell from being exposed to the heat released by the oven [90]. Capillary filling leads to a relatively stable environment within the cell, and ultimately continuous and high-flux molecular beams. This is the method used in this work, and the technical details of the molecular gas line can be found in Section 3.4.2 and Section 3.5.

Laser ablation

In laser ablation, gas-phase atoms or molecules are produced inside the buffer gas cell itself by focusing a pulsed laser onto a solid precursor target. In the simplest cases, the solid phase of the molecule is stable and can be used directly as the solid precursor. This can be done for solid metals such as Na or Yb for producing their respective metal vapours, and molecules like PbO which are stable in their solid phase [138].

More commonly, however, the desired diatomic molecule MX is only stable in the solid phase in the form $\mathrm{M_aX_b}$. When these stable forms are a glass or ceramic, the best ablation targets are often formed by grinding the solid into a fine powder and then pressing or sintering the powder into the solid target. BaF, CaH, SrF, YO and ThO are examples of some molecules that can be prepared using this method [139].

It is possible to introduce a greater variety of molecules with a high flux into the cell using laser ablation than with capillary filling. However, the number of molecules produced in each pulse is inconsistent, temperatures can rise to several thousand Kelvin in local regions of the cell near the ablation target, and the environment in the cell is unstable and far from thermal equilibrium. This can lead to significant variation in the properties of the resulting molecular beam [139].

2.1.2 Thermalisation

It is often difficult to model the gas dynamics and thermalisation process for ablation-loaded molecules because of the extreme variability in the conditions created within the cell. A detailed analysis of thermalisation for ablation-loaded molecules can be found in reference [140]. The description of the thermalisation that occurs within the cell will be limited to capillary-loaded molecules, which is the method used for the experiments described in this thesis.

Buffer gas density

Cryogenic refrigerators are used to achieve the low buffer gas cell temperatures, which typically range between 2 and 20 K. A 6 K and 17 K buffer gas cell were used in this work. The buffer gas can be delivered to the cell using a simple gas fill line because it has a high vapour pressure at low temperatures. The gas line is often thermally connected to cold regions of the apparatus so that cooling occurs before the buffer gas even enters the cell. The buffer gas also thermalises with the cell walls once steady-state conditions are reached inside the cell.

The mean thermal velocity of the buffer gas inside the cell is given by Equation 2.1, where k_B is the Boltzmann constant, T_0 is the temperature of the cell, and m_b is the mass of the buffer gas. The '0' subscript refers to the cell under steady-state conditions. The mean thermal velocity is approximately 178 ms^{-1} for 6 K helium or 134 ms^{-1} for 17 K neon.

$$\bar{v}_{0,\mathrm{b}} = \sqrt{\frac{8k_\mathrm{B}T_0}{\pi m_\mathrm{b}}} \tag{2.1}$$

The molecular conductance of the cell aperture of area A determines the flow rate out of the cell $f_{\text{out}} = n_{0,\text{b}} \bar{v}_{0,\text{b}} A_{\text{aperture}}/4$, and can be used to calculate the density of the buffer gas in the cell under steady-state conditions. Although the number density of the molecular gas may be substantially higher at the cell entrance, it is usually less than 1% of the number density of the buffer gas in all other regions of the cell. Therefore, under steady-state conditions, the flow rate out of the cell f_{out} is largely determined by the flow rate of the buffer gas entering the cell $f_{0,\text{b}}$, and can be approximated by $f_{\text{out}} = f_{0,\text{b}}$. Thus, the density of the buffer gas in the cell under steady state conditions can be calculated using Equation 2.2, where A_{aperture} is the area of the exit aperture of the buffer gas cell. Even at extremely high buffer gas densities when the flow out of the cell is fluid-like rather than effusive, Equation 2.2 can be used as a rough approximation of the buffer gas density in the cell since the difference is quite small [141].

$$n_{0,\text{b}} = \frac{4 f_{0,\text{b}}}{A_{\text{aperture}} \bar{v}_{0,\text{b}}} \tag{2.2}$$

Typical values are between 1 to 100 sccm for the flow rate (where 1 sccm is approximately 4.5×10^{17} gas atoms per second), and between 1 to 5 mm for the aperture diameter, yielding buffer gas densities of approximately 10^{15} to 10^{17} atoms per cm^3 within the cell under steady state conditions [141]. For the experimental apparatus constructed in this work, the buffer gas density is approximately 5×10^{15} atoms per cm^3 within the cell under normal operating conditions.

Translational thermalisation

The critical part of buffer gas cooling involves the thermalising elastic collisions between the cold buffer gas and hot molecular gas within the cell. To gain a better understanding of the translational cooling process, these collisions can be modelled using a hard sphere approximation for both the buffer and molecular gas.

For hard sphere elastic collisions, momentum and energy conservation can be used to determine the relationship between the incoming and outgoing velocities of the colliding partners. The amount of energy lost by the molecule in each collision can then be determined by assuming that the initial velocity of the buffer gas atom is much smaller than the magnitude of the molecule's velocity. Ultimately, this can be used to find the fractional amount of energy lost (denoted by κ^{-1} in Eq. 2.3) and the temperature change (Eq. 2.4) of the molecule for each collision with a buffer gas atom, as derived in reference [142] and [126]. ΔE is the change in energy of the molecule, E_{tot} is the total energy of the collision, m is mass, T is temperature, and the buffer gas (molecular gas) is denoted by the subscript 'b' ('m').

$$\frac{1}{\kappa} = \frac{\Delta E}{E_{\text{tot}}} = \frac{2m_{\text{b}}m_{\text{m}}}{(m_{\text{b}} + m_{\text{m}})^2} \tag{2.3}$$

$$\Delta T_{\text{m}} = \frac{-(T_{\text{m}} - T_{\text{b}})}{\kappa} \tag{2.4}$$

The temperature of the buffer gas remains at T_{b} throughout the cooling process because it is continually being cooled by the cell walls, which are held at a fixed temperature by the cryogenic refrigerator. The temperature of the molecular gas depends on the number of collisions $\mathcal{N}$ it has undergone with the buffer gas (written generally in Eq. 2.5), and will continuously decrease until it thermalises with the buffer gas at T_{b}. Because the temperature change per collision is assumed to be small compared to the number of collisions, a differential equation can be used to model the temperature change of the molecular gas as a function of the number of collisions (Eq. 2.6).

$$T_{\text{m}}(\mathcal{N}) - T_{\text{m}}(\mathcal{N}-1) = \frac{T_{\text{m}}(\mathcal{N}-1) - T_{\text{b}}}{\kappa} \tag{2.5}$$

$$\frac{dT_{\text{m}}(\mathcal{N})}{d\mathcal{N}} = \frac{T_{\text{m}}(\mathcal{N}) - T_{\text{b}}}{\kappa} \tag{2.6}$$

The temperature of the molecular gas when it enters the cell provides the initial condition $T_{\mathrm{m}}(0)$ necessary to solve the differential equation; the solution is

$$\frac{T_{\mathrm{m}}(\mathcal{N})}{T_{\mathrm{b}}} = 1 + \left(\frac{T_{\mathrm{m}}(0)}{T_{\mathrm{b}}} - 1\right) e^{-\mathcal{N}/\kappa}. \tag{2.7}$$

Equation 2.7 can be rearranged in order to calculate the number of collisions needed to cool the molecular gas to a given temperature $T_{\mathrm{m}}(\mathcal{N})$. For example, Equation 2.8 can be used to find the number of collisions required to cool the molecular gas to within 10% of the cell temperature T_0.

$$\mathcal{N} = -\kappa \ln\left(\frac{1.1T_0 - T_{\mathrm{b}}}{T_{\mathrm{m}}(0) - T_{\mathrm{b}}}\right) \tag{2.8}$$

Approximately 31 collisions are needed to thermalise room temperature (300 K) ND_3 to within 1% of the temperature of a 6 K helium buffer gas cell. Recalling from Equation 2.3 that $\kappa = ((m_{\mathrm{b}} + m_{\mathrm{m}})^2)/(2m_{\mathrm{b}}m_{\mathrm{m}})$, it can be seen that the masses of both the molecular gas and the buffer gas affect the number of collisions necessary to achieve thermalisation. For a helium buffer gas and ND_3 molecular gas, $\kappa = 3.6$; for a heavier molecule such as CH_3F, $\kappa = 5.3$ and approximately 45 collisions are required for thermalisation with the helium buffer gas.

Molecular species such as ND_3 and CH_3F are better cooled with a heavier buffer gas such as neon, for which $\kappa = 2.0$ (ND_3) and 2.1 (CH_3F). However, neon only has sufficient vapour pressure at temperatures above approximately 14 K. Helium must be used if thermalisation to temperatures below 14 K is required. For the 17 K cell used experimentally, 15 collisions are required to thermalise room temperature ND_3 to a temperature close to that of the neon buffer gas. Figure 2.3 shows the temperature of the molecular gas as a function of the number of collisions for a variety of molecular and buffer gas collision partners.

The experimental apparatus should be designed such that the molecular gas will

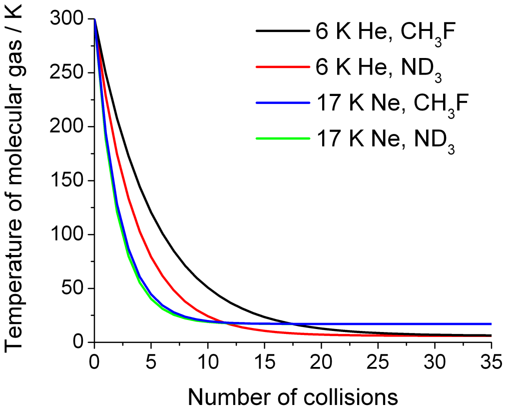

Figure 2.3: In buffer gas cooling, the translational temperature of the molecular gas gradually thermalises with the buffer gas through elastic collisions. The temperature of the molecular gas after $\mathcal{N}$ collisions with the buffer gas atoms can be calculated using Equation 2.7. The number of collisions necessary to achieve thermalisation is shown here for two different buffer gases (6 K helium, mass = 4; 17 K neon, mass = 20) and two different molecular gases (ND$_3$, mass = 20; CH$_3$F, mass = 34).

undergo approximately 100 collisions before exiting the cell to ensure thermalisation with the buffer gas. Assuming $m_\mathrm{m} \gg m_\mathrm{b}$, the mean free path of the molecule in the buffer gas is given by [143]

$$\lambda_{\text{m-b},0} = \frac{(n_{0,\mathrm{b}}\sigma_{\text{b-m}})^{-1}}{\sqrt{1 + m_\mathrm{m}/m_\mathrm{b}}}. \tag{2.9}$$

The density of the buffer gas under steady state conditions $n_{0,\mathrm{b}}$ is approximately 5×10^{15} atoms per cm^3 (calculated using Eq. 2.2). Although the elastic collision cross section $\sigma_{\text{b-s}}$ varies with temperature, the thermally averaged cross section can be used as an approximation, and is typically around 10^{-14} cm^2 for helium-molecule collisions. Therefore, the mean free path of ND$_3$ in a helium buffer gas cell is approximately 8×10^{-5} m and the molecules will have travelled about 0.8 cm along the axis of the buffer-gas cell after 100 collisions. The exact thermalisation length will vary depending on the buffer gas, molecular gas, gas densities, cell temperature and other factors. For these reasons, a cell with a 2 cm length was constructed to ensure thermalisation of the molecular gas under a variety of conditions. Increasing the length of the cell too much, however, decreases the extraction efficiency of the molecules from the cell because a greater number will be lost by freezing to the cell wall rather than exiting through the aperture, as described in Section 2.1.3.

Thermalisation of internal states

As seen in the previous section, buffer gas cooling is an effective method for creating translationally cold molecules through thermalising collisions with a cold buffer gas. It is also effective at creating rotationally cold molecules. Although using a hard sphere approximation worked well for modelling the number of elastic collisions necessary to achieve translational thermalisation, the same approximation cannot be applied for rotational relaxation rates, which depend strongly on the molecular structure [126].

However, a rough approximation of the number of collisions required to achieve rotational thermalisation can be calculated from the ratio of the elastic collision cross section to the rotational relaxation cross section (for a single rotational de-excitation step) of the molecule with the buffer gas, $\sigma_{b-m}/\sigma_{rot}$. For helium buffer gas with typical values of $\sigma_{b-m} \approx 10^{-14}$ cm^2 and $\sigma_{rot} \approx 10^{-(15-16)}$ cm^2 [137], this means about 10 - 100 collisions are required for rotational thermalisation. Buffer gas cooling is therefore an effective method for generating translationally and rotationally cold molecules.

Vibrational quenching cross sections are usually several orders of magnitude smaller than those for translational or rotational relaxation [137]. Often more than 10^8 elastic collisions occur before a vibrational relaxation collision [144]. The difference in the rotational and vibrational relaxation cross sections is a result of the differences in the timescale of each motion relative to the collision. Molecular rotation occurs on roughly the same timescale as the collision between the molecule and the cold buffer gas atom, while vibrational motion is much faster than the collision. Any changes in the interaction potential of the collision based on vibrational motion will be averaged out, therefore any favourable orientations that may exist are inaccessible on the timescale of the collision [32]. Most vibrational energies are typically $\geq$ 1000 cm^{-1} for the species of interest, although some of the bending modes are lower in ND_3 and CH_3F. Therefore, few molecules ($< 1\%$) will be in excited vibrational states at temperatures between 150 to 300 K.

Rotational state populations

An important advantage of buffer gas cooling is its ability to produce rotationally, as well as translationally, cold molecules. This provided the motivation for using a buffer-gas-cooled molecular beam rather than a room temperature effusive source for loading the electrostatic quadrupole guide in the experimental apparatus. This section discusses the rotational state populations of symmetric top molecules that are in a thermodynamic equilibrium, in particular ND_3 and CH_3F.

The internal rotational state of a symmetric top molecule can be described with the quantum numbers $|J, K, M\rangle$, where J characterises the total angular momentum of the molecule, K characterises the projection of the total angular momentum on the molecular axis, and M characterises the projection of the total angular momentum on an external axis in space. M is particularly relevant when the energy of a molecule is affected by an external field, such as the energy of polar molecules in an electric field, which is described by the Stark effect (Section 2.2.1).

In the absence of an external field, the rotational energy of state $|J, K, M\rangle$ is given by Equation 2.10 for oblate symmetric tops (ND_3), and Equation 2.11 for prolate symmetric tops (CH_3F).

$$E_{\text{rot}}(J, K) = BJ(J+1) + (C-B)K^2 \tag{2.10}$$

$$E_{\text{rot}}(J, K) = BJ(J+1) + (A-B)K^2 \tag{2.11}$$

The rotational constant A (and similarly for B and C) is defined as $A = h/(8\pi^2 I_{\mathrm{A}})$. I_{A} is the moment of inertia about molecular axis A and can be calculated using $I_{\mathrm{A}} = \sum_i m_i r_i^2$, where m is the mass of an atom at a radial distance r from the molecular axis A. Also by definition, I_{A} describes the minimum moment of inertia while I_{C} describes the maximum moment of inertia for a molecule. Therefore, $I_{\mathrm{C}} > I_{\mathrm{B}} = I_{\mathrm{A}}$ for oblate symmetric tops, while $I_{\mathrm{C}} = I_{\mathrm{B}} > I_{\mathrm{A}}$ for prolate symmetric tops. The rotational constants for various molecules used in this work are provided in Table 2.1, along with dipole moments and inversion splittings, which are discussed later in Section 2.2.1.

Table 2.1: Rotational constants, dipole moments, and inversion splitting for various molecules studied in this work. ND_3 [145, 146] and NH_3 [147, 148] are oblate symmetric top molecules, CH_3F [149] is a prolate symmetric top molecule, and NH_2D [150, 151] and NHD_2 [150] are asymmetric top molecules.

Molecule	A / cm^{-1}	B / cm^{-1}	C / cm^{-1}	μ_{a} / D	μ_{b} / D	μ_{c} / D	W_{inv} / cm^{-1}
ND_3	-	5.14	3.12	0	0	1.497	0.053
NH_3	-	9.9402	6.3044	0	0	1.497	0.712
CH_3F	5.1820	0.85179	-	1.86	0	0	-
NH_2D	9.6775	6.4109	4.6964	0.1848	0	1.4652	0.4059
NHD_2	7.445	5.344	3.753	0	0.21	1.47	0.171

The molecular partition function can be used to determine the internal rotational state populations of an ensemble of molecules that are in thermodynamic equilibrium, provided the temperature, volume, and number of particles is fixed; the system is also permitted to exchange heat with the environment. The fractional population of molecules in state $|J, K, M\rangle$ is given by Equation 2.12.

$$N(J,K,M) = g_{\mathrm{M,I}} e^{-E_{\mathrm{rot}}(J,K,M)/k_{\mathrm{B}}T} \left(\sum_{J,K} g_{\mathrm{M,I}} e^{-E_{\mathrm{rot}}(J,K,M)/k_{\mathrm{B}}T} \right)^{-1} \tag{2.12}$$

A degeneracy factor g must be included when different quantum states, not explicitly included in the sum, have the same energy. The molecular symmetry plays a key role in determining the nuclear spin degeneracy factor g_{I}. Table 2.2 summarises the spin statistical weights for a symmetric top with a three-fold axis of symmetry. In the absence of an external field, the rotational states also exhibit a degeneracy in the M quantum states ($g_{\mathrm{M}} = 2J + 1$). The overall degeneracy factor is simply a product of the two separate degeneracy factors, $g_{\mathrm{M,I}} = g_{\mathrm{M}} g_{\mathrm{I}}$. It should be noted that the ortho and para levels of a molecule (with a n-fold axis of symmetry) do not mix by collisions with buffer gas atoms (which are isotropic); the ortho and para configurations thermalise separately to different thermal equilibrium rotational states [126].

Table 2.2: The nuclear spin statistical weights are presented for a symmetric top molecule with a three-fold axis of symmetry, such as ND_3 and CH_3F. The weights are determined by the number of eigenstates that preserve the correct symmetry upon exchange of identical nuclei for a particular symmetry operation, based on analysis of the molecular symmetry group. The nuclear spin is $I = 1$ ($I = 1/2$) for the indistinguishable deuterium (hydrogen) atoms in ND_3 (CH_3F). The table is modified from [146].

	Statistical weights g_{I}	type
$K \in \{K \mid K = \pm 3n, n \in \mathbb{N}\}$	$\frac{1}{3}(2I+1)(4I^2+4I+3)$	
$K \in \{K \mid K \neq \pm 3n, n \in \mathbb{N}_0\}$	$\frac{1}{3}(2I+1)(4I^2+4I)$	
$K = 0$, no vib. inversion	$\frac{1}{3}(2I+1)(4I^2+4I+3)$	
$K = 0$, vib. inversion	$\frac{1}{3}(2I+1)(2I-1)I$	fermion
J even, $\lvert+\rangle$ or J odd, $\lvert-\rangle$	$\frac{1}{3}(2I+1)(2I+3)(I+1)$	boson
$K = 0$, vib. inversion	$\frac{1}{3}(2I+1)(2I+3)(I+1)$	fermion
J odd, $\lvert+\rangle$ or J even, $\lvert-\rangle$	$\frac{1}{3}(2I+1)(2I-1)I$	boson

The rotational state distribution of a sample of ND_3 molecules in thermal equilibrium can be calculated using Equation 2.12. Figure 2.4 shows a comparison of the rotational state distributions of ND_3 at three different temperatures. There is a large number of rotational states occupied at room temperature, with rotational states higher than $J = 15$ being populated. The number of occupied rotational states drops dramatically as the temperature of the thermalised source of molecules decreases; by 6 K, only the lowest few rotational states are populated. It is clear that after the

ND_3 molecules have undergone approximately 100 collisions with the buffer gas and thermalised to the temperature of the cell, the sample will be rotationally cold with only the lowest few rotational states populated.

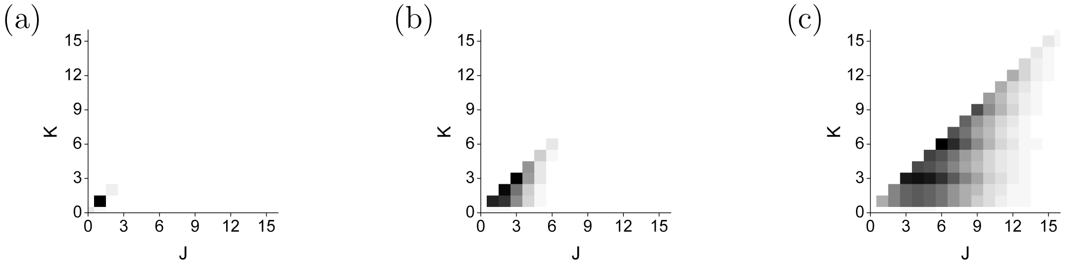

Figure 2.4: Calculated rotational state distributions for a thermalised source of ND_3 molecules at a temperature of (a) 6 K, (b) 50 K, and (c) 300 K. This assumes the same rotational temperature for both ortho and para components, and the ortho-to-para ratio is the statistical equilibrium value of 1.0. The shading indicates the relative populations of the quantum states $|J, |K|\rangle$.

2.1.3 Extraction of molecules from the cell

After the molecules have been introduced to the cell and thermalised with the buffer gas, they are extracted from the cell to form the buffer-gas-cooled molecular beam. Although the buffer gas exhibits significant vapour pressure at the cell temperature, the molecules will freeze and be lost as soon as they come in contact with the cell wall. Therefore, it is important that the molecular gas is extracted from the cell before it has time to diffuse to the walls.

The extraction behaviour is characterised by a dimensionless parameter $\gamma_{\text{cell}} \equiv \tau_{\text{diff}}/\tau_{\text{pump}}$. The time it takes a molecule to diffuse to the cell wall is given by τ_{diff}. The time it takes a molecule to travel from the molecular inlet (for capillary filling) to the exit aperture while entrained in the macroscopic buffer gas flow is given by τ_{pump}, and is described as being 'pumped-out' of the cell. The cell parameters used in the following discussion are: diameter of the exit aperture d; cell length L, which is the distance between the molecule inlet and exit aperture (inlet and exit are oriented to face each other); and cell width and height $w = h = D$ (see Figure 2.2).

For diffusion of the molecular gas in the buffer gas, the diffusion constant δ is given by

$$\begin{aligned}\delta &= \frac{3}{16(n_{0,\mathrm{m}} + n_{0,\mathrm{b}})\sigma_{\text{b-m}}}\left(\frac{2\pi k_{\mathrm{B}} T_0}{\mu}\right)^{1/2} \approx \frac{3}{16 n_{0,\mathrm{b}}\sigma_{\text{b-m}}}\left(\frac{2\pi k_{\mathrm{B}} T_0}{m_{\mathrm{b}}}\right)^{1/2} \\ &= \frac{3\pi}{32}\frac{\bar{v}_{0,\mathrm{b}}}{n_{0,\mathrm{b}}\sigma_{\text{b-m}}},\end{aligned} \tag{2.13}$$

where the approximation comes from assuming $n_{0,\mathrm{m}} \ll n_{0,\mathrm{b}}$ and $m_{\mathrm{m}} \gg m_{\mathrm{b}}$ [143]. The formation of dimers or clusters generally only affects the diffusion of the molecules in the cell when the molecular gas density is very high [152]. The mean-squared displacement of a molecule from its starting point after diffusion for a time t is given by $\langle \Delta x^2 \rangle = 6\delta t$ [153]. The diffusion timescale can then be found using

$$\tau_{\mathrm{diff}} = \frac{\langle \Delta x^2 \rangle}{6\delta} = \frac{D^2}{6\delta} = \frac{16}{9\pi}\frac{n_{0,\mathrm{b}}\sigma_{\text{b-m}} D^2}{\bar{v}_{0,\mathrm{b}}}, \tag{2.14}$$

making the appropriate substitution for the diffusion constant δ using Equation 2.13. This gives the time it would take for the molecular gas to diffuse to the wall of the buffer gas cell.

Assuming the molecular gas becomes entrained in the buffer gas flow, the pump-out time is well approximated by the buffer gas pump-out time because the molecular gas density is typically less than 1% of the buffer gas density. The pumpout time is therefore given by

$$\tau_{\mathrm{pump}} = \frac{N_{0,\mathrm{b}}}{\Phi_{\mathrm{b}}} = \frac{4 n_{0,\mathrm{b}} D^2 L}{n_{0,\mathrm{b}}\bar{v}_{0,\mathrm{b}} A_{\mathrm{aperture}}} = \frac{1}{\pi}\frac{D^2 L}{\bar{v}_{0,\mathrm{b}} d^2}, \tag{2.15}$$

where the total number of buffer gas atoms in the cell is $N_{0,\mathrm{b}} = n_{0,\mathrm{b}} D^2 L$ and the buffer gas flux through the cell aperture is $\Phi_{\mathrm{b}} = n_{0,\mathrm{b}}\bar{v}_{0,\mathrm{b}} A_{\mathrm{aperture}}/4$ [136].

The estimates for τ_{diff} (Eq. 2.14) and τ_{pump} (Eq. 2.15) can then be substituted into the definition for γ_{cell},

$$\gamma_{\text{cell}} \equiv \frac{\tau_{\text{diff}}}{\tau_{\text{pump}}} = \frac{16 n_{0,\text{b}} \sigma_{\text{b-m}} d^2}{9L}. \tag{2.16}$$

The extraction of the molecules from the buffer gas cell can be divided into two regimes - the ‘diffusion limit’ where $\gamma_{\text{cell}} \lesssim 1$ and the ‘hydrodynamic entrainment limit’ where $\gamma_{\text{cell}} \gtrsim 1$ [136]. In the diffusion limit, the molecules diffuse to the cell walls faster than they are extracted from the cell. This often leads to a low flux of molecules out of the cell because most of the molecules have frozen to the cell walls and are lost before reaching the exit aperture. However, the velocity distribution of the resulting beam tends to reflect the velocity distribution of the thermalised molecules found within the cell [138]. The extraction efficiency f_{ext} is the ratio of the number of molecules entering the cell compared to the number of molecules leaving through the exit aperture to form the beam. Increasing the buffer gas density in the diffusion limit tends to increase the extraction efficiency, although the exact relationship (linear, exponential, cubic, etc.) depends on the molecular species involved [138].

In the hydrodynamic entrainment regime, extraction efficiencies of approximately 10% are common, although efficiencies as high as 40% have been observed [136]. The extraction efficiency tends to plateau after a high buffer gas density is reached. Fewer molecules are lost by freezing to the cell wall in the hydrodynamic entrainment regime, leading to a higher flux of molecules out of the cell and ultimately a brighter molecular beam. However, the velocity distribution of the exiting molecules may differ significantly from the distributions found within the cell.

For typical cell geometries and conditions, thermalisation usually occurs in less than 3 ms, while τ_{diff} and τ_{pump} tend to range between 1 - 10 ms [141]. Thus, the buffer gas cell must be constructed to ensure that thermalisation occurs before the molecules are extracted from the cell. Increasing the length of the cell will ensure that a sufficient number of collisions have occurred between the molecules and the buffer gas to achieve thermalisation before the molecules exit the cell. However, this tends to decrease γ_{cell} and shift the extraction of the molecules toward the diffusion limit, generating a lower flux of molecules out of the cell. Still, good thermalisation and efficient extraction can can be achieved with careful consideration of the cell geometry and gas densities. The buffer gas cell used in this work is typically operated in the hydrodynamic entrainment regime.

2.1.4 Properties of buffer-gas-cooled beams

The previous sections have provided an overview of the processes occurring within the buffer gas cell; this section describes the buffer-gas-cooled beams that are emitted from the cell. Although the molecules are the interesting part of the beam, they represent less than 1% of the number density of the buffer gas, and have little impact on the properties of the beam. Therefore to a good approximation, it can be assumed that the flow properties of the beam are determined exclusively by the buffer gas.

Flow regimes

Just as γ_{cell} characterises the extraction of the molecules from the cell (Section 2.1.3), a dimensionless parameter called the Reynolds number Re can be used to characterise the gas flow of the beam emitted from the cell. By definition, the Reynolds number is the ratio of inertial to viscous forces in a fluid flow. The Reynolds number can be related to the buffer gas cell parameters [141],

$$Re \approx \frac{2d_{\text{aperture}}}{\lambda_{\text{b-b},0}} \approx \frac{8\sqrt{2}f_{0,\text{b}}\sigma_{\text{b-b}}}{d_{\text{aperture}}\bar{v}_{0,\text{b}}}. \tag{2.17}$$

Beam properties are primarily determined by collisions that occur near the exit aperture, so it is appropriate that the Reynolds number gives information about the number of collisions that occur within the distance d_{aperture} of the exit aperture itself. The aperture diameter has a significant impact on the gas flow and is the most important geometric parameter in characterising beam properties [52].

The gas flow out of the cell can be divided into three different regimes based on the Reynolds number [141]. For $Re \lesssim 1$, there are very few collisions near the aperture and the thermal distribution present in the beam is similar to that found in the cell; this is called the 'effusive' regime. The 'fully hydrodynamic' or 'supersonic' regime occurs when $Re \gtrsim 100$. The large number of collisions near the aperture produce a beam with properties similar to supersonic expansion beams and the gas flow tends to exhibit more fluid-like behaviour. When the Reynolds number falls between these extremes ($1 \lesssim Re \lesssim 100$), an 'intermediate' or 'partially hydrodynamic' regime results. As indicated by the name, the beam properties no longer reflect the thermal distributions present in the cell, but the flow is not completely fluid-like either. This is the most common regime for buffer-gas-cooled beams.

Forward velocity

The forward velocity of the molecular species is designated as $v_{\parallel,\text{m}}$. Equation 2.18 gives the forward velocity of effusive beams derived in [52]. Because there are no collisions between the molecular species and the buffer gas near the aperture in the effusive regime, the forward velocity of the (heavy) molecular species is related to its thermal velocity as it would be in an effusive beam ($v_{\parallel,\text{m}} \approx 1.2\bar{v}_{0,\text{m}}$).

$$v_{\parallel} \approx \frac{3\pi}{8}\bar{v} \approx 1.2\bar{v} \tag{2.18}$$

Although the effusive regime leads to beams with the lowest forward velocity of the molecular species, it is technically difficult to construct a cell which produces purely effusive buffer gas beams. Some groups have had success using a 'double cell' geometry [136, 154]. The first cell has the dimensions and properties of a standard buffer gas cell. The second cell is placed in front of the exit aperture of the first cell and acts as a 'slowing cell.' The relatively low pressure in the second cell leads to fewer collisions near the second aperture and produces a beam closer to the effusive limit.

In the intermediate regime, collisions near the exit aperture lead to an effect called 'velocity boosting.' The large density gradient near the aperture means that molecules exiting the cell undergo collisions primarily in the forward direction (toward the exit aperture) [138]. The lighter buffer gas has a larger thermal velocity than the molecules ($\bar{v}_{0,\mathrm{b}} > \bar{v}_{0,\mathrm{m}}$), so the molecules are accelerated, or 'boosted,' to a forward velocity $v_{\parallel,\mathrm{m}} > \bar{v}_{0,\mathrm{m}}$. The forward velocity of the molecule increases linearly with the Reynolds number (and consequently with the buffer gas density within the cell) in the range of $1 \lesssim Re \lesssim 10$ [139]. After this point, the velocity tends asymptotically toward its maximum value characteristic of a supersonic beam.

For supersonic beams that expand over a sufficiently large distance, the final forward velocity of the beam is given by [52]

$$v_{\parallel} = \sqrt{\frac{5k_BT_0}{m}} = \bar{v}_0\sqrt{\frac{5\pi}{8}} \approx 1.4\bar{v}_0, \tag{2.19}$$

where T_0 is the temperature of the gas at the exit aperture before expansion. For buffer gas cells operated in the fully hydrodynamic regime, the large number of collisions near the aperture accelerates the forward velocity of the molecules to the forward velocity of the light buffer gas, $v_{\parallel,\mathrm{m}} \approx v_{\parallel,\mathrm{b}} \approx 1.4\bar{v}_{0,\mathrm{b}}$. This is the upper limit of the forward velocity for the molecular species leaving the cell.

The spread (FWHM) of a thermal 1D Maxwell-Boltzmann distribution can be used to approximate the forward velocity spread in the effusive regime, and is given by

$$\Delta v_{\parallel,\mathrm{m}} = \sqrt{\frac{8\ln(2) k_{\mathrm{B}} T_0}{m_{\mathrm{m}}}} = \bar{v}_{0,\mathrm{m}}\sqrt{\pi\ln(2)} \approx 1.5\bar{v}_{0,\mathrm{m}}. \tag{2.20}$$

The forward velocity spread tends to decrease for high Reynolds numbers present in the hydrodynamic flow regime, which is characteristic of isentropic expansion of the buffer gas into the vacuum [141].

Angular divergence

The angular spread of the beam is characterised by the parameter $\Delta\theta$, which is the FWHM of the angular distribution [141]. The angle θ from the aperture normal is the point at which, at a fixed distance from the aperture, the number density is half the total number density in the beam. This point should be far enough from the aperture such that the aperture can be approximated as a point source from which the molecules are ballistically expanding. The forward velocity $v_\parallel$ and transverse velocity spread $\Delta v_\perp$ can then be related to the angular spread of the beam as shown in Figure 2.5.

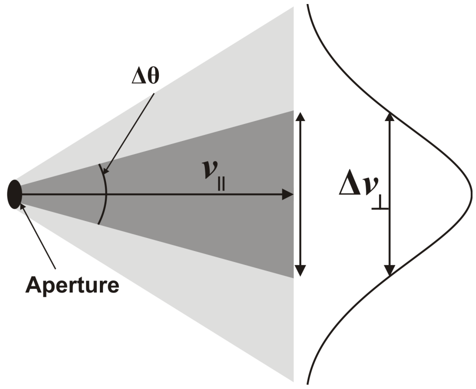

Figure 2.5: Angular spread $\Delta\theta$ of buffer-gas-cooled beams that corresponds to the FWHM of the angular distribution. The darker shading denotes a higher number density in the beam. The geometric relationship between the forward velocity $v_\parallel$, transverse velocity spread $\Delta v_\perp$, and angular spread $\Delta\theta$ is also shown. Modified from [141].

The angular spread can be calculated using

$$\tan(\Delta\theta/2) = \frac{\Delta v_\perp/2}{v_\parallel}. \tag{2.21}$$

Furthermore, the solid angle $\Delta\Omega$ subtended by $\Delta\theta$ can be found using $\Delta\Omega = 2\pi(1 - \cos(\Delta\theta/2))$. The angular spread is $\Delta\theta = 120°$ and the solid angle spread is $\Delta\Omega = \pi$ for buffer gas beams in the effusive regime [52].

For some species, there is little change in the angular divergence of the beam from the effusive regime to the fully hydrodynamic regime, suggesting that the transverse velocity spread and forward velocity spread increase at similar rates as the Reynolds number increases [139, 155]. For other species, especially at the start of the intermediate regime where $1 \lesssim Re \lesssim 10$, the transverse velocity spread remains relatively constant while the forward velocity increases linearly with the Reynolds number, leading to a decreasing beam divergence [138]. This suggests that there is no universal description appropriate for the angular divergence of buffer-gas-cooled beams in the intermediate regime, but that the angular spread of an effusive beam provides an upper limit to the divergence of buffer-gas-cooled beams.

2.1.5 Summary

It is difficult to design a buffer gas source that has sufficient thermalisation, good extraction efficiency, and produces a purely effusive beam. Most buffer gas sources operate in the effusive or intermediate regimes. Purely effusive buffer gas beams tend to exhibit lower extraction efficiency of the molecular gas from the cell. Operating with higher buffer gas densities can increase the extraction efficiency, but also tends to create beams in the intermediate flow regime, in which the forward velocity of the molecules changes with the density of the buffer gas.

Changing the cell dimensions, aperture size, and cell conditions (gas densities and temperature), can produce buffer-gas-cooled beams with slightly different properties. Further refinement can be achieved by using a slit-shaped exit aperture, which allows for good extraction ($\gamma_{\text{cell}} > 1$) while still generating effusive beams (low Reynolds numbers) [138]. The use of a second 'slowing cell,' as described earlier in Section 2.1.4, can also enhance the beam properties [154].

Certain experiments, such as collision studies, are impossible to conduct inside the buffer gas cell, as the presence of the buffer gas atoms would significantly affect the results. Experiments conducted outside of the cell often suffer from low molecular density, which decreases with the square of the distance from the cell due to beam divergence. Many of these problems are solved by using electrostatic [156] or magnetic guides [90] to move the buffer-gas-cooled molecules away from the cell exit and into the experimental region. The electrostatic and magnetic guides may also be used as velocity filters to select the slowest molecules from the buffer-gas-cooled beam for collision studies, trap loading, or other applications. In this work, a buffer-gas-cooled beam is loaded into an electrostatic velocity filter. The interaction of polar molecules with electric fields is described in the next section, and the theory of electrostatic velocity selection is described in Section 2.3.

2.2 Interaction of polar molecules with electric fields

Electrostatic velocity selection depends on the interaction of polar molecules with inhomogeneous electric fields. A description of the molecular Stark effect is provided in this section, and the theory of electrostatic velocity selection is discussed in Section 2.3. In order to gain a more intuitive understanding of the Stark effect, a semi-classical description of the rotational motion of polar molecules in an electric field is provided before describing the corresponding quantum mechanical calculations. Both the classical and quantum mechanical derivation of the Stark effect are adapted from [157, 158].

2.2.1 Stark effect: semi-classical description

Similar to a spinning top, the molecular axis of a symmetric top molecule will precess about the total angular momentum vector when there is no external field. A secondary motion arises in an external electric field because of the torque now applied to the molecular axis, which is aligned with the dipole moment. The secondary motion is a slower precessional motion of the total angular momentum about the direction of the field [157]. These two types of precessional motion are depicted in Figure 2.6(a).

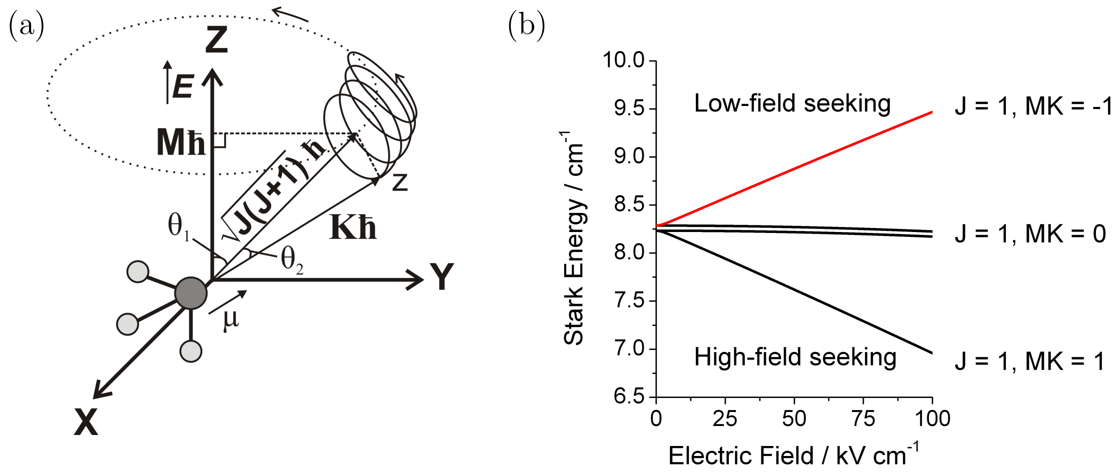

Figure 2.6: (a) Semi-classical description of molecular rotation of a symmetric-top molecule in an electric field, and the implications for the orientation of the molecular dipole moment. Modified from [158]. (b) Calculated Stark effect for ND_3 in the $|J, K\rangle = |1, 1\rangle$ rotational state. J describes the total angular momentum of the molecule, K describes the angular momentum about the principal moment of inertia of the molecule ($\hat{z}$), and M describes the angular momentum about the axis of the applied external electric field ($\hat{Z}$).

The projection of the total angular momentum on to the electric field remains constant as the molecule precesses. However, the projection of a rotating molecule's dipole moment on the electric field axis changes with time, depending on the phase of rotation. Therefore, the time-averaged projection of the molecular dipole moment on the electric field is needed to calculate the Stark effect, and is given by [159]

$$\begin{aligned}\langle\cos\theta\rangle &= \langle\cos\theta_1\cos\theta_2+\sin\theta_1\sin\theta_2\cos\gamma(t)\rangle\\ &= \cos\theta_1\cos\theta_2 = \frac{|\vec{M}|}{|\vec{J}|}\frac{|\vec{K}|}{|\vec{J}|}.\end{aligned} \tag{2.22}$$

The angle $\gamma(t)$ describes the phase of the precession of the molecular axis about the total angular momentum vector $\vec{J}$, while the other angles are illustrated in Figure 2.6(a). Also shown in the figure is the projection of $\vec{J}$ onto the space-fixed axis $\hat{Z}$ and the molecular axis $\hat{z}$, with magnitudes given by $M\hbar$ and $K\hbar$ respectively.

The Stark energy, calculated from the projection of the molecular dipole moment $\vec{\mu}$ onto the electric field $\vec{\varepsilon}$, is shown in Equation 2.23. The additional substitution of $\sqrt{J(J+1)}\hbar$ for the magnitude of $\vec{J}$ is also made.

$$W_{\text{Stark}} = -\vec{\mu}\cdot\vec{\varepsilon} = -\mu\varepsilon\frac{|\vec{M}|}{|\vec{J}|}\frac{|\vec{K}|}{|\vec{J}|} = -\mu\varepsilon\frac{MK}{J(J+1)} \tag{2.23}$$

The behaviour of a molecule in an electric field can be classified based on the sign of its effective dipole moment, which is defined as $\mu_{\text{eff}} = \mu\langle\cos\theta\rangle$. 'Low-field seeking' molecules gain Stark potential energy with increasing electric field strength because their effective dipole moment opposes the electric field ($\mu_{\text{eff}} < 0$). These molecules are repelled from regions of high electric field. Conversely, 'high-field seeking' molecules lose potential energy with increasing field strength because their effective dipole moment is aligned with the electric field ($\mu_{\text{eff}} > 0$).

Figure 2.6(b) shows the calculated Stark effect for ND_3 in the $|J,K\rangle = |1,1\rangle$ state, with the low-field seeking state highlighted in red. The low and high-field seeking molecules are explained quantum mechanically by rotational wavefunctions with opposite polarisations with respect to the electric field. The effective dipole moment is constrained to a discrete set of values because of the quantisation of M

and K. Further details on the quantum mechanical description of the Stark effect are provided in the next section.

2.2.2 Stark effect: quantum mechanical description

The Hamiltonian operator for the interaction of a polar molecule with a homogeneous electric field is given by the scalar product of the dipole moment $\vec{\mu}$ and electric-field $\vec{\varepsilon}$ vector operators, $H_{\text{Stark}} = -\vec{\mu} \cdot \vec{\varepsilon}$. The dipole moment is defined relative to the molecule-fixed frame (molecular axis aligned to the $\hat{z}$ axis), while the electric field is defined relative to the space-fixed frame (electric field aligned with the $\hat{Z}$ axis). Writing both vectors as first-rank irreducible spherical tensor operators allows a transformation between the two coordinate systems through a relatively simple rotation. Using the Euler angles, $\Omega = (\phi, \theta, \chi)$ (described in [157]), to define the orientation of the molecular axis relative to the space-fixed frame and the Wigner rotation matrix $D^1_{0q}(\Omega)$, the electric field vector operator can be written in terms of the molecular frame irreducible spherical tensor components [157]

$$T^1_q(\vec{\varepsilon}) = \varepsilon D^1_{0q}(\Omega). \tag{2.24}$$

Similarly, the spherical tensor components of the dipole moment operator in the molecule-fixed frame are given by

$$T^1_1(\vec{\mu}) = -\frac{1}{\sqrt{2}}(\hat{\mu}_x + i\hat{\mu}_y) \tag{2.25}$$

$$T^1_0(\vec{\mu}) = \hat{\mu}_z \tag{2.26}$$

$$T^1_{-1}(\vec{\mu}) = \frac{1}{\sqrt{2}}(\hat{\mu}_x - i\hat{\mu}_y) \tag{2.27}$$

Equation 2.28 combines these formulations to give the scalar product of the molecular dipole moment and electric field vector operators written in the same frame [157].

$$H_{\text{Stark}} = -\sum_{q=-1}^{1} (-1)^q T_q^1(\vec{\mu}) \cdot T_{-q}^1(\vec{\varepsilon}) \tag{2.28}$$

In the symmetric top basis, a sum of integrals over the Euler angles can be used to calculate the matrix elements of the Stark Hamiltonian,

$$\langle J'M'K'|H_{\text{Stark}}|JMK\rangle = -\varepsilon \sum_{q=-1}^{1} (-1)^q T_q^1(\vec{\mu}) \int \mathrm{d}\Omega \, \langle J'M'K'|\Omega\rangle D_{0-q}^1(\Omega)\langle\Omega|JMK\rangle. \tag{2.29}$$

The total angular momentum associated with molecular rotation is given by the quantum number J, while its projection onto the space-fixed and body-fixed axis is given by M and K, respectively. This simplified description of the Stark Hamiltonian ignores coupling to other sources of angular momenta, which lead to the fine and hyperfine structures present in rotational energy spectra.

The Euler-angle representation of the symmetric-top wavefunction can be directly related to the Wigner rotation matrix [157], $\langle\Omega|JMK\rangle = \sqrt{(2J+1)/(8\pi^2)} D_{MK}^J(\Omega)^*$, which is needed to solve the integral in Equation 2.29 using standard angular momentum algebra [157]. The matrix representation of the Stark Hamiltonian is then given by

$$\begin{aligned}\langle J'M'K'|H_{\text{Stark}}|JMK\rangle &= -\varepsilon\sqrt{(2J+1)(2J'+1)} \\ &\times \sum_{q=-1}^{1} (-1)^{M-K'} T_q^1(\vec{\mu}) \begin{pmatrix} J' & 1 & J \\ -M' & 0 & M \end{pmatrix} \begin{pmatrix} J' & 1 & J \\ -K' & -q & K \end{pmatrix}.\end{aligned} \tag{2.30}$$

The molecule-field interaction is rotationally invariant about the space-fixed axis, since by definition $\hat{Z}$ is aligned with the electric field vector. Therefore the matrix representation of H_{Stark} is diagonal in M. Furthermore, the selection rules for dipole-allowed rotational transitions, $J' = J, J \pm 1$ and $K' = K, K \pm 1$, mean that the matrix is tridiagonal in J and K. The Stark effect simplifies dramatically for symmetric-top molecules because the $T^1_1(\vec{\mu})$ and $T^1_{-1}(\vec{\mu})$ components of the dipole moment are zero. The first-order Stark effect for symmetric top molecules is therefore given by

$$W^{(1)}(\varepsilon) = \langle J'M'K'|H_{\text{Stark}}|JMK\rangle = -\frac{MK}{J(J+1)}\mu\varepsilon. \tag{2.31}$$

The quantum mechanical derivation leads to the same first-order Stark effect, and therefore the same magnitude for the Stark energy in a weak electric field, that was obtained earlier with the semi-classical description (Eq. 2.23). Higher order perturbation terms are needed to calculate the Stark energy levels in large electric fields, or for molecules with closely spaced rotational levels. Appendix A explains how the quantum-state specific Stark energy levels are calculated for both symmetric and asymmetric top species. These are required for the Monte Carlo simulations of the electrostatic guiding process described in Section 2.4. In very large electric fields, ‘pendular states’ are created when the Stark effect is strong enough to quench the molecular rotation about any axis apart from the field direction [160].

2.3 Theory of electrostatic velocity selection

2.3.1 Basic principles

Inhomogeneous electric fields can be used to exert a force on neutral, polar molecules that exhibit a Stark effect, as described in the previous section. Furthermore, it is possible to manipulate the motion of molecules in large electric fields if they exhibit a strong Stark effect. Several experimental techniques have been developed that use this interaction to isolate slow-moving molecules, with a key method being electrostatic velocity selection. Unlike most methods, which actually cool or slow down the molecules, this involves selectively filtering out molecules in the low velocity tail of the velocity distribution.

A sample of gas from an effusive source exhibits a Maxwell-Boltzmann distribution of velocities, so even at room temperature there is a small fraction of molecules with very low translational energy. Electrostatic velocity selection separates molecules in the low-velocity tail of the distribution from the rest of the molecules in the effusive source, as only the slowest moving molecules are guided around the bend of the electrostatic guide. The guide consists of four parallel rods to which voltages are applied in a quadrupolar configuration. A continuous beam of translationally cold ($\sim$3 K) molecules can be produced using this method, at a rate of approximately 10^{10} molecules per second and density of about 10^8 molecules per cm^3, from a room temperature effusive source of molecules [161].

Figure 2.7(a) shows the Maxwell-Boltzmann distribution of velocities from an effusive source of ND_3 for various temperatures. Compared to a room temperature source, a buffer-gas-cooled molecular source has a larger fraction of low velocity molecules ($v < v_{\mathrm{max}}$) that can be successfully guided around the bend. The experimental parameters of the buffer gas cell may also yield a greater number of slow-moving molecules in the source that are available for guiding, increasing the density and flux of the guided beam.

The schematic shown in Figure 2.7(b) illustrates the concept of electrostatic velocity selection. A room-temperature effusive source of molecules emitted from a narrow capillary is often used to load molecules into the electrostatic guide. In this work, a buffer-gas-cooled molecular beam is used for the molecular source instead. A two-dimensional transversely confining potential is created within the guide by applying voltages of opposite polarity to adjacent electrodes.

Translational velocity selection occurs primarily in the bent section of the guide.

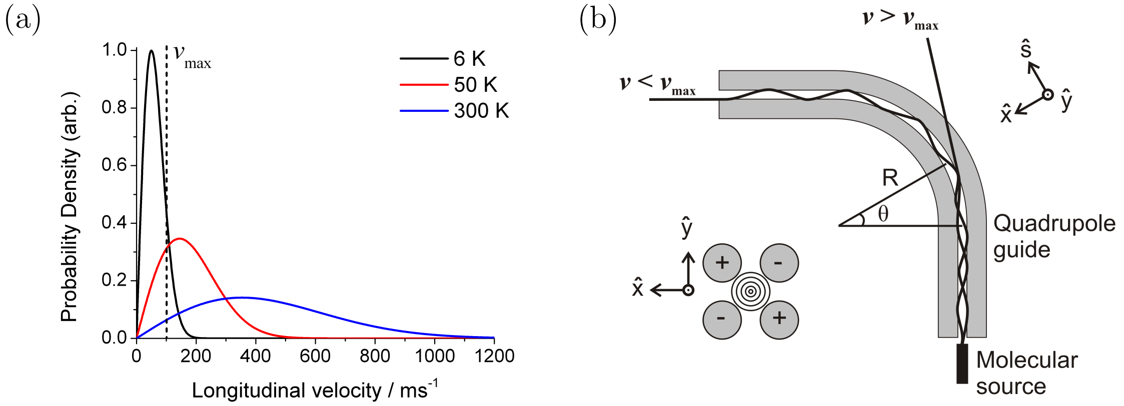

Figure 2.7: (a) Maxwell-Boltzmann distribution of velocities from an effusive source of ND_3 for various temperatures. (b) Schematic of electrostatic velocity selection. Only molecules in the low-velocity tail of the distribution are guided around the bend. The maximum velocity of molecules that are successfully guided around the bend is $v_{\max}$. Modified from [158]

Only molecules travelling at velocities below $v_{\max}$ will be confined by the electric field and successfully guided around the right-angle bend. Molecules travelling faster than $v_{\max}$ will not be confined by the electric fields around the bend, and will be lost from the guide. A good vacuum system is needed to pump away these molecules in order to minimise collisions between the background gas and successfully guided molecules. $v_{\max}$ depends on various parameters such as the bend radius of the guide and the potentials applied to the electrodes, as described in Section 2.3.3.

The bend acts as a low-pass velocity filter to create a beam of translationally cold molecules; however, if the source is at room temperature then the beam is not rotationally cold. For a room temperature source of molecules, many different rotational states are populated (refer to Section 2.1.2 and Figure 2.4). Each rotational state will have a different effective dipole moment, and therefore exhibit different Stark shifts and cut-off velocities. The molecular beam exiting the guide will be enriched in rotational states possessing a large Stark shift and will lack a sharp velocity cut-off [110].

The number of rotational states populated in a buffer-gas-cooled source of molecules is much smaller than for a room-temperature source, which enhances the quantum state purity of the molecular beam exiting the guide. Reaction cross sections may depend strongly on the rotational state, and thus, indirectly, on rotational cooling. Therefore, a buffer-gas-cooled source of molecules may be useful for studying low temperature reactions. For example, if a specific orientation allows reactants to approach along a more favourable reaction pathway of the PES, then decreasing the rotational temperature may actually increase the reaction rate [162].

2.3.2 Trapping potentials

When discussing the motion of molecules in the straight section of the guide, the guide axis is defined as the 'longitudinal' or 'z' direction. The 'transverse' direction is perpendicular to the guide axis, where the 'x' and 'y' designations refer to the horizontal and vertical coordinates perpendicular to the guide axis, respectively.

When describing the motion of molecules in the bent section of the guide, it is sometimes more convenient to use a curvilinear coordinate system that rotates with the guide electrodes. The horizontal (radial) and vertical directions within the guide are still described by the $\hat{x}$ and $\hat{y}$ unit vectors, respectively. The unit vector tangent to the centre-line of the bent section of the guide of radius R is given by $\hat{s}$. The progression of the molecule around the bend is defined by θ, which ranges from zero at the start of the bend to 90° when the molecule reaches the end of the bend. This coordinate system is illustrated in Figure 2.7(b). The position and velocity of a molecule inside the guide are given by

$$\mathbf{r} = x\hat{\mathbf{x}} + y\hat{\mathbf{y}} + (R+x)\theta\hat{\mathbf{s}} \tag{2.32}$$

$$\dot{\mathbf{r}} = \dot{x}\hat{\mathbf{x}} + \dot{y}\hat{\mathbf{y}} + (R+x)\dot{\theta}\hat{\mathbf{s}}. \tag{2.33}$$

The adiabatic potential $W(x, y, \theta)$ in the quadrupole electric field depends on the Stark state of the molecule, and determines the force experienced by the molecule according to $\mathbf{F} = -\nabla W(x, y, \theta)$. Furthermore, the three-dimensional force experienced by the molecule in the curvilinear coordinate system is given by

$$\mathbf{F} = m\mathbf{a} = m\big(\ddot{x} - (R + x)\dot{\theta}^2\big)\hat{\mathbf{x}} + m\ddot{y}\hat{\mathbf{y}} + m\big(2\dot{x}\dot{\theta} + (R + x)\ddot{\theta}\big)\hat{\mathbf{s}}. \tag{2.34}$$

This expression is derived from Newton's equations of motion in combination with Lagrange's equations [158].

The electrostatic guide used in this work consists of four parallel electrode rods positioned at the vertices of a square. A high voltage is applied to the electrodes, with adjacent electrodes held at opposite polarity, as shown in Figure 2.8(a). The resulting quadrupole electric field generated between the electrodes has a minimum at the centre of the guide and creates a two-dimensional confining potential transverse to the guide axis for molecules in low-field-seeking states. The potential barrier depends on the Stark shift at the electric field maximum, $W_{\text{Stark}}(E_{\text{max}})$, located at the edge of the electrodes. Any molecule whose kinetic energy does not exceed the potential barrier will be confined to the guide. As the potential barrier depends on the rotational quantum state of the molecule, the maximum kinetic energy of the trapped molecule is also state-dependent.

The electric field in the bent section of the guide can be approximated by the electric field in the straight sections when the bend radius R is much larger than the inner radius r of the quadrupole. This approximation is no longer valid for bend radii less than about 5 mm with a 1 mm inner radius, at which point distortions occur in the electric field [158]. The tangential force depends on $\partial W/\partial\theta$ and therefore becomes zero under this approximation. Furthermore, conservation of angular momentum gives the expression

$$\frac{\mathrm{d}}{\mathrm{d}t}\big((R + x)^2\theta\big) = 0. \tag{2.35}$$

As described above, the transverse kinetic energy of a molecule must be less than

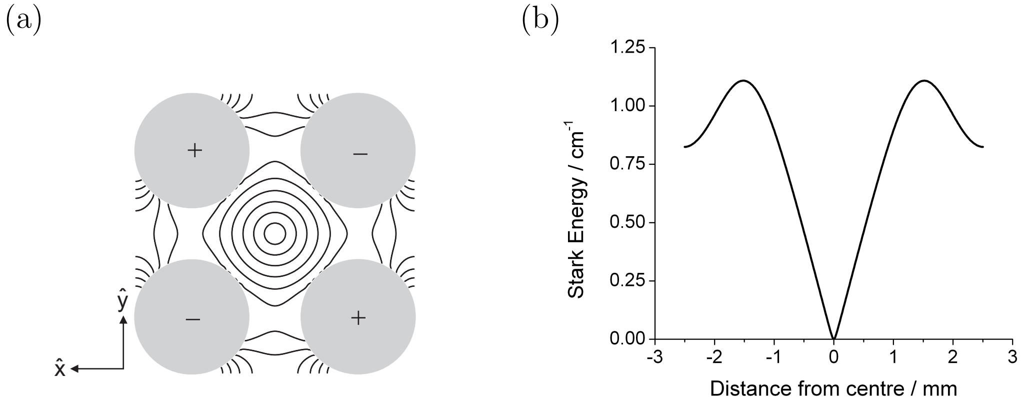

Figure 2.8: (a) Electric field contours for a ± 5kV quadrupole guide. The inner contour line corresponds to 5 kV/cm and the outer to 90 kV/cm, with 15 kV/cm intervals. (b) The cross section through the Stark potential for ND_3 molecules in the $|J, MK\rangle = |1, -1\rangle$ low-field seeking state in the quadrupole geometry used experimentally.

the Stark potential energy to be confined within the straight sections of the guide. The Stark force that confines the low-field-seeking molecules to the centre of the guide becomes the centripetal force guiding the molecules around the bend. The centripetal Stark force must exceed the centrifugal force mv_z^2/R in order for the molecules to be successfully guided around the bend. The longitudinal velocity is coupled to the horizontal velocity in the bent section of the guide. Therefore, the effective confining potential becomes radially asymmetric, and the trap depth of the guide decreases depending on the initial longitudinal velocity of the molecule entering the bend. Molecules that were previously confined in the straight sections are now lost from the guide, either through collisions with the electrodes or simply escaping the quadrupole guide.

Conservation of angular momentum in the bent section of the guide (Eq. 2.35) means that integration of the centrifugal force term in Equation 2.34 can be used to determine the effective potential experienced by the molecules in the horizontal and vertical directions. The effective potential depends on the initial tangential velocity

v_z according to the expression [158]

$$V(x,y) = W(x,y) - mv_\mathrm{z}^2 \ln\left(1 + \frac{x}{R}\right). \tag{2.36}$$

2.3.3 Maximum velocity and flux of guided molecules

Using the coordinate system described in Section 2.3.2, the transverse velocity is given by $v_\perp = \sqrt{v_\mathrm{x}^2 + v_\mathrm{y}^2}$. The initial position of the molecule at the guide entrance, specifically its radial distance from the guide axis, and its Stark shift will dictate if its transverse velocity is low enough to be confined within the guide. By equating the transverse kinetic energy of the molecule with its Stark potential energy, we can calculate the maximum transverse velocity of guided molecules in the straight section of the guide,

$$v_{\perp,max} = \sqrt{v_x^2 + v_y^2} = \sqrt{\frac{2W_\mathrm{Stark}(E_\mathrm{max})}{m}}. \tag{2.37}$$

The molecules propagate freely along the guide axis in the straight sections of the guide; it is only in the bent section of the guide that longitudinal velocity selection occurs. Some state selection may occur in the straight sections because those states with the least positive Stark shifts will not be guided away from the electrodes. Molecules are successfully guided around the bend with a radius of curvature of R provided their centrifugal force mv_z^2/R is less than the centripetal Stark force, which is approximately $W_\mathrm{stark}(E_\mathrm{max})/r$ for polar molecules with a linear Stark shift. The maximum longitudinal cut-off velocity can therefore be calculated by equating the centrifugal force to the centripetal Stark force and making the substitution for $v_{\perp,\mathrm{max}} = \sqrt{v_\mathrm{x}^2 + v_\mathrm{y}^2} = \sqrt{\frac{2W_\mathrm{Stark}(E_\mathrm{max})}{m}}$,

$$v_\mathrm{z,\ max} = \sqrt{\frac{W_\mathrm{Stark}(E_\mathrm{max})R}{rm}} = \sqrt{\frac{R}{2r}} v_{\perp,\mathrm{max}}. \tag{2.38}$$

A bend radius of $R = 100$ mm and a quadrupole inner radius of $r = 1.12$ mm is used in this work, with a voltage of ± 5 kV typically applied to the electrodes. For ND_3 in the $|1, -1\rangle$ low-field-seeking state, this corresponds to a longitudinal velocity cut-off of approximately 243 ms^{-1}. Lower velocity cut-offs can be achieved by using a smaller bend radius or a lower voltage. The velocity cut-off is approximately 188 ms^{-1} for an applied voltage of ± 3 kV, and 106 ms^{-1} for an applied voltage of ± 1 kV. A sharp velocity cut-off does not exist in reality because more than one quantum state is populated. The velocity cut-off depends on the Stark potential, which in turn is dependent on the rotational state of the molecule. Thus, the mixture of rotational states populated at a given temperature leads to a broadening of the longitudinal cut-off velocity.

The transverse and longitudinal velocities are coupled in the bent section of the guide, which decreases the depth of the transverse confining potential. The maximum transverse velocity in the bent section of the guide $v_{\perp,\mathrm{max,\ b}}$ is therefore smaller than the maximum transverse velocity in the straight section of the guide $v_{\perp,\mathrm{max}}$. It depends on the initial longitudinal velocity of the molecules entering the bend and can be calculated using [158].

$$v^2_{\perp,\mathrm{max,\ b}} = v^2_{\perp,\mathrm{max}} - v^2_{\mathrm{z}} \frac{2r}{R}. \tag{2.39}$$

The guided flux of molecules in a specific quantum state $|n\rangle$ can be approximated using [158]

$$\Phi_{\mathrm{n}} \approx \Phi_{\mathrm{n},0} \left(\frac{R}{2r}\right) \left(\frac{W_{\mathrm{max}}}{k_{\mathrm{B}}T}\right)^2, \tag{2.40}$$

where $\Phi_{\mathrm{n},0}$ denotes the flux of molecules leaving the effusive source in the quantum state $|n\rangle$. This means the guided flux depends quadratically on the trapping electric field for polar molecules with linear Stark shifts, because $W_{\mathrm{Stark}} = -\mu_{\mathrm{eff}}|\vec{E}|$ for these molecules [163]. However, this approximation is only valid when the thermal velocity of the molecular source is much greater than the longitudinal cut-off velocity of the electrostatic guide, which is not the case for most buffer-gas-cooled molecular sources and other low-temperature thermal gases. Additionally, as noted earlier, the radius of curvature R must be much larger than the inner radius of the guide r.

A general description of electrostatic velocity selection, with specific details about the trapping potentials, maximum guided velocities, and flux of the beam, has been provided in this section. In order to gain a better understanding of the guiding process, and to help direct the design and construction of the experimental apparatus, Monte Carlo trajectory simulations were carried out. These are described in the next section.

2.4 Monte Carlo simulations

First, an overview of the molecular source and electric field used in the Monte Carlo trajectory simulations is provided. Then, the effect of various experimental parameters on the guiding process is investigated, such as the voltage, bend radius, and guide geometry. The loss of molecules from the guide due to multiple bends, gaps between the electrodes, and the distance to the detector is also discussed. Finally, the section ends with a discussion of the effect that the quantum rotational state has on the guidability of the molecules.

2.4.1 Computational details

Molecular source model

Experimentally, a buffer-gas-cooled molecular beam is used to load molecules into the electrostatic guide. As described in Section 2.1, the molecules may exit the cell in various different gas flow regimes depending on the experimental parameters. However, for the purpose of these Monte Carlo simulations, which serve to explain the electrostatic guiding process, the molecular source is assumed to be effusive and obey simple gas kinetic theory. At a more advanced level, the Direct Simulation Monte Carlo method (DSMC) can be used to simulate the detailed gas dynamics within the buffer gas cell, and leads to a more complete understanding of the properties of the experimental molecular source [164]. Some progress has been made on this by Laura Pollum and others in the group, but the details are beyond the scope of this work.

The initial velocity and angular distribution of the molecules used in the simulations are those of an effusive molecular source. The initial positions of the molecules are randomly generated to form a uniform distribution over a 0.5 mm-radius disk simulating the buffer gas cell exit aperture. A transformation sampling procedure from a Maxwell-Boltzmann distribution of a source held at temperature T is then used to assign initial velocities. The angular distribution of the molecules exiting the buffer-gas cell is approximated as approaching the cosine law $j(\theta) = \cos(\theta)$, which accurately describes the angular velocity of effusive sources where the exit aperture is much smaller than the mean free path of the molecules [52].

The electric field and trapping potential

The quadrupole guide used in the experiments consists of 2 mm diameter electrodes with a 1 mm separation between adjacent electrodes, leading to an inner radius of approximately 1.12 mm (see Section 3.6.3 for technical details of the electrodes). SIMION 3D software is used to calculate the electric potential within the quadrupole guide, using this electrode configuration and an applied voltage of ± 5 kV unless otherwise specified. The electrode configuration is simulated using a three-dimensional grid with a grid unit of 0.02 mm. SIMION then calculates the electric potential U at each grid point, and the electric field E using $E = -\nabla U(x, y, z)$. Finally, third order polynomial interpolation can be used to create a continuous electric field distribution. Figure 2.8(a) shows contours of the electric field generated within the quadrupole guide, with a maximum of approximately 90 kV/cm found at the surface of the electrodes.

The electric field shows an approximately linear dependence on the distance from the guide axis, although there is a slight perturbation from cylindrical symmetry close to the electrodes. The electric field maximum along a line bisecting neighbouring electrodes is nearly identical to the maximum along a line passing through the centre of the electrodes themselves, creating a trapping potential approximately equivalent in all transverse directions. The electric fields calculated in the straight sections of the guide are used for the bent section as well, which is a reasonable approximation as long as the inner radius of the guide is much smaller than the radius of curvature of the bend.

The force experienced by a polar molecule at any given point within the guide can be found by recalling that the force is calculated from the gradient of the Stark energy, $\mathbf{F}(\mathbf{r}) = -\nabla W_{\text{Stark}}(\mathbf{r})$. The Stark energy is calculated in MATLAB using the method described in Appendix A.1 for specific rotational states. From this, the force experienced by a molecule at a given distance from the guide centre can then be determined. A cross section through the adiabatic Stark potential experienced by the molecules within the guides is shown in Figure 2.8(b). In the bent section of the guide, the centrifugal force must be included in the force calculations.

Trajectory simulations

The initial parameters used in the trajectory simulations were based on the quadrupole guide previously built in the Softley group [158]. This includes a 1 mm gap between the molecular source and the guide entrance, and a guide consisting of two straight sections (167.5 mm and 610.0 mm) separated by a 90° bend with a 12.5 mm radius of curvature.

After the initial position and velocities of the molecules are defined (as described in Section 2.4.1), the simulation starts with a period of free flight between the effusive molecular source and the guide entrance. Those molecules that successfully make it to the guide entrance are then propagated along the first straight section of the guide. A velocity Verlet algorithm is used to simulate the evolution of the molecules in the guide, with the velocity and position given by Equation 2.41 and Equation 2.42, respectively, after time-step Δt.

$$v(t + \Delta t) = v(t) + \frac{1}{2}a(t)\Delta t \tag{2.41}$$

$$x(t + \Delta t) = x(t) + v(t)\Delta t \tag{2.42}$$

Molecules that do not collide with the electrodes or escape from the quadrupole guide are then propagated through the bent section, and finally the second straight section of the guide. Experimentally, the molecules are detected approximately 20 mm after the exit of the guide. The positions and velocities of successfully guided molecules in the simulations are therefore recorded after a final period of free flight. The simulations are easily extended to other experimental set-ups by including additional bent or straight sections with the desired radii or lengths.

2.4.2 Quadrupole versus hexapole guides

In addition to aiding our understanding of the guiding process and analysing the data, the Monte Carlo simulations were useful in making certain decisions about the construction of the experimental apparatus. One of the first questions investigated was the difference between quadrupole and hexapole guides.

The electric field contours and resulting Stark potentials experienced by ND_3 molecules in the low-field seeking $|J, MK\rangle = |1, -1\rangle$ state are shown in Figure 2.9 for a hexapole and quadrupole arrangement of electrodes. The geometry of both the hexapole and quadrupole guides are based on configurations that have been used previously in the group; the inner radius of the hexapole guide is 4 mm, while the inner radius of the quadrupole guide is only 1.12 mm. For technical reasons, a quadrupole guide was chosen for the experimental apparatus before the comparison between a hexapole and quadrupole guide with a similar inner radius was completed. Therefore, a discussion of the Monte Carlo simulations for the hexapole and quadrupole guides will be limited to the geometries shown in Figure 2.9(a). For the same applied voltage of ±5.0 kV, the maximum confining electric field near the surface of the electrodes is much smaller for the hexapole (35 kV/cm) than for the quadrupole (90 kV/cm). This leads to a lower confining Stark potential within the guide for the hexapole, as shown in Figure 2.9(b). Additionally, the electric field is closer to being cylindrically symmetric for the hexapole guide than for the quadrupole guide.

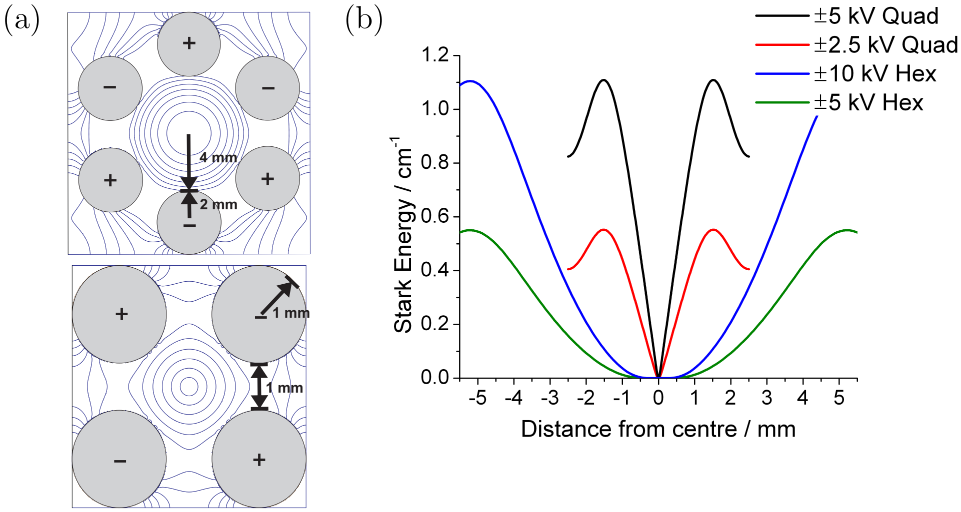

Figure 2.9: (a) Electric field contours for the ± 5.0 kV hexapole (quadrupole) guide. The inner contour line corresponds to 5 kV/cm (5 kV/cm) and the outer to 35 kV/cm (90 kV/cm) at intervals of 5 kV/cm (15 kV/cm). (b) The cross section through the Stark potential for ND_3 molecules in the $|J, MK\rangle = |1, -1\rangle$ low-field seeking state for hexapole and quadrupole guides at various voltages.

In the region of low electric field near the centre of the guide axis, the Stark effect for ND_3 is close to linear for the quadrupole guide and quadratic for the hexapole guide. This leads to two competing effects, although neither is included in the simulations. First, molecules that enter the guide slightly off-centre from the guide axis will experience a greater repulsive potential barrier at the entrance of the quadrupole guide compared to the hexapole guide [165]. Therefore, the hexapole guide exhibits a larger effective entrance for the low velocity molecules from the molecular source. Second, non-adiabatic 'Majorana' transitions (Section A.1) are more likely to occur in regions where the Stark energy shifts are small compared to other possible perturbations. In these regions, the molecule is more likely to undergo a transition to a different quantum state, which may result in the molecule being lost from the guide if the transition is from a low-field seeking state to a non-guidable or a high-field seeking state. Molecules are more susceptible to these 'Majorana' transitions in the hexapole guide, which has a larger region around the guide axis where small Stark energy shifts can occur. Furthermore, the probability of non-adiabatic transitions increases with longer interaction times between the molecule and the inhomogeneous electric field. As a result, the slow moving molecules with longer interaction times are more likely to be affected by the 'Majorana' transitions.

The lower trapping depth in the hexapole leads to a lower longitudinal velocity cut-off. This can be seen in Figure 2.10(a), which shows the longitudinal velocity distribution for an initial 4 K thermal source of molecules exiting the buffer gas cell and the velocity distribution of the simulated molecules successfully guided around the bend of the hexapole and quadrupole guides.

The simulations shown here are for the $|J, MK\rangle = |1, -1\rangle$ state of ND_3. Molecules in different rotational states exhibit different effective dipole moments, and therefore the depth of the effective potential is quantum-state specific. This is discussed in detail in Section 2.4.6. However, for a 4 K thermal source of molecules, 28.1% of molecules are in the $J = 0$ non-guidable state, 71.2% are in the $J = 1$ state, and $< 1\%$ of molecules are in states with $J \geq 2$ (for a 6 K source, 12.1% are in $J = 0$, 82.8% in $J = 1$, and 5.1% in $J \geq 2$). Therefore, this is a reasonable approximation to make which greatly simplifies the simulations.

Because only one rotational state is used in these simulations, the guided molecules exhibit a sharp longitudinal velocity cut-off for the hexapole guide (Fig. 2.10). This

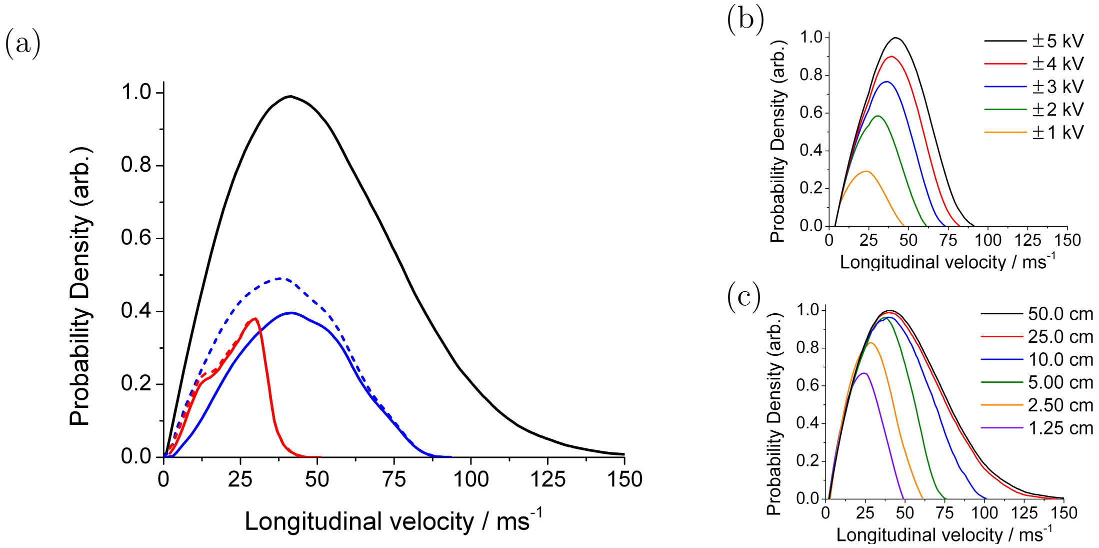

Figure 2.10: (a) Longitudinal velocity distributions for the 4 K buffer gas source of molecules (black), and for hexapole (solid red) and quadrupole (solid blue) guided molecules with an applied voltage V = ± 5.0 kV. Dashed curves show distributions when there is no gap between the source of molecules and the guide entrance. (b) Final velocity distributions of guided molecules for various applied voltages for a 12.5 mm quadrupole guide, and (c) various bend radii for a ±5 kV hexapole guide.

may be observed experimentally for buffer-gas-cooled sources of molecules in which only a few low-energy rotational states are occupied. However, for room temperature molecular sources, the velocity cut-off tends to be broadened due to contributions from many different rotational states, each with a different velocity cut-off. The velocity cut-off is not broadened in the quadrupole because the larger trapping potential for these parameters means that a much greater proportion of the high velocity molecules present in the initial distribution are successfully guided. The number of high velocity molecules in the initial distribution already starts to decrease before the longitudinal cut-off velocity of the quadrupole guide is reached, contributing to the broadening of the high velocity tail of the quadrupole distribution. Small distortions of the transversely symmetric electric field may also contribute to the broadening of the velocity cut-off in the quadrupole guide (Fig. 2.9(a)). Molecules entering the guide off-centre from the guide axis will have different potential energies that contribute to the velocity cut-off broadening, as well as the mixing of the transverse velocity with the longitudinal velocity in the bent sections of the guide [166].

The greater loss of the slowest molecules from the quadrupole guide arises from the difference in inner radius of the guides, approximately 1.12 mm for the quadrupole guide and 4 mm for the hexapole guide used in these simulations. In the 1 mm gap between the molecular source and the guide entrance, the molecules enter a region of free flight. The slowest longitudinal molecules often have greater transverse velocities and therefore spread out farther in this region. Thus, the slow molecules are more likely to be outside of the relatively narrow quadrupole guide entrance compared to the wider hexapole guide. Eliminating the 1 mm region of free flight in the simulations has little effect for the wide hexapole, but regains the low-velocity tail of the distribution for the quadrupole (Fig. 2.10). Unfortunately, the gap cannot be eliminated experimentally because that would involve placing the electrodes in contact with the exit plate of the buffer gas cell. A gap of approximately 1 mm is necessary to prevent molecular ice that builds up inside the cell and around the exit aperture from extending to the electrodes and potentially leading to electrical discharges.

Although there are several advantages to using a hexapole guide, such as a more transversely symmetric electric field and a larger effective entrance to the guide for slow molecules, alignment of six electrodes presents greater technical challenges compared to a quadrupole with only four electrodes. A quadrupole was selected for the experimental electrostatic guide because of these construction difficulties, since the guide must be very long (2148.8 mm in the final construction) with large portions in cryogenic regions.

2.4.3 Voltage and bend radius dependence

Higher voltages increase the trap depth of the electrostatic guide and lead to faster molecules being successfully guided around the bend (Fig. 2.10(b)). As described in

Section 2.3.3 and seen in Equation 2.40, the guided flux should depend quadratically (quartically) on the trapping electric field, and therefore on the voltage applied to the electrodes, for molecules with linear (quadratic) Stark shifts in quadrupole (hexapole) guides. However, this relationship is not valid when the thermal velocity of the gas is of similar magnitude to the longitudinal cut-off velocity of the guide, such as for the 4 K source when the highest voltage settings are used in the simulations (Fig. 2.10(b)). The initial velocity distribution is clearly seen to affect the velocity distribution at the end of the filter, as a large portion of the initial distribution is successfully guided even for sub-maximal voltages.

A larger bend radius means that faster molecules will be successfully guided around the bend. This is because the centrifugal force mv_{z}^2/R only exceeds the confining centripetal Stark force arising from the two-dimensional transverse potential of the guide at higher velocities. This is illustrated in Figure 2.10(c) for a hexapole guide. Similar to the voltage dependence of the guided flux shown in Figure 2.10(b) for a quadrupole guide with a 4 K thermal molecular source, the increase in guided flux achieved by increasing the bend radius plateaus after a large portion of the initial distribution is successfully guided.

Although a bend radius of 12.5 mm was used in electrostatic velocity experiments conducted previously in the group using a quadrupole guide [158], it was decided to use the much larger bend radius of 100 mm when constructing the current experimental apparatus. The main reason for this change was to be able to study molecules with much weaker Stark shifts than had been previously investigated. A small bend radius would lead to insufficient guided flux for molecules with weak Stark shifts. Typically, a voltage of ±5 kV is applied to the electrodes. Electrical discharges tend to occur for higher voltages when the apparatus is cooled down, so this is the maximum voltage used experimentally. The guide may be more susceptible to electrical discharges at cryogenic temperatures due to the formation of molecular ice around the exit aperture, which is only 1 mm away from the end of the electrodes. Lower voltages are only used if lower-velocity distributions are desired, because the guided flux will also decrease with the lower voltages.

2.4.4 Betatron oscillations

The longitudinal velocity distribution for the hexapole guide (Fig. 2.10(a)) exhibits a hump in the low-velocity tail of the distribution. This feature is due to the betatron oscillations that occur as the molecules are guided around the bend. In the straight sections of the guide, motions in the x and y (radial) directions are fully mixed, but are not coupled to motion in the z (longitudinal) direction. Upon entering the bent section of the guide, however, the forward tangential motion couples to the radial motion in order to conserve angular momentum, and the resulting oscillations around the equilibrium orbit are called betatron oscillations [167].

To study the effect of these oscillations, the initial longitudinal velocity was set to a specific value and the resulting velocity distributions of the molecules exiting the guide were compared for the hexapole and quadrupole guides (Fig. 2.11). In the absence of betatron oscillations, a molecule entering the guide with a longitudinal velocity of 25 ms^{-1} should exit with the same longitudinal velocity. In reality, however, the molecule exits the guide with a velocity that may be slightly shifted from its initial velocity.

The molecules undergo betatron oscillations with larger amplitudes in the hexapole guide compared to the quadrupole guide because of the larger inner radius (approximately 4 mm versus 1.12 mm). This can lead to unusual features in the velocity distribution, such as the low velocity hump, especially for configurations in which molecules only undergo a few oscillations while travelling around the bend. The velocity distribution is smoother for the quadrupole guide because the molecules undergo

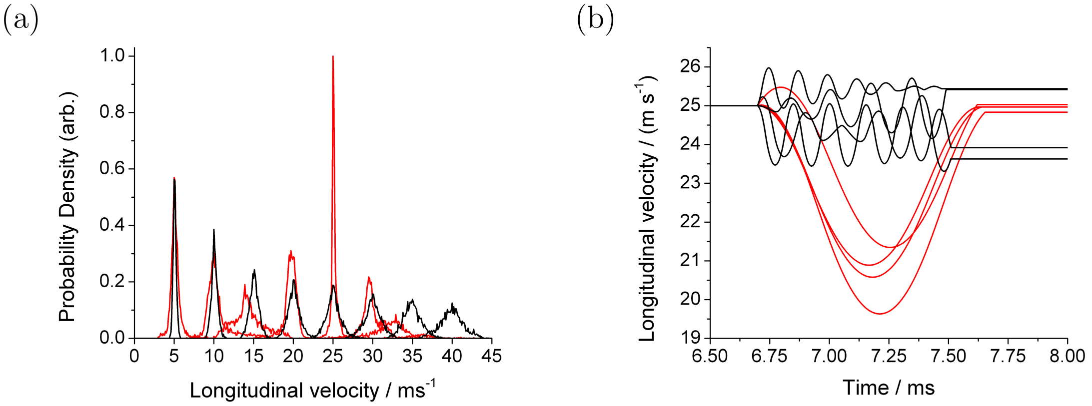

Figure 2.11: (a) Final velocity distributions for initial values between 5 ms^{-1} to 40 ms^{-1} for a ± 5.0 kV hexapole (red) and quadrupole (black) guide. (b) Example betatron oscillations of the forward velocity in the bent section of ±5 kV hexapole (red) and quadrupole (black) guides for the set initial velocity of 25 ms^{-1}. The variation in the velocity of the molecule as it travels around the bend is shown as a function of time of flight from the source.

several oscillations of small amplitude, leading to less potential deviation from the initial longitudinal velocity.

2.4.5 Guide loss – multiple bends, section gaps, and distance to detector

Multiple bends

In the experimental apparatus, the electrostatic guide moves the molecules away from the exit of the buffer gas cell, out of the main cryogenic chamber, and delivers them to the detection region of the assembly. Details of the design and construction of the experimental apparatus are provided in Chapter 3. As explained in Chapter 3, the total path length of the electrostatic guide is very long (2148.8 mm) and includes three 90° bends, each with a radius of curvature of 100 mm. The four straight sections are 20 mm, 596.5 mm, 263.8 mm, and 797.3 mm, respectively.

Monte Carlo simulations were run in order to assess the number of molecules lost from the guide at each section (Table 2.3). These were done for a molecular source at a thermal equilibrium of 6 K, 10 K, 50 K, and 300 K. The fraction of molecules remaining in the guide after the first straight section reflects the initial acceptance of the guide, which is greater for the 6 K source compared to the 300 K source. Also, a much larger fraction of the initial distribution is still confined within the guide at the end of the fourth straight section for the 6 K molecular source.

Table 2.3: The fraction of molecules that will be lost from the electrostatic guide with the addition of multiple bends, as predicted from Monte Carlo trajectory simulations. The percentage of molecules from the initial distribution that are still guided are given when the initial thermal equilibrium of the molecular source is 6 K, 10 K, 50 K, and 300 K. No gaps are included in this simulation.

Location	Percentage of initial population still in guide			
	6 K	10 K	50 K	300 K
1^{st} straight section	39.67	33.16	17.28	9.06
1^{st} bent section	36.76	29.02	7.97	0.77
2^{nd} straight section	36.50	28.75	7.90	0.76
2^{nd} bent section	35.58	27.35	6.76	0.62
3^{rd} straight section	35.50	27.31	6.74	0.62
3^{rd} bent section	34.81	26.33	6.05	0.54
4^{th} straight section	34.71	26.26	6.03	0.54

A greater fraction of molecules are lost after the first bend for the 300 K distribution. This is because the thermal velocity of the molecular source is similar to the longitudinal velocity cut-off for the 6 K source, so a large proportion of the initial distribution will be successfully guided around the bend provided they have sufficiently low transverse velocities. The thermal velocity at 300 K is much greater than the longitudinal cut-off velocity, so a significant portion of the molecules are expected to be lost after the first bend. Molecules are still lost from the guide after the later bends and straight sections, although the magnitude of the loss is much smaller then the initial transverse and longitudinal velocity selection in the first straight and bent sections of the guide. This is likely due to the coupling of the longitudinal and transverse velocities through the betatron oscillations in the bent sections of the guide. As a result, some molecules will have boosted transverse (longitudinal) velocities and will be lost in the subsequent straight (bent) sections of the guide.

There are several factors not included in the simulations that also contribute to molecular loss from the guide. For example, collisions with background gas and non-adiabatic Majorana transitions contribute to losses from the guide, and will lead to a lower fraction of molecules from the initial distribution reaching the end of the fourth straight section than predicted by the simulations. There were many technical challenges to constructing an electrostatic guide with a large bend radius and a very long total path length. Imperfections in the alignment of the electrodes, and therefore slight deviations in the confining electric field contained within the guide, likely contribute to molecular losses. Due to the long overall path length, the guide was physically broken into six different segments during the construction of the apparatus. The alignment issues are particularly difficult at these joins. Therefore, it is difficult to accurately ascertain the loss percentage given experimental imperfections and assumptions implicit in the Monte Carlo simulations.

Gaps between electrode sections

The electrostatic guide transfers molecules from the exit of the buffer gas cell in the cryogenic region of the experimental apparatus to the UHV detection chamber, as described in Chapter 3. After running the experiment for several hours, the cryogenic region must be warmed up in order to melt the molecular ice that forms around the exit aperture of the buffer gas cell and eventually blocks molecules from exiting the cell. A large amount of gas is released during this process, which can pollute the UHV detection chamber. The ultimate aim is to place an ion trap in the detection chamber in order to study chemical reactions between the laser cooled and trapped atoms and the cold molecules exiting the electrostatic guide. This large release of gas after every day of running the experiment may potentially cause problems with the UHV chamber of the ion trap.

A very thin gate valve has been designed by Pittman and O'Connor [168] for use in transferring ions from the source to the ICR cell in mass spectrometry with a very high transmission efficiency. When closed, a vacuum of $< 10^{-10}$ mbar can be achieved in the region of the mass spectrometer while the source is open to atmosphere. Although this would clearly be advantageous when combining with the ion trap, the current design of the thin gate valve requires a gap of 5.21 mm between two sections of the quadrupole guide. Monte Carlo trajectory simulations were done to determine the effect of different sized gaps on the number of molecules lost from the guide and the velocity distributions of the molecules remaining in the guide.

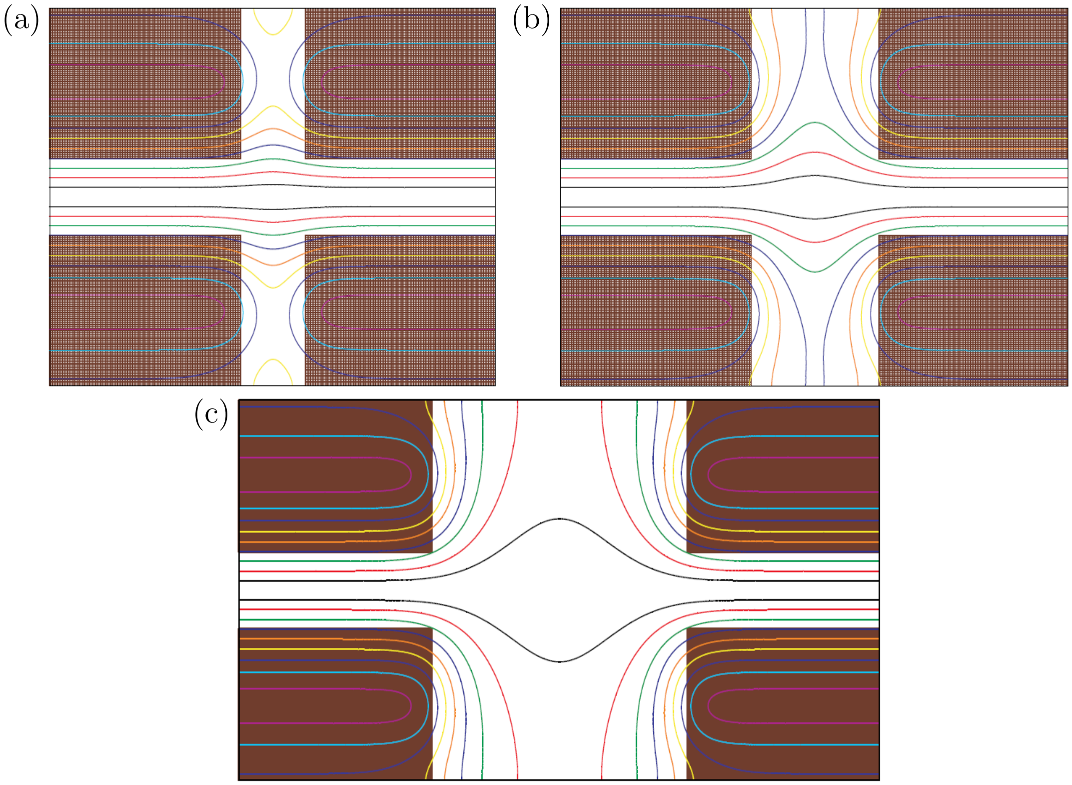

Figure 2.12: SIMION 3D software is used to calculate the electric field present in the gaps between the electrodes of adjacent sections, for (a) 1 mm, (b) 2 mm, and (c) 4 mm gaps. The contours lines are shown for electric field strengths of 10 kV/cm (inner, black) to 90 kV/cm (outer, pink), with contours provided every 10 kV/cm.

SIMION 3D software was used to calculate the electric field when there is a gap between the electrode sections of the guide, as shown in Figure 2.12. Although the distortion of the electric field is only minor for small gaps, large distortions are present for gaps greater than about 3 mm. Therefore, in order to simplify the Monte Carlo simulations, the gap between the electrodes was approximated by a region of free flight rather than using the electric fields calculated in SIMION.

The position-velocity phase diagrams are shown in Figure 2.13 for molecules from a 5 K source after a straight section of guide, after the region of free flight in the 5 mm gap between the electrodes, and at the end of the adjacent section of the guide. When the molecules are in the gap and have minimal or no confining electric field, the transverse velocities of the molecules cause the molecules to spread out radially. Molecules with low longitudinal velocities often have large transverse velocities and are outside of the guide entrance at the end of the gap. Additionally, velocities may be shifted to higher values as a result of acceleration of the molecules by the fringe fields present at the ends of the electrodes. The velocity distribution of the guided molecules after the gap is shown in Figure 2.14 for the Monte Carlo simulations.

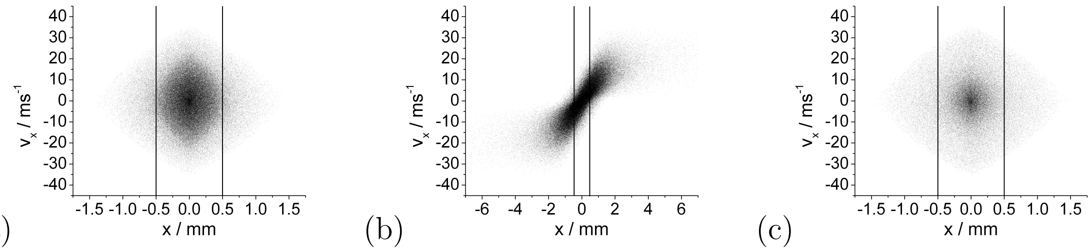

(a) (b) (c)

Figure 2.13: The position-velocity phase diagrams are shown for the horizontal x direction. These are calculated for a 5 K source of molecules (a) after a straight section of quadrupole guide and before the gap, (b) after a 5 mm gap, and (c) after a second straight section of guide located after the gap. Vertical lines show the inner radius of the quadrupole guide and the number of molecules are indicated by the density of the dots.

The fraction of molecules that will be lost from the guide for various gap sizes is provided in Table 2.4. A 5 mm gap for a 5 K source of molecules leads to a significant loss of molecules. The thin gate valve described in [168] would need to be modified

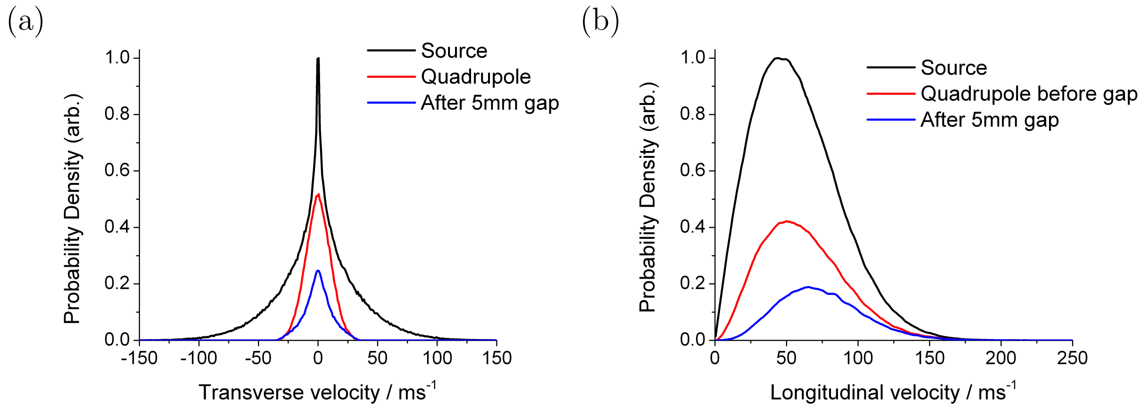

Figure 2.14: The (a) transverse and (b) longitudinal velocity distributions of a 5 K source of molecules guided by a quadrupole before and after a 5 mm gap.

such that a much smaller gap existed between the two sections of the electrostatic guide. A similar valve was used in [91] which could be pushed manually through a 1 mm gap in the electrodes.

Table 2.4: The percentage of molecules that will be lost from the electrostatic guide when there are gaps between adjacent sections of the guide, as predicted from Monte Carlo trajectory simulations.

Size of gap / mm	Percentage of molecules lost in gap	
	5 K	300 K
0.5	6.7	1.2
1	12.8	1.9
2	26.7	2.6
3	39.0	4.7
4	49.1	6.1
5	54.8	8.2

Distance to the detector

Once the molecules exit the guide, they enter a field-free region before reaching the detector. The molecular beam disperses in the absence of any confining electric fields. Placing the detector close to the guide exit will increase the number of guided molecules that directly hit the target detector. For example, the molecules must enter the active area of the ionisation cage when detecting the molecules with mass spectrometry. The active ionisation volume has a radial distance of $r \leq 7.5$ mm for the mass spectrometer used in these experiments. Figure 2.15 shows the fraction of molecules from the Monte Carlo simulations reaching the ionisation volume of the mass spectrometer for a 5 K and 300 K molecular source. The fraction of molecules reaching the detector decreases as the distance between the detector and the guide exit increases. The effect is more pronounced for the 5 K molecular source because the molecules are moving slower toward the detector giving the molecular beam more time to diverge before hitting the detector.

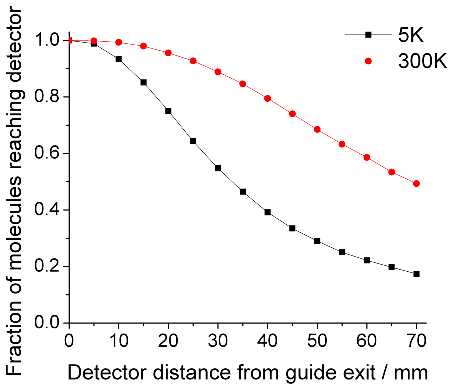

Figure 2.15: The fraction of molecules hitting the detector decreases as the detector is positioned farther from the guide exit. This is shown for the guided molecules from a 300 K (red) and 5 K (blue) source of molecules.

2.4.6 Effect of rotational state on guiding

The rotational state of a molecule determines its effective dipole moment relative to an external axis, and therefore its Stark energy in an inhomogeneous electric field. The Stark energy, calculated using the method described in Section A.1, is shown in Figure 2.16(a) and (b) for ND_3 in various $|J, MK\rangle$ rotational states. The transverse confining potential experienced by the molecule within the quadrupole guide can be determined from the Stark energy, and is shown in Figure 2.16(c) and (d).

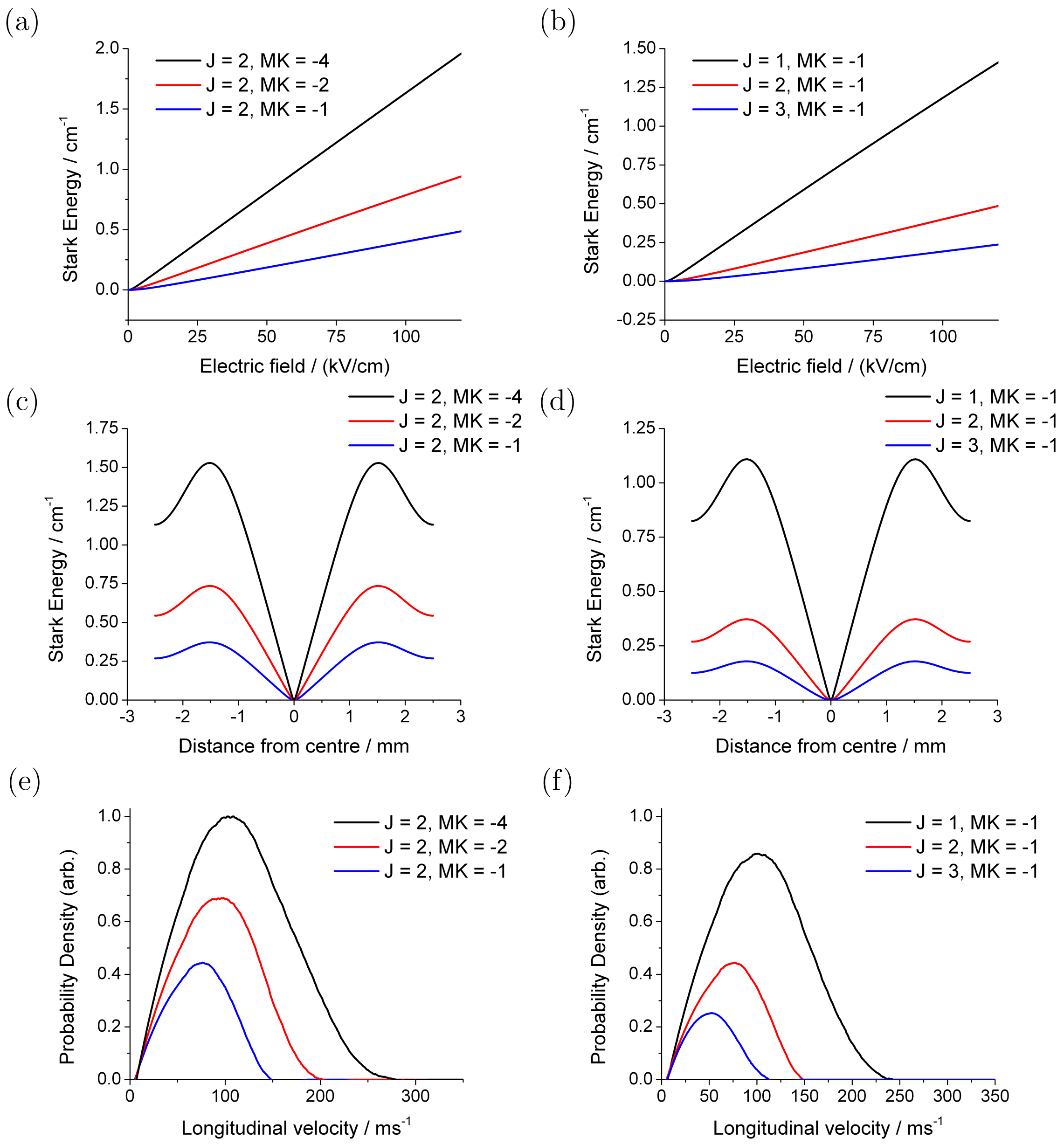

Figure 2.16: (a), (b) The Stark energy calculated for ND_3 molecules in various rotational states, over the range of electric fields typically found experimentally in the quadrupole guide. (c), (d) Rotational state dependence of the Stark potential energy experienced by molecules within the quadrupole guide, shown for a cross section of the transverse x direction. (e), (f) Longitudinal velocity distributions of successfully guided molecules determined from Monte Carlo simulations of the guiding process for an initial temperature of 25 K.

Monte Carlo trajectory simulations can be used to determine the longitudinal velocity distributions of guided molecules in each of these rotational states, as shown in

Figure 2.16(e), (f). These simulations are for a quadrupole guide with a bend radius of 100 mm (which is used experimentally) and for a molecular source temperature of 25 K. Rotational states with larger Stark energies at the electric field maximum found near the guide electrodes will experience a stronger confining Stark potential. This leads to a larger centripetal Stark force in the bent section of the guide, the successful guiding of molecules with higher velocities, and a greater flux of molecules in that particular rotational state at the guide exit compared to the distribution in the molecular source. A detailed study on the guidability of individual rotational states in an electrostatic hexapole guide has also been reported by Bertsche and Osterwalder [169].

The longitudinal velocity cut-off is rotational-state dependent, and can be calculated using Equation 2.38. Table 2.5 summarises the cut-off velocities for the lowest few rotational states of ND_3 for the experimental apparatus. These match up well with the longitudinal velocity distributions obtained using the Monte Carlo trajectory simulations shown in Figure 2.16(e) and (f). The velocity cut-off appears to be slightly higher than shown in the distribution for the rotational state $|2,-4\rangle$; this is likely due to the proximity to the upper region of the initial 25 K distribution of velocities and therefore the lack of molecules in the source with velocities much higher than the velocity cut-off.

Table 2.5: The Stark shift is provided for several low-energy rotational states $|J, MK\rangle$ of ND_3 at an electric field of 90 kV/cm, which is typically the maximum field strength found within the quadrupole guide. For a quadrupole guide with a 100 mm radius of curvature and an inner radius of 1.12 mm, the longitudinal velocity cut-off can then be calculated for each rotational state.

$\|J, MK\rangle$	Stark shift / cm^{-1}	$v_{z,\max}$ / ms^{-1}
$\|1,-1\rangle$	1.07	238.63
$\|2,-1\rangle$	0.36	137.94
$\|2,-2\rangle$	0.71	194.28
$\|2,-4\rangle$	1.47	280.04
$\|3,-1\rangle$	0.17	95.28

Although electrostatic velocity selection does not specifically cool the rotational degrees of freedom of molecules, it does enhance the population of rotational states exhibiting strong Stark shifts. Monte Carlo simulations can be used to determine the 'guidability' factor of the rotational state. Rotational states with weak Stark shifts are not well guided, and most of the molecules are lost from the guide (low guidability). Rotational states with strong Stark shifts are well guided, and a large fraction of the initial number of molecules entering the guide are successfully confined along the entire length of the guide and are delivered to the detection region (high guidability).

For a thermal distribution of rotational states of ND_3 at 25 K, 99.9% of the molecules will be in a rotational state with $J \leq 5$. Therefore, the 'guidability' factor is determined for all the low-field seeking rotational states of ND_3 (and NH_3) with $J \leq 5$ by determining the percentage of molecules from a 25 K source that are successfully guided around a 100 mm bend quadrupole guide. The results are provided in Table 2.6. These are particularly useful in the PGOPHER simulations of the (2+1) REMPI spectra obtained for ND_3 and NH_3, as described in Section 5.3.

Simulated velocity distributions are shown for a molecular source at 6 K, 10 K, and 25 K, with contributions from each of the low-field seeking rotational states explicitly shown. The contributions from each state depends on both the initial population of the state (which is determined by the temperature of the source and described in Section 2.1.2), and on the 'guidability' of the state in the quadrupole guide. At 6 K, very few rotational states contribute to the longitudinal velocity distribution; the $|J, MK\rangle = |1, -1\rangle$ rotational state is the largest contributor to the longitudinal velocity distribution of the resulting molecular beam. Although the $|1, -1\rangle$ rotational state is still the largest contributor to the longitudinal velocity distribution by 25 K, many other rotational states also contribute to the total population and resulting velocity distribution of the guided molecular beam. As demonstrated in Figure 2.17, one of the main advantages of using the low temperature buffer-gas-cooled molecular beams

Table 2.6: The Stark shift is provided for all low-field seeking rotational states with $J \leq 5$ at an electric field of 100 kV/cm (typically the maximum field strength found within the quadrupole guide near the surface of the electrodes). This strongly influences the percentage of molecules from the initial 25 K molecular source that are successfully guided by a quadrupole with a 100 mm radius of curvature, as calculated from Monte Carlo trajectory simulations.

	ND$_3$		NH$_3$	
$\vert J, MK\rangle$	Stark Shift / cm^{-1}	Percentage guided / %	Stark Shift / cm^{-1}	Percentage guided / %
$\vert 1,-1\rangle$	1.18	15.18	0.92	13.33
$\vert 2,-1\rangle$	0.40	5.09	0.20	1.92
$\vert 2,-2\rangle$	0.79	10.57	0.54	7.14
$\vert 2,-4\rangle$	1.63	19.85	1.35	16.40
$\vert 3,-1\rangle$	0.19	2.12	0.06	0.36
$\vert 3,-2\rangle$	0.39	4.97	0.19	1.88
$\vert 3,-3\rangle$	0.59	7.86	0.36	4.24
$\vert 3,-4\rangle$	0.81	10.87	0.55	7.26
$\vert 3,-6\rangle$	1.22	15.70	0.94	12.21
$\vert 3,-9\rangle$	1.85	21.98	1.56	18.58
$\vert 4,-1\rangle$	0.11	0.97	0.2	0.09
$\vert 4,-2\rangle$	0.23	2.60	0.08	0.52
$\vert 4,-3\rangle$	0.35	4.20	0.16	1.37
$\vert 4,-4\rangle$	0.47	6.03	0.25	2.83
$\vert 4,-6\rangle$	0.72	9.74	0.48	6.10
$\vert 4,-8\rangle$	0.97	13.01	0.71	9.24
$\vert 4,-9\rangle$	1.10	14.47	0.83	10.69
$\vert 4,-12\rangle$	1.47	18.48	1.19	15.09
$\vert 4,-16\rangle$	1.98	22.82	1.68	19.62
$\vert 5,-1\rangle$	0.07	0.45	0.01	0.03
$\vert 5,-2\rangle$	0.15	1.33	0.04	0.22
$\vert 5,-3\rangle$	0.23	2.59	0.08	0.53
$\vert 5,-4\rangle$	0.31	3.56	0.13	1.09
$\vert 5,-5\rangle$	0.39	4.80	0.19	1.80
$\vert 5,-6\rangle$	0.48	6.24	0.26	2.91
$\vert 5,-8\rangle$	0.64	8.65	0.40	4.85
$\vert 5,-9\rangle$	0.73	9.78	0.48	6.15
$\vert 5,-10\rangle$	0.80	10.85	0.55	7.25
$\vert 5,-12\rangle$	0.98	13.11	0.71	9.31
$\vert 5,-15\rangle$	1.22	15.70	0.95	12.25
$\vert 5,-16\rangle$	1.31	16.69	1.03	13.29
$\vert 5,-20\rangle$	1.65	20.07	1.35	16.44
$\vert 5,-25\rangle$	2.07	23.29	1.77	20.29

for loading the electrostatic guide is that very few rotational states are populated in the guided beam. Molecular beams with high quantum state purity are often useful in studies of low temperature chemical reactions.

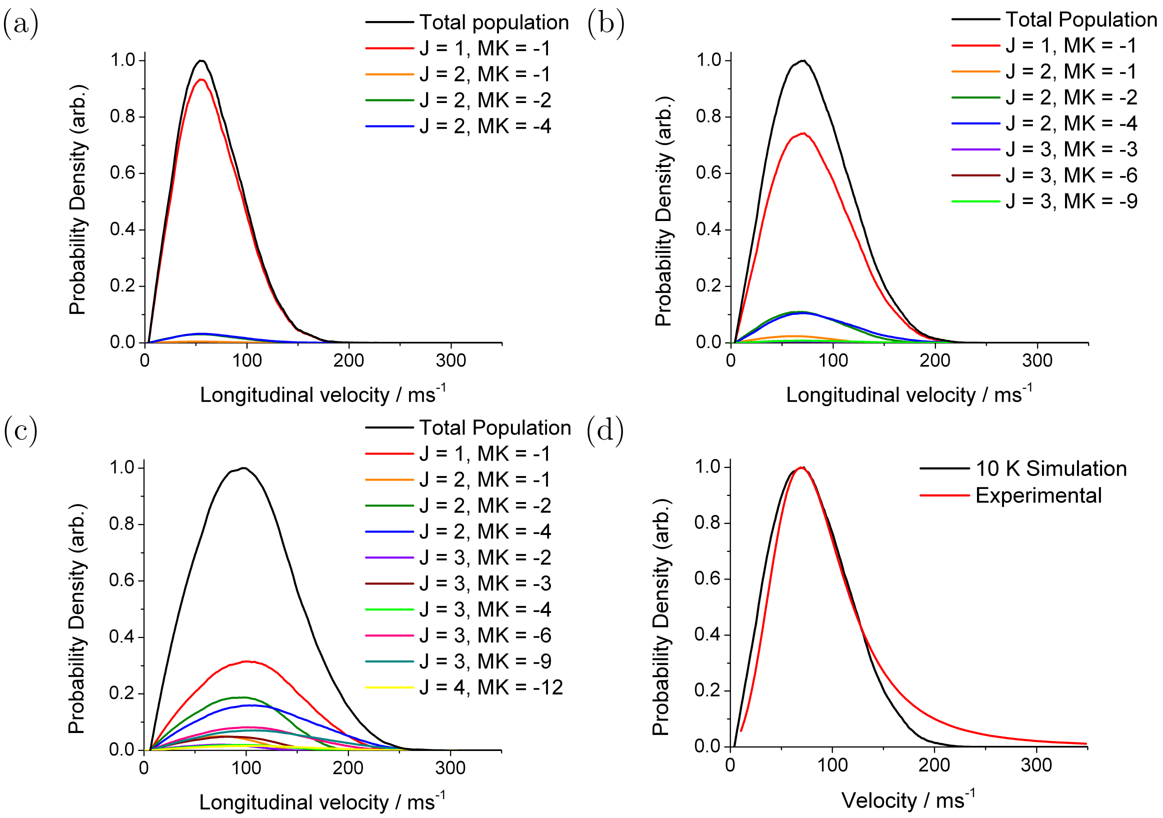

Figure 2.17: The simulated longitudinal velocity distributions of guided molecules in a quadrupole with a single bend of 100 mm radius of curvature, and an applied voltage of ±5 kV, for a molecular source at (a) 6 K (b) 10 K and (c) 25 K. The contributions from each of the most populated rotational states at the end of the guide are shown below the cumulative velocity distribution. (d) The simulated velocity distribution for the 10 K effusive source and the experimentally determined velocity distribution for standard conditions in the buffer-gas cell (1.0 sccm ND_3, 0.6 mBar He, 6 K cell), and an applied voltage of ±5 kV to the guide electrodes.

Even though the simulations are for an effusive source and simplified guide, the simulation of the 10 K effusive source closely matches the experimentally determined velocity distribution for the buffer-gas-cooled molecular source under standard conditions (1.0 sccm ND_3, 0.6 mBar He, 6 K), as shown in Figure 2.17(d). There are slightly fewer low-velocity molecules in the experimental velocity distribution compared to the simulation. This is likely due to factors that are not included in the simulation, such as the fringe fields between the end of the guide and the grounded mesh that may accelerate molecules [158], and limit the detection of molecules with velocities below about 10 ms^{-1}. The simulation only includes the $J \leq 5$ rotational states. The increased population in the high-velocity tail of the experimental velocity distribution may be from higher rotational states with stronger Stark shifts, and consequently higher velocity cut-offs.

A detailed description of the two direct cooling techniques combined in this work has been provided in this Chapter. The theory of buffer gas cooling, from the introduction of molecules into the cell to the properties of the resulting buffer-gas-cooled beams, was described first in Section 2.1. Then, the interaction of polar molecules with inhomogeneous external electric fields was discussed in Section 2.2 with particular emphasis on the molecular Stark effect for symmetric top molecules such as ND_3. This was followed by an explanation of the basic principles of electrostatic velocity selection in Section 2.3. The Chapter concluded with the Monte Carlo trajectory simulations in Section 2.4 that were used to gain a better understanding of the guiding process and aid in the design of the experimental apparatus. Further details on the design and construction of the experimental apparatus are provided in the next chapter.

Chapter 3

Production of cold molecules by electrostatic extraction of buffer-gas-cooled beams – experimental design and set-up

3.1 Overview of experimental design

This chapter provides a detailed description of the design and construction of the experimental apparatus. General considerations relating to experiments conducted in the cryogenic regime (below 125 K) are provided where appropriate. For a more comprehensive treatment of these matters please see references [170] and [171].

Cold molecules are produced by electrostatic extraction of a buffer-gas-cooled beam. The experimental apparatus employed in this production of cold molecules is shown in Figure 3.1, with a more detailed picture provided in Figure 3.2. The buffer gas cell is attached to the 6 K second stage of a pulse tube cryocooler. The helium buffer gas line is thermally connected to the 31 K first and 6 K second stages.

Thermal contact is minimised to the molecular gas line to prevent freezing. Radiation shields reduce the heat load experienced by the cryocooler. The buffer-gas-cooled molecules effuse out of the cell, enter the quadrupole guide, and are directed away from the cell and helium buffer gas. The molecules are guided around two (three in later modifications) 90° bends by the quadrupole guide, and enter a differentially pumped vacuum chamber where they are detected by either mass spectrometry or REMPI. The experimental apparatus is based on the design in [91].

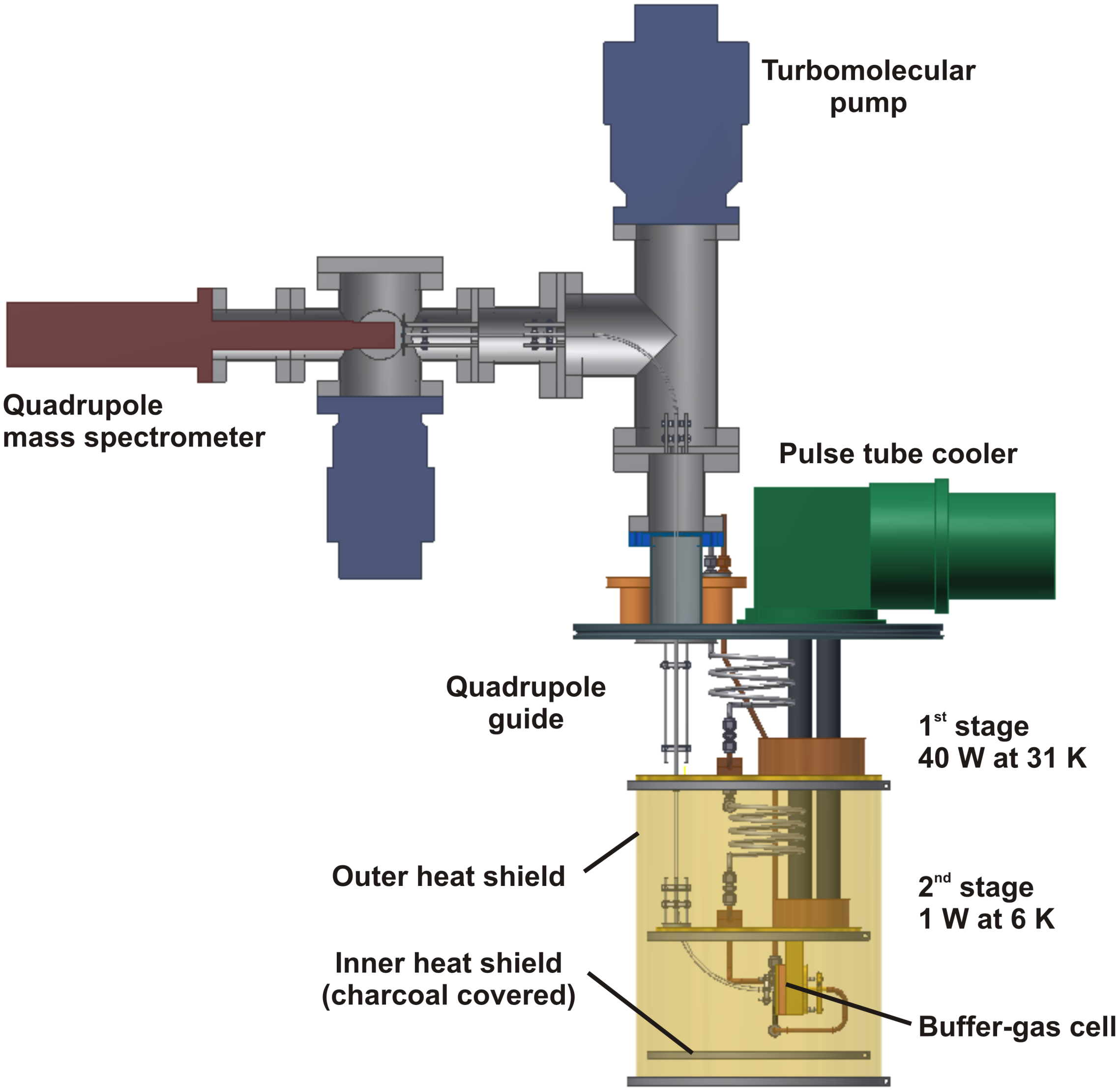

Figure 3.1: Design of the experimental apparatus showing detection with the quadrupole mass spectrometer after two bends of the guide.

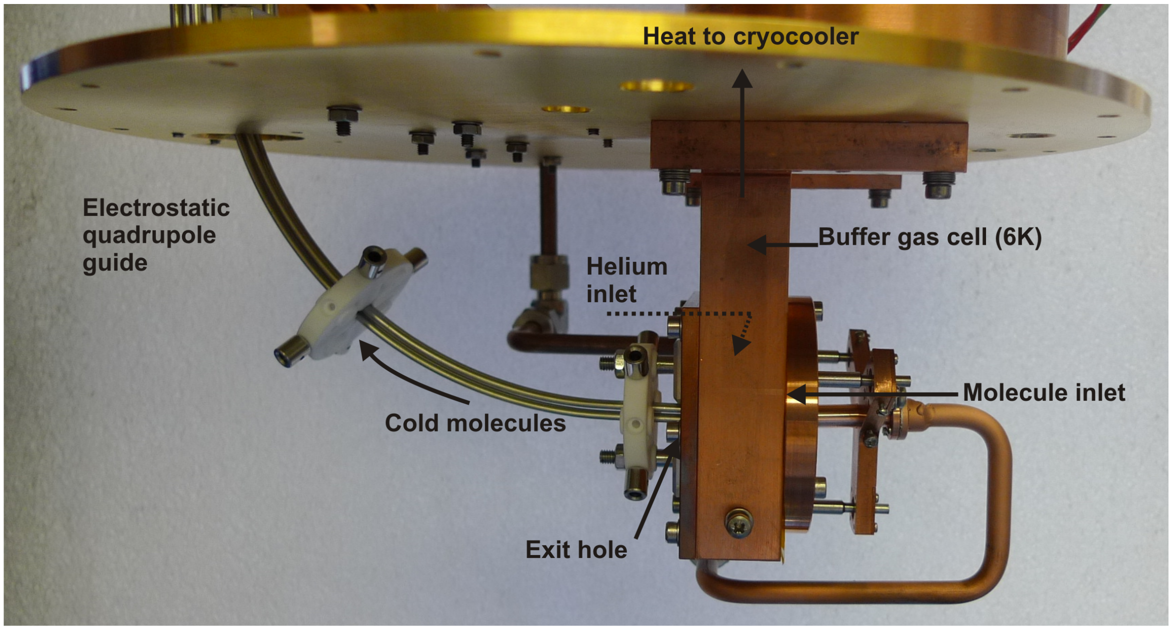

Figure 3.2: Detailed view of the buffer gas cell and electrostatic guide. Thermal contact is minimised between the molecule inlet and the cold buffer gas cell. The molecules are cooled via collisions with the buffer gas, and effuse out of the cell by the exit aperture. The cold molecules are then moved to the detection region by the electrostatic quadrupole guide.

The apparatus is designed such that everything is mounted from either the top flange (NW400ISO-K flange) or the stages of the pulse-tube cryocooler, which must be oriented vertically. This allows the main outer chamber and the heat shields to be removed vertically and provides access to the buffer gas cell and electrostatic guide without the need to dismantle any of the delicate assemblies, such as the molecular gas inlet (Fig. 3.11) and the electrostatic guide entrance located at the buffer gas cell exit (Fig. 3.12). The electrostatic guide exits the top flange via a CF114 port. The four CF70 ports in the top flange provide feedthroughs for: the gas lines; the high voltage supply to the electrodes; electrical connection to the temperature sensors; and power supplies for the molecular line heating blocks. The main chamber is a rolled tube of 3 mm thick 304L stainless steel, with an inner diameter of 400 mm and a total length of 600 mm, with NW400ISO-K bored flanges on either end. The retaining ring sits in the groove of the flange and encircles the large O-ring and centring ring. Twelve double claw-clamp assemblies are used on each flange (top and bottom) to form the vacuum seal by compressing the O-ring between the flanges.

There are some disadvantages to mounting everything from the top flange. In order to access the internal components in the main chamber, the apparatus must be mounted with sufficient clearance for the 600 mm tall main chamber to be detached from the top flange and lowered to the ground. The electrostatic guide leaves the main chamber through the top flange before bending back horizontally for detection, so the final straight section of the guide is 2.01 m above the floor. In order to send lasers safely through the detection chamber for REMPI detection, the electrostatic guide had to be extended with an additional bend to bring the end of the guide to table height (Fig. 5.2). The electrostatic guide is designed with a large radius of curvature (100 mm, both bends) so that sufficient signal can be obtained for molecules with relatively weak Stark shifts. The electrostatic guide needs to complete the first bend entirely within the inner heat shield so that it can pass vertically through the copper plates and out through the top flange. To accommodate the large bend radius of the electrostatic guide and vertical assembly, the pulse-tube cryocooler is mounted 65 mm from the centre of the top flange, and the copper plates attached asymmetrically to the cryocooler stages.

There are four ports, two CF114 and two CF70, arranged at 90° angles around the main chamber, with like sizes diametrically opposed. An active ion pressure gauge (AIGX - 8, D04852000, BOC Edwards) is attached to one of the CF70 ports, providing a pressure reading for the main cryogenic chamber. A second pressure gauge is attached to a port on the detection chamber at the end of the electrostatic guide. An UHV pressure burst disk (7420030, Caburn MDC Vacuum Products) is attached to the second CF70 port on the main chamber. A large amount of the molecular gas freezes to the cold surfaces when operating under cryogenic conditions. The molecules return to the gas phase once the cryocooler is turned off and the apparatus begins warming up, and can generate a significant amount of pressure in the chamber. There is a risk of over pressurising the chamber and damaging components if the turbomolecular pumps or backing pumps fail during warm-up. The burst disk is designed to break if the pressure exceeds 1.7 bar in the main chamber, safely releasing the pressure. The ports are located 491 mm from the top flange face so they are level with the buffer gas cell inside the main chamber. Although the CF114 ports are currently blanked off, viewing ports could be installed to give visual access to the buffer gas cell.

There are three turbomolecular pumps used in the apparatus. One turbomolecular pump (Turbovac 361, 750 Hz, Leybold Vacuum) is mounted to the bottom flange of the main chamber and is backed by an oil-free scroll pump (XDS10, Edwards) in order to prevent oil contamination of the cryogenic chamber. The second turbomolecular pump (Turbovac 361, 750 Hz, Leybold Vacuum) is placed opposite the bend in the electrostatic guide as it leaves the main chamber through the top flange. The third turbomolecular pump (Turbovac 151, 833 Hz, Leybold Vacuum) is attached to the detection chamber where the molecules exit the electrostatic guide and are detected by the mass spectrometer. This pump was later moved to the start of the third bend after extending the guide and modifying the apparatus for REMPI detection. The electrostatic guide is supported by mounting plates inserted between flange faces of the connecting vacuum chambers, which also serve as differential pumping stages between the turbomolecular pumps. At room temperature, the pressure in the main chamber and detection chamber is on the order of 10^{-6} mbar and 10^{-8} mbar, respectively. Under cryogenic conditions, the pressure in each chamber drops to about 10^{-8} mbar in the main chamber and 10^{-9} mbar in the detection chamber.

3.2 Cryogenics

3.2.1 Pulse-tube cryocooler

In general, three main techniques may be used to bring molecules into the cryogenic regime: direct immersion in cryogenic liquid, attachment to a cold head filled with cryogenic liquid from a supply dewar, and the use of a cryocooler. Cryocoolers are essentially expensive cryogenic refrigerators. The closed-loop refrigeration system makes them easy to operate and eliminates the need to directly handle cryogenic liquids. However, cryocoolers are expensive, must be well maintained, require long cool-down and warm-up times, have a low cooling power, and may introduce vibrations into the experimental apparatus.

The basic principle of operation for a pulse-tube cryocooler is detailed below, and illustrated in Figure 3.3. The main components are a compressor unit, a regenerator, a cold stage, a pulse tube, and a reservoir volume. Room temperature helium gas is compressed by a piston in the compressor unit. The compressed gas, which is now heated, flows past both the regenerator and cold stage to enter the pulse tube. A heat exchanger at the far end of the pulse tube cools the gas as it exits the pulse tube and enters the room-temperature reservoir, until the pressure equalises between the pulse tube and reservoir. Upward movement of the piston in the compressor unit causes the gas in the pulse tube to cool through adiabatic expansion. The relatively high pressure gas in the reservoir forces the cold gas in the pulse tube to flow back toward the cold stage, where it absorbs heat from the cold stage and transfers it to the heat exchanger in the regenerator. Gas flow stops once again when the pressure equalises between the pulse tube and reservoir [172].

Flow straightening at both ends of a long pulse tube minimises gas turbulence and ensures the gas in the middle section stays within the tube. This creates a temperature gradient in the gas that isolates the cold and hot heat exchanges at either end of the pulse tube. The regenerator is made from stacks of fine-mesh screen with high surface area and heat capacity. The regenerator cools the incoming compressed gas before it reaches the cold stage during the first half of the refrigeration cycle, and then transfers the heat back to the cold gas as it flows past at the end of the cycle.

Regenerator losses can be large when operating at higher frequencies, but may be reduced by flowing about 10 % of the gas directly between the piston compressor and warm end of the pulse tube via a secondary orifice. Additional improvements for high frequency operation are achieved by restricting the gas flow between the warm end of the pulse tube and the reservoir by inserting a long narrow inertance tube. The absence of moving parts at the cold end significantly increases the reliability of the pulse-tube cryocooler. Additionally, vibrations at the cold stage are reduced by about two orders of magnitude compared to the commonly used two-stage Gifford-McMahon cryocooler. Refer to [173] for details on the Gifford-McMahon cryocooler.

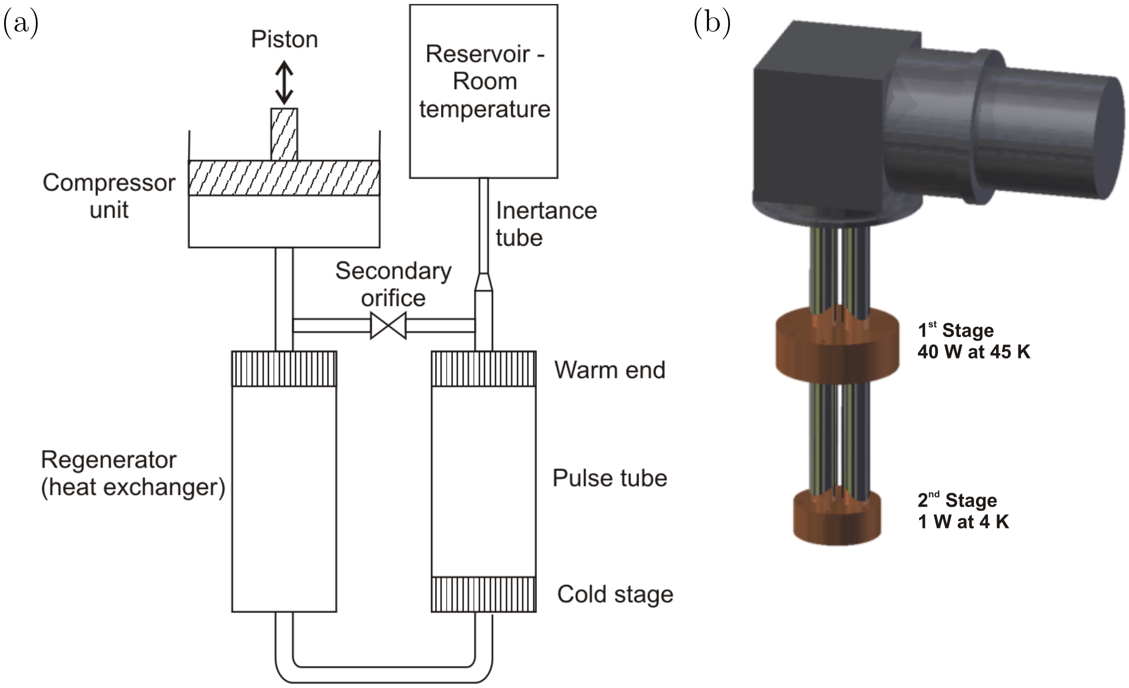

Figure 3.3: (a) Schematic illustrating the main components and operation of a pulse-tube cryocooler, adapted from [171]. (b) Image of the pulse-tube cryocooler Sumitomo RP-082B.

The cryocooler used in the experiment is a two-stage pulse-tube cryocooler from Sumitomo Cryogenics (RP-082B) with a water-cooled 50 Hz compressor unit (F70 HV). Radiation shields are thermally connected to the first stage (40 W, 45 K) and second stage (1 W, 4.2 K) of the cryocooler to reduce the heat load. Further details of the heat shields are provided in Section 3.3. It typically takes 5 hours to cool down and 60 hours to warm up to room temperature (Fig. 3.4). However, the apparatus only needs to warm-up above the freezing point of the molecular gas used, not all the way to room temperature, after each day of operation. The warming-up process can be accelerated by using the two heating blocks located on the molecular gas line and flowing helium gas into the main chamber during the later stages of warm-up.

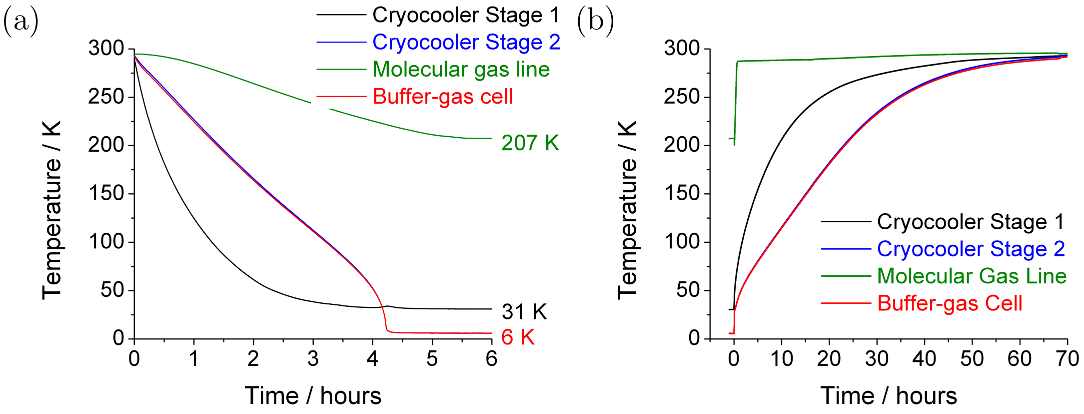

Figure 3.4: Silicon diode temperature sensors are placed on the first stage of the cryocooler, the second stage of the cryocooler, the bottom of the buffer gas cell, and the Y-piece used to attached the molecular gas line to the buffer gas cell. (a) Typical cool-down curve. (b) Typical warm-up curve.

3.2.2 Materials and general considerations

Heat transfer is one of the most important considerations in the experimental design. For example, thermal connection is maximised between the buffer gas cell and the cryocooler stage, while the heat transfer is minimised to the molecular gas line to prevent freezing. Using the correct materials with specific thermal properties is essential to achieve the desired heat transfer between various components. The thermal conductivity for several materials used in the apparatus is listed in Table 3.1.

Table 3.1: The thermal conductivity [W/(m·K)] for common construction materials used in cryogenic experiments, modified from [171].

Material	4 K	40 K	295 K
Al 5083	3.3	33	118
Brass (UNS C3600)	2.0	19	86
Copper OFHC (RRR≈100)	630	1470	397
Stainless steel 304, 316	0.27	4.7	15
Ti (6%Al-4%V)	—	1.9	7.4
Polyimide (Kapton)	0.011	0.083	0.19
Polyethylene terepthalate (Mylar)	0.038	0.096	—
Macor	0.075	—	—
Pyrex glass (borosilicate)	0.10	0.25	1.1

Materials can also behave very differently in cryogenic conditions than at room temperature. High purity metals, identified by large electrical residual-resistance ratios (RRR), have much higher thermal conductivities at low temperatures. The thermal conductivity of Cu(RRR=200) is an order of magnitude greater than Cu(20) at 4 K, despite having similar thermal conductivities at room temperature [171]. High purity oxygen-free copper (OFHC) is expensive and difficult to machine, so it is only used to make the buffer gas cell. Standard purity copper is used to make the other components that require high thermal conductivity. Kapton film (polyimide), Mylar foil, glass and ceramics (Macor) are ideally suited for components that must have low thermal conductivity. Unfortunately these materials also have long cool down times, so metals with low thermal conductivities such as austenitic stainless steel (an alloy containing chromium and nickel, AISI 304, 316) are commonly used as well.

The thermal conductance across solid interfaces (the contact area between two adjacent components) is much lower under cryogenic conditions than at room temperature. Therefore, not only is the material used to make each component important in cryogenic design, but also how the components are joined together. Various methods are used to improve the heat conductance between the components in the apparatus, most of which are copper. Gold-plating copper components reduces the surface oxidation and increases the heat conductance across the interface (Table 3.2), as does increasing the force holding the parts together. Placing thin indium foil between components fills the gaps and irregularities in their surfaces, effectively cold welding the pieces together. When there is a large surface area between components, or the force holding them together is small, thermal grease such as Apiezon N can enhance the thermal conductance across the solid interface [171].

Many components are thermally anchored to the copper plates attached to both stages of the cryocooler, which extend the surface area available to make thermal connections and form the top covers for the heat shields (Section 3.3). The copper plates are gold-plated to maximise the heat conductance across the interface with the cryocooler stages. Applying a thin layer of Apiezon N grease between the plates and cryocooler stages further reduced the cool down time by approximately 20 minutes.

Table 3.2: Heat conductance across solid interfaces in W/K, modified from [171].

Interface materials	4.2 K	77 K
Gold/gold	2×10^{-1}	
Copper/copper	1×10^{-2}	3×10^{-1}
Steel/steel	5×10^{-3}	3×10^{-1}

Components may break or become loose due to differences in thermal contraction when cycling between room temperature and cryogenic conditions if unsuitable materials are used. Epoxies and plastics exhibit the highest thermal contraction, while glasses and ceramics exhibit the lowest. Metals typically fall between those extremes (Table 3.3). Including some slack in wiring prevents end connections from breaking. Brass or aluminium screws are used to secure copper components when a tight join is required. The component may become loose if normal stainless steel screws are used because copper contracts more than stainless steel. Stycast 2850 FT epoxy is filled with silica powder so that its thermal contraction is closer to copper, making it less likely to crack when used in permanent connections.

Table 3.3: Thermal contraction of commonly used construction materials in cryogenic experiments, modified from [171]. The first column gives the percentage that the length of material will contract, relative to its overall length, when cooled from 293 K to 4 K. The second column gives the coefficient of thermal expansion for materials at 293 K. A larger value indicates that a material will expand (or contract) more for a given temperature change.

Material	$(\Delta L/L_{293\text{-}4\ K})$ / %	$\alpha_{293\ K}$ / 10^{-6} K^{-1}
Pyrex	0.055	3.0
Titanium	0.151	8.5
SS 316	0.30	15.2
Copper	0.324	16.7
Brass 70/30	0.37	17.5
Aluminium	0.415	22.5
Stycast 2850 FT	0.44	28

Materials used as structural supports at room temperature are sometimes unsuitable in cryogenic conditions as they become brittle and may fracture. This applies to most metals with a body-centred-cubic (bcc) or a hexagonal-close-packed (hcp) crystal structure. Fortunately, metals such as copper, aluminium, and austenitic stainless steel with a face-centred-cubic (fcc) crystal structure retain their ductility even at low temperatures [174]. Kapton does not embrittle at low temperatures, but epoxies tend to crack and should therefore be applied in thin layers.

The maximum weight that can be attached to each stage of the cryocooler is 10 kg. The heat shields and copper plates are the heaviest components. The inner heat shield and plate only weigh 4.99 kg and are attached directly to the second stage of the cryocooler without additional support. The outer heat shield and plate originally weighed 10.19 kg. Sections 6 mm deep were machined out of the 8 mm thick copper plate (Fig. 3.5(a)) to reduce its weight. The outer heat shield and plate now weigh

9.07 kg. Two stainless steel rods (6 mm diameter, 165.5 mm long) anchored in the top flange provide additional support to the copper plate and cryocooler stage, which is especially important given the asymmetric design of the apparatus (Fig. 3.5(b)).

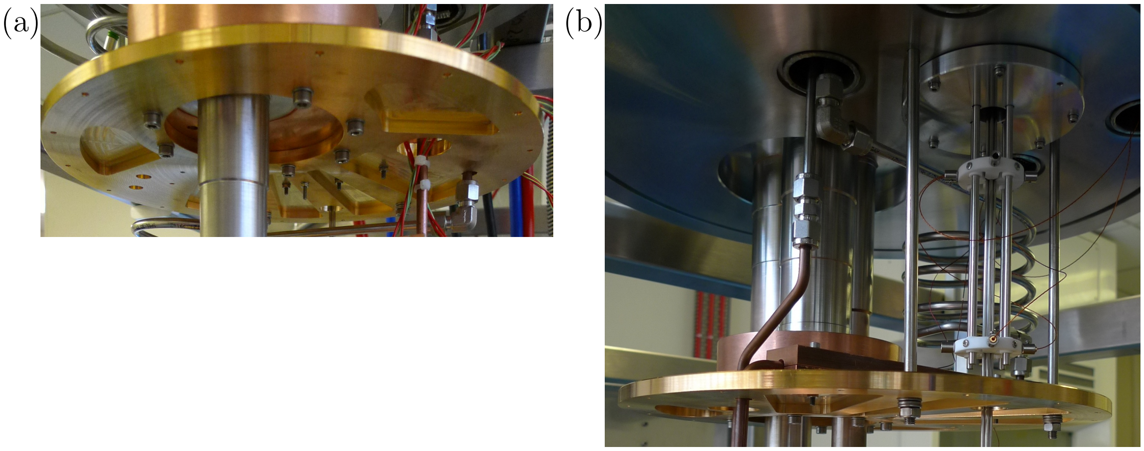

Figure 3.5: The maximum weight that can be attached to each stage of the cryocooler is 10 kg. The outer heat shield and components attached to the first stage approach this maximum, so sections of the copper plate are cut out to reduce the weight (a), and two stainless steel rods connect the copper plate to the top flange (b) for additional support.

One concern is that the support rods create a heat link between the room temperature top flange and the 31 K first stage, increasing the heat load on the cryocooler. Heat conduction $\dot{q}_{\text{cond}}$ through a solid with a uniform cross-sectional area A and length L can be calculated using

$$\dot{q}_{\text{cond}} = \frac{A}{L}\int_{T_1}^{T_2} \lambda(T)dT = \frac{A}{L}\left(\int_{4\ K}^{T_2} \lambda(T)dT - \int_{4\ K}^{T_1} \lambda(T)dT\right), \tag{3.1}$$

where T_1 and T_2 are the temperatures at the ends of the solid and $\lambda(T)$ is the temperature-dependent thermal conductivity of the material. The thermal conductivity integrals with reference to 4 K are readily available for common materials such as stainless steel. Using the values provided in [171],[1] the conduction heat flow through the stainless steel support rods is 5.16×10^{-1} W. This is small compared to the 3.88 W

---

[1] $\int_{4\text{ K}}^{300\text{ K}} \lambda(T)dT = 3.06$ kW/m and $\int_{4\text{ K}}^{30\text{ K}} \lambda(T)dT = 0.0424$ kW/m for stainless steel

of thermal radiation incident on the first stage outer heat shield (Section 3.3.1) and does not significantly increase the heat load on the cryocooler.

3.2.3 Temperature sensors

Cryogenic thermometers are characterised by their accuracy (the difference between the measured value and the true temperature), and their reproducibility after being cycled many times from room temperature to cryogenic conditions. Primary thermometers are based on a measured quantity from which temperature can be calculated directly. For example, a primary thermometer may be based on the equation of state of a gas. Secondary thermometers must be calibrated with a primary thermometer or at a fixed temperature point, such as a triple point transition, because temperature cannot be calculated directly from the measured property. Secondary thermometers are often more convenient and have greater sensitivity than primary thermometers. Two types of secondary thermometers are used in the apparatus, with measured outputs of either resistance or voltage.

Platinum resistance thermometers (PT-102-AL, Lake Shore Cryotronics) are used in the heating blocks placed on the molecular gas line (Section 3.4.2). They have a range of 14 K to 873 K with an uncalibrated accuracy of ± 1.3 K at 70 K and ± 0.5 K at 305 K. They exhibit excellent reproducibility (± 5 mK at 77 K) and have a low long-term calibration drift. The platinum resistance sensor is mounted into a flat aluminium block with two platinum leads [175].

Silicon diode thermometers (one calibrated DT-470-CU-1.4L and three uncalibrated DT-470-CU-13, Lake Shore Cryotronics) are placed on the buffer gas cell (calibrated sensor), the copper plates attached to the first and second stage of the cryocooler, and the Y-piece supporting the molecular gas line at the inlet of the cell. They have a range of 1.4 K to 475 K with a calibrated (uncalibrated) accuracy of

± 12 mK at 1.4 - 10 K and ± 30 mK at 10 - 305 K (± 1 K at 2 - 100 K and ± 1% at 100 - 305 K). They exhibit reasonable reproducibility (± 5 mK at 4.2 K, ± 20 mK at 77 K) and low long-term calibration drift. The silicon diodes are indium soldered into gold-plated copper bobbins, with four phosphor-bronze leads (Quad-Lead cryogenic wire 36 AWG, QL-36, Lake Shore Cryotronics). The phosphor-bronze wire has a low thermal conductivity, and Kapton (polyimide) insulation, which is well suited for cryogenic use [175]. A temperature monitor (218S, Lake Shore Cryotronics) displays the readings from the four silicon diodes, which are recorded every 10 seconds by a LabView program that interfaces with the monitor.

The wires connecting the temperature sensors to the electrical feedthroughs on the room temperature top flange have a temperature gradient along their length. The accuracy of the temperature reading may be affected by thermoelectric voltages generated by the temperature gradient, although this is minimised by heat sinking the wire leads just before they connect to the temperature sensor. The silicon diode sensor leads are wrapped around large (HSB-40) and small gold-plated OFHC copper heat sink bobbins (HSB-8, Lake Shore Cryotronics) that are bolted to the copper plates attached to the first and second stages of the cryocooler, respectively.

3.3 Heat shields

3.3.1 Thermal radiation

The thermal motion of atoms and molecules in matter, and in particular the motion of charged particles, causes all surfaces to emit thermal (electromagnetic) radiation in all directions. The amount of energy radiated by a body depends on its temperature T, surface area A, and surface emissivity ϵ. The surface emissivity is defined by the surface reflectivity R$_f$ as $\epsilon \equiv 1 - R_f$, and indicates that surfaces good at reflecting thermal radiation also emit very little thermal radiation themselves. The Stefan-Boltzmann equation quantifies the radiative heat flow $\dot{q}_{\text{rad}}$ from a surface, $\dot{q}_{\text{rad}} = \sigma\epsilon A T^4$, where σ is the Stefan-Boltzmann constant[2] [171]. Furthermore, the net heat exchange between a cold surface (1) and a warm surface (2) is given by

$$\dot{q}_{rad} = \sigma E A (T_2^4 - T_1^4), \tag{3.2}$$

where A is a geometry dependent area factor and E is calculated from

$$E = \frac{\epsilon_1 \epsilon_2}{\epsilon_2 + (\frac{A_1}{A_2})(\epsilon_1 - \epsilon_1\epsilon_2)}. \tag{3.3}$$

Although this is only true for long coaxial cylinders or concentric spheres, a good approximation can be made by replacing A with the area of the enclosed inner surface A_1.

A rough approximation of the net heat exchange between several surfaces can be calculated to give an idea of the importance of radiation heat shields (Table 3.5). The main body of the buffer gas cell has dimensions of 20 mm × 60 mm × 100 mm, and the heat shield dimensions are given in Table 3.4. The thermal radiation experienced by the buffer gas cell from the room temperature main chamber in the absence of any heat shielding is quite high at 1.64×10^{-1} W. As seen in the Stefan-Boltzmann equation for heat exchange (Eq. 3.2), the thermal radiation strongly depends on the temperature difference between the surfaces. The inclusion of an intermediate temperature heat shield reduces the thermal radiation experienced by the buffer gas cell by four orders of magnitude to 1.86×10^{-5} W.

This value was calculated based on a polished copper buffer gas cell, which has a surface emissivity of 0.02[3] [171]. If the copper surface of the cell is highly oxidised,

---

[2] $\sigma = 5.67 \times 10^{-8}$ W/(m^{2}K^4)

[3] The main chamber is made of stainless steel with an emissivity of 0.07. The radiation heat shields

however, the emissivity increases to 0.6 and the net heat exchanged with the outer heat shield rises to 2.73×10^{-4} W. An inner heat shield is attached to the second 6 K stage of the cryocooler so that there is a low temperature isothermal region around the buffer gas cell and various components, such as the Macor electrode holders, whose emissivity will be much higher than polished copper. The copper heat shields are electroplated with a 0.25 micron layer of gold (PMD Group Ltd) to keep the surfaces highly polished and free from oxidation. The heat shields must be kept clean of fingerprints, pump oil, and other surface contaminants which can also increase the emissivity of a surface.

Under normal operating conditions the outer and inner heat shields are attached to the 31 K first and 6 K second stages of the cryocooler, respectively. The thermal radiation incident on the outer heat shield is 3.88 W, and only 1.60×10^{-4} W on the inner heat shield. When the outer heat shield is removed, the thermal radiation on the inner heat shield rises dramatically to 1.87 W. This places too great a heat load on the cryocooler, whose second stage can now only reach approximately 17 K as opposed to 6 K with both heat shields in place. This provides an excellent opportunity to study the cold molecular beam produced under two different buffer gas cell temperatures. Holes are drilled in the copper plates that act as the top cover of the heat shields to allow the gas lines, wires, and electrostatic guide to enter and exit the regions enclosed by the heat shields. Where possible, the holes are mis-aligned to break up the line of

Table 3.4: Dimensions (in mm) of the inner and out heat shields, and the main cryogenic vacuum chamber, that are used in calculating the net heat exchanged between surfaces (Eq. 3.2).

	Outer diameter	Wall thickness	Vertical height
Main chamber	406	3	600
Outer heat shield	300	1.2	370
Inner heat shield	251.4	1.2	155

---

are plated in gold with an emissivity of 0.02.

sight from the main chamber to the buffer gas cell, minimising the thermal radiation experienced by the buffer gas cell in the low temperature region of the apparatus.

Table 3.5: The radiative heat flow between various surfaces is calculated using the modified Stefan-Boltzmann equation (Eq. 3.2).

Outer surface	Inner surface	Net heat exchange / W
Main chamber (298 K)	Buffer gas cell (6 K)	1.64×10^{-1}
Outer heat shield (31 K)	Buffer gas cell (6 K)	1.86×10^{-5}
Outer heat shield (31 K)	Buffer gas cell (6 K, highly oxidised)	2.73×10^{-4}
Main chamber (298 K)	Outer heat shield (31 K)	3.88
Outer heat shield (31 K)	Inner heat shield (6 K)	1.60×10^{-4}
Inner heat shield (6 K)	Buffer gas cell (6 K)	—
Main chamber (298 K)	Inner heat shield (6 K)	1.87

3.3.2 Construction

The heat shields must be large enough to enclose the buffer gas cell and associated components, but sufficiently light weight to satisfy the 10 kg maximum weight requirement that can be attached to each cryocooler stage. The dimensions are given in Table 3.4. A thin sheet of copper (1.2 mm) bends around the outside of a flat faced copper ring, one positioned at the top and another at the bottom edge of the cylinder. A slightly larger diameter aluminium split ring fits around the outside of the copper sheet. A screw fastens the ends of the outer aluminium ring together, clamping the copper sheet rigidly into place, forming the walls of a cylindrical tube. The inner copper rings (top and bottom) have 18 equally spaced, tapped (M3) holes. A circular copper disk, 1.2 mm thick, is bolted to the bottom copper ring to form the base of the cylindrical heat shield. The heat shields are then attached to the gold-plated copper plates secured to each cryocooler stage, which form the 'tops' of the heat shields.

Material choice is critical to the design of the heat shields because of differences in thermal contraction. Aluminium is used for the outer split ring because it has

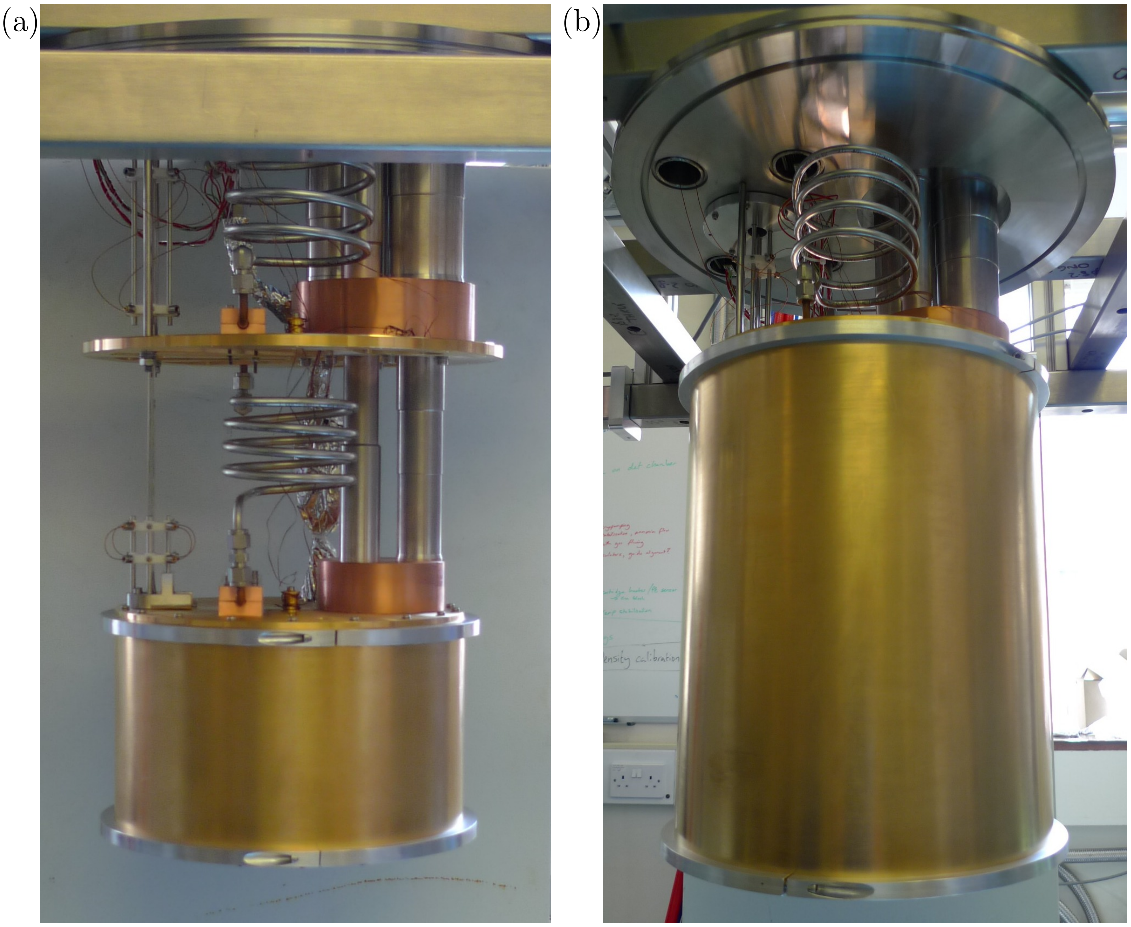

Figure 3.6: Gold-plated copper heat shields are attached to each stage of the cryocooler to minimise the thermal radiation experienced by the buffer gas cell and the low temperature region of the cryocooler, and reduce the heat load on the cryocooler. (a) The outer heat shield removed so that the inner heat shield is visible. When operated under this configuration, the second stage of the cryocooler, and therefore also the buffer gas cell, only reaches 17 K rather than 6 K. (b) Outer heat shield in place.

a larger coefficient of expansion than copper. As the apparatus cools down from room temperature to the cryogenic operating conditions, the aluminium outer ring contracts more than the copper and the clamp system effectively self-tightens. The clamp system would have loosened if the outer ring had been made from stainless steel which has a smaller coefficient of expansion (contracts less during cool-down) than copper (Table 3.3).

Although initial attempts at constructing the cylindrical heat shields from the thin copper sheets involved welding the edges together, the welding tended to warp the thin copper sheets and leave a rough join. The concentric ring clamping system was designed instead, which has the additional advantage of being able to leave a small gap in the wall of the heat shield where the ends of the copper sheet meet. This allows the large amount of gas that is released during the warm-up phase to escape from within the heat shields and be pumped away by the turbomolecular pump attached to the bottom of the main chamber. Again, the seams in the heat shields should be mis-aligned so there is no direct line of sight from the room temperature main chamber to the buffer gas cell. A 110 mm diameter hole is cut into the base plate of the outer heat shield, and a 130 mm diameter thin disk re-attached with screws and a stack of several washers to off-set it from the base plate. The additional gap further helps the gas escape from within the heat shields during warm-up.

3.3.3 Charcoal helium pump

The pressure within the heat shields and main chamber must be less than 10^{-6} mbar in order for collisions between the guided molecules and background gas to be negligible [135]. This also helps to avoid large discharges between guide electrodes. Any 6 K surface acts as a cryopump for the molecular gas that exits the cell but fails to be guided out of the main chamber. Activated charcoal adsorbs helium, most effectively in the temperature range between 4 and 10 K, and can be used as a helium pump. The helium is released from the charcoal between 10 - 20 K when the system warms up, and is pumped out of the main chamber by the turbomolecular pump, effectively re-charging the charcoal [176].

High thermally conducting Stycast epoxy 2850-FT, with a 20 minute working time, is used to attach the charcoal to the inner surface of the 6 K heat shield (Fig. 3.7). The inner wall and base of the heat shield is coated with a thin layer of Stycast epoxy and covered first with coarse grained activated charcoal (208c 8xUS RGF 3172, Chemviron Carbon) followed by finer grains (AEJ1 12xUS RGF 3172, Chemviron Carbon), and light pressure is applied. Excess charcoal is gently tapped off after being left to cure for 24 hours. The charcoal covers a surface area of approximately 1500 cm^2 of the inner heat shield with a helium pumping speed of 6500 ls^{-1}.[4]

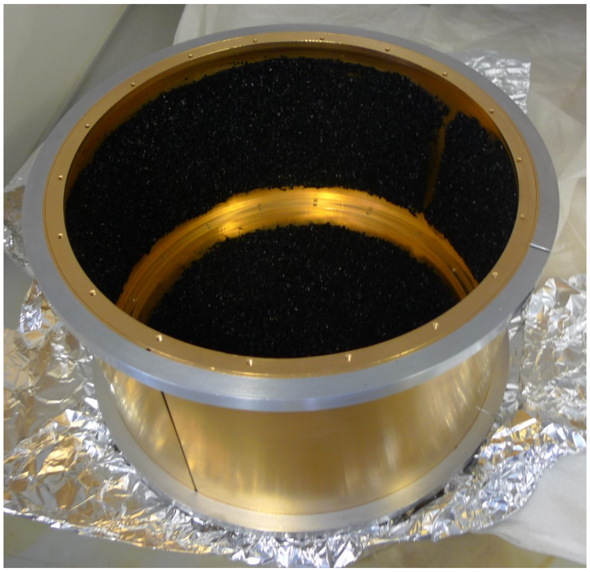

Figure 3.7: Interior view of the inner heat shield. The activated charcoal coating the inner surface acts as a helium pump in the temperature range of 4 to 10 K.

3.4 Gas lines

3.4.1 Buffer gas line

The buffer gas line is designed to thermalise the helium with each of the cryocooler stages prior to entering the buffer gas cell. However, thermal connection between stages of the cryocooler, and between the room temperature main chamber and the first stage of the cryocooler, must also be minimised to limit the heat load placed on the cryocooler. The buffer gas line is therefore broken into four segments, two made

---

[4] Activated charcoal granules have a pumping speed of 4.3 $\text{l}/(\text{s}\cdot\text{cm}^2)$ for helium at 5 K [177].

from stainless steel (low thermal conductivity) and two from copper (high thermal conductivity, Table 3.1). The gas lines are made from 1/4" Swagelok seamless tubing (OD = 6.35 mm, ID = 3.9 mm) because instabilities in the buffer gas flow may result from smaller diameter tubing [178].

As shown in Figure 3.6, the first stainless steel segment of buffer gas line undergoes several windings of a coil as it runs from the feedthrough connection in the top flange to the first stage of the cryocooler. The coils provide a compact means of increasing the tube length because heat conduction through a solid is inversely proportional to its length (Eq. 3.1). The second segment of the buffer gas line is copper and runs along the top of the gold plated copper plate attached to the first stage of the cryocooler, then descends a short distance through a hole in the plate into the region between the cryocooler stages. In order to maximise the thermal connection between the buffer gas line and the cryocooler stage, it passes through a tightly fitting channel in a rectangular copper block bolted to the plate. Apiezon N, a cryogenic thermal contact grease (as described in Section 3.2.2), is applied between the tubing and the halves of the copper block, and between the bottom of the copper block and the plate. The buffer gas line changes to a coiled section of stainless steel tubing in the region between the cryocooler stages, and another copper block thermally connects the final copper segment of tubing to the plate attached to the second stage of the cryocooler (Fig. 3.8(a)).

A small copper block is used to clamp the buffer gas line to the side of the buffer gas cell. The helium gas enters the cell through a 6.3 mm hole in the side wall. A thin (0.13 mm) piece of indium foil is placed between the copper block and the side of the cell, sealing the entrance while providing good thermal connection between the components (Fig. 3.8(b)).

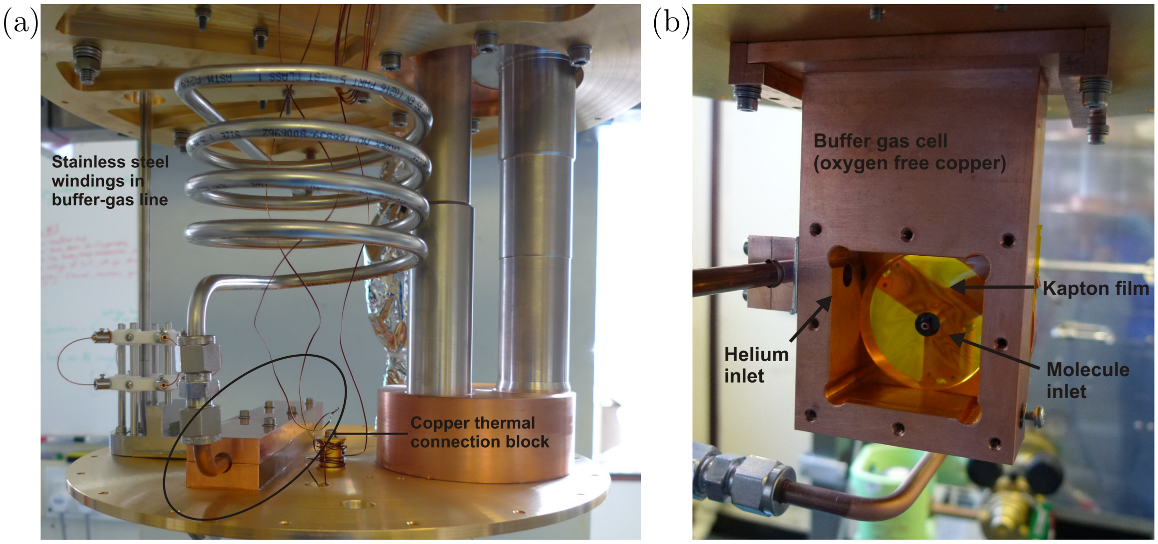

Figure 3.8: (a) The buffer gas line is shown in the region between the stages of the cryocooler. The coiled stainless steel segment of the gas line minimises the heat transfer between cryocooler stages, and thus the heat load on the cryocooler. The copper block provides a thermal connection between the buffer gas line and the cryocooler stage, acting to cool the helium buffer gas before it enters the buffer gas cell. (b) Inside view of the buffer gas cell showing the helium inlet.

3.4.2 Molecular gas line

Unlike the buffer gas line, the molecular gas line is kept thermally disconnected from the cryogenic environment. Two heating blocks are placed along the line: one between the cryocooler stages and one just before entering the buffer gas cell. The molecular gas line is made entirely of copper tubing so the heating blocks are effective along the full length. This prevents cold spots from developing that might cause the molecular gas to freeze and block the gas line. The copper heating block measures 15 mm × 30 mm × 45 mm with a central cylindrical slot for a cartridge heater (50 Ω 50 W, Lake Shore Cryotronics). The PT-102-AL temperature sensor is mounted to the bottom of the copper block. A thin piece of indium foil is wrapped around the molecular gas line to ensure the heating block fits tightly onto the line with good thermal connection. The desired temperature set-point is obtained by using an in-house built control box to regulate the feedback loop between the PT-102-AL temperature sensors and the cartridge heaters (Fig. 3.9).

The molecular line is wrapped in Mylar reflective film below the first stage of the cryocooler to minimise the thermal connection to the surrounding cryogenic environment (Fig. 3.8(a)). Ideally the line should be kept at a temperature just above the freezing point of the molecular gas so that there is sufficient vapour pressure, while limiting the heat load placed on the buffer gas cell. This will also ensure efficient buffer gas cooling within the cell [90]. The heating-blocks, shown in Figure 3.9, are programmed with a set-point of 214 K for deuterated ammonia (195 K freezing point). Temperature readings from the silicon diode placed on the Y-piece securing the gas line to the buffer gas cell indicate the actual temperature of the ammonia at the cell inlet is approximately 210 K.

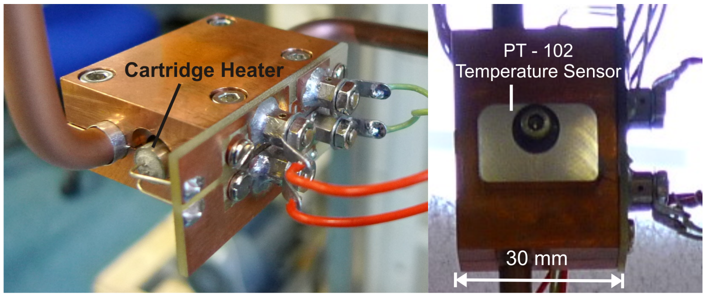

Figure 3.9: The molecular gas line is heated by a cartridge heater fit into a copper block and clamped around the gas line. A PT-102-AL temperature sensor attached to the bottom of the heating block (shown on the right) monitors the temperature as part of the feedback loop controlling the cartridge heater.

The molecule inlet to the cell is the most difficult place to isolate the hot (210 - 300 K) molecular gas line from the cryogenic environment and the cold (6 K) buffer gas cell. As shown in Figure 3.10(a), a flat-faced copper cap is welded to the end of the molecular gas line. The base of the molecule inlet is bolted into the tapped holes in the flat-faced end of the welded cap, with a piece of indium foil sandwiched between to seal the connection. The end of the molecule inlet nozzle (2 mm outer diameter, 1 mm internal diameter) passes through a 2 mm hole in the thin Kapton film that serves as the front wall of the buffer gas cell and extends 3 mm into the cell. Stycast epoxy seals the connection between the inlet nozzle and the Kapton film. The Kapton film (0.025 mm thick) is held in place by a copper ring bolted to the exterior of the cell. Kapton film has a very low thermal conductivity (Table 3.1), which serves to minimise heat transfer between the molecule inlet and the Kapton film front wall of the buffer gas cell.

The molecular gas line is supported and aligned to the centre of the cell by a Y-shaped copper piece that is attached, via stainless steel pegs fastened to the copper ring, to the buffer gas cell. The molecular gas line, Y-piece, and molecule inlet are all hot (210 - 300 K). The Kapton film, copper ring, and stainless steel pegs are all cold (6 K). Circular grooves are machined into the ends of the Y-piece where three glass balls (3 mm diameter, borosilicate[5]) are positioned around each stainless steel leg. The glass balls are held in the groove by a thin copper cover (Fig. 3.10(b)), and a screw on the side puts sufficient pressure on the balls to securely hold the stainless steel legs in place. Minimal surface area is in contact between the glass balls and the stainless steel legs, both of which have low thermal conductivity, further reducing the heat transfer between the hot Y-piece and the cold stainless steel legs.

3.4.3 Gas flow control and calibration

The buffer gas flow is controlled by a UDV 146 all-metal regulating valve (PF 152 034, Pfeiffer Vacuum), which may be operated manually or with thermo-mechanical regulation. An input voltage between 0 to 20 V DC can be applied to resistance heating coils (≈ 30 Ω) that change the temperature and length of a bolt, which in turn controls the amount of gas flowing through the valve. A LabView program interfaces with a U3-

---

[5] Lime soda glass (aka float glass) has a marginally lower thermal conductivity than borosilicate (0.937 W/mK and 1.1 W/mK, respectively [179]). However, it is more brittle and has a larger thermal coefficient of expansion than borosilicate, so is more likely to be damaged during assembly or the repeated cooling and warming cycles of normal operation.

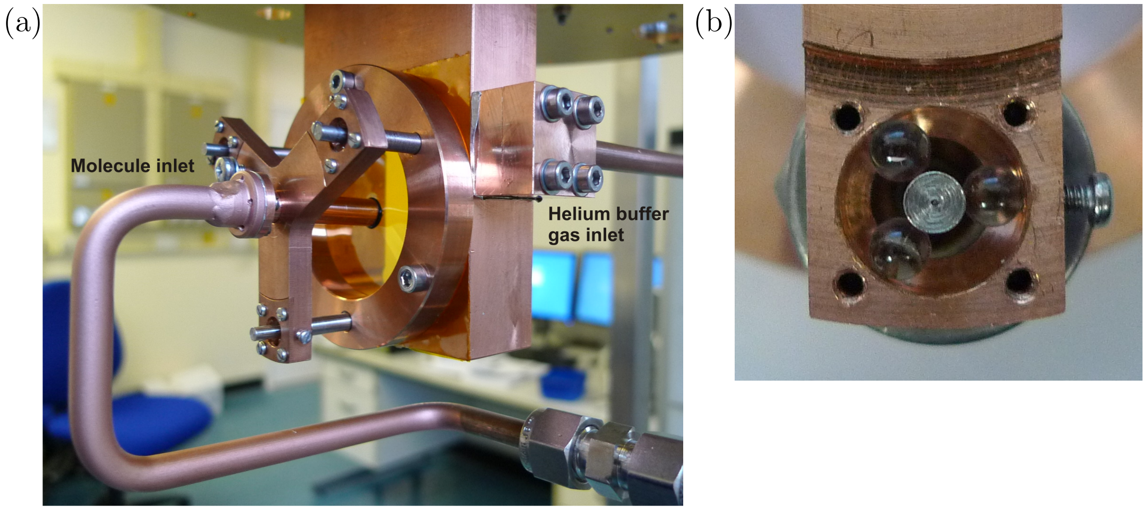

Figure 3.10: (a) Thermal connection between the hot molecular gas line (210 K) and the cold buffer gas cell (6 K) is minimised by using Kapton film for the front wall of the buffer gas cell (low thermal conductivity) and mounting the molecular gas line to the stainless steel legs with glass ball contact points. (b) Close up image of the glass balls at the end of the Y-piece that are positioned around the stainless steel leg and secured in place with the screw visible on the right (copper cover removed for clarity).

HV LabJack, in combination with a home-built power supply and voltage amplifier, to thermo-mechanically regulate the valve. A pressure gauge (Ceravac Transmitters CTR 90, 15941, Leybold Vacuum) located just past the regulator valve is used to monitor the buffer gas pressure entering the gas line in the main cryogenic chamber, and is displayed on a Center One operating unit (Center One, 230002, Leybold Vacuum).

The desired buffer gas pressure is entered in the LabView program as the set-point. If the actual pressure reading from the CTR90 pressure gauge is greater than the set-point, a greater voltage is sent to the valve via the LabJack, which increases the temperature and length of the bolt, decreasing the opening in the valve and ultimately lowering the pressure. The opposite process occurs when the pressure reading is lower than the set-point. At the start of operation, the valve is manually opened so that the buffer gas pressure is approximately ten times the value of the desired set-point. Once the pressure is stable, the LabView program is started and automatically regulates the valve so that the actual pressure matches the set-point. The feedback method used to regulate the buffer gas pressure is a PID (Proportional Integral Derivative) control loop. The PID algorithm is given by

$$u(t) = K\left(e(t) + \frac{1}{T_\mathrm{i}}\int_0^t e(\tau)d\tau + T_\mathrm{d}\frac{de(t)}{dt}\right). \tag{3.4}$$

The symbol u is the control signal (input voltage to the valve), and e is the control error, or the difference between the set point and the measured process variable (buffer gas pressure). The parameters K (proportional gain), T_i (integral time), and T_d (derivative time), determine the weight given to the current error or deviation from the set-point, past error accumulation, and future deviations when calculating the voltage to send to the valve. The proportional term determines the sensitivity of the system to error. When implementing the PID algorithm, the integral term is approximated by Equation 3.5 and the derivative term by Equation 3.6.

$$\int_0^{t_k} e(\tau)d\tau \approx \sum_{i=1}^{k} e(t_i)\Delta t \tag{3.5}$$

$$\frac{de(t_k)}{dt} \approx \frac{e(t_k) - e(t_{k-1})}{\Delta t} \tag{3.6}$$

The integral term prevents the steady state error present in purely proportional control systems, and the set-point is often reached more quickly. However, the measured process variable (buffer gas pressure) may overshoot the set-point before ultimately stabilising. The magnitude of the overshoots can be reduced by including, or more heavily weighting, the derivative term. The compromise is a slower response when changing the set-point and potentially introducing long-term oscillations due to increased sensitivity to noise in the error term [180]. The optimal values for the parameters were determined using an auto-tuning procedure available with LabView's PID Control Toolkit ($K = 7.371$, $T_\mathrm{i} = 0.149$ min, $T_\mathrm{d} = 0.030$ min).

The molecular gas flow is controlled by a digital mass flow controller (F-200CV-

002-AAD-22-E, Bronkhorst). FLOW-BUS software, using the DDE-server, is used to operate the mass flow controller. The unit is calibrated for ammonia and can deliver between 0.1 and 5.0 sccm (standard cubic centimetres per minute) of gas to the system with an accuracy of ±1% FS (full span of the flow meter). A gas conversion factor, C, is used to determine the flow rate for other molecular gases. An example calculation is shown in Equation 3.7 for determining the flow rate for CH_3F.

$$C = \frac{c_{p_1} \cdot \rho_1}{c_{p_2} \cdot \rho_2} = \frac{0.524 \ \frac{\mathrm{cal}}{\mathrm{g\ K}} \cdot 0.7693 \ \frac{\mathrm{g}}{\mathrm{l}}}{0.29 \ \frac{\mathrm{cal}}{\mathrm{g\ K}} \cdot 1.534 \ \frac{\mathrm{g}}{\mathrm{l}}} = 0.9062 \tag{3.7}$$

The variable c_p is the specific heat,[6] ρ is the density under standard conditions, gas 1 is the calibrated gas (ND_3) and gas 2 is the gas to be measured (CH_3F). For example, if a flow meter calibrated for ND_3 (5.0 sccm maximal flow rate) has an output signal reading 15% for CH_3F, then the actual flow rate of CH_3F is given by Equation 3.8.

$$Flow\ rate = 0.9062 \cdot 5 \text{ sccm} \cdot \frac{15}{100} = 0.6796 \text{ sccm} \tag{3.8}$$

3.5 Buffer gas cell

The buffer gas cell is made from oxygen-free copper, since defects in a metal significantly reduce its thermal conductivity at cryogenic temperatures (Section 3.2.2). Oxygen-free copper is very difficult to machine, however, so only the main body of the buffer gas cell is made from it; the remaining components are made with standard purity copper. The internal dimensions of the buffer gas cell are 40 mm × 40 mm × 20 mm (height × width × length).

The buffer gas cell and exit plate are designed so that a cell extension can be

---

[6] The c_p value used is for a temperature approximately 50°C higher than the operating temperature of the flow meter. This is because the gas flow meter works by measuring the ΔT along a heated capillary tube through which a portion of the gas flow is directed [181].

inserted between them, increasing the length of the buffer gas cell if desired. The copper clamps used to attach the buffer gas cell to the cryocooler stage enables the cell to shift backward if an extension is used without changing the electrostatic guide assembly at the exit of the cell. Simple changes to the molecular gas line routing would accommodate for the new position of the cell. Although increasing the cell length would provide a colder sample of molecules exiting the cell, the number of molecules exiting the cell would be reduced as more molecules would freeze to the larger area walls. The molecules exit the cell sufficiently cooled for our current purposes, so the extension has not been tested. There would not be enough collisions between the buffer gas and the molecules of interest to provide sufficient cooling before exiting the cell if a significantly shorter cell was used. Refer to Section 2.1 for further details on buffer gas cooling.

A thin layer of Apiezon N grease is applied between the top of the buffer gas cell and the copper plate attached to the second stage of the cryocooler to increase the heat transfer across the solid interface. Silicon diode temperature sensors placed on the plate close to the cryocooler stage and on the bottom of the buffer gas cell confirm there is little difference in temperature between the two locations. We currently manipulate the temperature of the buffer gas cell by removing the outer heat shield; an alternative method would be to sandwich insulating material between the buffer gas cell and the cryocooler stage.

The helium buffer gas enters the cell through a 6.3 mm hole in the side wall, located behind the copper block clamping the buffer gas line to the cell. The capillary method is used to deliver the molecules into the buffer gas cell, and the inlet is carefully designed to minimise the formation of molecular ice that could potentially block the entrance. The molecular gas line is described in Section 3.4.2, so only the molecule inlet itself will be detailed here. As shown in Figure 3.11, the main body of the inlet is a 6.3 mm outer diameter, 3 mm inner diameter copper tube. The inlet nozzle has a

2 mm outer diameter, 1 mm inner diameter, and is 3 mm long. There is a flat surface where the nozzle end meets the main body of the inlet. This is pressed up against the Kapton film front wall of the buffer gas cell, and the connection is sealed with Stycast epoxy to prevent the molecular gas leaking out of the cell. By extending the hot (210 - 300 K) nozzle 3 mm into the cell, any ice that forms along the front wall of the buffer gas cell is less likely to block the entrance. The compromise is that a greater heat load is placed on the buffer gas cell, and the molecules may not be as efficiently cooled by the time they reach the exit of the buffer gas cell.

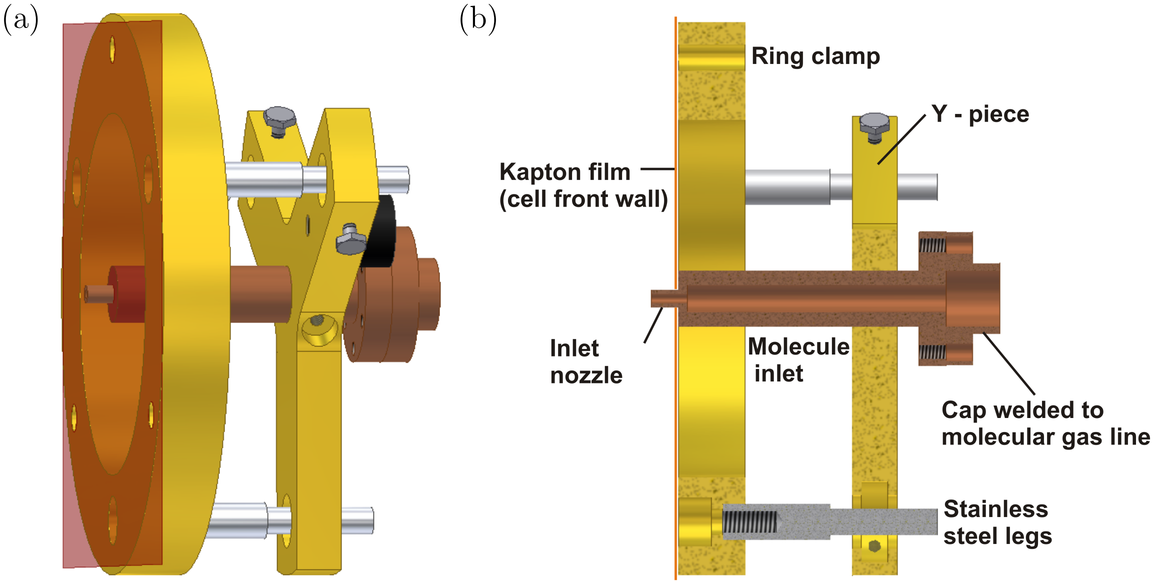

Figure 3.11: (a) The molecular gas is brought into the cell via the capillary method. A cap is welded to the copper tubing of the molecular gas line and used to attach the molecule inlet. The molecule inlet and Y-piece are hot (210 - 300 K) and are thermally disconnected from the cold (6 K) stainless steel pegs, ring clamp and Kapton film front wall of the cell. The inlet nozzle extends 3 mm into the buffer gas cell to prevent ice that forms on the Kapton film front wall of the cell from blocking the entrance. (b) Cross-sectional view of the molecule inlet assembly.

The back wall of the buffer gas cell is formed by a 4 mm thick copper plate. The exit aperture is a 1 mm hole punched out of Kapton film that covers the 18 mm diameter hole in the centre of the exit plate. The Kapton film is fixed in place with two stainless steel clamps bolted to the exit plate. The exposed edges of the Kapton film are also glued to the exit plate with Stycast epoxy to seal the exit. The run time of the experiment is limited by loss of signal resulting from molecular ice blocking the exit aperture, which typically occurs after about 5 hours of operation under normal conditions. If a longer run time is required in future modifications, it may be possible to attach a very thin copper plate with Nichrome heating wires glued to the surface to the Kapton film covering the exit. Localised heating of the exit would melt the ice blockage and temporarily regain the signal without significantly raising the temperature of the entire cell [91].

The Macor insulator holding the electrostatic guide is bolted to the exit plate with two stainless steel pegs. The pegs are designed to hold the stainless steel clamps for the Kapton film against the exit plate as well. Ideally, the end of the electrodes of the electrostatic guide are place as close as possible to the exit aperture in order to capture the largest number of molecules exiting the buffer gas cell. However, ice formation on the electrodes occurs if the guide is placed too close to the exit aperture. This can lead to electrical discharges and the inability of the electrodes to maintain a high voltage. The end of the electrodes are therefore placed 1 mm from the exit aperture.

3.6 Electrostatic guide

3.6.1 Conditioning and operation

The quadrupole guide is made from hand-polished stainless steel rods (2 mm diameter, circular cross-section). Although micro-protrusions on the surface of the electrodes may lead to electrical breakdown, hand-polished and electro-polished electrodes behaved similarly in previous room temperature electrostatic guiding experiments conducted within the group [158]. Specially designed Macor insulators hold the electrode rods in place and maintain a 1 mm separation between adjacent electrodes. The

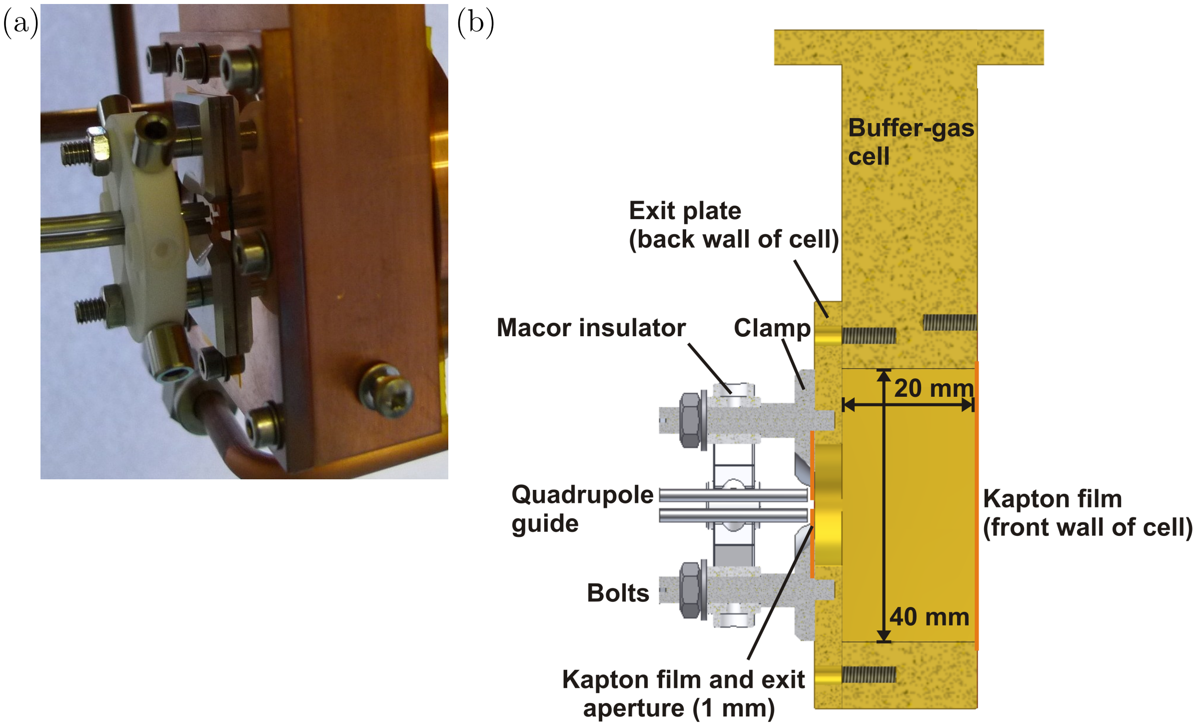

Figure 3.12: (a) The molecules exit the cell through a 1 mm aperture in Kapton film that covers a larger diameter hole in the copper exit plate. The electrostatic guide is placed 1 mm from the exit aperture. The Macor insulator is attached to stainless steel bolts fastened to the exit plate, which also secure the clamps for the Kapton film. (b) Cross-sectional view of the exit assembly.

quadrupole electric field is generated by applying high voltages to the electrodes, up to ± 5 kV when operated under cryogenic conditions. This corresponds to maximal electric field strengths of approximately 90 kV/cm at the surface of the electrodes, while the electric field minimum is found at the centre of the guide. Refer to Section 2.3 for further details on electrostatic guiding and the behaviour of polar molecules in external electric fields.

Electrical breakdown between the electrodes can occur as a result of the high voltage applied to the electrodes. Several measures are taken, both in the operation of the apparatus and in the initial design of the electrostatic guide, in order to maintain the high voltage across the closely spaced electrodes and to minimise potential damage to the apparatus from the electrical breakdown. The positive and negative voltage power supplies are connected to a digital ammeter and several large resistors placed in series before attaching to the electrodes. The electrodes are conditioned by slowly increasing the applied voltage until the maximum operating voltage is slightly exceeded while monitoring the current flowing between the electrodes on the ammeter. The resistors help to moderate large currents that can be generated during electrical breakdown events. Each time the chamber is opened and the electrodes are exposed to air, they are conditioned (under vacuum conditions) to approximately ± 6 kV at room temperature. The conditioning process may take several hours and the mini-discharges at sub-maximal voltages are thought to remove gas and mircoparticles from the surface of the electrodes [182]. If conditioning is difficult to achieve under high vacuum, helium gas is admitted to the chamber or the small turbo-molecular pump attached to the detection chamber is temporarily turned off, and the conditioning process is repeated.

A constant voltage is applied to the electrodes to generate a continuous beam of cold molecules under most operating conditions. Alternatively, the longitudinal velocity distribution of the guided molecules can be obtained by pulsing the voltage applied to the guide electrodes and recording the arrival times of the molecules at the mass spectrometer on an oscilloscope (500 MHz WaveSurfer, Teledyne LeCroy Oscilloscopes). A square-wave function generator (Synthesized Function Generator, DS345, Stanford Research Systems), with a frequency set between 3 to 10 Hz, drives two fast high-voltage switches (Behlke HTS151) that pulse the quadrupole electrodes between ground and high-voltage. It is necessary to remove the ammeters and protective resistors when operating the guide in this configuration, so extra care is taken when conditioning to prevent damage to the electrodes or insulators.

3.6.2 Insulators

In previous room-temperature electrostatic guiding experiments conducted within the group, damage to the PEEK insulators supporting the electrodes suggested that electrical breakdown was occurring at those points, and limited the high voltage that could be applied to the electrodes [158]. Replacing damaged insulators in the cryogenic experiment would be very difficult, so the support insulators were re-designed to provide a longer over-the-surface path length between the electrodes. The insulators are now made of Macor, which is less likely to melt than PEEK, and are produced by Precision Ceramics, UK. Macor is a machinable glass-ceramic that has low thermal expansion and out-gassing, as well as low thermal conductivity even under cryogenic conditions (Table 3.1 and Table 3.3). The electrodes are held in the Macor insulators through a specially designed 'pin' assembly. M1.6 tapped holes are drilled, perpendicular to the curved surface, into the electrodes to a depth of approximately 1 mm (halfway through the electrode). A small precision compression spring (CI 010BC 03 S316, Lee Spring Limited) and screw are inserted into a hollow, stainless steel 'pin', which in turn is placed into a hole in the Macor insulator. The screw pulls the electrode tight against the insulator (Fig. 3.13).

Electrical connections to the electrodes are made by inserting the capped end of a wire into the hollow head of the pin and securing the cap with a screw. The wire is insulated with Kapton and the end cap is made by crimping a brass connector to the end of the wire and machining the end to a smooth round knob (Fig. 3.14). There are also holes in the insulator for support rods to pass through, which are secured to the insulator with M2 screws. The ends of the support rods are then attached to an appropriate mount. When the support rods need to be secured at points between flange faces, the ends of the rods are attached to stainless steel mounting plates with knife edges along the rim. When bolting the vacuum chamber together, the

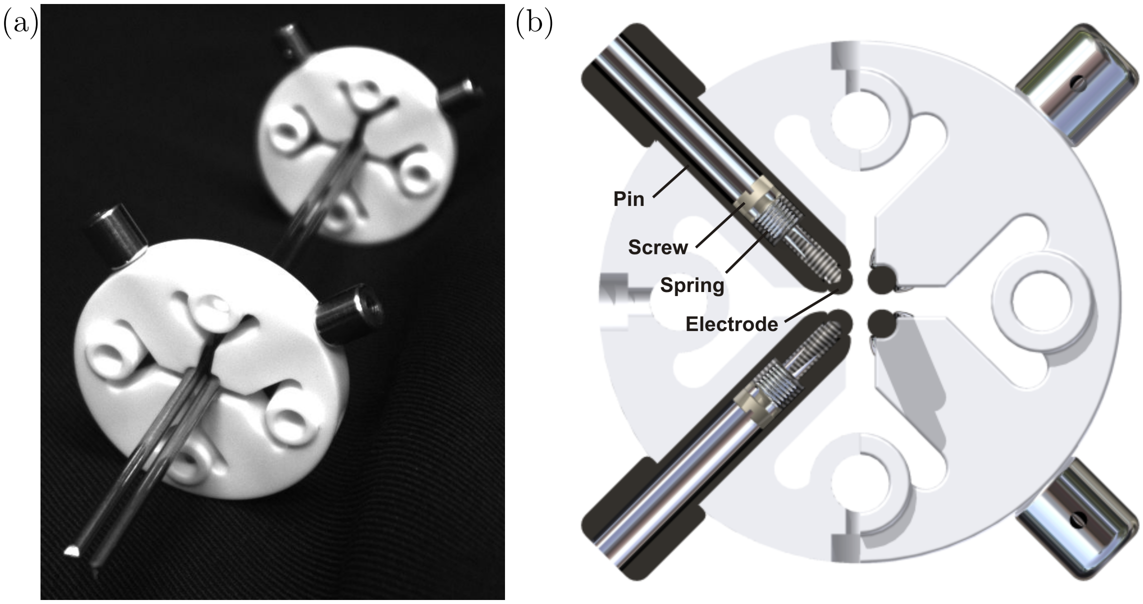

Figure 3.13: (a) Assembly of a straight section of the electrostatic quadrupole guide. The Macor insulators, electrodes, and pins are visible. (b) Partial cross section of the insulator pin assembly. A M1.6 screw and small compression spring are inserted into the hollow pin. The entire pin assembly is then inserted into the MACOR insulator, and the screw tightened into a tapped hole in the electrode. This pulls the electrode tight against the insulator and locks it into the correct position.

bolts pass through both flanges and the mounting plate, sandwiching them together (Fig. 3.14(b)). These mounting plates provide differential pumping stages between sections of the vacuum chamber that are connected to turbo-molecular pumps. Large holes are bored out of the solid face in order to connect sections of vacuum chamber to the nearest pump.

3.6.3 Electrodes

The electrostatic guide is broken into several shorter segments due to the long total path length of the guide. Currently, adjacent segments are placed end to end with no gap (or as little gap as possible when assembling the guide) to minimise the loss of molecules from the guide. Electrical connections are made between the electrodes (Fig. 3.14). A segmented guide with 1 mm gaps between adjacent electrodes, however,

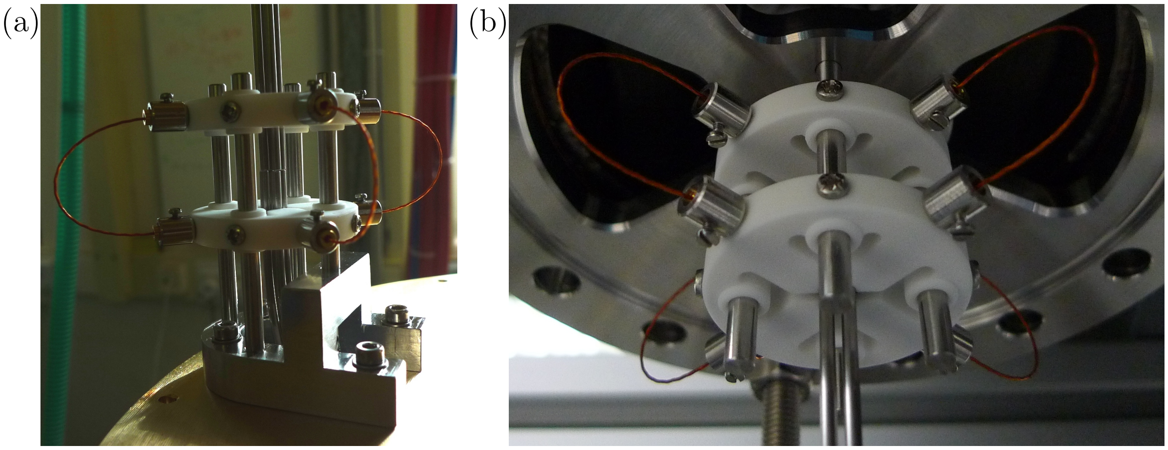

Figure 3.14: Electrical connection between segments of the electrostatic guide. (a) Brass end cap of the Kapton coated wire fits into the hollow head of the pin where a screw secures the wire in place. (b) The insulators are held in place by support rods that are attached to stainless steel mounting plates inserted between flange faces.

may be useful in future modifications of the apparatus. It has been demonstrated that a segmented quadrupole guide can be used, similar to a mechanical chopper [183], to select pulses of molecules with specifically tuned velocities rather than producing a continuous beam of slow molecules. By carefully selecting a timing sequence to switch the different segments of the guide on and off, a molecular beam with a narrow velocity distribution can be obtained [135]. Additionally, a small gap in the guide could allow a gate valve to be inserted between the cryogenic portion of the vacuum chamber and the room temperature sections leading to the detection chamber. The thin gate valve described in [168] is able to maintain a vacuum of $< 10^{-10}$ mbar on one side of the valve while the other side is open to atmosphere. This would be particularly useful when the current assembly is combined with an ion trap. The ultra-high vacuum could be maintained in the ion trap chamber, while the main cryogenic chamber came up to atmosphere during the warm-up phase needed to completely regain the signal after operating for several hours.

In the initial construction of the apparatus, the guide was divided into four segments, two completely straight and two with bends, for a total guide length of 1161 mm.

All bent segments include a ninety degree bend with a radius of curvature of 100 mm along the centre of the guide (inner electrodes have a bend radius of 98.5 mm while outer electrodes have a bend radius of 101.5 mm), with variable lengths of straight sections on each side of the bend. The bent segments are formed by shaping the stainless steel rods around circular plastic moulds. Grooves are machined into metal plates to check that the radius of curvature is correct for each electrode. An insulator is mounted near the apex of the curve in order to maintain the correct alignment of the electrodes, necessary for such a large radius of curvature.

The first segment of the quadrupole guide is mounted 1 mm from the exit aperture of the buffer gas cell. Soon after the initial straight length, the segment bends upward through the plate attached to the second stage of the cryocooler. The second segment of the guide goes straight through the plate attached to the first stage of the cryocooler and through the top flange of the main chamber. The third segment of the guide bends the molecular beam horizontally again, before the fourth and final straight segment of the guide delivers the molecules to the detection chamber, where they exit the guide and travel 20 mm in free flight to the quadrupole mass spectrometer (Fig. 3.1). The large electric fields generated at the end of the electrodes can influence the operation of the mass spectrometer. A grounded mesh (85% transmission) was initially used to shield the mass spectrometer, although a small stainless steel cap that enclosed the end of the guide, again with a mesh covering, proved more effective (Fig. 3.15).

In the initial construction of the apparatus, the molecular beam exits the guide horizontally at a height of 2.01 m above the floor. For safety and practical reasons, it was necessary to extend the electrostatic guide and bring the molecular beam down to table height before switching to the REMPI detection set-up. An additional bent section and straight section were added to bring the total path length of the electrostatic guide to 2148.8 mm (Fig. 5.2).

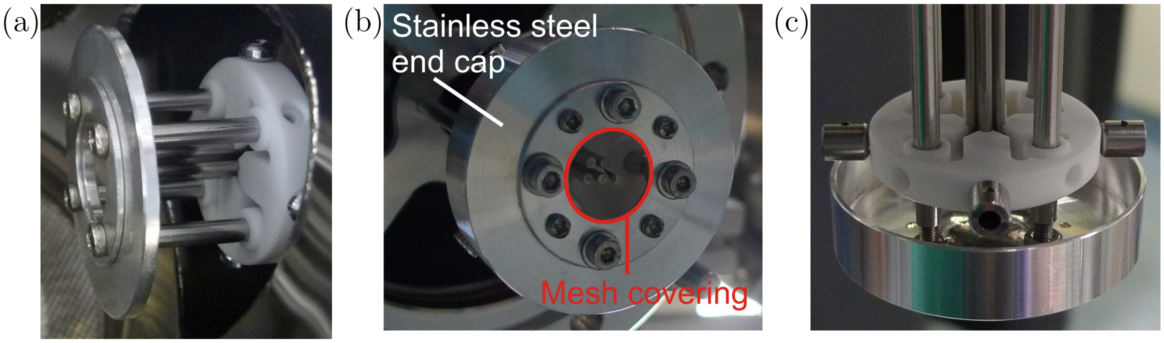

Figure 3.15: (a) Grounded mesh (85% transmission) to shield the mass spectrometer from the large electric fields generated at the end of the electrostatic guide. (b), (c) A later version involving a stainless steel cap enclosing the end of the guide.

Chapter 4

Characterisation of the cold molecular beam using mass spectrometry

4.1 Mass spectrometry

This chapter details the use of mass spectrometry to characterise the guided buffer-gas-cooled molecular beam. Molecules exit the guide and pass through a fine mesh attached to the end of a grounded stainless steel cap, which is placed around the end of the electrodes to shield the quadrupole mass spectrometer (QMS) from the high voltages applied to the guide (described in Section 3.6.3 and shown in Figure 3.15).

The mass spectrometer (QME 200, Pfeiffer) consists of an ioniser, quadrupole mass filter, and an ion detector. Electron impact ionisation is used to create molecular ions in the ioniser region, with the electrons emitted from a heated filament. Once formed, the molecular ions are then focused onto the quadrupole mass filter. A combination of DC and RF voltages are set so that only ions with a specific charge-to-mass ratio have stable trajectories and pass successfully through the quadrupole filter. Finally,

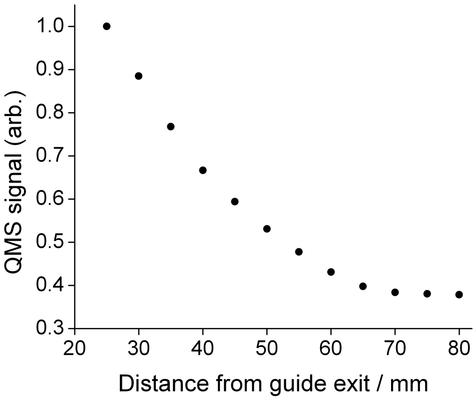

Figure 4.1: The QMS ion signal recorded as the distance between the end of the guide and the QMS detector is increased by mounting the QMS on a z-translational stage. The maximum ion signal is obtained at the point of closest separation, 25 mm, and normalised to one. Standard conditions are used: 1.0 sccm ND_3, 0.6 mbar He, 6 K buffer gas cell, and ±5 kV voltage.

these selected molecular ions are focused onto the detector, where the ion current is measured directly or an electron current proportional to the molecular ion current is measured using a multi-channel electron multiplier [184].

There are several factors that affect the detection efficiency of the mass spectrometer. The beam divergence increases with distance from the guide exit, as the molecules enter a region of free flight between the guide and the mass spectrometer. Fewer molecules enter the ionisation region of the QMS, and the detection efficiency drops. This was predicted from the Monte Carlo simulations (Fig. 2.15) and supported experimentally by attaching the mass spectrometer head to a z-translator stage (Fig. 4.1). The signal plateaus at a distance of approximately 65 mm from the guide exit; most of the molecules detected beyond 65 mm are likely from the background molecular gas that has accumulated in the chamber rather than molecules exiting the guide and directly entering the QMS head.

Low-velocity molecules tend to spread over a larger solid angle because of the similar magnitude of the transverse and longitudinal velocities, decreasing the chances of reaching the detector. This can be seen from the Monte Carlo simulations of the decay of the signal with distance from the guide (Fig. 2.15). The signal drops off more quickly at comparable distances between the guide exit and the QMS head for the 5 K molecular source than for the 300 K molecular source. However, the slow molecules that do enter the ionisation region have a greater ionisation probability because of the longer interaction time in the region.

The detection of the molecules by the mass spectrometer is also affected by fringe electric fields present between the end of the quadrupole guide and the grounded mesh (Fig. 3.15). Simulations have shown that the fringe field accelerates slow molecules exiting the guide [158]; molecules with velocities of 10 ms^{-1} are accelerated to approximately 20 to 25 ms^{-1} by the time they reach the mass spectrometer.

4.2 Longitudinal velocity distributions

Under typical operating conditions, a constant voltage is applied to the guide electrodes in order to produce a continuous beam of cold molecules. However, the velocity distribution of the guided molecules can be determined by pulsing the voltage applied to the electrodes off and on and recording the arrival times of the molecules at the mass spectrometer. A representative arrival time trace, also known as a time-of-flight (TOF) trace, is shown in Figure 4.2(a). The TOF traces are averaged over about five hundred cycles at a repetition rate of 2.5 Hz. The trace is shown for the standard conditions used in the buffer gas cell: 1.0 sccm flow rate of ND_3, 0.6 mbar pressure of helium at the gas inlet, in a 6 K buffer gas cell, and with an applied voltage of ±5 kV to the guide electrodes. A more detailed description of the standard conditions is provided in Section 4.4.

A square waveform generator creates pulses that are on for 250 ms, and off for 150 ms. With a total path length of 2173.8 mm (2148.8 mm long guide and 25 mm

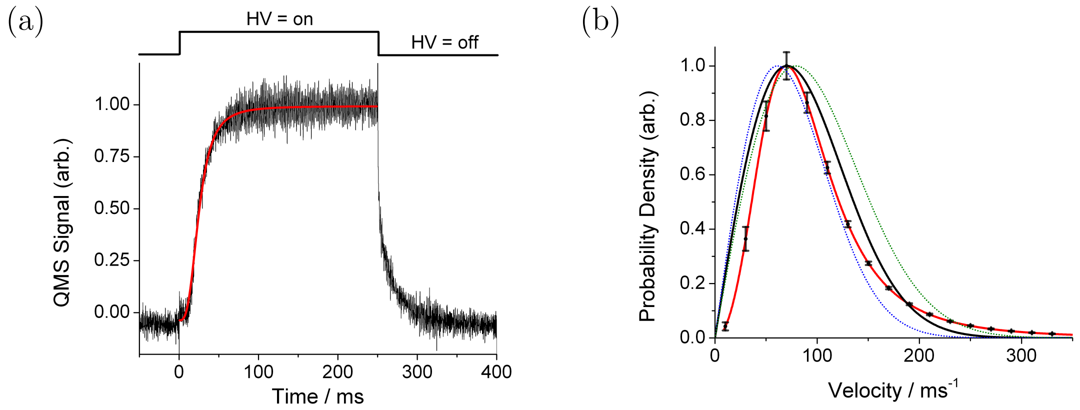

Figure 4.2: (a) Representative arrival time trace obtained by pulsing the voltage applied to the guide. The logistic function used to model the signal is shown in red. (b) The velocity distribution of guided ND_3 calculated from the modelled TOF trace (red). The error bars represent the uncertainty in the velocity distribution as a result of the fitting procedure, and are calculated from the standard deviations in the fitted parameters of the logistic function. Maxwell-Boltzmann distributions are shown for 9 K (blue, dot), 12 K (black, solid), and 15 K (green, dot) for comparison.

distance between guide exit and QMS), this means that the slowest molecules that can reach the QMS in 250 ms are travelling at 8.7 ms^{-1}. Increasing the pulse length beyond 250 ms did not affect the calculated velocity distributions. As explained in Section 4.1, very few molecules with velocities below 10 ms^{-1} reach the detector even for longer pulses. Furthermore, it is often difficult to distinguish the signal increases from the background noise beyond 250 ms because the change in signal is so small. The only electrical interference in the signal due to rapidly switching the high voltage is a short spike at the start and end of the pulse sequence, which is visible in Figure 4.2(a).

There is a short time delay between turning on the high voltage and detection of the molecules by the QMS, determined by the time it takes the fastest molecules to travel the length of the guide. For example, the longitudinal velocity cut-off is 239 ms^{-1} for ND_3 molecules in the $|J, MK\rangle = |1, -1\rangle$ state for the electrostatic guide used experimentally (calculated using Eq. 2.38). It would take these molecules approximately 9 ms to travel from the guide entrance to the QMS, which is roughly when the first visible increase in signal from baseline occurs. The signal starts to plateau after about

30 ms, when molecules travelling at approximately 70 ms^{-1} start reaching the guide. This is the most probable velocity of the guided molecules, as calculated later in this section. The signal remains relatively constant after about 60 ms, when the fractional increase in flux is a result of molecules arriving with velocities below about 35 ms^{-1}; at this point the bulk of the signal is produced by the constant flux of guided molecules. As soon as the high voltage is turned off, the confining field vanishes and the molecules rapidly disperse from the guide. The signal has fully decayed after 150 ms.

As mentioned earlier, the signal from the TOF trace $S(t)$ can be used to calculate the longitudinal velocity distribution $f(v)$ of the guided molecules given the total path length L from the guide entrance to the detector [185]. Recall that because the source of molecules is continuous (while the voltage applied to the electrodes is pulsed), the signal represents the cumulative probability distribution of the guided molecules; faster molecules are continuing to arrive as the slower ones first reach the detector. The time t it takes for a molecule travelling at velocity v to reach the QMS is given by $t = L/v$. The first derivative of this quantity, $\delta t = -L/v^2 \delta v$, is useful for determining the velocity distributions. The increase in the signal during the infinitesimal time interval δt is due to molecules with velocities in the interval δv, as shown by

$$f(v)(-\delta v) = \frac{S(t+\delta t) - S(t)}{\delta t} \delta t. \tag{4.1}$$

The increasing signal is due to the arrival of progressively slower molecules at the detector, leading to the negative sign in above equation. After making the appropriate substitution for t and δt, and as $\delta t \to 0$, the velocity distribution can then be calculated using

$$f(v)(\delta v) = \frac{L}{v^2} \dot{S}(t) \delta v = \frac{L}{v^2} \dot{S}(L/v) \delta v. \tag{4.2}$$

A logistic function is used to model the signal instead of directly differentiating the experimental data because of high-frequency noise in the signal. The fitting procedure, including the logistic function, is described in detail in Appendix B. An example of the velocity distribution calculated from the TOF trace using this method is shown in Figure 4.2(b) for standard buffer gas cell conditions (1.0 sccm ND_3, 0.6 mbar He, 6 K cell). The uncertainty in the velocity distribution as a result of the fitting procedure can be calculated from the standard deviations in the fitted parameters, as presented in Figure 4.2(b).

As the velocity distributions of the guided molecules do not represent a thermal equilibrium distribution, it is difficult to assign a translational temperature to the molecular beam. A longitudinal temperature can be estimated by matching the most probable velocity in the experimental distribution to the most probable velocity of a one-dimensional Maxwell-Boltzmann thermal distribution. A 12 K Maxwell-Boltzmann distribution provides the best match to the data presented in Figure 4.2(b). Maxwell-Boltzmann distributions for 9 K and 15 K are also shown for comparison. When the term ‘translational temperature’ is used in this work, it refers to the thermal energy of the molecular beam rather than a thermodynamic equilibrium temperature.

An alternative way to characterise the longitudinal velocity distributions is to relate the most probable velocity[1] v_p to a peak kinetic energy T_p using the relationship $mv^2/2 = k_\mathrm{B}T$ [186]. Thus, T_p represents an estimate of the thermal energy of the molecular beam. Furthermore, the width of the velocity distributions can be compared using the FWHM of the distributions (i.e. the width of the distribution Δv at $f(v_\mathrm{p})/2$). In the example shown in Figure 4.2(b), the most probable velocity and the FWHM associated with the velocity distribution are 70.39(0.28) ms^{-1} and 85.06(0.40) ms^{-1}, respectively. This corresponds to a peak kinetic energy of 5.96(0.05) K. The error in the parenthesis is found from the standard deviations in the fitted parameters of the logistic function used to model the experimental data.

---

[1] The most probable velocity v_p of the molecules corresponds to the velocity at which the calculated velocity distribution $f(v)$ reaches its maximum value (i.e. where $df/dv = 0$).

4.3 Voltage dependence

Perhaps the simplest way of changing the translational 'temperature' of the guided beam of molecules is to change the voltage applied to the electrodes. A lower applied voltage creates a weaker electric field within the guide and thus a lower confining potential, ultimately leading to a lower velocity cut-off. The shifted velocity cut-off means that the beam of guided molecules exhibits a colder translational temperature. The trade off is that there is also a lower flux of guided molecules, because a smaller fraction of the initial distribution of molecules at the buffer gas source are successfully guided.

The mass spectrometer is set-up to record the current from (singly charged) ions of a specific mass, in this case 20 amu for ND_3, while a constant voltage is applied to the electrodes. Increasing the voltage leads to a greater flux of molecules reaching the QMS, and therefore an increased ion current. This is shown in Figure 4.3 for 1.0 sccm ND_3 and 0.6 mbar He for a 6 K buffer gas cell. Note that this is recorded with the guide in continuous mode. These are considered the 'standard' operating conditions, and are described in more detail in Section 4.4.1 and Section 4.4.2.

The QMS data presented in this chapter represent numerous 'single runs' that are considered representative of the data, based on repeated runs at different times in the day and on different days. Furthermore, each data point represents the average QMS current recorded over a short time period (typically 20 to 90 seconds involving 5 to 20 measurements of the QMS current). The error bars in Figure 4.3 denote one standard deviation from the average QMS current. The error is similar in other QMS scans, and is therefore not included in the rest of the figures presented in this chapter.

As explained in Section 2.3.3, molecules with linear Stark shifts, such as ND_3, are expected to have a guided flux that depends quadratically on the applied voltage. The quadratic dependence is observed experimentally for a room temperature molecular

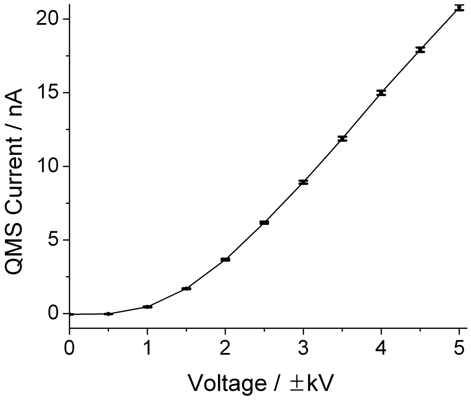

Figure 4.3: The voltage applied to the electrostatic guide is varied while the current is recorded at the QMS; the current is proportional to the flux of guided ND_3 molecules reaching the QMS detector. The error bars represent one standard deviation from the average QMS current recorded at each voltage. Standard conditions are used in the buffer gas cell (1.0 sccm ND_3, 0.6 mbar He, 6 K cell).

source [158]. However, this relationship is only valid when the velocity cut-off of the guide is much smaller than the thermal velocity of the molecular source. The thermal velocity of the molecular source is significantly lower for the buffer-gas-cooled molecular beam used in this experiment. Therefore, the quadratic dependence is only observed at the lower voltages (when the cut-off velocity is much lower). At higher applied voltages, the cut-off velocity approaches the thermal velocity of the molecular source, and the relationship transitions from a quadratic to a linear dependence. If voltages greater than ± 5 kV could be applied to the electrodes, the signal may even start to plateau due to the large portion of the initial distribution that would be successfully guided; further increases in voltage would only lead to a marginal increase in the guided flux.

The guide can also be operated in a pulsed mode in order to determine the velocity distribution of the guided molecules, as described in Section 4.2. The TOF traces of ND_3 have been recorded for a range of applied voltages, under standard operating conditions of the buffer gas cell (1.0 sccm ND_3, 0.6 mbar He, 6 K cell). The amplitude

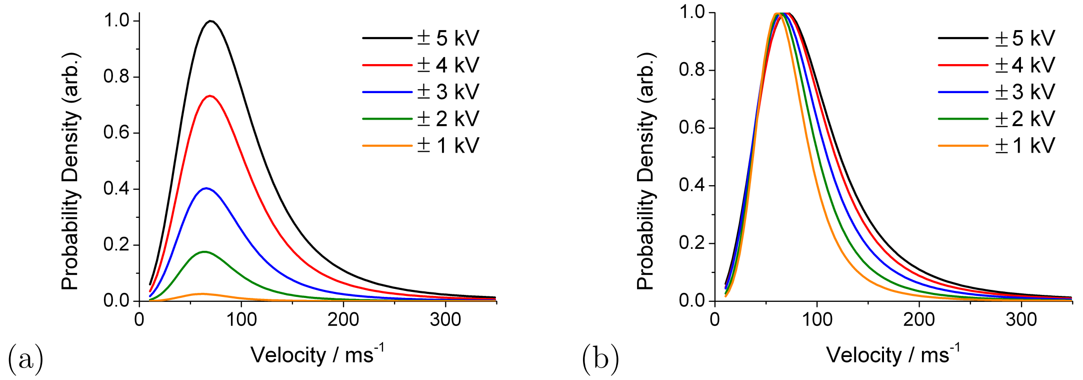

Figure 4.4: The velocity distributions of ND_3 are determined from the TOF traces recorded for a range of voltages applied to the quadrupole guide. Standard conditions are used in the buffer gas cell (1.0 sccm ND_3, 0.6 mbar He, 6 K cell), and the distributions are shown for (a) probability densities relative to the guided flux and (b) peak probability densities scaled to one.

of the TOF trace increases with increasing voltage, as expected for the increased flux of molecules reaching the QMS. The signal also begins to rise at an earlier time and at a steeper degree for higher applied voltages because of the faster molecules that are successfully guided.

Using the method described in Section 4.2, the ND_3 velocity distributions have been calculated from the TOF traces recorded at different applied voltages and are shown in Figure 4.4. The relative velocity distributions (Fig. 4.4(a)) provide information about the fraction of molecules from the initial distribution that are successfully guided, in addition to the translational temperature of the beam, for a range of different applied voltages. In order to facilitate a comparison between the low and high velocity tails, the distributions have been scaled in Figure 4.4(b).

The low-velocity tail of the distribution is largely unaffected by the increasing voltages. The trailing edge of the distribution, however, is shifted to higher velocities with increasing voltage. The most probable velocity v_{p} and widths of the distribution are summarised in Table 4.1. The peak kinetic energy T_{p} of the molecules (corresponding to the most probable velocity) and the relative guided flux determined from the QMS signal are also listed. The most probable velocity is approximately 10 ms^{-1} lower for an applied voltage of ± 1 kV compared to ± 5 kV, corresponding to shift of nearly 1.5 K in the thermal energy of the molecules. This is accompanied by a decrease in the width of the distribution, but also a significant reduction in the flux of the molecules. Unless otherwise stated, a voltage of ± 5 kV is applied to the electrodes and is considered the 'standard' operating voltage of the experimental apparatus throughout this work.

Table 4.1: The velocity distributions obtained when applying different voltages to the quadrupole guide can be characterised by a number of parameters, including the most probable velocity v_{p} and the FWHM. This can be related to the peak kinetic energy T_{p} of the molecules. The error in the parenthesis is found from the standard deviations in the fitted parameters of the logistic function used to model the experimental data. Finally, the relative flux of the guided molecules can be found from the ion current recorded at the QMS for the particular applied voltage. The data is obtained using standard conditions in the buffer gas cell (1.0 sccm ND_3, 0.6 mbar He, 6 K cell).

Voltage / ± kV	v_{p} / ms^{-1}	FWHM / ms^{-1}	T_{p} / K	QMS Current / nA	Relative flux (arb.)
1.0	62.16(1.03)	55.15(1.46)	4.65(0.15)	0.45	0.02
2.0	63.90(0.75)	64.56(1.06)	4.91(0.12)	3.66	0.18
3.0	65.95(0.34)	74.81(0.48)	5.23(0.05)	8.92	0.43
4.0	69.71(0.23)	81.99(0.32)	5.84(0.04)	14.99	0.72
5.0	70.73(0.32)	87.45(0.45)	6.02(0.05)	20.79	1.0

4.4 The effect of changing molecular and buffer gas densities

Changing the amount of molecular and buffer gas entering the cell affects the translational and rotational temperature of the molecules exiting the cell, and ultimately the flux of cold molecules at the end of the guide. Unfortunately, compromises must be made between maximising the internal cooling of the molecules and maximising the guided flux. Additionally, run time optimisation must also be taken into account, because molecular ice formation at the entrance and exit of the cell reduces the flux of molecules out of the cell and ultimately limits the operation time of the experiment. Section 4.6 describes the run time optimisation in more detail.

Because the longitudinal velocity cut-off depends on the Stark shift of the molecule and therefore on its rotational state, it is possible to infer some information about the rotational state populations from the longitudinal velocity distributions. However, rotational state distributions can be determined directly from (2+1) REMPI spectroscopy (as described in Chapter 5). Therefore, analysis of the longitudinal velocity distributions in this chapter will be limited to describing the translational temperature of the molecules.

4.4.1 Molecular gas

The effect of molecular gas density on the flux and velocity distribution of the guided molecules is described in this section. The QMS signal was recorded for various flow rates of ND_3 entering the buffer gas cell, while keeping the pressure of the buffer gas at the inlet of the cell constant, and is shown in Figure 4.5. The QMS signal is proportional to the flux of guided molecules. Increasing the amount of ND_3 at low flow rates significantly increases the flux of molecules exiting the guide. The relatively low density of molecules present in the cell means that the molecules undergo a sufficient number of cooling collisions with the buffer gas before exiting the cell. Increasing the ND_3 flow rate from 0.1 to 1.5 sccm therefore results in a significant increase in the number of successfully guided ND_3 molecules.

At higher flow rates, the flux begins to plateau despite increases to the amount of ND_3 entering the cell. The saturation of the signal can be explained by a reduction in the effectiveness of the buffer gas cooling. At high molecular densities within the cell,

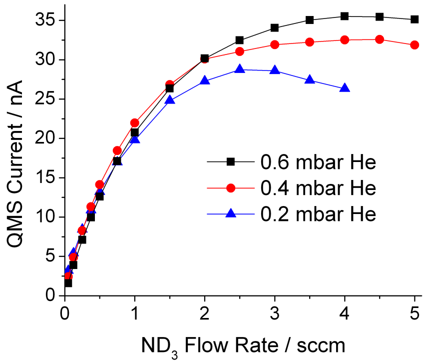

Figure 4.5: The pressure of the buffer gas at the inlet of the cell is kept constant while varying the flow rate of ND_3 molecular gas entering the 6 K cell. The guided flux is proportional to the current recorded at the QMS.

there is not enough buffer gas to effectively cool the additional molecules entering the cell. Increasing the flow rate leads to insufficient cooling, with some molecules exiting at higher longitudinal velocities. A smaller fraction of the molecules are successfully guided around the bend of the quadrupole and the guided flux does not increase. As expected, the flux plateaus at higher molecular gas flow rates for higher densities of buffer gas in the cell. When the buffer gas is kept at a very low density in the cell (Fig. 4.5, 0.2 mbar helium), the guided flux may even decrease slightly for very high flow rates of ND_3.

TOF traces are recorded for a range of molecular gas flow rates, shown in Figure 4.6(a) for the constant inlet pressure of 0.6 mbar of helium buffer gas. The amplitudes of the TOF traces increase for higher molecular flow rates because of the increased flux of guided molecules. Figure 4.6(b) shows the velocity distributions calculated from the TOF traces, all scaled to a maximum probability density of one. The low-velocity tail of the distribution is largely unaffected by changes to the molecular gas flow rate.

The upper tail of the distribution is shifted toward higher velocities for larger molecular gas flow rates. For a given buffer gas density, increasing the molecular flow

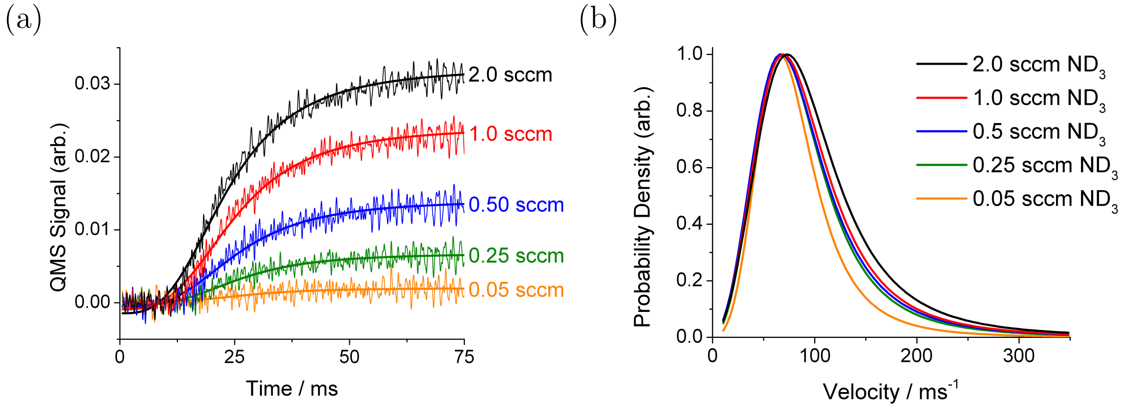

Figure 4.6: (a) The leading edge of the TOF traces recorded for various ND_3 flow rates for 0.6 mbar helium buffer gas in a 6 K cell. The solid lines show the logistic functions used to model the signal. (b) Longitudinal velocity distributions calculated from the TOF traces.

rate leads to a decreased efficiency of buffer gas cooling, and therefore molecules exit the cell with slightly higher velocities. The trend is most noticeable for very low or very high flow rates; the effect is not as large for intermediate flow rates. The peak velocity, thermal energy, and guided flux for a number of molecular flow rates are listed in Table 4.2. The peak velocity and thermal energy shift to slightly higher values for increasing molecular flow rates.

For a given buffer gas density, both the translational and rotational cooling will be enhanced at lower molecular flow rates. The relatively sharp high velocity cut-off for the 0.05 sccm flow rate of ND_3 (Fig. 4.6) is likely due to enhanced rotational cooling, which leads to the population of fewer rotational states. For higher flow rates, a greater number of rotational states may be populated. Each rotational state exhibits a different Stark shift and therefore a different longitudinal velocity cut-off, leading to a broadening of the tail of the velocity distribution.

The flow rate of 1.0 sccm is considered the optimal flow rate for ND_3 with our buffer gas cell geometry and experimental apparatus. The appreciable molecular flux achieved at this flow rate off sets the slightly higher translational temperature of the molecular beam (compared to the lowest flow rates). Although even greater fluxes can be obtained for higher flow rates, the exit aperture will become blocked with molecular ice earlier and limit the run time of the experiment.

4.4.2 Buffer gas

The effect of buffer gas density on the flux and velocity distribution of the guided molecules is described in this section. Figure 4.7(a) shows the QMS current recorded for three different ND_3 flow rates over a wide range of inlet pressures for the helium buffer gas in a 6 K cell. For very low amounts of buffer gas, there are not enough buffer gas atoms to effectively cool the molecular gas. Most molecules leave the cell at too great a velocity to be successfully guided around the bend, leading to a low QMS signal. Increasing the amount of buffer gas increases the effectiveness of buffer gas cooling, leading to more molecules being guided around the bend and a greater QMS signal.

After a certain point, however, the QMS signal actually decreases for increasing amounts of buffer gas due to an effect called 'velocity boosting.' Three different flow regimes can be used to describe buffer-gas-cooled beams: effusive, intermediate, and fully hydrodynamic. A more detailed description of each is provided in Section 2.1.4. The molecular beams are in the intermediate flow regime for the buffer gas cell ge-

Table 4.2: Parameters characterising the guided ND_3 velocity distributions for different flow rates of ND_3, keeping all other conditions within the buffer gas cell constant (± 5 kV, 0.6 mbar He, and 6 K cell).

ND_3 flow rate / sccm	v_p / ms^{-1}	FWHM / ms^{-1}	T_p / K	QMS Current / nA	Relative flux (arb.)
0.05	66.98(1.96)	66.61(2.77)	5.40(0.32)	1.58	0.05
0.25	68.34(0.91)	79.60(1.29)	5.62(0.15)	7.10	0.24
0.50	68.00(0.47)	83.01(0.67)	5.56(0.08)	12.59	0.42
1.0	70.39(0.28)	85.06(0.40)	5.96(0.05)	20.75	0.69
2.0	74.15(0.18)	92.24(0.25)	6.61(0.03)	30.16	1.0

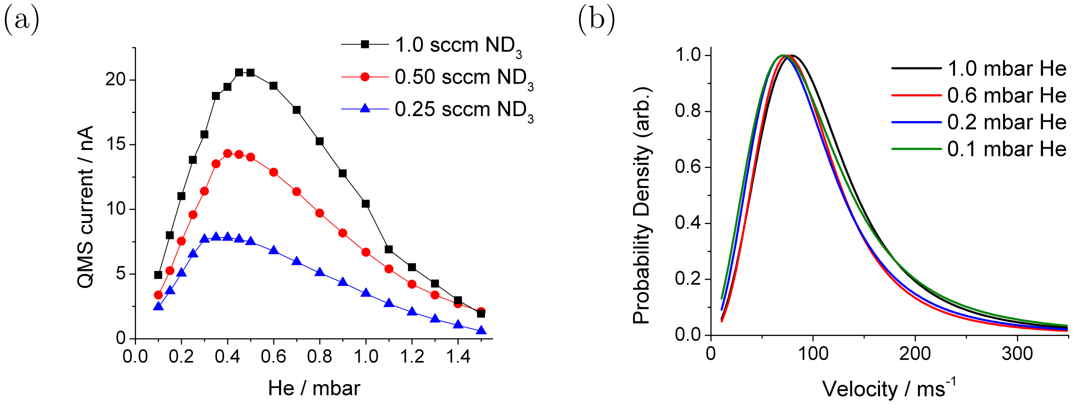

Figure 4.7: (a) The QMS signal of the guided molecules is recorded for a fixed ND_3 flow rate over a range of inlet pressures of the buffer gas in a 6 K cell. (b) Longitudinal velocity distributions calculated from TOF traces for several different inlet pressure of buffer gas for the fixed ND_3 flow rate of 1.0 sccm in a 6 K cell, with a guide voltage of ±5 kV.

ometry and conditions used experimentally. Collisions near the exit aperture between the heavy molecules and the light buffer gas atoms (which are concentrated near the exit aperture) lead to 'velocity boosting' of the molecules exiting the cell. This corresponds to the onset of supersonic expansion. Refer to [141] for a detailed description of velocity boosting. The forward velocity of the molecules exiting the cell increases with increasing buffer gas density until reaching the maximum velocity characteristic of a fully hydrodynamic beam of approximately $1.4\bar{v}_{\mathrm{b}}$, where $\bar{v}_{\mathrm{b}}$ is the thermal velocity of the buffer gas (Eq. 2.19). When the QMS signal, and therefore guided molecular flux, starts decreasing for increasing amounts of buffer gas in the cell, the increased effectiveness of the buffer gas cooling is outweighed by the velocity boosting effect. The molecules exit the buffer gas cell with higher forward velocities, and therefore a smaller fraction of molecules are successfully guided around the bend.

Figure 4.7(b) shows the velocity distributions for a flow rate of 1.0 sccm ND_3 for different amounts of helium buffer gas. At low buffer gas densities, increasing the inlet pressure from 0.1 to 0.2 mbar helium increases the efficiency of the buffer gas cooling and shifts the trailing edge of the velocity distribution to lower velocities without affecting the leading edge of the distribution. The slowest molecules exiting the cell may be more susceptible to velocity boosting since they spend a longer period of time near the exit aperture. By 0.6 mbar helium, the low velocity tail of the distribution is shifted to slightly higher velocities due to velocity boosting of the slowest molecules, although the trailing edge is largely unaffected by the boosting. By 1.0 mbar helium, however, both the leading and trailing edges of the velocity distribution are shifted to higher velocities due to the velocity boosting.

Table 4.3 summarises the ND_3 velocity distributions obtained for a range of buffer gas pressures in the cell. Although the peak velocity and thermal energy initially decrease for increasing amounts of buffer gas, the velocity boosting that occurs for large densities of buffer gas in the cell eventually reverses the trend. The FWHM also decreases for increasing amounts of buffer gas initially, and is relatively small even at higher buffer gas densities. This is likely due to the buffer-gas-cooled beam approaching the fully hydrodynamic flow regime, where there is typically a small spread of forward velocities.

Table 4.3: Parameters characterising the guided ND_3 velocity distributions are shown for a range of helium buffer gas pressures at the inlet of the 6 K cell, while keeping the ND_3 flow rate constant at 1.0 sccm, with a guide voltage of ±5 kV.

He flow rate / mbar	v_p / ms^{-1}	FWHM / ms^{-1}	T_p / K	QMS Current / nA	Relative flux (arb.)
0.1	72.78(1.41)	108.97(2.00)	6.37(0.25)	4.92	0.24
0.2	70.73(0.58)	96.68(0.82)	6.02(0.10)	11.02	0.54
0.4	73.81(0.58)	90.87(0.83)	6.55(0.10)	19.46	0.95
0.6	75.86(0.70)	92.24(0.99)	6.92(0.13)	19.55	0.95
0.8	79.96(0.93)	97.70(1.32)	7.69(0.18)	15.25	0.74
1.0	80.64(1.32)	103.85(1.96)	7.82(0.26)	10.43	0.51

For higher flow rates of ND_3, the buffer gas density for which the molecular flux is maximised shifts to slightly higher values (Fig. 4.7). For a flow rate of 1.0 sccm ND_3, an inlet pressure of 0.6 mbar helium was found to be the optimal setting. Larger amounts of buffer gas would increase the run time of the apparatus and enhance the efficiency of rotational cooling, but at the expense of increased velocity boosting and a lower molecular flux.

4.5 Cell temperature and choice of buffer gas

Helium is the most commonly used buffer gas in cryogenic applications. It has a sufficiently large vapour pressure for most applications at temperatures as low as 300 mK [187]. However, since the buffer gas cell is operated in the intermediate flow regime in order to obtain a greater flux than would be possible in the effusive regime, the forward velocity of the molecules may be boosted by as much as 1.4 times the thermal velocity of the buffer gas (refer to Section 2.1.4 and Section 4.4.2 for more details). Thus, using a heavier buffer gas with a lower thermal velocity may be advantageous.

Although neon can only be used down to temperatures of approximately 14 K before the vapour pressure drops too low to be effective as a buffer gas, its thermal velocity may still compare favourably to that achieved by the lower temperature but much lighter helium gas. For example, the thermal velocity of 6 K helium is 178 ms^{-1} while the thermal velocity of 17 K neon is only 134 ms^{-1}. The use of neon at higher operating temperatures can lead to other technical advantages as well. In order to maintain a high vacuum outside of the cell, large area adsorbents such as activated charcoal must be used for helium, whereas any cold surface acts as a cryopump for neon.

The velocity distributions obtained when using 6 K helium, 17 K helium, and 17 K neon as the buffer gas are shown in Figure 4.8, and the parameters characterising the distributions are listed in Table 4.4. Refer to Section 3.3.1 for details on how the temperature of the buffer gas cell is varied. The 17 K neon buffer gas produces a

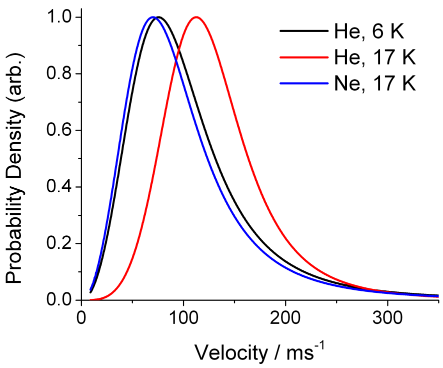

Figure 4.8: ND_3 velocity distribution for different buffer gases and cell temperatures. The ND_3 flow rate is 1.0 sccm and the inlet pressure of the buffer gas is 0.6 mbar in all cases.

molecular beam with a slightly lower translational temperature than the 6 K helium buffer gas, and a significantly lower translational temperature than the 17 K helium buffer gas. As shown in Chapter 5, however, the 17 K buffer gas cell leads to less rotational cooling of the molecules. This is the main disadvantage of using neon as the buffer gas since rotational cooling is desirable in many low temperature experiments.

Table 4.4: Parameters characterising the guided ND_3 velocity distributions are provided for two different buffer gas cell temperatures (6 K and 17 K) and for two different buffer gases (helium and neon). A flow rate of 1.0 sccm ND_3 was used with an inlet pressure of 0.6 mbar buffer gas.

Buffer gas	Cell temperature / K	v_p / ms^{-1}	FWHM / ms^{-1}	T_p / K
Helium	6	75.86(0.70)	92.24(0.99)	6.92(0.13)
Helium	17	112.41(1.37)	89.50(1.93)	15.20(0.37)
Neon	17	70.05(0.06)	88.14(0.08)	5.90(0.01)

The ultimate goal is to study low temperature chemical reactions using the electrostatically extracted buffer-gas-cooled beams as the source of cold molecules. The ability to control the translational and rotational temperature of the molecular source provides a valuable opportunity to study the effect of internal cooling on reaction rates. Small changes to the translational temperature (Section 4.4) and rotational temperature (Section 5.4.2 and Section 5.4.1) of the molecules can be achieved by changing the density of the buffer gas or the molecular gas within the cell. The translational and rotational temperature of the molecular beam can also be altered by operating the buffer gas cell at 6 K or 17 K. A 17 K neon buffer gas cell produces a molecular beam with a higher rotational temperature (Section 5.4.3), but similar translational temperature, to a molecular beam from a 6 K helium buffer gas cell. A comparison between these two configurations may be particularly useful in studying the effect of internal cooling on reactions rates.

The molecular beam produced from the buffer gas cell at 17 K when using either helium or neon as the buffer gas can be characterised in the same manner as the 6 K helium buffer gas cell. Figure 4.9(a) shows the QMS signal for a constant 1.0 sccm flow rate of ND_3 over a wide range of inlet pressures of the buffer gas. The larger thermal velocity of helium at 17 K compared to 6 K (299.97 ms^{-1} and 178.21 ms^{-1}, respectively) means that the molecules are boosted to higher velocities in the 17 K cell at the same helium buffer gas density. The higher forward velocity of molecules exiting the cell leads to a smaller fraction of molecules being successfully guided around the bend, and ultimately a lower flux of molecules at the QMS. Therefore, the molecular flux peaks at a much lower inlet pressure of helium buffer gas at 17 K compared to 6 K. The thermal velocity of neon at 17 K is only 134.15 ms^{-1}, lower than the thermal velocity of helium at either 6 K or 17 K. This leads to a slightly greater molecular flux at high buffer gas densities compared to the helium buffer gas cells.

Figure 4.9(b) shows the QMS signal for a constant inlet pressure of the buffer gas over a wide range of ND_3 flow rates. At low molecular flow rates, the molecular flux reaching the end of the guide increases rapidly with increasing molecular flow rate for both 6 K helium and 17 K neon. The molecular flux eventually plateaus at higher flow rates when there are too many molecules entering the cell to be cooled effectively by the buffer gas. With 17 K helium, the signal is very small for lower molecular

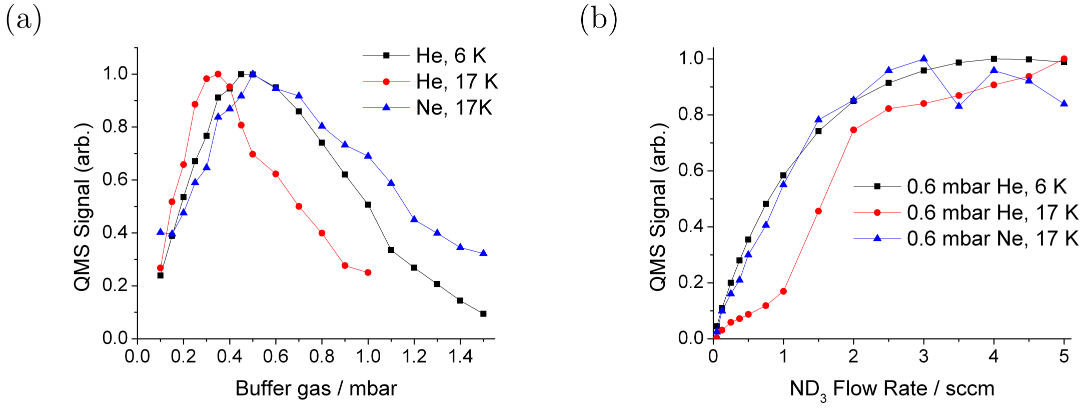

Figure 4.9: (a) The QMS signal of the guided molecules is recorded for a fixed ND_3 flow rate of 1.0 sccm over a range of inlet pressures of the buffer gas for different cell temperatures. (b) The pressure of the buffer gas at the inlet of the cell is kept constant at 0.6 mbar while varying the flow rate of ND_3 molecular gas entering the cell for different cell temperatures.

flow rates, increases rapidly for intermediate flow rates, and then starts to taper off but does not quite plateau for higher flow rates. This is because the molecular flux actually peaks at approximately 0.35 mbar helium at 17 K; little signal is observed at the lower flow rates for 0.6 mbar helium, and saturation of the buffer gas cooling (at which point the signal plateaus) only occurs at higher flow rates.

ND_3 velocity distributions determined for the fixed ND_3 flow rate of 1.0 sccm over different inlet pressures of helium in a 17 K cell are shown in Figure 4.10(a). The velocity boosting clearly affects both the leading and trailing edge of the distributions and the peak velocity shifts from 96.70(1.12) ms^{-1} to 127.44(13.30) ms^{-1} for 0.2 mbar and 0.8 mbar helium buffer gas, respectively. Figure 4.10(b) shows the velocity distributions for the fixed buffer gas pressure of 0.6 mbar helium for a range of ND_3 flow rates. For a fixed buffer gas density in the cell, the buffer gas cooling becomes less effective for larger molecular gas flow rates. Although the leading edge of the distribution is largely unaffected, the trailing edge shifts toward higher velocities. The peak velocity also increases from 107.63(5.53) ms^{-1} to 119.58(1.92) ms^{-1} for 0.25 sccm and 2.0 sccm ND_3 flow rates, respectively.

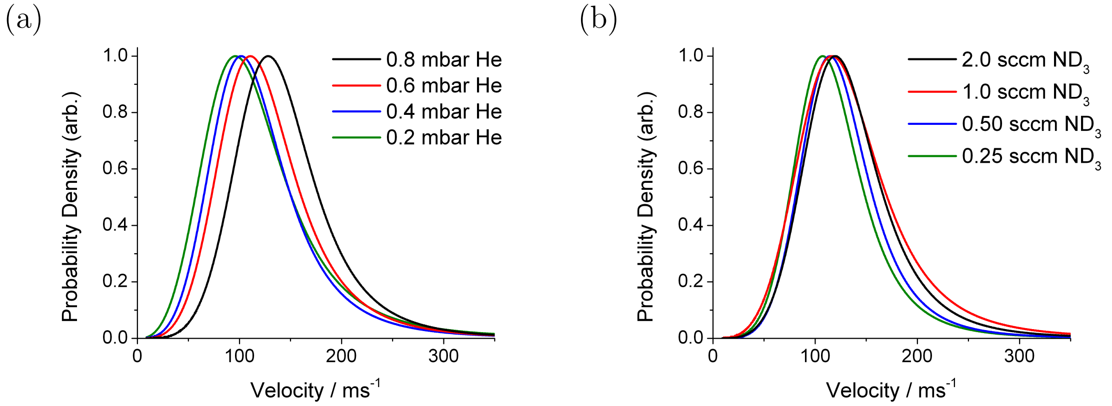

Figure 4.10: ND$_3$ velocity distributions for a 17 K helium buffer gas cell for (a) different inlet pressures of the buffer gas at the fixed ND$_3$ flow rate of 1.0 sccm and (b) for different molecular gas flow rates at the fixed inlet pressure of 0.6 mbar helium.

As with the 6 K helium cell, the thermal energy of the guided molecular beam can be lowered by decreasing the voltage applied to the electrodes (Fig. 4.11(a)), but at the expense of a decreased molecular flux. The molecular flux can be significantly increased without greatly affecting the velocity distributions by increasing the ND$_3$ molecular flow rate into the cell (Fig. 4.11(b)). The leading edge of the distribution is unaffected and the trailing edge is only slightly shifted to higher velocities when the ND$_3$ flow rate is increased from 0.25 sccm to 2.0 sccm. However, operating at a higher molecular flow rate limits the run time of the apparatus, as the exit blocks with molecular ice much sooner (refer to Section 4.6 for more details on experimental run time). It should be noted that both ND$_3$ and neon are ionised by our mass spectrometer and have an indistinguishable charge-to-mass ratio. Although only ND$_3$ contributes to the increasing signal in the TOF traces, the baseline current is higher than normal due to the ionisation and detection of neon. This could be overcome by using a mass spectrometer with a tunable electron energy ionisation source. Although the neon is not guided, a low pressure diffuses into this part of the apparatus.

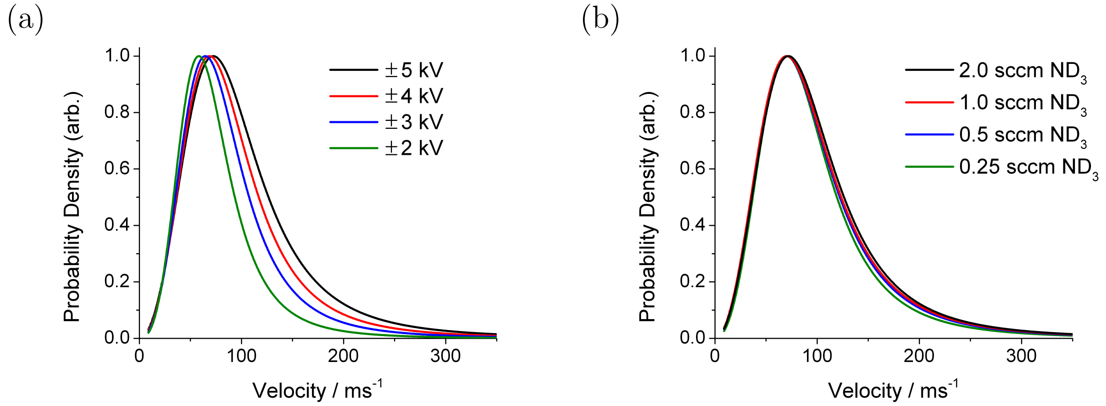

Figure 4.11: ND_3 velocity distributions for a 17 K neon buffer gas cell for (a) different applied voltages at the fixed ND_3 flow rate of 1.0 sccm and the inlet pressure of 0.6 mbar and (b) for different molecular gas flow rates at the fixed inlet pressure of 0.6 mbar neon.

4.6 Run time optimisation

The molecular gas line is insulated from the cryogenic environment and heated to approximately 210 K to prevent the ND_3 molecules from freezing and blocking the gas line. Once the molecules enter the 6 K buffer gas cell, any molecules that come in contact with the walls freeze and stick to the wall. Only a small fraction of the molecules entering the cell actually reach the exit aperture, so a layer of molecular ice gradually builds up on the cell walls as the molecular gas is flowed continuously into the cell.

As the layer of molecular ice grows, the 1 mm diameter exit aperture of the cell can become blocked and the flux of molecules exiting the cell is reduced. Although the molecular ice may also block the molecular and buffer gas entrances to the cell, this is usually less of an issue because the molecular inlet is kept around 210 K and the helium inlet has a large internal diameter of 6.3 mm. Figure 4.12(a) shows how the peak height of the $|J, K\rangle = |1, 1\rangle$ (2+1) REMPI signal (see Chapter 5 for more details on detection and characterisation with (2+1) REMPI spectroscopy), which is proportional to the guided molecular flux, decays over the course of 7 hours of

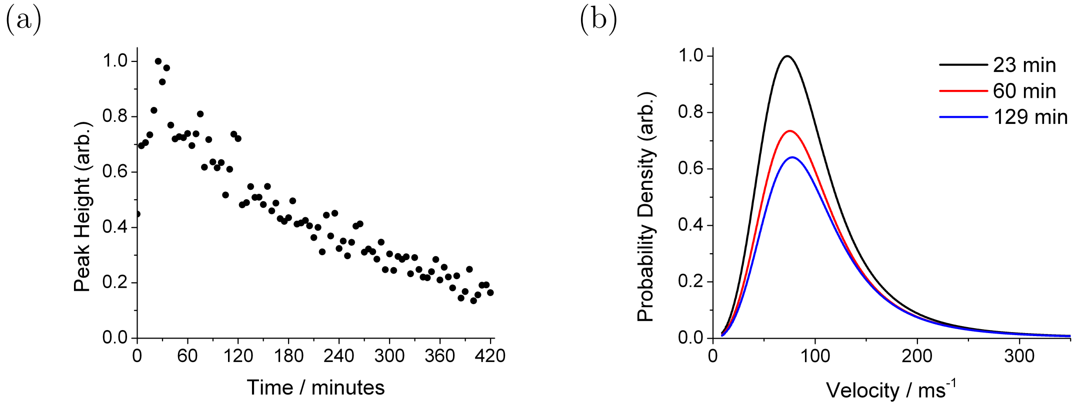

Figure 4.12: (a) The peak height of the $|J, K\rangle = |1, 1\rangle$ (2+1) REMPI signal recorded at 5 minute time intervals for standard cell conditions (1.0 sccm ND_3, 0.6 mbar helium, 6 K cell). (b) ND_3 velocity distributions calculated at three different times throughout the day for identical operating conditions (standard cell conditions).

continuous running with the standard operating conditions (1.0 sccm ND_3, 0.6 mbar helium, 6 K cell). Small shifts in the laser wavelength were corrected for by scanning across a small region near the peak rather than just recording the signal at the peak wavelength. The initial increase in signal over the first thirty minutes is likely due to steady-state or 'equilibrium' conditions being established in the cell. During this time, the molecular and buffer gas densities in various regions throughout the cell may be quite different from the steady-state conditions. Additionally, an equilibrium may need to be established between the gas phase molecules in the cell and the layer of molecular ice forming on the cell walls. After this initial equilibration period, the signal decays steadily over the seven hours of operation.

The apparatus must be warmed up to room temperature before the molecular ice melts completely and the initial flux is fully recovered. The apparatus takes about a day to warm-up. An alternative solution that locally heats the exit aperture or the buffer gas cell without placing a large heat load on the cryocooler and experimental apparatus could extend the run time of the apparatus before the long warm-up period is required. One such solution, implemented in a buffer gas cell by [91], involves attaching nichrome heater wire to a small piece of thin copper foil, which is then fixed to the Kapton film around the exit aperture. While this did extend the overall run time of the buffer gas cell, the initial flux level was not fully recovered after ice was melted from the immediate vicinity of the exit aperture.

The properties of the molecular beam leaving the buffer gas cell are significantly affected by the diameter of the exit aperture, as described in Section 2.1.4. Thus, apart from reducing the flux of molecules exiting the buffer gas cell, the reduction in the diameter of the exit aperture as a result of the ice formation also affects the properties of the buffer-gas-cooled beam. Figure 4.12(b) shows the velocity distribution of ND_3 recorded at three different times during the day for standard cell operating conditions (1.0 sccm ND_3, 0.6 mbar helium); the molecular flux is reduced while the peak velocity and thermal energy are shifted to slightly higher values (Table 4.5). Since the molecular ice formation around the exit aperture affects both the flux and velocity distribution of the buffer-gas-cooled beam, numerous runs throughout the day are required to yield a robust result, and conditions within the cell should be corrected for when possible.

Table 4.5: Parameters characterising the guided ND_3 velocity distributions are shown for identical operating conditions of the cell (standard cell conditions of 1.0 sccm ND_3, 0.6 mbar helium, 6 K cell) obtained at different times throughout the day.

Time / min.	v_p / ms^{-1}	FWHM / ms^{-1}	T_p / K	Relative flux (arb.)
23	72.78(0.09)	80.62(0.13)	6.37(0.02)	1.0
60	75.52(0.14)	83.70(0.19)	6.86(0.02)	0.76
129	77.57(0.08)	86.77(0.11)	7.24(0.01)	0.69

4.7 Application to other species: CH_3F and NH_3

ND_3 was selected for the in-depth characterisation of the molecular beam because its strong linear Stark shift is ideal for electrostatic guiding and because (2+1) REMPI spectra are easily recorded. However, this technique is generally applicable to most polar molecules; it is a versatile tool that can be used to generate cold molecular beams for a wide array of molecules.

A detailed study of the reaction $CH_3F + Ca^+ \rightarrow CH_3 + CaF^+$ at low translational temperatures has been conducted previously in the group using a room temperature source of CH_3F molecules to load the electrostatic quadrupole guide [111]. Once the buffer-gas-cooled experimental apparatus is combined with an ion trap, this will be the first target reaction studied in order to determine the effect of rotational cooling on the reaction rate. Since the optimal conditions for maximal flux of translationally and rotationally cold molecules are different for different molecules, it is important to characterise the cold molecular beam source for each molecule of interest. This is most easily done before combining with the ion trap.

Figure 4.13(a) shows the QMS signal over a range of CH_3F flow rates for the fixed buffer gas inlet pressure of 0.4 mbar. The trend is similar to ND_3 in a 6 K cell (Fig. 4.5), for which a flow rate of 1.0 sccm was found to be the optimal setting. At 1.0 sccm CH_3F, however, the run time was significantly shorter than with 1.0 sccm ND_3 (due to molecular ice formation blocking the exit aperture). Therefore, a flow rate of only 0.68 sccm is the optimal setting for CH_3F in order to extend the run time of the apparatus. Figure 4.13(b) shows the QMS signal over a wide range of inlet pressures of the buffer gas for the fixed flow rate of 0.68 sccm CH_3F. The optimal conditions for CH_3F in a 6 K cell are obtained using a 0.68 sccm flow rate of CH_3F with an inlet pressure of 0.4 mbar helium.

The velocity distributions of CH_3F show similar trends to those obtained for ND_3. For a fixed buffer gas inlet pressure, the trailing edge of the distribution is shifted to slightly higher velocities with increasing CH_3F molecular flow rate, while the leading edge remains unaffected (Fig. 4.14(a)) due to the slightly diminished effectiveness of the buffer gas cooling with the increasing amount of CH_3F entering the cell. Similar to ND_3, the velocity distributions for a range of buffer gas inlet pressures for a fixed

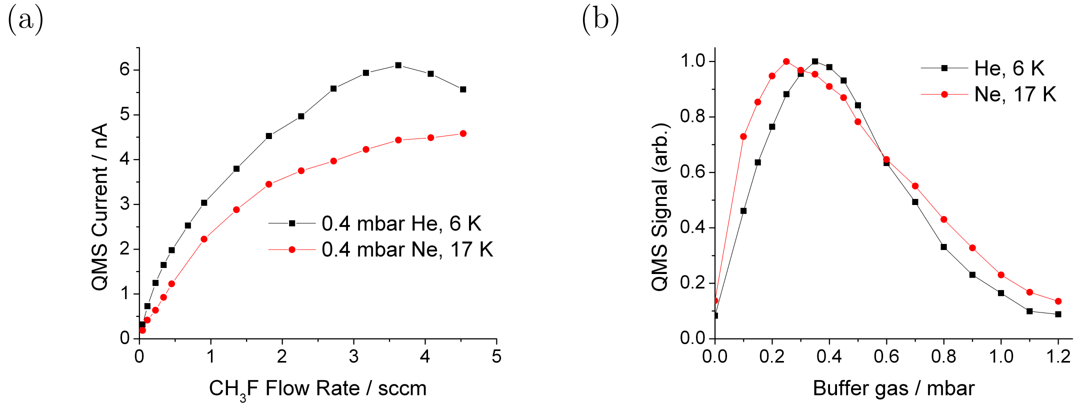

Figure 4.13: (a) The QMS signal of the guided molecules is recorded for a fixed buffer gas inlet pressure (0.4 mbar helium for the 6 K cell, 0.4 mbar neon for the 17 K cell) while varying the flow rate of CH_3F molecular gas entering the cell. (b) The CH_3F flow rate is kept constant at 0.68 sccm over a range of buffer gas inlet pressures, shown for helium in the 6 K cell and neon in the 17 K cell with a guide voltage of ±5 kV.

flow rate of CH_3F (Fig. 4.14(b)) reflect the effect of velocity boosting. At low buffer gas densities in the cell, increasing the amount of buffer gas increases the efficiency of buffer gas cooling and causes the trailing edge of the velocity distribution to shift to lower velocities without significantly affecting the leading edge. For intermediate buffer gas densities, the slowest molecules in the cell (which spend a longer time near the exit aperture) are boosted to higher velocities, causing the leading edge of the distribution to shift to higher velocities without significantly affecting the trailing edge. Both the leading and trailing edges of the distribution are shifted to higher velocities for large buffer gas densities in the cell, when most of the molecules exiting the cell experience velocity boosting toward the thermal velocity of the light buffer gas.

Reducing the voltage applied to the guide electrodes significantly reduces the translational temperature of the guided molecules (Fig. 4.14(c)), shifting the trailing edge of the velocity distribution to much lower velocities. However, this is achieved at the expense of molecular flux. The velocity distributions obtained for a 6 K helium cell and a 17 K neon cell (Fig. 4.14(d)) demonstrate that the translational temperature of the resulting molecular beam of CH_3F are comparable using either set-up. This

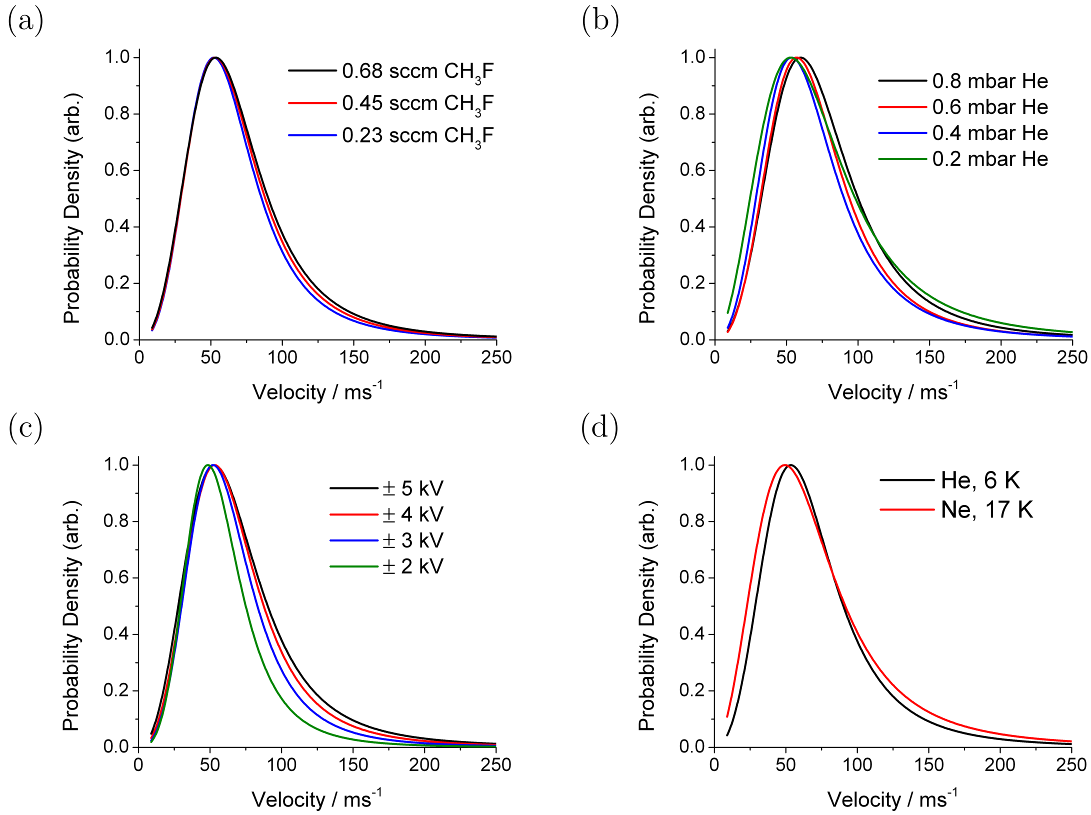

Figure 4.14: CH_3F velocity distributions for a wide range of buffer gas cell conditions. (a) Different CH_3F molecular flow rates for the fixed buffer gas inlet pressure of 0.4 mbar helium in a 6 K cell. (b) Different buffer gas inlet pressures for a fixed CH_3F flow rate of 0.68 sccm in a 6 K cell. (c) Varying the voltage applied to the guide electrodes for a fixed CH_3F flow rate of 0.68 sccm, with a buffer gas inlet pressure of 0.4 mbar helium in a 6 K cell. (d) The black (red) line shows the velocity distribution of CH_3F for a flow rate of 0.68 sccm in a 6 K (17 K) cell with an inlet pressure of 0.4 mbar helium (neon).

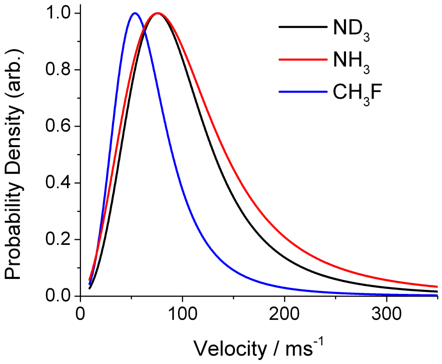

Figure 4.15: Velocity distributions for different molecular gases in a 6 K helium buffer gas cell. The optimal conditions differ for each molecular gas: 1.0 sccm flow rate and inlet pressure of 0.6 mbar helium for ND_3 and NH_3; and 0.68 sccm flow rate and inlet pressure of 0.4 mbar helium for CH_3F.

provides a nice tool to investigate the effect of rotational cooling on reactions of CH_3F because although the translational temperature is similar for the 6 K helium and the 17 K neon buffer gas cell, the rotational temperature is significantly greater in the 17 K cell (as demonstrated for ND_3 in Chapter 5). Similar trends were found in the CH_3F velocity distributions for changing molecular and buffer gas densities using a 17 K neon buffer gas cell.

Figure 4.15 compares the velocity distributions (obtained using the optimal settings determined for each molecule) for ND_3 (1.0 sccm flow rate, 0.6 mbar helium), NH_3 (1.0 sccm flow rate, 0.6 mbar helium) and CH_3F (0.68 sccm flow rate, 0.4 mbar helium) in a 6 K buffer gas cell. The mass of the molecule has a large impact on the cut-off velocity achieved by the guide. CH_3F has a significantly lower cut-off velocity than ND_3 or NH_3 due to its much larger mass. Since ND_3 is only 3 amu heavier than NH_3, there is only a small shift in the ND_3 cut-off velocity to lower values compared to NH_3.

4.8 Summary

A detailed characterisation of the cold molecular beam using mass spectrometry has been described in this chapter. The effect of various conditions within the buffer gas cell on the molecular flux was studied by applying a continuous voltage to the electrostatic guide electrodes. The impact on the velocity distributions and thermal energy of the molecular beam was investigated by pulsing the guide off and on and recording the arrival time of the molecules at the mass spectrometer. A colder sample of molecules can be achieved by lowering the voltage applied to the electrodes, but this also reduces the molecular flux.

The molecular beam properties can be altered by changing the molecular and buffer gas densities within the cell. Higher molecular flow rates lead to increased molecular flux, but also slightly higher translational temperatures due to less effective buffer gas cooling. Increasing the buffer gas density increases the efficiency of cooling, and initially leads to increased molecular flux and colder beams. However, the effects of velocity boosting at high buffer gas densities ultimately leads to higher velocity distributions and a lower guided flux of molecules. The additional constraint for determining the optimal conditions for the buffer gas cell is the run time of the experiment, which is limited by molecular ice formation blocking the exit aperture.

The optimal conditions for ND_3 in a 6 K buffer gas cell are a flow rate of 1.0 sccm and a helium inlet pressure of 0.6 mbar. A higher molecular gas flow rate would increase the molecular flux, but would also limit the run time and efficiency of both translational and rotational cooling. Larger amounts of buffer gas would increase the run time of the apparatus and enhance the efficiency of rotational cooling, but at the expense of increased velocity boosting and a lower molecular flux. Overall, the changes in the velocity distributions are quite small for the range of experimental parameters used.

The electrostatic extraction of buffer-gas-cooled beams is a general technique that can be used to produced a cold source of a wide variety of molecules, such as NH_3 and CH_3F. The optimal conditions for NH_3 are the same as for ND_3, while the optimal conditions for CH_3F are a flow rate of 0.68 sccm and a helium inlet pressure of 0.4 mbar. When the buffer gas apparatus is combined with a linear Paul ion trap to study chemical reactions, the run time of the apparatus also needs to be balanced against the slower reaction at lower fluxes.

The thermal velocity of neon at 17 K is actually slightly lower than the thermal velocity of helium at 6 K because it is much heavier than helium. Due to the effects of velocity boosting, this means that the molecular beam produced by a 6 K helium buffer gas cell has a similar translational temperature to a beam produced by a 17 K neon buffer gas cell. The rotational temperature of the molecular beam, however, is significantly higher in the 17 K neon buffer gas cell. This provides an excellent opportunity to explore the effect of rotational cooling on reaction rates when the experimental apparatus is eventually combined with an ion trap. A detailed characterisation of the rotational state distributions of the molecular beam using (2+1) REMPI is presented in the next chapter.

Chapter 5

Characterisation of the cold molecular beam using (2+1) REMPI

After the translational temperature and guided flux of the molecular beam was fully characterised using mass spectrometry, as described in Chapter 4, resonance-enhanced multiphoton ionisation (REMPI) was used to establish the rotational state distribution of the molecular beam. A brief description of REMPI spectroscopy is provided in Section 5.1, while Section 5.2 details the modifications that were made to the experimental apparatus to convert from mass spectrometry to REMPI detection. The rest of the chapter focuses on the (2+1) REMPI spectra of cold molecular beams of ND_3, with the REMPI spectra of NH_3 and the ammonia isotopologues NHD_2 and NH_2D also shown in Section 5.5.

5.1 Principles of REMPI Spectroscopy

Multiphoton excitations of isolated gas phase molecules can reveal detailed information about the excited electronic states and ground state of the molecule, including the structure, energetics and reactivity of these states. A model (2+1) resonance-enhanced multiphoton ionisation (REMPI) scheme is shown in Figure 5.1. In this example, the molecular species, M, is initially in its ground state $|1\rangle$. For the case illustrated, given photons with frequency between ν_1 and ν_3, at least three such photons must be absorbed for species M to be ionised. The probability of a three-photon absorption (and resulting ionisation) increases significantly when there is a real excited state of the neutral molecule, $|2\rangle$, resonant in energy with two absorbed photons $E = 2h\nu_2$; thus, this example would be referred to as (2+1) REMPI. In other situations, an excited state might be resonant with one or three absorbed photons, and this would be known as (1+1) or (3+1) REMPI. Note that you can also have (2+2) or even (1+2) REMPI in principle, if two photons are required to ionise the resonant state.

For (2+1) REMPI, there are two additional requirements for enhanced ionisation to be observed at the excitation frequency ν_2. First, there must be a non-zero transition probability for the $|2\rangle \leftarrow |1\rangle$ two-photon excitation. Second, the excited state $|2\rangle$ must be relatively stable, so that the final one-photon ionisation step will proceed with reasonable probability relative to the decay of the excited state. The (2+1) REMPI spectrum can then be obtained by varying the excitation wavelength and measuring the resulting ion yield [188].

The multiphoton transition operator $\hat{\mathrm{O}}$ is represented by the qth component of the spherical tensor of rank k, $\mathrm{T}^k_q(\hat{\mathrm{O}})$. The product of the irreducible representations for the wavefunctions of states $|1\rangle$ and $|2\rangle$ and of the transition operator must contain the totally symmetric representation in order for the $|2\rangle \leftarrow |1\rangle$ transition to be allowed. In other words, the transition moment $\langle 2|\mathrm{T}^k_q(\hat{\mathrm{O}})|1\rangle$ must be non-zero.

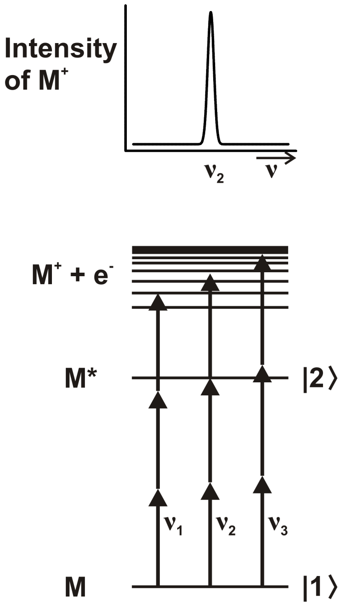

Figure 5.1: A schematic illustration of a model (2+1) REMPI scheme. Ionisation of the molecular species, M, is enhanced at frequency ν_2 where absorption of two photons excites the molecule from its ground state $|1\rangle$ to an intermediate state $|2\rangle$. Ionisation occurs when a third photon is absorbed by the species in the intermediate state $|2\rangle$. Modified from [188].

Due to symmetry considerations, one-photon transitions involve components of rank 1, while two-photon transitions involve components of rank $k = 0$ and/or 2, and three photon transitions involve components of rank $k = 1$ and 3. Furthermore, two-photon transitions of rank $k = 0$ must involve a transition between states of the same symmetry. In this thesis, the (2+1) REMPI detection of ND_3 involves the $\tilde{B}^1E''(\nu_2 = 5) \leftarrow \tilde{X}(1)$ transition. The relevant spherical tensor rank is $k = 2$ because the process is a two-photon transition and the ground and excited states are of different symmetry (C_{3v} and D_{3h}, respectively). The component of the spherical tensor is $q = \pm 1$ because the excited electronic state is doubly degenerate E″ [188].

Transitions forbidden in one-photon spectroscopy may be permitted in multiphoton excitations, leading to population in previously inaccessible excited states. Additionally, excited states may lie at energies that are technically difficult to reach in one-photon absorption but are easily accessible using visible or near ultraviolet photons in multiphoton absorption. Multiphoton cross-sections tend to be extremely small, however, since two or more photons must be absorbed by the same molecule. Typical values for cross-sections are 10^{-17} cm^2, 10^{-50} cm^2, and 10^{-84} cm^2 for one-, two-, and three-photon absorptions, respectively [188]. Despite the small cross-sections, multiphoton transitions are frequently achieved using high intensity light sources such as focused, tunable dye lasers with nanosecond pulses.

Intermediate $\tilde{\mathrm{B}}$ state of ND_3

Extensive spectroscopic studies have been undertaken on ND_3, yielding a considerable amount of information about the ground and excited states of the molecule [189, 190]. Nitrogen's doubly occupied $3\mathrm{a}_1$ lone pair orbital gives ground-state ammonia its pyramidal $C_{3\mathrm{v}}$ structure. REMPI spectroscopy relies on resonant intermediate states being sufficiently long-lived such that there is a reasonable likelihood of absorbing a final photon and ionising. Most of the favourable intermediate states are Rydberg excited states, in which one electron from the $3\mathrm{a}_1$ ground state orbital is promoted to a Rydberg orbital with $n \geq 3$. The Rydberg orbital is large and spatially diffuse while the nuclei and other valence electrons form a positive ion core. These excited states have planar $D_{3\mathrm{h}}$ equilibrium geometries like the NH_3^+ ion.

As a consequence of the change in geometry from the pyramidal ground state to the planar excited state, the electronic transition occurs by the excitation of the out-of-plane bending mode, ν_2. The ensuing long vibronic progression leads to a complex spectrum. Multiphoton studies of supersonic beams with internally cooled molecules yield simplified spectra that have been crucial in the spectral assignment of numerous rovibrational states of ammonia [190, 191].

Excitation of an electron from the $3\mathrm{a}_1$ ground state of ammonia to a mixed Rydberg ($3\mathrm{s}\sigma$)/anti-bonding valence (σ^*) orbital produces the first excited singlet state of ammonia, the $\tilde{\mathrm{A}}^1\mathrm{A}_2''$ state. Almost all levels of the $\tilde{\mathrm{A}}$ state of ammonia have very short lifetimes (sub-picosecond) [192], however, which makes this state ill-suited for REMPI spectroscopy. Many studies of ammonia involve the $\tilde{\mathrm{C}}' \leftarrow \tilde{\mathrm{X}}$ transition instead. However, the predissociation rate of the $\tilde{\mathrm{C}}'$ state increases with larger ν_2' quantum numbers, and within a given ν_2' level the rate increases with the amount of rotation about the in-plane (x, y) axes by the parent molecule [193].

The singlet excited electronic state $\tilde{\mathrm{B}}^1\mathrm{E}''$ lies at an energy just below the $\tilde{\mathrm{C}}'$ origin. In the $\tilde{\mathrm{B}} \leftarrow \tilde{\mathrm{X}}$ system, the electron is promoted from the $3\mathrm{a}_1$ orbital in the pyramidal ground state to the $3\mathrm{pe}'$ orbital in the planar excited state in both ND_3 and NH_3. All ν_2' levels of the ND_3 $\tilde{\mathrm{B}}$ state with bending vibrational quantum number $\nu_2' \leq 6$ have a lifetime of ~ 0.25 ns, independent of the rotational level [191]. The longer lifetime of the intermediate state $\tilde{\mathrm{B}}$ compared to $\tilde{\mathrm{A}}$, and the rate of predissociation of the intermediate state being independent of rotational level, are some advantages of using the $\tilde{\mathrm{B}} \leftarrow \tilde{\mathrm{X}}$ transition in ND_3.

All rotational levels of the lower component of the inversion doublet $\tilde{\mathrm{X}}(0)$ are HFS, and will not be guided by the electrostatic quadrupole guide [194]. All rotational levels of the upper component $\tilde{\mathrm{X}}(1)$ however, are LFS and may be guided. Furthermore, excitation from the $\tilde{\mathrm{X}}(1)$ level of the ground state will only occur to odd vibrational levels in the ν_2 progression, which have the required E' symmetry [194]. In this work, the $\tilde{\mathrm{B}}^1\mathrm{E}''(\nu_2' = 5) \leftarrow \tilde{\mathrm{X}}(1)$ transition was used in the (2+1) REMPI spectroscopy study of ND_3.

5.2 Experimental apparatus - REMPI modifications

The buffer-gas-cooled molecules exiting the buffer gas cell are guided away from the cell, out of the main cryogenic chamber, and finally delivered to the detection chamber by the quadrupole guide. The molecules are ionised after exiting the electrostatic guide, and then accelerated and focused onto microchannel plates (MCPs) for de-

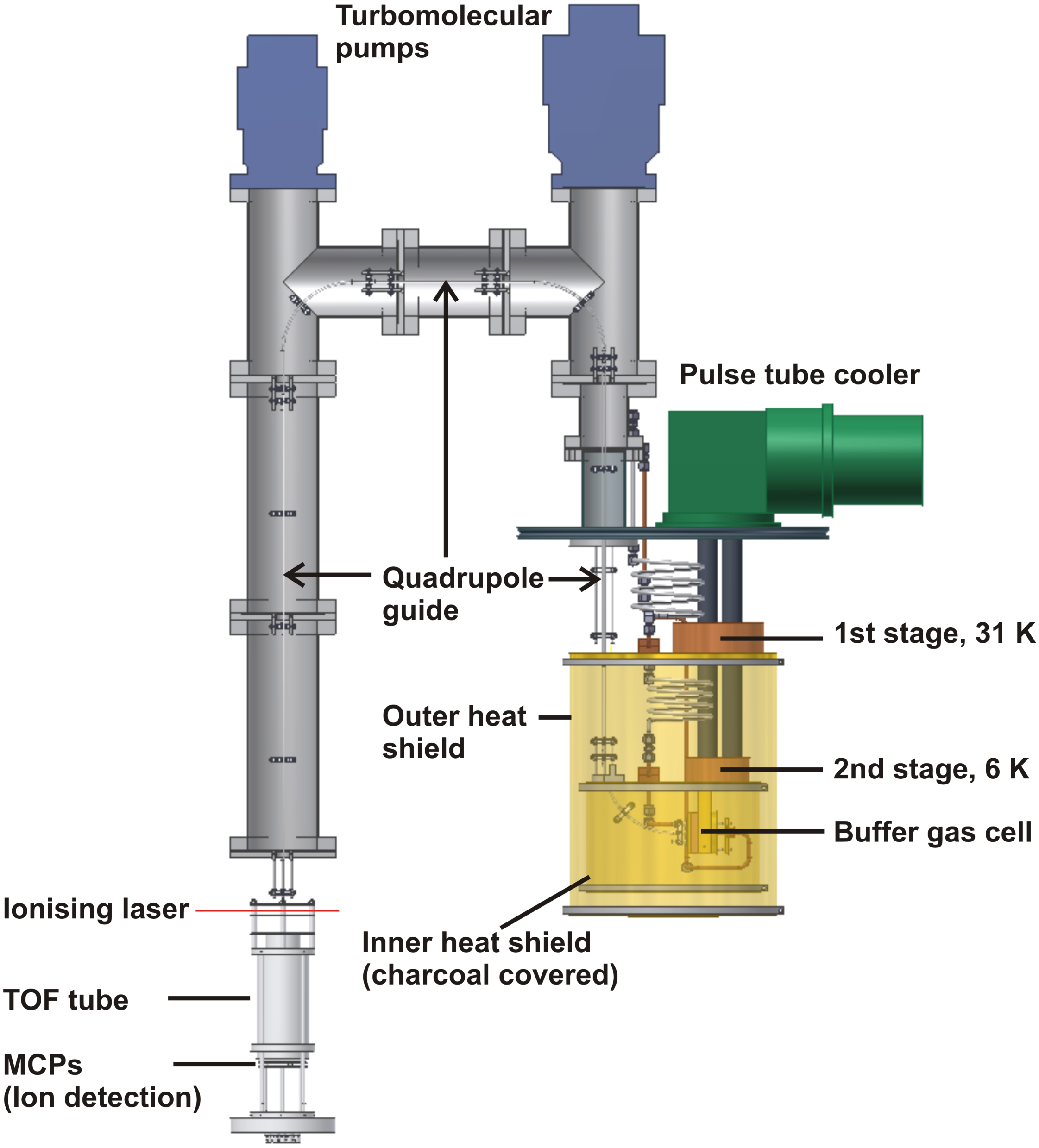

Figure 5.2: Design of the experimental apparatus showing detection with REMPI after three bends of the guide.

tection. The ion detection set-up is based on a Wiley-McLaren time-of-flight mass spectrometer (TOF-MS) [195].

The TOF-MS consists of three plates (repeller, extractor, and ground plate) held at different voltages, a field free drift tube, and MCPs for detecting the ions (Fig. 5.3).

A large hole in the centre of each plate permits the molecules or ions to pass through the different regions. Fine mesh (85% transmission) covers the holes, and is glued in place with conducting silver epoxy. The first plate (repeller plate) is positioned 6 mm away from the end of the electrostatic guide. Molecules exit the guide, pass through the repeller plate, and enter the ionisation region. Typical voltages applied to the TOF-MS plates and MCPs are given in Table C.1, and more details on the TOF-MS are provided in Appendix C.

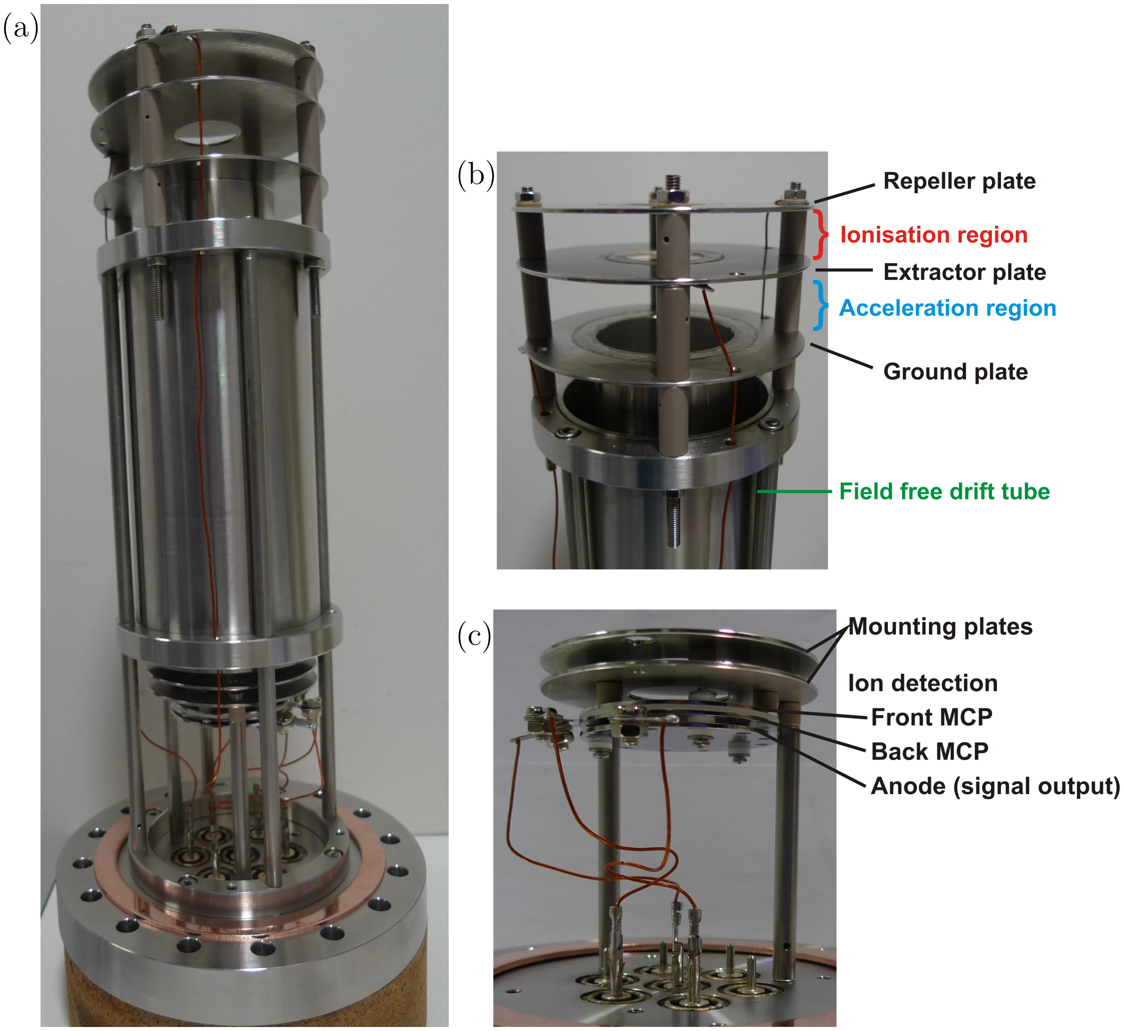

Figure 5.3: The molecular ions are detected using a time-of-flight mass spectrometer (TOF-MS) pictured here. The cold molecules exit the guide and enter the ionisation region of the TOF-MS, where a tunable dye laser ionises the molecules using a (2+1) REMPI scheme. The ions are then accelerated toward and detected by the MCPs, located at the base of the field free drift tube.

A 532 nm frequency doubled ND:YAG laser (Continuum SL III - 10, Electro-Optics Inc.) is used to pump a dye laser (Sirah CSTR-D-2400; DCM dye in ethanol) which is frequency doubled using a BBO crystal to reach UV wavelengths. Laser pulse energies of up to 10 mJ per pulse (UV, measured immediately before the chamber) are generated at a repetition rate of 10 Hz. A 30 cm focal length lens is used to focus the laser beam onto the molecular beam as it passes between the repeller and extractor plates (ionisation region of the TOF-MS).

Once the ions have formed in the ionisation region, they are accelerated toward the ion detector by a series of constant electric fields, one generated between the repeller and extractor plate, and the other between the extractor and ground plate. This arrangement is referred to as a Wiley McLaren TOF-MS; see Appendix C for more information. The charge-to-mass ratio (q/m) of the ions determines their velocity in the field free drift tube. For singly charged ions, the lightest ions reach the detector first, followed by heavier ions. The ion signal for the desired q/m ratio can be isolated by gating the detector output at the appropriate arrival time. The arrival time is generally proportional to the square root of the mass, assuming all ions have an equal increase in kinetic energy on acceleration. The ions are detected by sensitive microchannel plates (P/N 31373, Photonis) with a 25 mm diameter detection area.

5.3 PGOPHER simulations

REMPI is a powerful tool in gas-phase molecular spectroscopy and can provide a large amount of information about the ground and excited states of a molecule. However, while REMPI spectra may be relatively simple for small molecules, spectra rapidly become very complex as the size of the molecule increases. A simulation of the REMPI spectrum for the $\tilde{\mathrm{B}}^1\mathrm{E}''(\nu_2' = 5) \leftarrow \tilde{\mathrm{X}}(1)$ transition of ND_3 at 300 K is shown in Figure 5.4. The simulation was generated using PGOPHER [196], which is a program written and maintained by the group of Dr. Colin Western at the University of Bristol to simulate rotational, vibrational and electronic spectra. The rotational constants used for the ground and excited states of ND_3 were obtained from [197] and [198], respectively, and are shown in Table 5.1.

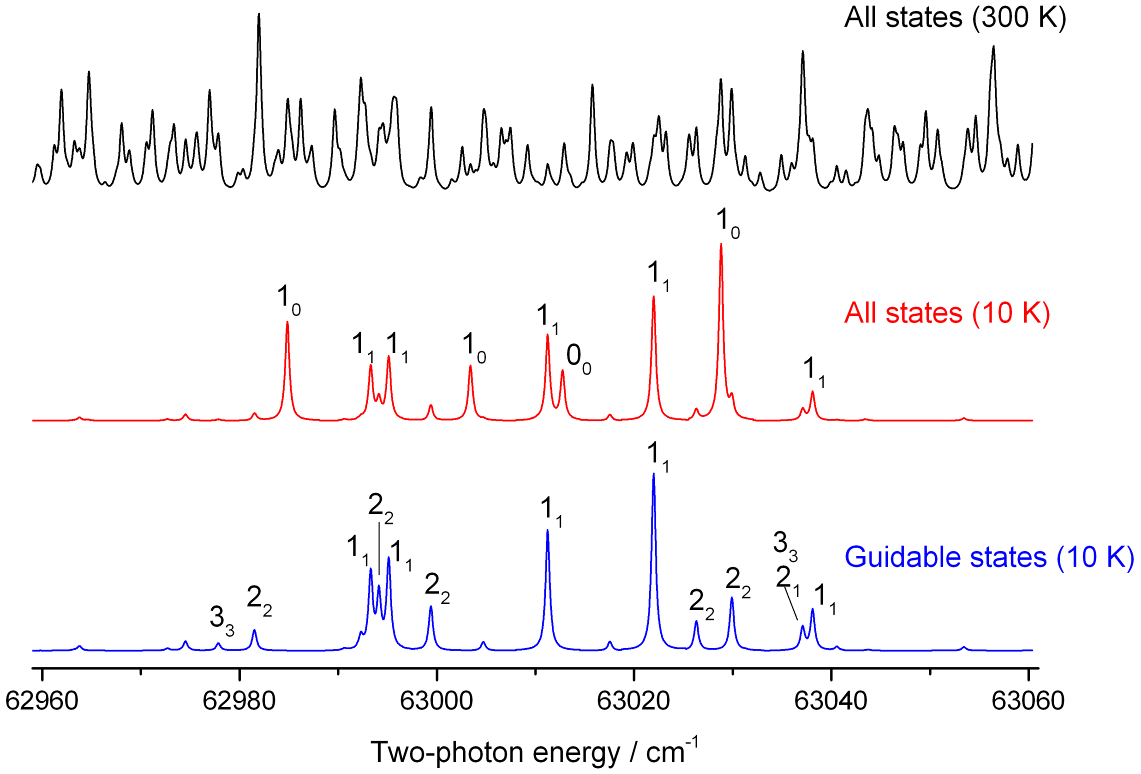

Figure 5.4: A PGOPHER simulation of the $\tilde{B}^1E''(\nu_2' = 5) \leftarrow \tilde{X}(1)$ transition of ND_3 for a 300 K (top panel, black) and 10 K (mid panel, red) thermal distribution of rotational states. The bottom panel (blue) shows a simulation of the spectrum obtained for a 10 K source of molecules, but only including the guidable states weighted according to how well they are guided (input as ground state populations in PGOPHER). Rotational states are designated by J_K.

The REMPI spectrum of a molecule even as small as ND_3 is remarkably complex at 300 K, due to the large number of rotational states that are populated. Supersonic beams that generate rotationally cold molecules are therefore often used in REMPI spectroscopy to reduce the complexity of the spectra. The PGOPHER simulations of

ND_3 at 300 K and 10 K shown in Figure 5.4 clearly illustrate the advantage of using rotationally cold molecular beams in REMPI spectroscopy.

As described in Section A.1, the Stark shift of a molecule depends on its rotational state. Therefore, the PGOPHER simulations cannot be compared directly with the REMPI spectra obtained experimentally because the molecules exiting the guide will not represent a thermal distribution of rotational states. Rotational states with strong Stark shifts are well guided and a larger fraction of those molecules will reach the end of the guide compared to rotational states with weak Stark shifts. Rotational states that do not exhibit a Stark shift, or are high-field seeking states (increasing Stark energy for decreasing electric field strength) are not guided at all and will be absent in the distribution of molecules at the end of the guide.

Instead, Equation 2.12 is used to determine the rotational state distribution of the ND_3 molecules exiting the buffer gas cell for a given temperature. The rotational state population is then multiplied by a 'guidability factor' determined from the Monte Carlo simulations of the guiding process (Section 2.4.6). The guidability factor for a specific rotational state is the fraction of molecules in that state that are successfully

Table 5.1: Rotational constants for the ground electronic state $\tilde{X}(1)$ and the $\tilde{B}^1(\nu_2' = 5)$ excited state of ND_3, as reported in [197] and [198], respectively. All parameters are in cm^{-1}, except for ζ which is dimensionless.

Ground state		Excited state	
B	5.1427599	B	4.4829
C	3.1141819	C	2.6949
D_J	1.978×10^{-4}	D_J	381×10^{-6}
D_{JK}	-3.490×10^{-4}	D_{JK}	-1209×10^{-6}
D_K	2.001×10^{-4}	D_K	789×10^{-6}
H_{JJJ}	2.32×10^{-8}	q_+	0.1589
H_{JJK}	-6.60×10^{-8}	q_-	0.1589
H_{JKK}	7.20×10^{-8}	ζ	0.8311
H_{KKK}	0	Origin	62992.580

guided at a given temperature. Table 2.6 lists the guidability factor for all low-field seeking rotational states with $J \leq 5$. The rotational state distribution of the molecules at the end of the guide (calculated from the initial population before guiding and the guidability factor of each state) can then be input into PGOPHER as the ground state population distribution of ND_3, to provide a simulation of the experimental REMPI spectra.

It should be noted that the ortho and para states of ND_3 do not interchange by collisions with the buffer gas (the states only mix through molecule-molecule D atom exchange collisions) and will thermalize separately to different equilibrium rotational states. Nevertheless, excellent agreement between the simulations (obtained assuming the same rotational temperature for both ortho and para components, and the ortho to para ratio is the statistical equilibrium value of 1.0) and the experimental spectra indicates that the difference in rotational temperature between the ortho and para states is minimal under our conditions.

With only select $|J, K\rangle$ rotational states being guided, the molecular beam at the end of the guide does not represent a thermal equilibrium distribution of rotational states, and cannot be defined by a rotational temperature. However, it is a useful term to use for comparing the rotational energy of the molecular beam generated under different buffer gas cell conditions. When the term 'rotational temperature' is used in this work, it specifically refers to the thermal equilibrium distribution of rotational states of the molecules exiting the buffer gas cell before electrostatic guiding. More generally, it also describes the rotational energy of the molecular beam after the electrostatic guide, when the actual rotational state distribution will be influenced by the 'guidability' of each rotational state.

The middle panel of Figure 5.4 shows the PGOPHER simulation of the REMPI spectrum of ND_3 for a 10 K thermal distribution of rotational states. The bottom panel shows the simulation for a distribution of rotational states that would be expected at the end of the quadrupole guide, assuming the molecules exiting the buffer gas cell were at a rotational temperature of 10 K.

The optimal conditions for a 6 K buffer gas cell are a flow rate of 1.0 sccm of ND_3 with a helium pressure of 0.6 mbar at the buffer gas inlet to the cell, with a ± 5 kV voltage applied to the quadrupole electrodes. These parameters were determined using mass spectrometry analysis of the molecular beam, as described in Chapter 4, and represent a compromise between producing a high flux of molecules with a low translational temperature, while ensuring a reasonable experimental run time before the exit aperture of the buffer gas cell becomes blocked with molecular ice.

Figure 5.5 shows the REMPI spectrum obtained when operating the 6 K buffer gas cell at these optimal settings. The inverted spectrum shows the PGOPHER simulation of guidable states reaching the end of the quadrupole, for a molecular source with a rotational temperature of 10 K. The relative population of the $|J, K\rangle$ rotational states, as established from the simulation, is provided in Table 5.2. This suggests that although the buffer gas cell is held at 6 K, the ND_3 molecules exiting the cell and entering the electrostatic guide are actually at a rotational temperature of approximately 10 K. The lowest rotational temperature that can be achieved by operating the cell with a very low ND_3 flow rate and large buffer gas inlet pressure is approximately 8 K, which is still slightly higher than the cell temperature. This has been observed in other groups working with buffer gas cells, and it has been suggested that the large region of Kapton film used to make the exit aperture in the back wall of the cell may contribute to the elevated rotational temperature of molecules leaving the cell [199].

Changing the molecular and buffer gas densities in the cell affects both the translational temperature (Section 4.4) and rotational temperature of the molecules exiting the cell. REMPI spectroscopy is used to analyse the rotational state distribution of the ND_3 molecular beam for a wide range of cell conditions in the next section (Section 5.4). As the rotational distribution is unaffected by the voltage applied to

Table 5.2: Relative population of the $|J, K\rangle$ rotational states as established from the simulations of the (2+1) REMPI spectra of ND_3 and NH_3 with a 6 K and 17 K buffer gas cell at the optimal settings.

	ND_3		NH_3	
$\|J, K\rangle$	6 K Cell	17 K Cell	6 K Cell	17 K Cell
$\|0, 0\rangle$	0	0	0	0
$\|1, 0\rangle$	0	0	0	0
$\|1, 1\rangle$	0.731	0.523	0.896	0.632
$\|2, 0\rangle$	0	0	0	0
$\|2, 1\rangle$	0.0242	0.0465	5.12×10^{-3}	0.0217
$\|2, 2\rangle$	0.218	0.313	0.0941	0.251
$\|3, 0\rangle$	0	0	0	0
$\|3, 1\rangle$	1.86×10^{-4}	0.0125	1.64×10^{-4}	3.44×10^{-4}
$\|3, 2\rangle$	1.98×10^{-3}	1.57×10^{-3}	5.55×10^{-6}	6.41×10^{-3}
$\|3, 3\rangle$	0.0242	0.0941	4.68×10^{-3}	0.0848
$\|4, 0\rangle$	0	0	0	0
$\|4, 1\rangle$	3.32×10^{-7}	2.01×10^{-5}	1.01×10^{-9}	2.26×10^{-6}
$\|4, 2\rangle$	4.10×10^{-6}	1.86×10^{-4}	4.15×10^{-8}	5.85×10^{-5}
$\|4, 3\rangle$	5.38×10^{-5}	1.50×10^{-3}	1.40×10^{-6}	9.09×10^{-4}
$\|4, 4\rangle$	4.94×10^{-4}	7.01×10^{-3}	1.43×10^{-5}	3.16×10^{-3}
$\|5, 0\rangle$	0	0	0	0
$\|5, 1\rangle$	1.42×10^{-10}	1.01×10^{-7}	2.94×10^{-14}	5.79×10^{-9}
$\|5, 2\rangle$	1.96×10^{-9}	1.05×10^{-6}	1.58×10^{-12}	1.96×10^{-7}
$\|5, 3\rangle$	2.76×10^{-8}	9.07×10^{-6}	6.12×10^{-4}	3.51×10^{-6}
$\|5, 4\rangle$	2.62×10^{-7}	4.38×10^{-5}	6.60×10^{-10}	1.29×10^{-5}
$\|5, 5\rangle$	5.18×10^{-6}	3.62×10^{-4}	2.21×10^{-8}	1.08×10^{-4}

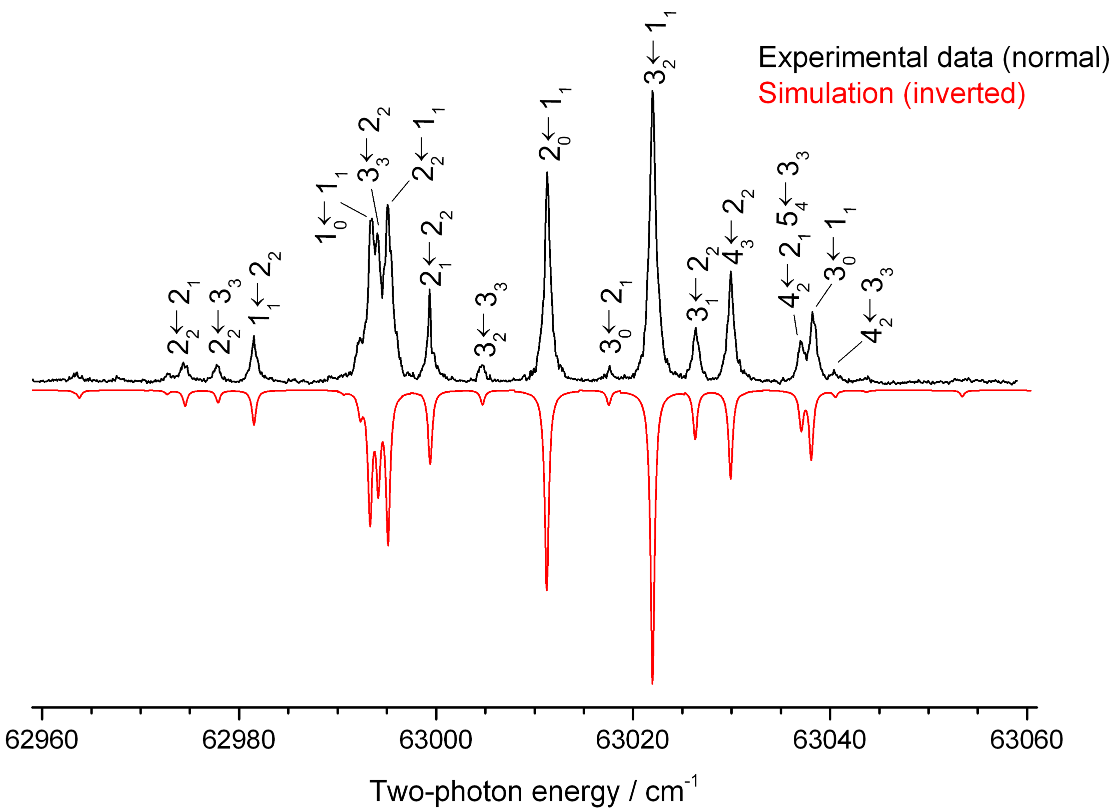

Figure 5.5: (2+1) REMPI spectrum for the $\tilde{B}\,^1E''(\nu_2' = 5) \leftarrow \tilde{X}(1)$ transition in ND_3, recorded following buffer gas cooling and electrostatic velocity selection for a 6 K buffer gas cell at the optimal settings (1.0 sccm ND_3, 0.6 mbar He). The inverted spectrum (red) shows the PGOPHER simulation for the guidable rotational states of ND_3 from a 10 K thermal distribution.

electrodes (results not shown), all REMPI spectra are collected at a voltage of ± 5 kV.

5.4 Rotational state distributions for different cell conditions

As shown in Figure 5.5, the rotational temperature of ND_3 molecules exiting a 6 K cell under standard conditions (1.0 sccm ND_3, 0.6 mbar He) is approximately 10 K. Although only the lowest few rotational states are populated at 10 K, the relative population of these states can change considerably for only small changes in the rotational temperature. Figure 5.6 shows the thermal population of rotational states with $J \leq 5$ for ND_3 as a function of temperature. Small changes to the rotational temperature can be achieved by changing the amounts of molecular and buffer gas present in the cell, as described in Section 5.4.1 and Section 5.4.2 respectively. Removing the outer heat shield so that the buffer gas cell only reaches 17 K will also change the rotational temperature of the molecules exiting the cell, as described in Section 5.4.3.

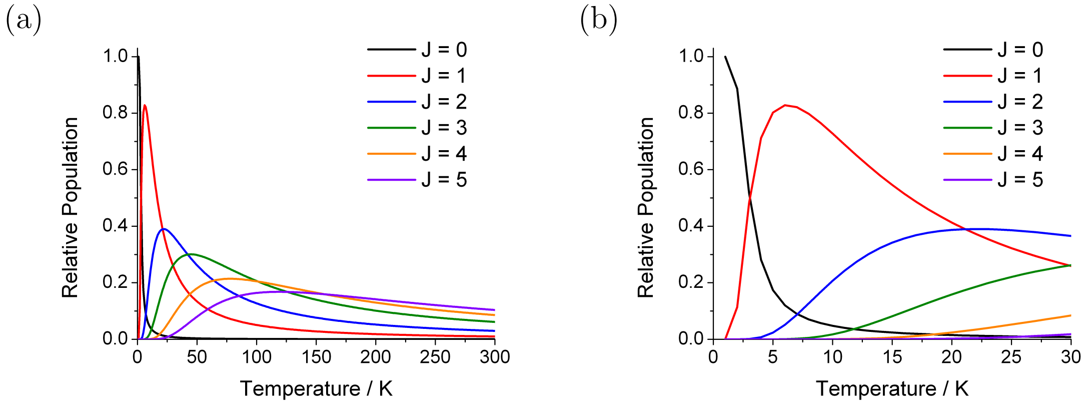

Figure 5.6: Calculated ND_3 thermal rotational populations as a function of temperature, assuming the same rotational temperature for both ortho and para components, and the ortho-to-para ratio is the statistical equilibrium value of 1.0.

5.4.1 Molecular gas flow rate

For a fixed buffer gas density in the cell, the degree of rotational cooling decreases as the amount of molecular gas entering the cell increases. The molecules will exit the cell with a higher rotational temperature, and the relative population of the rotational states will shift toward higher energy states. The middle panel of Figure 5.7 shows the REMPI spectrum of ND_3 obtained for standard 6 K cell conditions (1.0 sccm ND_3, 0.6 mbar He) while the top panel shows the spectrum obtained for the same helium inlet pressure but with twice the flow rate of ND_3 entering the cell (2.0 sccm ND_3, 0.6 mbar He). The intensity of the peaks arising from the $J_K = 3_3$ rotational state can be seen to increase significantly compared to peaks arising from the 1_1 and 2_2 rotational states. This indicates that the ND_3 molecules exiting the buffer gas cell with the higher molecular gas flow rate have a higher rotational temperature.

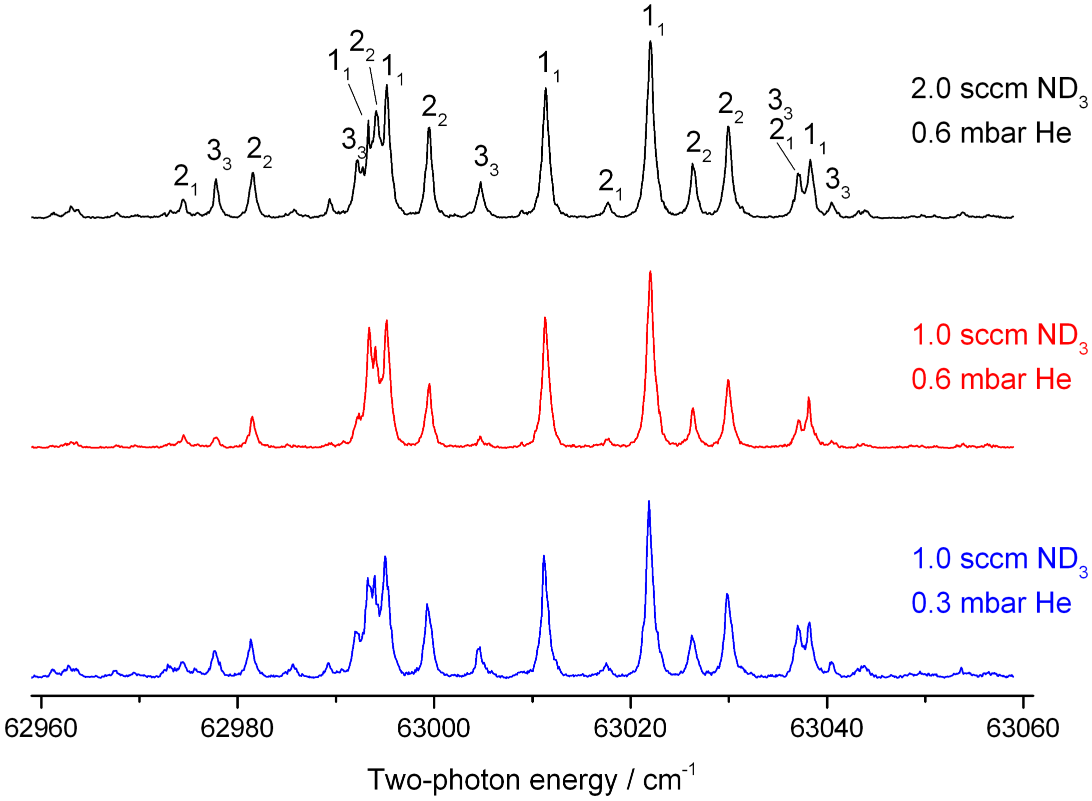

Figure 5.7: The middle (red) panel shows the REMPI spectrum of ND_3 for standard 6 K cell conditions (1.0 sccm ND_3, 0.6 mbar He). The top (black) panel shows the spectrum obtained when the molecular gas flow rate is doubled while keeping the buffer gas inlet pressure fixed (2.0 sccm ND_3, 0.6 mbar He). The bottom (blue) panel shows the spectrum obtained when the buffer gas inlet pressure is halved while keeping the molecular gas flow rate fixed (1.0 sccm ND_3, 0.3 mbar He).

A selected region of the ND_3 REMPI spectrum (from 62995 to 63045 cm^{-1}) is analysed for molecular gas flow rates ranging from 0.25 sccm to 3.5 sccm. The helium inlet pressure is kept fixed at 0.6 mbar. There is insufficient signal for flow rates lower than 0.25 sccm, while the signal becomes unstable with a severely limited run time due to molecular ice formation for flow rates higher than 3.5 sccm. The ND_3 REMPI spectra obtained at four different flow rates, all at the fixed helium inlet pressure of 0.6 mbar, are shown in Figure 5.8(a). The intensities of the 2_2 and 3_3 peaks clearly increase relative to the 1_1 peaks as the molecular flow rate increases across the four scans, as expected for molecules exiting the cell with higher rotational temperatures.

The heights of various peaks in the REMPI spectrum of ND_3, relative to the main 1_1 peak at 63021.95 cm^{-1}, are plotted against the molecular gas flow rate in Figure 5.8(c). As expected, the height of the 1_1 peak at 63038.11 cm^{-1} remains constant relative to the main 1_1 peak at 63021.95 cm^{-1}. The height of the 2_2 peaks increase over the entire range of molecular gas flow rates examined, shown for the peaks at 62999.42 and 63029.92 cm^{-1}.

Examination of the 3_3 peak at 63004.72 cm^{-1} shows there is almost no population of the $J = 3$ rotational state for the lowest flow rates of ND_3. Under these buffer gas cell conditions, the molecules exit the cell with rotational temperatures around 9 K. As the rotational temperature of the molecules increases along with the molecular flow rate, the $J = 3$ state gradually becomes populated and the 3_3 peak becomes visible. The peak height increases slowly at first and then more rapidly as the molecular flow rate and rotational temperature increases. This is consistent with the calculated thermal rotational populations shown in Figure 5.6.

The doublet peak composed of the 3_3 peak at 63037.07 cm^{-1}, the 2_1 peak at 63037.10 cm^{-1}, and the 1_1 peak at 63038.11 cm^{-1} clearly illustrates the changing rotational state populations as the molecular gas flow rate increases. The ratio of the height of the 3_3-2_1 peak to the 1_1 peak can be used to assign an approximate rotational temperature to the molecular beam. The ratio of the peaks measured experimentally is compared the the ratio of the doublet peaks generated using the PGOPHER simulations for a range of temperatures; the matching ratio yields an approximate rotational temperature of the molecular beam. This is shown in Figure 5.8(d), where the ratio of the doublet peak height measured experimentally as a function of the ND_3 flow

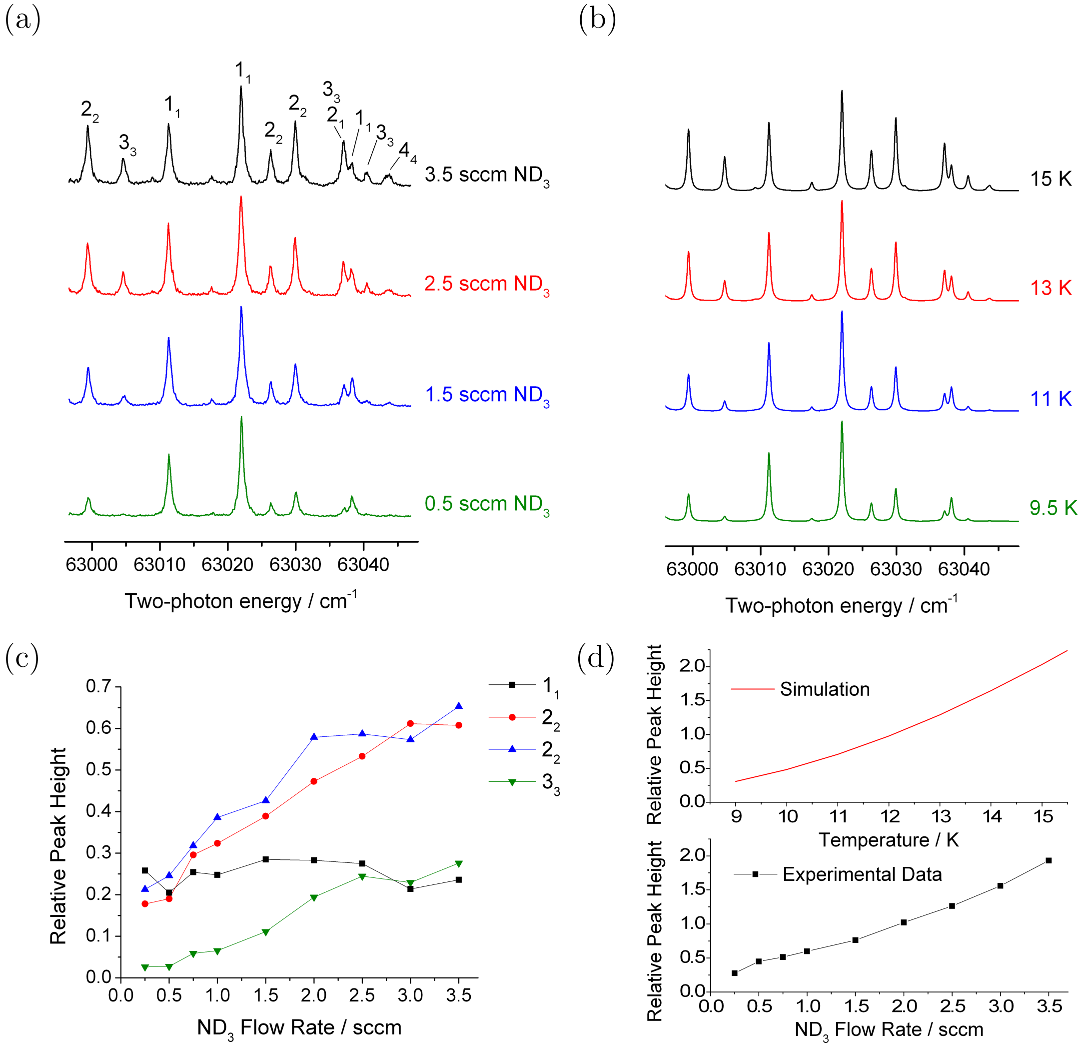

Figure 5.8: (a) ND_3 REMPI spectra recorded at a range of molecular gas flow rates, at a fixed helium inlet pressure of 0.6 mbar in a 6 K buffer gas cell. (b) Simulated REMPI spectra of guided molecules from a molecular source at a rotational temperature of 9.5, 11, 13, and 15 K. (c) The height of various peaks in the REMPI spectra, relative to the main 1_1 peak at 63021.95 cm^{-1}, as a function of the ND_3 flow rates. The relative peak heights are shown for the 1_1 peak at 63038.11 cm^{-1} (black squares), the 2_2 peak at 62999.42 cm^{-1} (red circles), the 2_2 peak at 63029.92 cm^{-1} (blue up-triangles), and the 3_3 peak at 63004.72 cm^{-1} (green down-triangles). (d) Relative height of the 3_3-2_1 peak at 63037.07-63037.10 cm^{-1} to the 1_1 peak at 63038.11 cm^{-1}, as a function of the ND_3 flow rate. The relative height of the doublet peaks from the PGOPHER simulations is also plotted as a function of the input temperature. Matching the relative peak height from the experimental data with the simulations yields an approximate rotational temperature of the molecular beam.

rate is overlaid with the peak ratio calculated from the simulations as a function of temperature.

Figure 5.8(b) shows the PGOPHER simulations (including the initial distribution and guidability of each rotational state) with matching doublet peak ratios to the experimentally measured values for the four representative traces shown in Figure 5.8(a). Comparison of the simulated spectra to the experimental spectra shows a good match for the relative intensities of the other peaks. Using this approximation, the rotational temperature of the molecular beam can be seen to vary between 9.5 and 15 K for ND_3 flow rates ranging between 0.25 to 3.5 sccm (for the fixed helium inlet pressure of 0.6 mbar in a 6 K buffer gas cell). The effect of changing the buffer gas inlet pressure on the rotational state distribution of the molecular beam is discussed in the next section.

5.4.2 Buffer gas inlet pressure

The previous section showed that the rotational temperature of the molecules exiting the buffer gas cell increases for increasing densities of molecular gas in the cell, while holding the buffer gas density constant. The opposite trend is observed when varying the buffer gas density. The rotational temperature of the molecules exiting the cell decreases for increasing amounts of buffer gas in the cell, while holding the molecular gas density constant. The bottom panel of Figure 5.7 shows the REMPI spectrum of ND_3 obtained when the helium inlet pressure is set to 0.3 mbar for a flow rate of 1.0 sccm ND_3. The middle panel shows the spectrum obtained for standard cell conditions, which is twice the helium inlet pressure for the same molecular gas flow rate (0.6 mbar, 1.0 sccm ND_3). The intensity of the 3_3 peaks relative to the 1_1 and 2_2 is much lower for the standard cell conditions, indicating the molecules exit the cell with a lower rotational temperature than for a cell operating with a helium inlet pressure of only 0.3 mbar.

Again, a selected region of the ND_3 REMPI spectrum (from 62995 to 63045 cm^{-1}) is analysed for helium inlet pressures ranging from 0.1 mbar to 1.5 mbar, similar to the analysis described in the previous section for the range of molecular gas flow rates. For helium inlet pressures lower than 0.1 mbar, the signal is unstable and rapidly decreases as the exit aperture becomes compromised by the formation of molecular ice, in the absence of sufficient amounts of buffer gas in the cell. Even at 0.1 mbar helium, the signal drops significantly over long scans of the entire REMPI spectrum. Therefore, only short scans can be recorded for helium inlet pressures of 0.1 mbar. There is insufficient signal for helium inlet pressures greater than 1.5 mbar due to velocity boosting, which leads to fewer successfully guided molecules and a lower molecular flux. These effects are discussed in more detail in Section 4.4.2, where the forward velocity and molecular flux of the guided beam are analysed using mass spectrometry.

The ND_3 spectra obtained at four different helium inlet pressures, while keeping the molecular gas flow rate constant at 1.0 sccm, are shown in Figure 5.9(a). The intensities of the 3_3 and 2_2 peaks relative to the 1_1 peak drops dramatically when the helium inlet pressure is increased from 0.1 to 0.3 mbar, suggesting that there is a large decrease in the rotational temperature of the molecules exiting the cell over this range. A much smaller change in the peak intensities is observed when the buffer gas inlet pressure is increased to 0.5 mbar, and hardly no change at all is visible when the inlet pressure is increased still further to 0.7 mbar. This suggests that there is a maximum amount of rotational cooling that can be achieved for a specific molecular gas flow rate.

This can be seen clearly in Figure 5.9(c), which shows how the height of various peaks, relative to the main 1_1 peak at 63021.95 cm^{-1}, change over the range of helium inlet pressures. The height of the 2_2 peaks at 62999.42 and 63029.92 cm^{-1}, and the 3_3 peak at 63004.72 cm^{-1}, decrease rapidly for relatively small increases in the helium

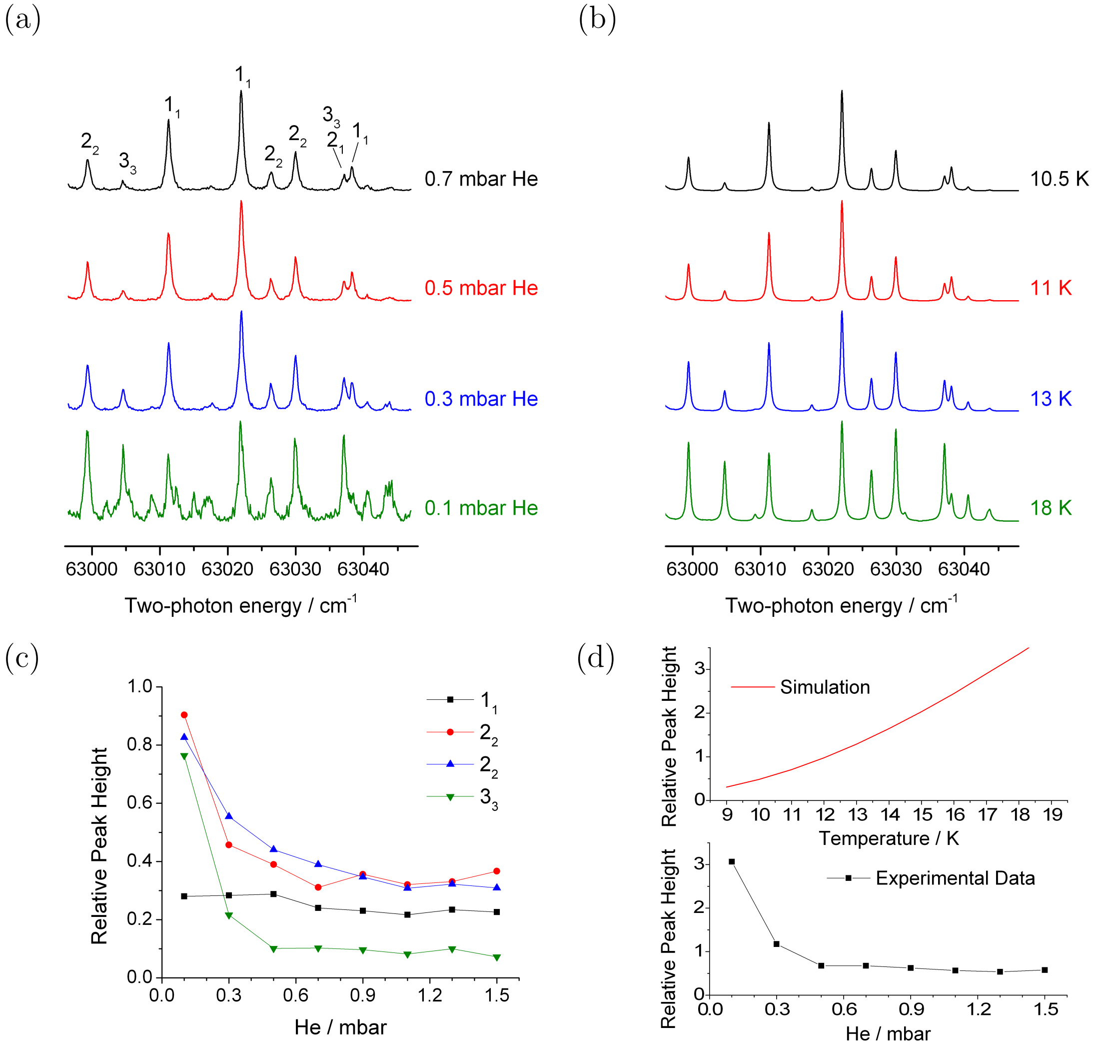

Figure 5.9: (a) ND_3 REMPI spectra for a range of buffer gas inlet pressures, at a fixed ND_3 flow rate of 1.0 sccm in a 6 K buffer gas cell. (b) Simulated REMPI spectra of guided molecules from a molecular source at a rotational temperature of 10.5, 11, 13, and 18 K. (c) The height of various peaks in the REMPI spectra, relative to the main 1_1 peak at 63021.95 cm^{-1}, as a function of the helium inlet pressure. The relative peak heights are shown for the 1_1 peak at 63038.11 cm^{-1} (black squares), the 2_2 peak at 62999.42 cm^{-1} (red circles), the 2_2 peak at 63029.92 cm^{-1} (blue up-triangles), and the 3_3 peak at 63004.72 cm^{-1} (green down-triangles). (d) Relative height of the 3_3-2_1 peak at 63037.07-63037.10 cm^{-1} to the 1_1 peak at 63038.11 cm^{-1} as a function of the helium inlet pressure. The relative height of the doublet peaks is also shown for the PGOPHER simulations as a function of the input temperature. Matching the relative peak height from the experimental data with the simulations yields an approximate rotational temperature of the molecular beam.

inlet pressure when there is initially very little helium in the cell. Though more slowly, the peaks continue to decrease for increasing helium pressures until approximately 0.9 mbar. After that point the peak heights remain relatively constant for further increases in the helium inlet pressure. Thus, for a flow rate of 1.0 sccm ND_3, the lowest rotational temperature of the molecules exiting the cell is reached around 0.9 mbar helium. As expected, the 1_1 peak at 63038.11 cm^{-1} stays at a similar height relative to the 63021.95 cm^{-1} 1_1 transition over the entire range of helium pressures.

The relative height of the 3_3-2_1 peak compared to the 1_1 peak in the doublet can be used to estimate the rotational temperature of the molecules exiting the cell for a range of helium pressures. The relative peak height of the doublet measured experimentally is matched to a spectrum simulated for a specific rotational temperature in Figure 5.9(d). Figure 5.9(b) shows the simulated spectrum matching the four representative traces plotted in Figure 5.9(a). The simulated spectra yields a good match for the relative intensities of the other peaks in the experimental spectra for the helium inlet pressures of 0.3, 0.5, and 0.7 mbar. However, there is a poor fit between the 18 K simulation and the 0.1 mbar helium experimental spectrum; there are several small peaks in the experimental spectrum that are not present in the simulated spectrum. There peaks are likely from strongly guided, high rotational states that are populated at higher rotational temperature, since the simulation only includes the lowest J rotational states.

Despite the fact that the buffer gas cell is held at 6 K, the ND_3 molecules may exit the cell with higher rotational temperatures if the helium inlet pressure is very low, such that the molecular gas does not undergo a sufficient number of collisions to reach the lowest rotational temperatures. As mentioned earlier, however, the conditions within the cell are not stable at such low helium pressures, and the run time is severely limited by molecular ice formation blocking the exit aperture and reducing the signal. Increasing the amount of buffer gas leads to more effective cooling and decreases the rotational temperature of the molecules exiting the cell. A rotational temperature of approximately 10 K is achieved with 0.9 mbar helium. After this point, increasing the buffer gas inlet pressure further to 1.5 mbar does not significantly change the rotational temperature of the molecular beam.

Although a change in rotational temperature from approximately 9 K to 18 K can be achieved by changing the molecular and buffer gas densities in the cell, the conditions within the cell that lead to the highest rotational temperatures tend to be unstable. Instead, removing the outer heat shield so that the cell temperature is 17 K rather than 6 K can be used to achieve higher rotational temperatures with stable cell conditions, as discussed in the next section.

5.4.3 Rotational state distributions for a 17 K buffer gas cell

As discussed in Section 4.5, the translational temperature of the molecular beam is similar for a 6 K helium and 17 K neon buffer gas cell (peak kinetic energy of 6.92(0.13) K and 5.90(0.01) K, respectively). This is because the buffer gas cell is operated in the intermediate flow regime where the forward velocity of the molecules are boosted toward the thermal velocity of the buffer gas. The thermal velocity of neon at 17 K is slightly lower than the much lighter helium gas at 6 K, and significantly lower than helium at 17 K. Despite similar translational temperatures, the rotational temperatures for a 6 K helium and 17 K neon buffer gas cell are quite different. Figure 5.10 shows the REMPI spectrum recorded for standard conditions (1.0 sccm ND_3, 0.6 mbar helium or neon buffer gas) in a 6 K and 17 K cell. Molecules exit the 17 K cell at a higher rotational temperature than the 6 K cell, and consequently the intensity of the 3_3 and 4_4 peaks is much greater in the REMPI spectrum from the 17 K cell.

Figure 5.10 also shows the REMPI spectrum recorded when helium is used as

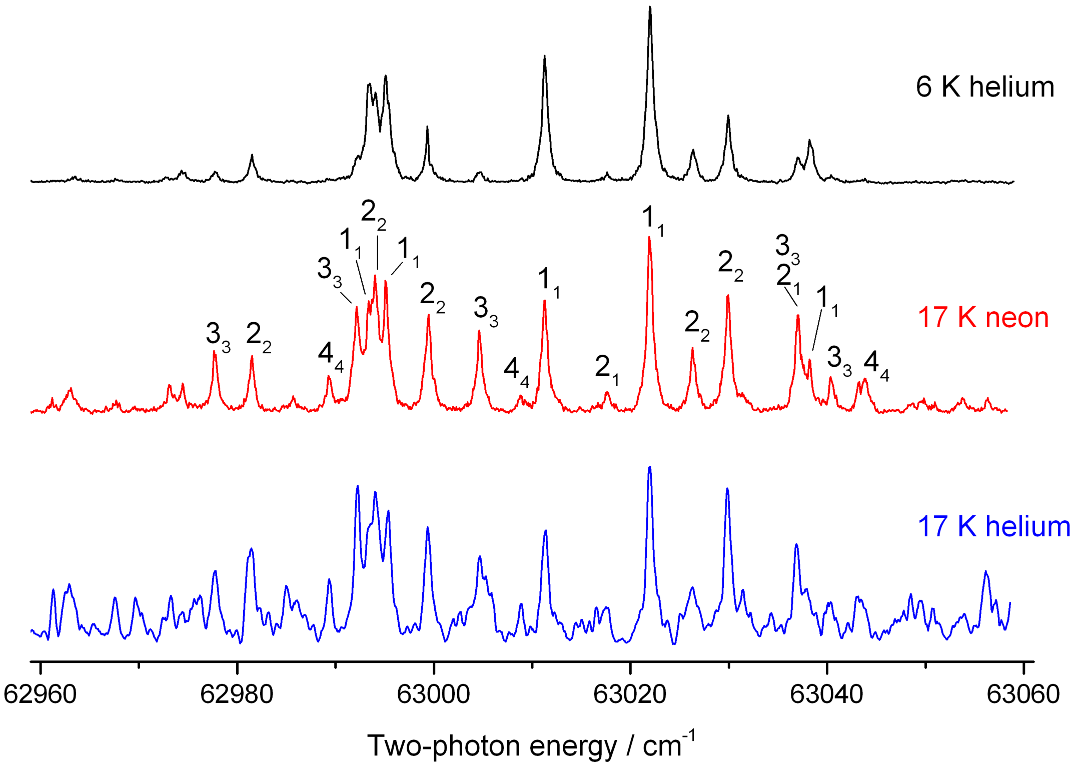

Figure 5.10: (2+1) REMPI spectrum of ND$_3$, $\tilde{\mathrm{B}}\,^1\mathrm{E}''(\nu_2' = 5) \leftarrow \tilde{\mathrm{X}}(1)$, recorded with a 6 K helium (top panel), 17 K neon (middle panel) and 17 K helium (bottom panel) buffer gas cell. A molecular gas flow rate of 1.0 sccm and a buffer gas inlet pressure of 0.6 mbar is used in all scans. Savitzky-Golay averaging is used to remove some of the noise from the 17 K helium spectrum.

the buffer gas in a 17 K cell. The rotational temperature of the molecular beam from the 17 K helium cell is seen to be slightly higher than that of the 17 K neon cell, suggesting that the heavier neon is a better suited buffer gas for ND_3. Furthermore, the translational temperature of the 17 K helium cell is also higher than the 17 K neon cell as a result of velocity boosting (peak kinetic energy of 15.20(0.37) K and 5.90(0.01) K, respectively; described in Section 4.5). The higher translational temperature leads to a lower molecular flux and therefore a lower signal to noise ratio in the REMPI spectrum for the 17 K helium buffer gas cell when compared to the 17 K neon spectrum. Additionally, the activated charcoal that is used as a helium pump is most effective from 4 to 10 K; it is much less effective at adsorbing helium at temperatures between 10 to 20 K. Collisions between molecules in the quadrupole guide and background gas will increase, particularly in the region enclosed by the inner radiation shield, and contribute to an increased loss of signal for the 17 K helium buffer gas cell. Because neon has a much lower vapour pressure than helium at 17 K, most cold surfaces act as a cryopump for the neon buffer gas. For these reasons, the rest of the analysis of the rotational state distributions in the 17 K cell are done using neon as the buffer gas instead of helium.

Small changes to the rotational temperature of the molecules emerging from the 17 K cell can be achieved by changing the amounts of molecular gas and buffer gas within the cell. Figure 5.11 shows how the rotational state distribution changes when the molecular gas flow rate is doubled compared to the standard cell conditions (1.0 sccm ND_3, 0.6 mbar Ne) and when the buffer gas inlet pressure is halved compared to the standard cell conditions. In both cases, the rotational cooling in the buffer gas cell is less effective, so the molecules exit with a higher rotational temperature. Population in the 3_3 and 4_4, and to a lesser extent the 2_2, rotational states increases relative to the 1_1 rotational state, as indicated by the increasing intensity of those peaks in the REMPI spectra relative to the 1_1 peaks.

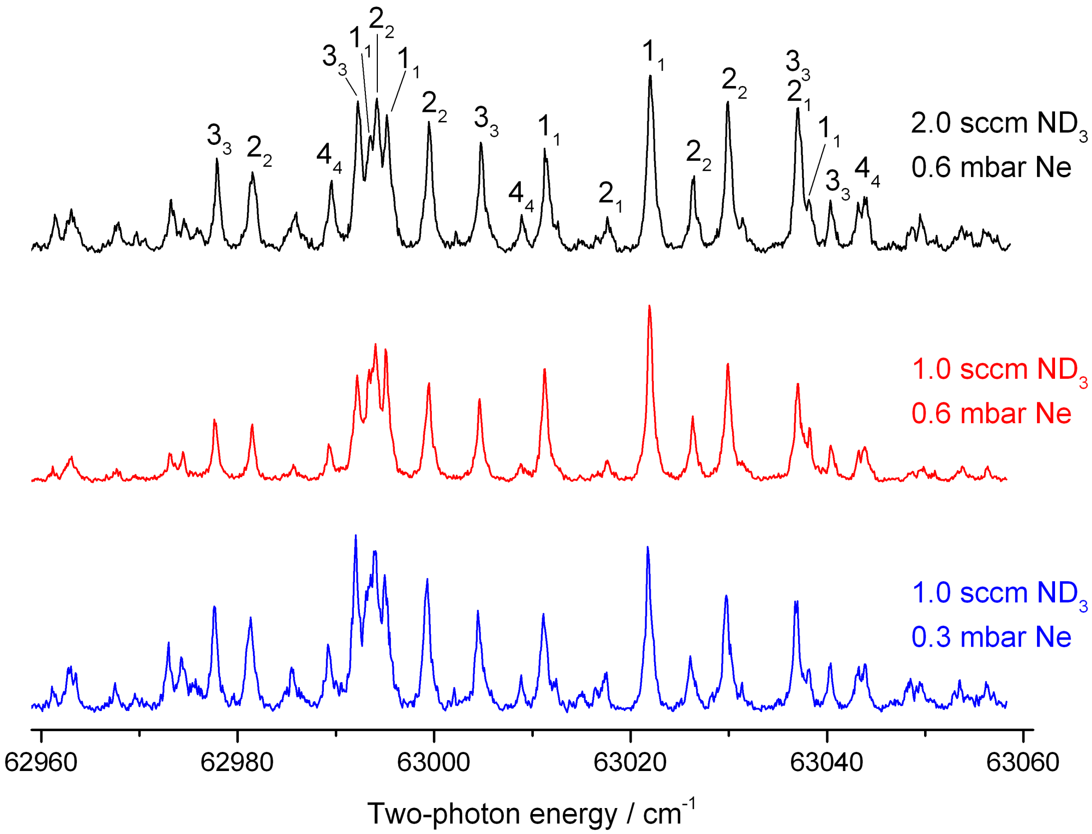

Figure 5.11: (2+1) REMPI of ND_3 from a 17 K buffer gas cell under standard conditions (middle panel). The molecular gas flow rate is doubled in the top panel, while the buffer gas inlet pressure is halved in the bottom panel, compared to the standard conditions (1.0 sccm ND_3, 0.6 mbar Ne).

The region from 62995 to 63045 cm^{-1} is again used to study the effect of changing gas densities on the rotational state distribution in greater detail for the 17 K buffer gas cell. The ND$_3$ flow rate is varied from 0.25 sccm to 3.5 sccm while holding the neon inlet pressure fixed at 0.6 mbar. Representative spectra are shown for flow rates of 0.5, 1.5, 2.5, and 3.5 sccm in Figure 5.12(a) . The increasing intensity of the 3_3 and 4_4 peaks relative to the 1_1 peaks as the molecular gas flow rate increases is indicative of the increasing rotational temperature of the molecular beam as the cooling becomes less effective in the buffer gas cell. The peak heights relative to the main 1_1 peak at 63021.95 cm^{-1} are plotted as a function of the molecular gas flow rate in Figure 5.12(c). Apart from the 1_1 peak at 63038.11 cm^{-1} which remains relatively constant over the range of molecular gas flow rates, the peaks for the 2_2, 3_3, and 4_4 rotational states increase as the ND$_3$ flow rate increases.

The neon inlet pressure is also varied from 0.2 mbar to 1.5 mbar while holding the ND$_3$ molecular gas flow rate fixed at 1.0 sccm. The lower limit of the range of buffer gas inlet pressures analysed for the 6 K cell was 0.1 mbar; conditions were too unstable at this pressure for the 17 K cell, so the lower limit was set at 0.2 mbar instead. Representative spectra are shown for inlet pressures of 0.3, 0.5, 0.7, and 0.9 mbar in Figure 5.12(b). As in the case with helium buffer gas at 6 K, increasing amounts of buffer gas leads to lower rotational temperatures of the molecules exiting the cell, and the intensity of the 3_3 and 4_4 rotational state peaks become smaller relative to the 1_1 peaks. The change in peak intensities is greatest when the buffer gas inlet pressure increases from 0.3 to 0.5 mbar. The change in peak intensities is smaller at higher buffer gas densities in the cell as the maximum achievable rotational cooling is approached (for the molecular gas flow rate of 1.0 sccm). The peak heights relative to the main 1_1 peak at 63021.95 cm^{-1} are plotted as a function of the neon inlet pressure in Figure 5.12(d). The 2_2, 3_3, and 4_4 peaks decrease as the neon inlet pressure increases up to approximately 0.9 mbar, after which point the peak intensities remain relatively

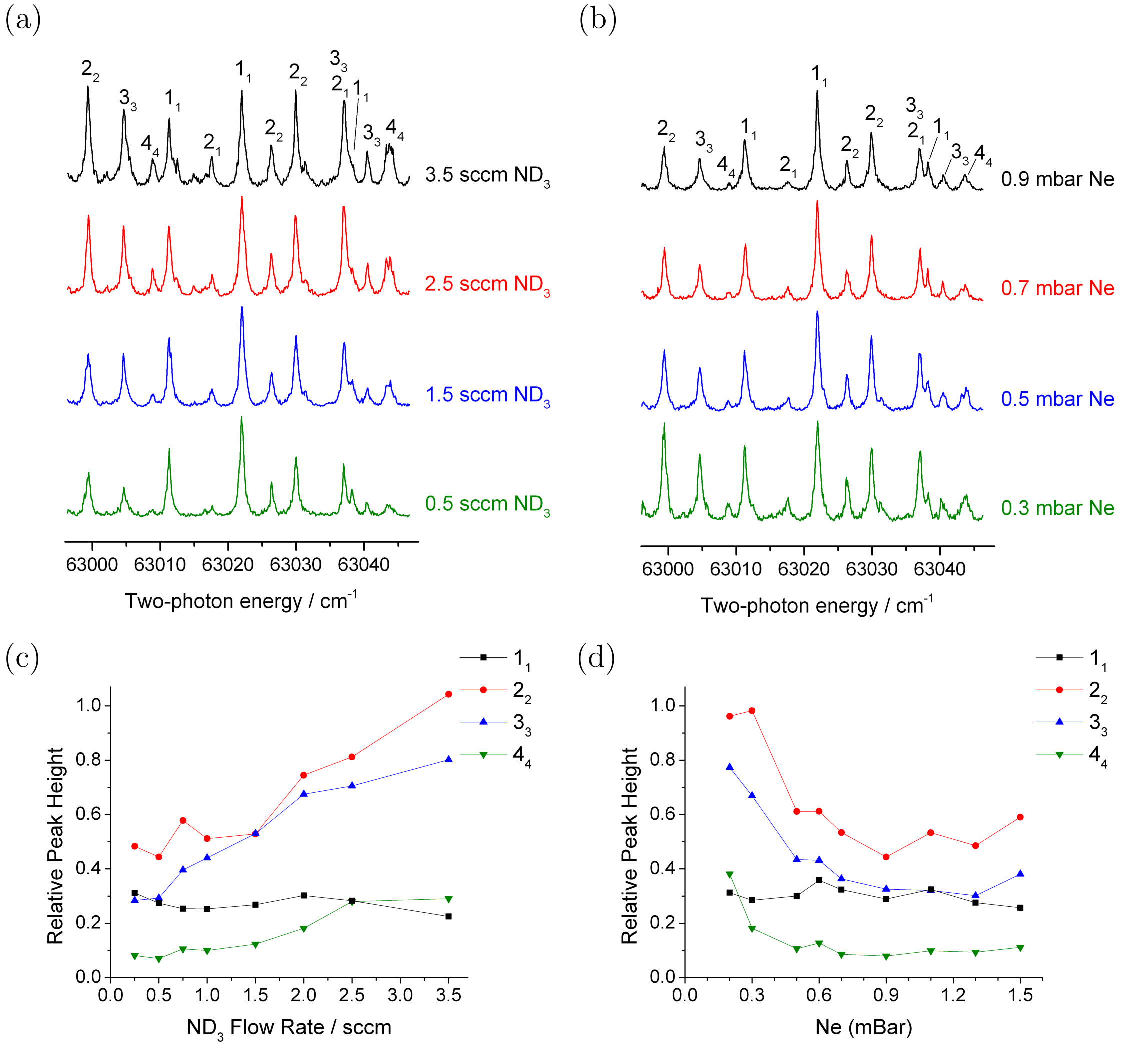

Figure 5.12: (a) ND_3 REMPI spectra for a range of molecular gas flow rates, at a fixed neon inlet pressure of 0.6 mbar in a 17 K buffer gas cell. (b) ND_3 REMPI spectra for a range of buffer gas inlet pressures, at a fixed ND_3 flow rate of 1.0 sccm in a 17 K buffer gas cell. (c) The height of various peaks in the REMPI spectra, relative to the main 1_1 peak at 63021.95 cm^{-1}, as a function of the ND_3 flow rate. The relative peak heights are shown for the 1_1 peak at 63038.11 cm^{-1} (black squares), the 2_2 peak at 62999.42 cm^{-1} (red circles), the 3_3 peak at 63004.72 cm^{-1} (blue up-triangles), and the 4_4 peak at 63008.81 cm^{-1} (green down-triangles). (d) For the same peaks as described in (c), the relative heights are plotted as a function of the neon buffer gas inlet pressure.

constant. The maximum amount of cooling that is possible for a molecular gas flow rate of 1.0 sccm has been achieved by this point, and the rotational temperature, and therefore rotational state distribution, changes very little as the buffer gas inlet pressure is increased beyond 0.9 mbar. As expected, the 1_1 peak at 63038.11 cm^{-1}

remains fairly constant throughout the range of buffer gas inlet pressures.

As described earlier, the relative height of the 3_3-2_1 peak compared to the 1_1 peak in the doublet can be used to estimate the rotational temperature of the molecules exiting the cell by matching the ratio measured experimentally to a simulated spectrum. Figure 5.13(a) shows how the doublet peak ratio changes over the range of ND_3 molecular gas flow rates studied for the 6 K helium and 17 K neon buffer gas cell. Figure 5.13(c) shows how the simulated doublet ratio changes as a function of rotational temperature, and can be used to approximate the rotational temperature of the experimental molecular beam. As the molecular gas flow rate is varied between 0.25 sccm and 3.5 sccm, the rotational temperature of the molecular beam ranges from about 9 K to 15 K for a fixed helium inlet pressure of 0.6 mbar in the 6 K cell. For a fixed neon inlet pressure of 0.6 mbar in the 17 K cell, the rotational temperature of the molecular beam ranges from about 13.5 K to 19.5 K over the same range of molecular gas flow rates. Although there is some overlap in the rotational temperature range of the molecular beams generated from a 6 K and 17 K cell, the molecular flux tends to be low at the extreme ends of the range and the cell conditions are often unstable with significant molecular ice formation at the high temperature limit. Therefore, it is advisable that the buffer gas cell only be run for extended periods of time in the middle of the achievable rotational temperature range for either the 6 K or 17 K buffer gas cell.

Similarly, Figure 5.13(b) shows how the doublet peak ratio changes over the range of buffer gas inlet pressures studied for the 6 K helium and 17 K neon buffer gas cells. As the helium inlet pressure is varied between 0.1 mbar and 1.5 mbar in the 6 K cell, the rotational temperature of the molecular beam ranges from about 18 K to 10 K for a fixed ND_3 flow rate of 1.0 sccm. For the same molecular gas flow rate, although the neon inlet pressure is only varied from 0.2 mbar to 1.5 mbar in the 17 K cell due to stability issues lower at inlet pressures lower than 0.2 mbar, the rotational

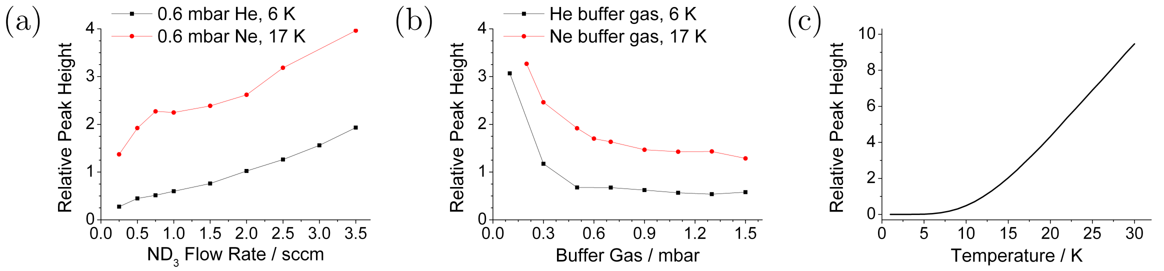

Figure 5.13: (a) Relative height of the 3_3-2_2 doublet peak at 63037.07-63037.10 cm^{-1} to the 1_1 doublet peak at 63038.11 cm^{-1}, as a function of ND$_3$ flow rate for the fixed buffer gas inlet pressure of 0.6 mbar helium in the 6 K cell and 0.6 mbar neon in the 17 K cell. (b) The relative height of the doublet peaks as a function of the helium inlet pressure in the 6 K cell and of the neon inlet pressure in the 17 K cell, for the fixed ND$_3$ flow rate of 1.0 sccm. (c) The relative height of the doublet peaks in the PGOPHER simulations as a function of the input rotational temperature.

temperature of the molecular beam ranges from about 18 K to 13 K. Figure 5.14 shows the experimental REMPI spectrum recorded with standard conditions for a 17 K neon buffer gas cell (1.0 sccm NH$_3$, 0.6 mbar Ne) and the corresponding simulation (the experimental doublet ratio matches the doublet ratio in the 15 K simulated spectrum). The relative intensities of the main peaks in the experimental spectrum are generally well matched by the simulation. However, there are several small, extra peaks in the experimental spectrum that are not present in the simulated spectrum. The simulation only includes the $J \leq 5$ rotational states, so these peaks are likely from strongly guided, higher rotational states that are populated at higher rotational temperatures. As determined from the simulation, the relative population of the $|J, K\rangle$ rotational states is provided in Table 5.2 for a molecular beam generated from a 17 K neon buffer gas cell using standard cell conditions.

It may seem odd that for the 17 K buffer gas cell, the rotational temperature of the buffer-gas-cooled molecular beam can be as low as 13 K for certain molecular and buffer gas conditions. However, it is important to recall that the buffer gas cell is operating in the intermediate flow regime between the diffusive and fully hydrodynamic limits (see Section 2.1.4 for more details on gas flow regimes out of the cell). In the effusive

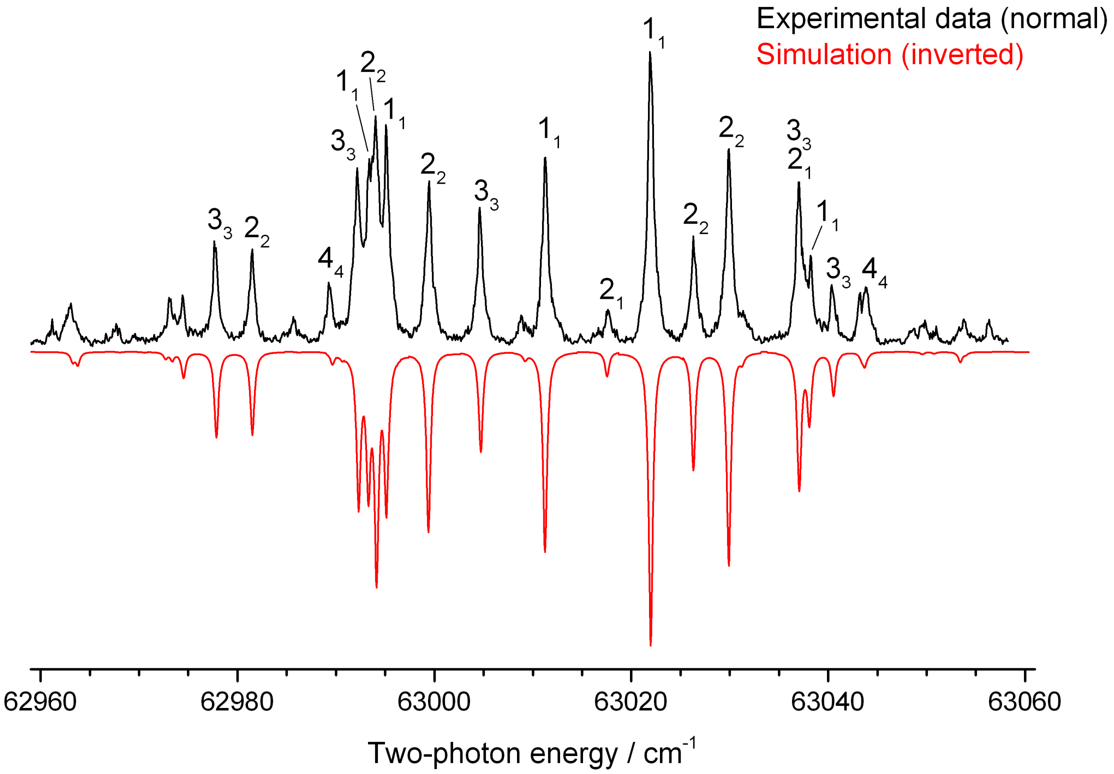

Figure 5.14: (2+1) REMPI spectrum for the $\tilde{\mathrm{B}}^1\mathrm{E}''(\nu_2' = 5) \leftarrow \tilde{\mathrm{X}}(1)$ transition in ND_3, recorded following buffer gas cooling and electrostatic velocity selection for a 17 K buffer gas cell at the optimal settings (1.0 sccm ND_3, 0.6 mbar Ne). The inverted spectrum (red) shows the PGOPHER simulation for the guidable rotational states of ND_3 from a 15 K thermal distribution.

regime, the rotational state distribution of the molecules exiting the buffer gas cell closely matches a thermal distribution at the cell temperature [138]. But in the fully hydrodynamic regime, the rotational temperature of the molecules may decrease below the temperature of the cell as the buffer gas expands isentropically into the vacuum region [141].

The rotational state distribution of the cold molecular beam of ND_3 has been fully characterised for the 6 K and 17 K buffer gas cell under a wide range of molecular gas and buffer gas conditions. The next section compares the results obtained for ND_3 to the ammonia isotopologues NHD_2, NH_2D, and NH_3.

5.5 (2+1) REMPI spectra of ammonia isotopologues

The electrostatic extraction of buffer-gas-cooled beams is a general technique that can be applied to a range of polar molecules in order to produce a rotationally and translationally cold beam of molecules. Extension of the (2+1) REMPI analysis of the cold ND_3 molecular beam to the other ammonia isotopologues, NHD_2, NH_2D, and NH_3, provides an interesting comparison to the results obtained for ND_3. Furthermore, ammonia and its mixed isotopologues are particularly useful in astrochemistry as a means of calculating the temperature of molecular gas in space [200] and in photochemistry in order to study the factors influencing the breaking of the N-H bond versus the N-D bond in partially deuterated isotopologues [201]. Both these applications require detailed characterisations of the REMPI spectroscopy of the ammonia isotopologues.

Comparing the REMPI spectra recorded for ND_3 and NH_3 with a 6 K and 17 K cell using standard molecular and buffer gas conditions (Fig. 5.15) reveals that the NH_3 peaks are much more diffuse than the sharp ND_3 peaks. This is caused by the large isotope effect on the lifetime of the 2^n levels of the $\tilde{\mathrm{B}}$ Rydberg state of ammonia; ND_3 has a lifetime of 0.25(2) ns while the lifetime of NH_3 is only 6.1(7) ps [191]. The predissociation mechanism is thought to occur via the $\tilde{\mathrm{A}}^1\mathrm{A}_2''$ state after the ν_3 degenerate asymmetric stretch causes a vibronic mixing of the $\tilde{\mathrm{B}} - \tilde{\mathrm{A}}$ states. Despite the large isotope effect, the lifetimes of the 2^n levels are independent of the vibronic bands of ν_2 for $n \leq 8$ (NH_3) and $n \leq 6$ (ND_3), and independent of the rotational state J_K [191]. This is quite different from the predissociation mechanism of the $\tilde{\mathrm{C}}'^1\mathrm{A}_1'$ state, which depends on the rotational state of the molecule [202]. Apart from the linewidth of the peaks, many of the features of the NH_3 REMPI spectra are similar to those for the ND_3 spectra, including the increasing intensity of the 3_3 and 2_2 peaks relative to the 1_1 peaks in the spectrum recorded with the 17 K buffer gas cell.

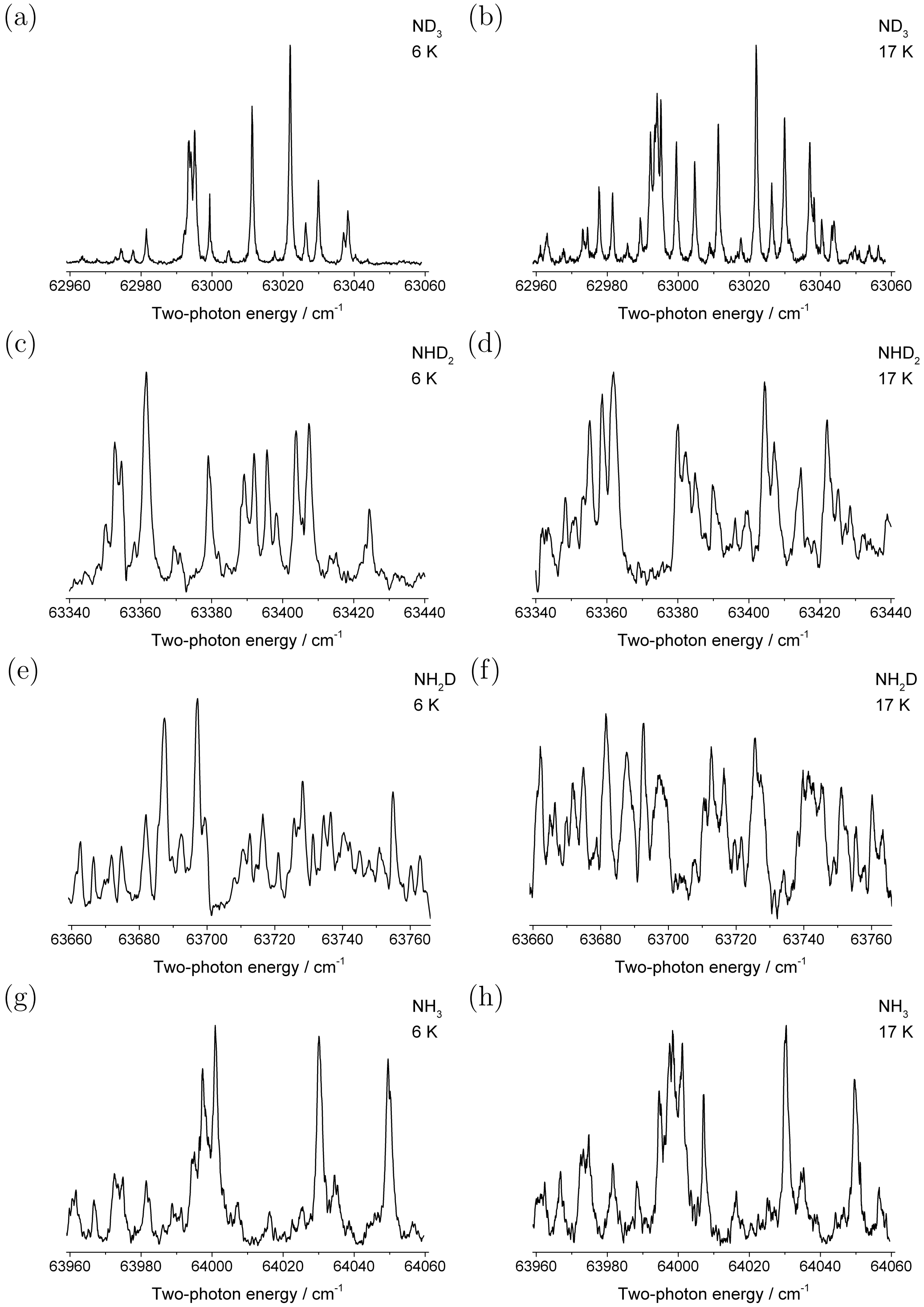

Figure 5.15: (2+1) REMPI $\tilde{\mathrm{B}}^1\mathrm{E}''(\nu_2' = 5) \leftarrow \tilde{\mathrm{X}}(1)$ spectra of ammonia isotopologues, recorded using standard cell conditions for a 6 K and a 17 K buffer gas cell (1.0 sccm molecular gas flow rate, 0.6 mbar buffer gas inlet pressure).

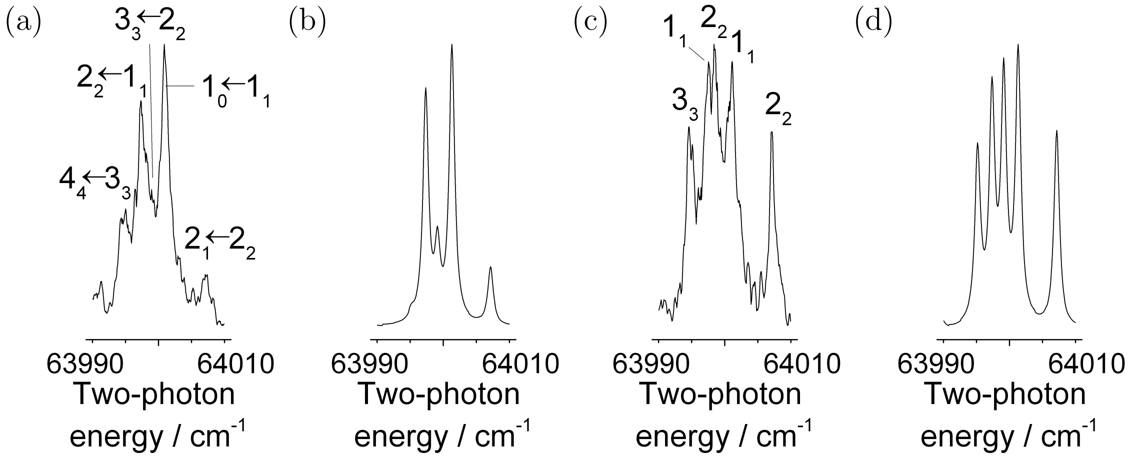

Figure 5.16: (2+1) REMPI $\tilde{\mathrm{B}}^1\mathrm{E}''(\nu_2' = 5) \leftarrow \tilde{\mathrm{X}}(1)$ spectra of NH_3, recorded using standard cell conditions for a buffer gas cell at (a) 6 K and (c) 17 K. PGOPHER simulations are shown for the guidable rotational states of NH_3 from a thermal distribution at (b) 14 K and (d) 25 K.

Just as the relative peak height of the doublet ratio in the ND_3 REMPI spectrum can be used to approximate the rotational temperature of the molecular beam, the relative height of the 2_2 peak at 64007.18 cm^{-1} compared to the 1_1 peak at 64001.35 cm^{-1} can be used in the NH_3 REMPI spectrum. Figure 5.16 shows the select region (from 63990 to 64010 cm^{-1}), which includes both these peaks, for the experimental spectra of NH_3 collected with a 6 K and 17 K buffer gas cell. The simulated spectra of the guided rotational states of NH_3 from a thermal distribution at 14 K and 25 K have the matching peak ratio to the experimental data and are also shown in the figure. The rotational temperature of NH_3 exiting the 6 K helium and 17 K neon buffer gas cell is higher than ND_3 for comparable conditions; the slightly more prolate shape of NH_3 may contribute to the decreased effectiveness of rotational cooling in the buffer gas cell. The relative population of the $|J, K\rangle$ rotational states of NH_3 for a molecular beam generated from a 6 K helium and 17 K neon buffer gas cell is provided in Table 5.2, as determined from the simulations. Similar to ND_3, only the lowest J levels exhibit significant rotational population in NH_3 for the buffer-gas-cooled and electrostatically guided molecular beam. This supports the conclusion that electrostatic extraction of a buffer-gas-cooled molecular beam is a generally applicable technique.

Although it is possible to store pure samples of NH_3 and ND_3, it is not possible for NH_2D or NHD_2; any initially pure samples of the mixed isotopologues would quickly become statistically weighted mixtures of all four isotopologues as a result of self-reaction at the container walls [201]. Therefore, a mixture of NH_3 and ND_3 in a ratio of 1:1 is prepared in a stainless steel bottle, yielding a statistical mixture of the isotopologues from intermolecular proton and deuterium exchanges. The gas mixture is introduced into the buffer gas cell via the molecular gas line and molecular inlet.

Relatively few studies have been conducted on the mixed isotopologues of ammonia, despite the large number of multiphoton spectroscopy studies that have been conducted on ND_3 and NH_3. The $\tilde{\mathrm{A}}\,^1\mathrm{A}_2''$ Rydberg state was first used to study the predissociation of NH_2D and NHD_2 in [203] and [204], respectively, while the spectroscopic parameters of the $\tilde{\mathrm{C}}'\,^1\mathrm{A}_1'$ Rydberg state for the mixed isotopologues were first derived in [201]. Similar to ND_3 and NH_3, the $\tilde{\mathrm{A}}$ state of the mixed isotopologues exhibits rapid predissociation which leads to severe line broadening of the spectrum, while the $\tilde{\mathrm{C}}$ state exhibits a rotational state dependent predissociation mechanism. Recently, the spectroscopic parameters have also been determined for the $\tilde{\mathrm{B}}\,^1\mathrm{E}''$ state of NHD_2 in [205], which is the Rydberg state used in this work.

The electronically excited $\tilde{\mathrm{B}}$ Rydberg state of the mixed isotopologues belongs to the lower symmetry $C_{2\mathrm{v}}$ point group compared to the $D_{3\mathrm{h}}$ point group of the ND_3 (and NH_3) excited state. This increases the rovibronic mixing between states, leading to increased predissociation of the partially deuterated isotopologues and broader linewidths in the REMPI spectra as shown in Figure 5.15 [201]. The broader linewidths cause many of the rotational lines to overlap. Furthermore, NH_2D has a greater density of rotational states than NHD_2, leading to a more complex REMPI spectrum. The spectra of ND_3 and NH_3 were recorded with pure samples; as NHD_2 and NH_2D were only partial components of a mixture, the molecular density, and thus the signal to noise ratio, will be lower compared with the isotopically pure samples (statistically: 37.5% NHD_2, NH_2D; 12.5% NH_3, ND_3).

The Jahn-Teller effect is the geometrical distortion of a non-linear molecule in a degenerate electronic state that reduces the overall energy of the molecule. A small Jahn-Teller effect is observed in the $\tilde{B}\,^1E''$ electronically degenerate state of ammonia (the Rydberg electron occupies the degenerate $3p_{x,y}$ orbitals in the plane of the molecule) [206]. The Jahn-Teller effect causes small shifts and splittings of the vibrational energy levels, but is too small to significantly reduce the electronic angular momentum of the state. Therefore, the state exhibits a large Zeeman effect, and electronic angular momentum terms are included in the rotational Hamiltonian of the state. In theory, partial isotopic substitution should only affect the vibrational and rotational Hamiltonian and not the electronic potential energy surfaces. However, the impact of partial isotopic substitution on the Jahn-Teller effect is difficult to assess as the degeneracy is formally lifted for NH_2D and NHD_2. Significant mixing of the nearly degenerate electronic states leads to perturbations and other anomalies in the spectra, as described in [205] and observed experimentally (Fig. 5.15).

For these reasons, the REMPI spectra of the mixed isotopologues are more complex than the spectra recorded for ND_3 and NH_3, making the peak assignment and analysis more challenging. Simulating the spectra is also more difficult because the Stark effect for asymmetric top molecules is needed to determine the transmission efficiency of the rotational states through the quadrupole guide. Furthermore, the rotational constants of the mixed isotopologues, in particular for the excited states, are not well know compared to ND_3 and NH_3 because of the limited number of experimental studies that have been conducted on the mixed isotopologues. This increases the number of variables that need to be considered when trying to fit the spectra. The rotational constants for NHD_2 were obtained from [205]; preliminary results for the rotational constants of NH_2D were provided by Dr. Colin Western through private communication, in advance of publication. The REMPI spectra of the ammonia isotopologues were recorded with Edward Steer, a member of the Softley group. A preliminary analysis suggests the rotational temperature of the mixed isotopologues is higher than for ND_3, but a full analysis by Steer is still ongoing at the time of writing of the thesis.

This study demonstrates that it is possible to simultaneously cool, guide, and detect samples of mixed isotopologues. Given the relatively weak Stark shifts of the ammonia isotopologues, the detection efficiency of the technique must therefore be quite high. These characterisations will be particularly useful when the apparatus is combined with the ion trap and the mixed isotopologues are used to conduct H/D fractionation studies. Chapter 6 provides more details about the next steps and future direction of the experimental apparatus.

5.6 Summary

A detailed characterisation of the cold molecular beam using (2+1) REMPI spectroscopy has been described in this chapter. The $\tilde{\mathrm{B}}^1\mathrm{E}''(\nu_2' = 5) \leftarrow \tilde{\mathrm{X}}(1)$ transition is used because the intermediate state $\tilde{\mathrm{B}}$ has a longer lifetime compared to $\tilde{\mathrm{A}}$, and the rate of predissociation of the intermediate state is independent of the rotational state of the molecule, unlike the $\tilde{\mathrm{C}}'$ state. The rotational temperature of the molecules exiting the buffer gas cell, and ultimately the rotational state populations at the end of the guide, can be altered by changing the molecular and buffer gas densities within the cell. Higher molecular flow rates lead to slightly higher rotational temperatures due to less effective buffer gas cooling. Increasing the buffer gas density increases the efficiency of cooling, and leads to the rotational state populations shifting to lower J states.

In order to simulate the REMPI spectra of the ND_3 molecules at the end of the guide, both the rotational state distribution from the thermal equilibrium of the molecules exiting the buffer gas cell and the 'guidability' of each state, as determined from the Monte Carlo simulations of the guiding process, must be calculated. The predicted rotational state distribution of the molecules at the end of the guide can then be input into PGOPHER as the ground state population distribution of ND_3 to provide a simulation of the experimental REMPI spectra. Generally, the simulated spectra provided good matches of the spectra recorded experimentally.

The ability to control both the translational and rotational temperature of the molecular beam is an extremely useful tool to have when studying low temperature chemistry. For example, the translational temperature of the molecular beam of ND_3 for standard conditions in a 6 K helium and 17 K neon buffer gas cell is similar (peak kinetic energies of 6.92(0.13) K and 5.90(0.01) K, respectively; described in Section 4.5) while the rotational temperature of the molecules exiting the 6 K and 17 K buffer gas cell is approximately 10 K and 15 K, respectively. Because of the different guidabilities of rotational states, the beams exiting the quadrupole guide are not at thermal equilibrium; these temperatures are only indicative of the range of states that are transmitted. A comparison between these two buffer gas cell set-ups will be particularly useful when investigating the effect of rotational cooling on reaction rates. Electrostatic extraction of a buffer-gas-cooled beam of molecules is a general technique that can be applied to many different molecules. In this work, the technique has been extended to ammonia isotopologues, and the REMPI spectra have been recorded for these cold molecules.

Chapter 6

Conclusions

6.1 Summary

In this thesis, two different experimental techniques have been combined to produce a rotationally and translationally cold molecular beam: buffer gas cooling and electrostatic velocity selection. Molecules entered the cold buffer gas cell, which was attached to a 6 K pulse tube cryocooler, and underwent thermalising elastic collisions with the buffer gas atoms. The internally cold molecules exited the buffer gas cell and were transported by the electrostatic quadrupole guide around three 90° bends before being delivered to the detection chamber.

There were several technical challenges to operating in the cryogenic regime (temperatures below 125 K), which had to be considered when designing the experimental apparatus. Gold-plated radiation heat shields are used to limit the heat load placed on the cryocooler. The buffer gas line was thermally connected to both stages of the cryocooler, while thermal contact was minimised to the molecular gas line to prevent molecular ice forming and blocking the line. This was particularly challenging at the molecular inlet nozzle, which delivers the molecules from the 'hot' (150 to 300 K) molecular gas line into the cold (6 K) buffer gas cell. Low thermally conducting materials, such as glass and Kapton film, were used at junctions where thermal contact must be minimised.

Monte Carlo trajectories were used to simulate the guiding process, providing one with a deeper understanding of how electrostatic velocity selection occurs. Two possible guide configurations were considered: a hexapole and a quadrupole arrangement. A hexapole guide created a more transversely symmetric electric field and had a larger effective entrance to the guide for slow molecules compared to a quadrupole guide. The electrostatic guide had to be very long to take the molecules from the cryogenic region of the buffer gas cell to the detection chamber; the guide included three 90° bends and had a total path length of 2148.8 mm. The long path length of the guide and the large bend radii presented a significant technical challenge for aligning six electrodes in a hexapole arrangement. Considering these technical challenges, a quadrupole guide configuration was selected as a compromise between ideal guide characteristics and ease of construction and implementation. A large bend radius (100 mm for all three bends) was used for the electrostatic guide so that sufficient signal can be obtained for molecules with relatively weak Stark shifts, which extends the range of molecules that may be investigated using this apparatus.

Mass spectrometry and (2+1) REMPI spectroscopy were used to characterise the cold molecular beam of ND_3 delivered to the detection chamber by the electrostatic guide. This is a general cooling technique that was also applied to CH_3F and the ammonia isotopologues NHD_2, NH_2D, and NH_3. The molecular flux and translational temperature of the beam were characterised using mass spectrometry. Generally, a compromise was made between molecular flux and translational temperature, as measures that lowered the translational temperature of the molecular beam often did so at the expense of molecular flux. Furthermore, molecular ice formation at the entrance and exit of the buffer gas cell limited the run time of the experiment and also had to be taken into consideration.

Changing the electrostatic guide voltage and changing the conditions within the buffer gas cell altered the properties of the resulting molecular beam. A lower voltage created a molecular beam with a lower translational temperature, but also led to a reduced molecular flux. The molecular flux increased for higher molecular flow rates. However, for a fixed buffer gas density in the cell, a higher molecular gas flow rate led to less effective buffer gas cooling, and the molecules left the cell at slightly higher translational temperatures. For a fixed molecular gas density, increasing the buffer gas density increased the efficiency of cooling and initially led to colder molecular beams. However, the buffer gas cell used in this work was operated in the intermediate, or partially hydrodynamic, flow regime. This meant that the molecular gas was velocity boosted toward the thermal velocity of the buffer gas, particularly at high buffer gas densities. As the buffer gas density in the cell increased, velocity boosting eventually caused molecules to exit the buffer gas cell at higher velocities. In turn, fewer molecules were successfully guided around the bend and a lower flux of molecules reached the detection chamber.

(2+1) REMPI spectroscopy of the $\tilde{\mathrm{B}}^1\mathrm{E}''(\nu_2' = 5) \leftarrow \tilde{\mathrm{X}}(1)$ transition was used to determine the rotational state distributions of guided ammonia molecules. For a fixed buffer gas density, higher molecular flow rates led to less effective internal cooling, and higher rotational temperatures. For a fixed molecular gas flow rate, higher buffer gas densities in the cell led to more effective internal cooling, and lower rotational temperatures. The rotational quantum state of a molecule determines the effective dipole moment experienced by the molecule relative to an external electric field. This affects the Stark shift of the molecule, and ultimately how well guided the molecule is in an electrostatic guide. Therefore, the 'guidablility' of each rotational state (as determined from the Monte Carlo simulations of the guiding process), in addition to the rotational state distribution from a thermal equilibrium of molecules exiting the buffer gas cell, were used to predict the rotational state distribution of the molecules at the end of the guide. These values were used as the ground state population distribution in PGOPHER simulations of the experimental spectra, and were found to yield simulated spectra in excellent agreement with the experimental data for ND_3.

Removing the outer radiation heat shield allowed the apparatus to be run with a 17 K cell, using either helium or neon as the buffer gas. The heavier neon gas has a slightly lower thermal velocity at 17 K than helium does at 6 K, which meant the molecules were less affected by velocity boosting in the neon buffer gas cell. Indeed, the translational temperature of the guided beam of ND_3 was similar in a 6 K helium and 17 K neon buffer gas cell operated at standard conditions (peak kinetic energy of 6.92(0.13) K and 5.90(0.01) K, respectively). Although the translational temperatures were similar, the rotational temperature of the molecules exiting the 6 K helium buffer gas cell was lower than for the 17 K neon cell (10 K and 15 K, respectively). The ultimate goal is to use the experimental apparatus as a source of cold molecules for low temperature chemical reactions. The 6 K helium and 17 K neon buffer gas cells provide an excellent opportunity to explore the effect of rotational cooling on branching ratios and reaction rates because the populations of rotational states exiting the guide differ markedly between these two regimes.

The cooling method used in the experimental apparatus is a general technique that can be applied to many different molecules. For example, mass spectrometry was used to characterise cold molecular beams of CH_3F, while (2+1) REMPI spectroscopy was applied to the ammonia isotopologues NHD_2, NH_2D, and NH_3. Despite the importance of cold ion-molecule reactions in the interstellar medium, very little experimental data exits on reaction rates and branching ratios for low temperature reactions due to the technical challenges of generating cold molecules in the laboratory [47]. Instead, trajectory-scaling formulae or extrapolations from room temperature values are commonly used to estimate these parameters. The electrostatic extraction of buffer-gas-cooled beams provides a translationally and rotationally cold source of molecules that can be used in low temperature chemical reactions. As described in the following section, the next stage of the experiment is to combine the buffer gas apparatus with a linear Paul ion trap in order to study reactions between the cold molecular beam and trapped ions in a Coulomb crystal. The rate constants determined in such experiments can then be used to contribute to the astronomical databases currently being developed for low temperature rate constants involving molecules of interest in astrochemistry [44]. They can also be used as a fundamental test of reaction rate theories for low temperature, fast (barrierless) processes.

6.2 Future work

Previously, our laboratory used a room temperature effusive source for the electrostatic quadrupole guide to study reactions of velocity selected polar molecules, such as CH_3F, CH_3Cl, and CH_2F_2, with Ca^+ Coulomb crystals [111]. Reaction rate constants were obtained at translational temperatures close to 1 K, but for rotational energy distributions resembling room temperature. In the future, the effects of rotational cooling on ion-molecule reactions will be studied by using the buffer-gas-cooled molecular source in conjunction with a linear Paul ion trap, as shown in Figure 6.1. Translationally and rotationally cold molecules exit the buffer gas cell, are moved away from the cell by an electrostatic quadrupole guide, and are delivered to the UHV detection chamber containing a linear Paul trap. The cold molecules can then react with either laser cooled Ca^+ ions or molecular ions sympathetically cooled into the Coulomb crystal.

I did some preliminary work on the geometry of the ion trap chamber and basic layout of the trap and accompanying parts within the chamber, in particular the entry of the guide into the trap chamber from the cyrogenic chamber. Laura Pollum undertook the detailed design work and construction of the trap, as described in [207]. The ion trap is currently being operated independently of the buffer gas apparatus

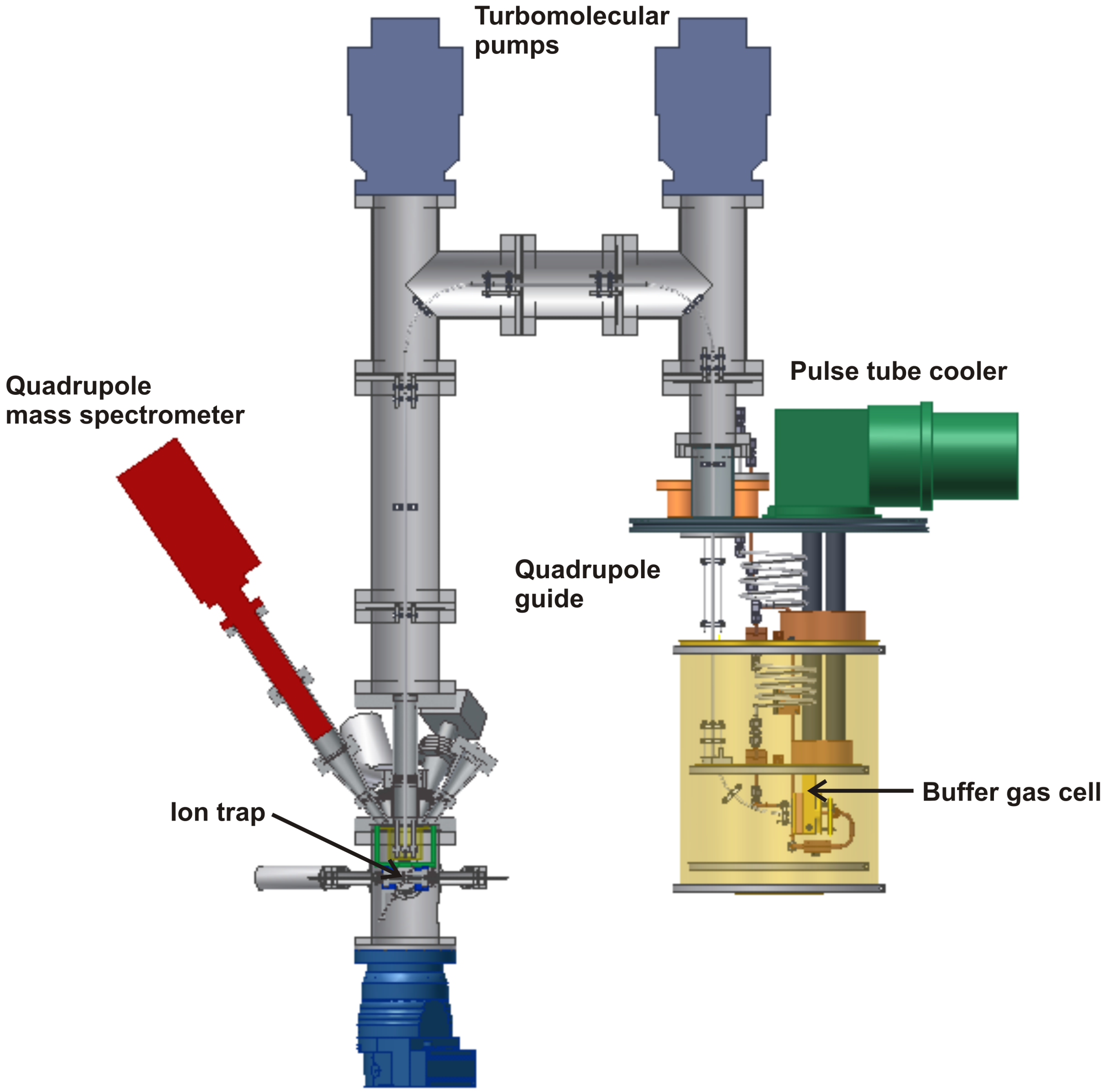

Figure 6.1: Design of the experimental apparatus showing the combined buffer-gas-cooled and electrostatically guided molecular source with a linear Paul ion trap.

to facilitate an investigation into how best to monitor reactions with this trap design. The combination of the buffer gas apparatus with the ion trap is imminent at the time of writing of this thesis. Details of the linear Paul ion trap design are shown in Figure 6.2. The linear Paul ion trap is mounted to a CF152 angled multiport flange for easy insertion into the detection chamber. The electrostatic quadrupole guide enters through the central flange to deliver the cold molecules to the ion trap. A small grounded cup encloses the end of the guide to provide differential pumping between the main buffer gas chamber and the UHV ion trap chamber. A turbomolecular pump attached to the bottom of the trap chamber maintains the UHV. Additionally, molecules are prevented from scattering off the ion trap electrodes by placing a skimmer plate between the end of the guide and the ion trap. A calcium oven is mounted below the ion trap and angled toward the trap centre.

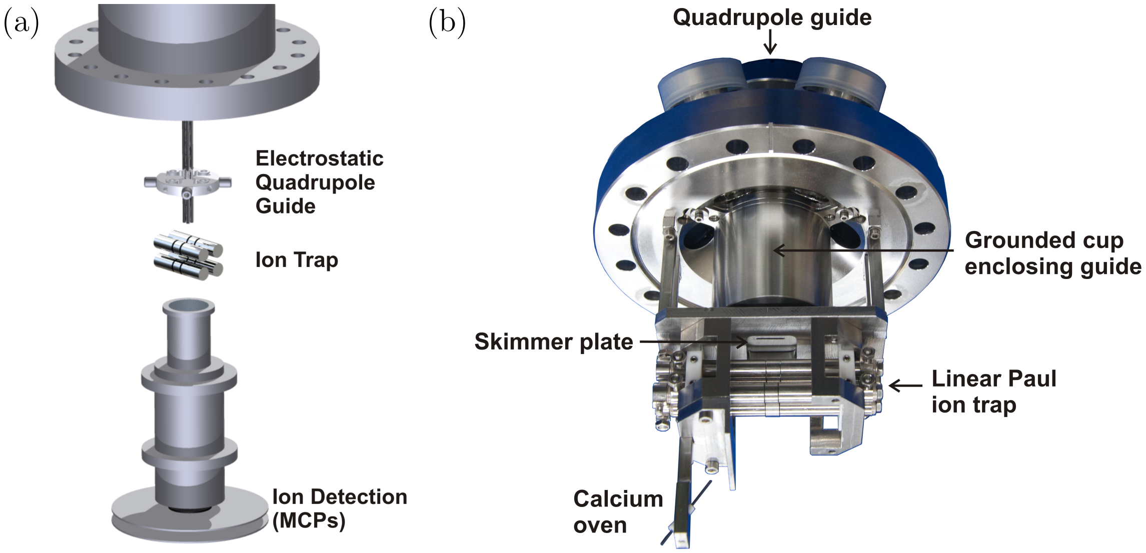

Figure 6.2: (a) Schematic illustrating the combination of the electrostatic guide with a linear Paul ion trap, and subsequent detection with MCPs located at the end of a time-of-flight tube. (b) Design of the linear Paul ion trap currently being constructed, which will be combined with the buffer-gas-cooled molecular source (photograph taken by Laura Pollum).

Ports on the angled multiport flange are used for electrical feedthroughs for the ion trap and calcium oven, a pressure gauge, a leak valve, and a quadrupole mass spectrometer. A time of flight tube and MCPs are positioned perpendicular to the trap axis. The objective lens of the imaging system is also placed perpendicular to the trap axis, on the opposite side of the ion trap to the time of flight tube. Two alignment tools are permanently attached to the ion trap, with a pinhole through which the cooling diode lasers pass; the ionisation beam is off-axis.

A combination of radiofrequency and static DC voltages are used to trap ions in a linear Paul ion trap [208]. The structure of the ensemble of trapped calcium ions is determined by the interaction of the Coulombic repulsion forces between the ions, their kinetic energies (or effective translational temperatures), and the trapping potential of the linear Paul trap [209]. Laser cooling is used to lower the translational temperature of the calcium ions to a few milliKelvin, at which point the ions form a well localised, three-dimensional lattice-like structure known as a Coulomb crystal [210, 211]. The Coulomb crystal can be visualised by using a CCD camera to capture the fluorescence emitted by individual calcium ions during the optical cooling cycle. The ellipsoidal shape of the calcium Coulomb crystal becomes flattened at the outer edges, or a dark core forms along the trap axis, with the addition of co-trapped species [209, 212]. This depends on the relative mass of the ion species involved, as lighter ions are localised closer to the trap axis. Changes in the shape of the crystal can therefore be used to monitor reaction progress with the trapped ionic species. Furthermore, a decrease in the fluorescence of the crystal can be used to directly monitor reactions with the laser cooled atomic ions, as shown in Figure 6.3(b).

Reactions between sympathetically cooled species are shown in Figure 6.3(b). The internal-state population of the sympatetically cooled molecular ions is typically determined by the black-body radiation from the room-temperature experimental apparatus, as co-crystallisation with the Ca^+ ions only cools the translational, and not the rotational, motion of the molecular ions [214]. Recently, however, a cryogenically cooled linear Paul trap has been constructed to address this issue by limiting the black-body radiation experienced by the molecular ions [215].

Once the buffer gas apparatus is combined with the ion trap, the reaction rate constants and branching ratios for a variety of cold ion-molecule reactions will be measured. The series of reactions between guided CH_3F, CH_2F_2 and CH_3Cl and Ca^+ ion Coulomb crystals will be investigated and compared to the results obtained using a room temperature source of molecules to load the electrostatic guide [111]. The apparatus will also be used to study the isotope effects for the H atom transfer in ion-

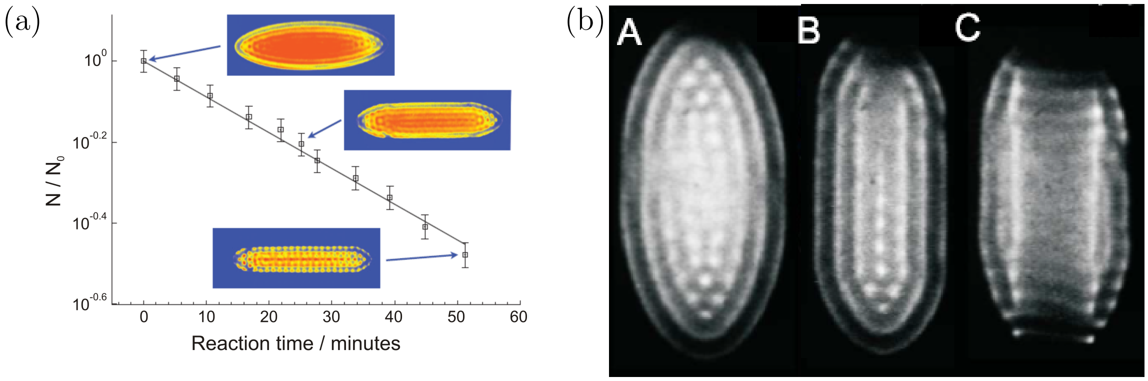

Figure 6.3: (a) Reaction progression between laser cooled and trapped Ca^+ ions in a Coulomb crystal and electrostatically guided CH_3F from a room temperature effusive source. Experimental images were supplied by Martin Bell. (b) Reaction between electrostatically guided ND_3 from a room temperature effusive source and sympathetically-cooled OCS^+ ions. The Ca^+ Coulomb crystal is shown (A) before sympathetic loading, (B) with OCS^+ sympathetically-cooled into the crystal, and (C) following the reaction between OCS^+ and ND_3. Experimental images were supplied by Alex Gingell.

molecule reactions with guided, cold beams of HDO, NH_2D, and NHD_2. An example is shown in Reaction (6.1).

$$\mathrm{Ca^+ + HDO \rightarrow CaOH^+(CaOD^+) + D(H)} \tag{6.1}$$

The reaction of sympathetically cooled ND_3^+ ions with cold guided beams of deuterated analogues of water and ammonia will also be investigated, for which there are a number of reaction channels open. These, and other studies involving polar molecules, will be used to contribute to the astrochemical databases currently being developed for low temperature reaction rate constants. They will also provide important data for comparison with quantum theories of low temperature reactions.

For example, rotationally state-selected ion-dipole reactions have been theoretically studied using rotationally adiabatic capture theory [216]. For the reaction of N^+ with ammonia, this model predicts a negative temperature dependence of the rate constant in all rotational states, but with the lowest two J states exhibiting the most pronounced effect. As the temperature decreases below 50 K, which is the temperature range found in the ISM, the rotational dependence of the reaction rate is predicted to increase. These important predictions about the rotational state dependence of ion-molecule reaction rates are yet to be experimentally verified, decades after the theoretical predictions were first published.

Appendix A

Stark effect

This appendix explains in greater detail how the quantum-state specific Stark energy levels of polar symmetric top molecules (Section A.1) and asymmetric top molecules (Section A.2) are calculated in external electric fields. The Stark energy levels are required to determine the force experienced by polar molecules in electrostatic guides, and were used in the Monte Carlo simulations of the guiding process described in Section 2.4.

A.1 Symmetric top molecules

The rotational energy levels for symmetric-top molecules are described in Section 2.1.2. The zero-field rotational energy levels for oblate (Eq. 2.10) and prolate (Eq. 2.11) symmetric top molecules are used to calculate the elements of the full Hamiltonian matrix (Eq. A.1). Recall from Section 2.2.2 that the Stark Hamiltonian is diagonal in M, and therefore the full Hamiltonian matrix is as well.

$$\langle J'M'K'|H|JMK\rangle = E_{\mathrm{rot}}(J,K)\delta_{J',J}\delta_{K',K} + \langle J'M'K'|H_{\mathrm{Stark}}|JMK\rangle \tag{A.1}$$

Only the z-components of the dipole moment operator contribute to the matrix elements of the Stark Hamiltonian for symmetric-top molecules. Therefore, the wavefunctions and Stark energy levels can be calculated by diagonalising the real symmetric matrix. The diagonalisation is repeated separately for each value of M because of the block-diagonal structure of the matrix.

Figure A.1 shows the Stark effect calculated using this method for two different symmetric top molecules, ND_3 and NH_3, over the range of electric fields typically used in this work. The code was modified from the original in-house built programme written by Martin Bell and described in [158]. Field-induced mixing of states with different J and K values can occur when the electric field is large, such as near the electrodes of the electrostatic guide where the field is approximately 100 kV/cm. This can lead to large deviations in the Stark energy levels from the first-order, linear approximations described in Section 2.2.2, as illustrated in Figure A.1. The effect of inversion splitting (described in the next section) is also important for these molecules, and is included in the energy level calculations.

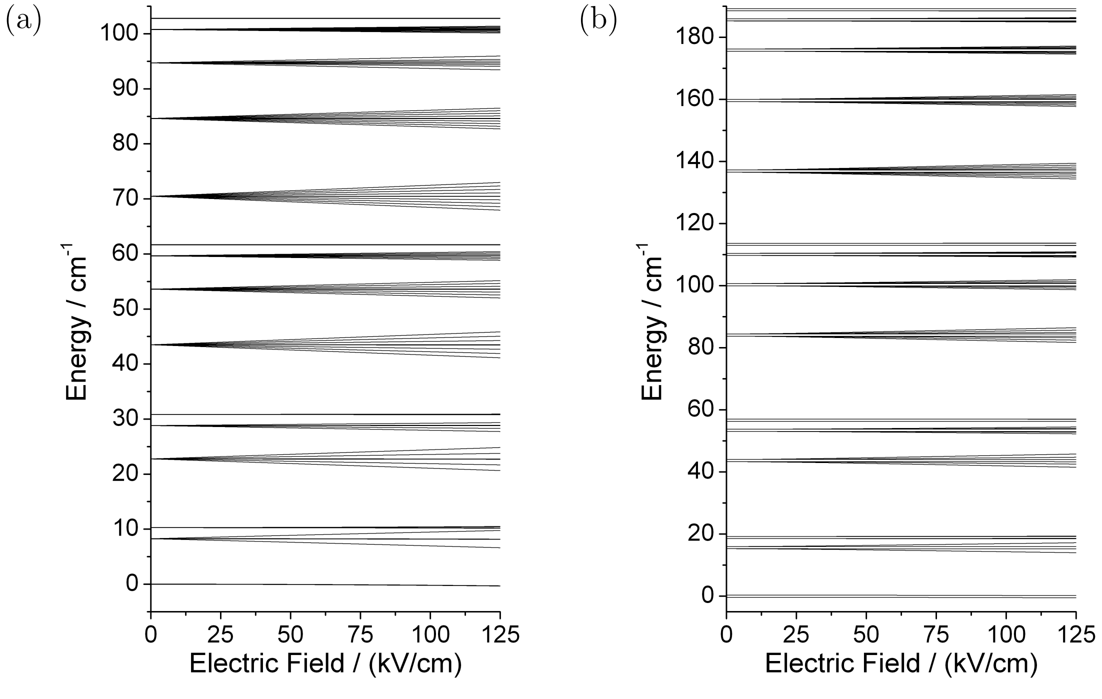

Figure A.1: The calculated Stark effect for symmetric top molecules (a) ND_3 and (b) NH_3 over the range of electric fields typically used in this work.

Inversion splitting

Vibrational inversion can significantly alter the Stark effect experienced by a molecule. The quantum number $|\epsilon = \pm 1\rangle$ can be used to describe the parity of the zero-field eigenstates, leading to the modified basis set shown in Equation A.2 for a symmetric top molecule.

$$|JMK, \epsilon = \pm 1\rangle = \frac{1}{\sqrt{2}}\Big(|JMK\rangle + \epsilon|J - M - K\rangle\Big) \tag{A.2}$$

In the extreme case where the inversion symmetry operation E^* is fully permitted, the linear Stark shift actually vanishes because no permanent dipole moment exists in the vibrational ground state [217]. However, a permanent dipole moment may arise if the ground state (symmetric, $|\epsilon = +1\rangle$) and first excited state (antisymmetric, $|\epsilon = -1\rangle$) of the inversion vibrational motion are close to degeneracy, and an external electric field causes a strong mixing of the two states. This is more likely to occur when the Stark energy is similar to the energy difference of the vibrational states [126]. High electric fields lead to an increased splitting of the inversion energy levels, and therefore strongly hinder molecular inversion; the molecular symmetry axis remains fixed relative to the electric field axis.

Equation 2.29 gives the matrix elements of the Stark Hamiltonian, which can be modified to include the effects of inversion splitting as shown in Equation A.3. The inversion splitting effects are included in the diagonal elements of the Hamiltonian matrix used to calculate the Stark effect for symmetric top molecules.

$$\begin{aligned}\langle JMK, \pm|H_{\text{Stark}}|J+1, MK, \pm\rangle &= -\frac{\mu\varepsilon}{J+1}\sqrt{\frac{((J+1)^2 - K^2)((J+1)^2 - M^2)}{(2J+1)(2J+3)}} \\ \langle JMK, \pm|H_{\text{Stark}}|JMK, \mp\rangle &= -\frac{|MK|}{J(J+1)}\mu\varepsilon\end{aligned} \tag{A.3}$$

Figure A.2 illustrates the effect of inversion splitting by comparing the Stark effect of ND_3 and NH_3 molecules in the $|J, K\rangle = |1, 1\rangle$ state. The difference is related to the higher mass of the deuterium atoms which therefore have a lower tunneling probability through the inversion barrier; thus, ND_3 has a lower inversion rate than NH_3. The tunnelling motion in the ν_2 umbrella vibrational mode will be quenched at smaller electric fields for ND_3, leading to a first-order Stark effect in weaker electric fields compared to NH_3. The smaller energy spacing also leads to a better mixing of the Stark interacting states in ND_3 and a stronger Stark effect compared to NH_3 [126].

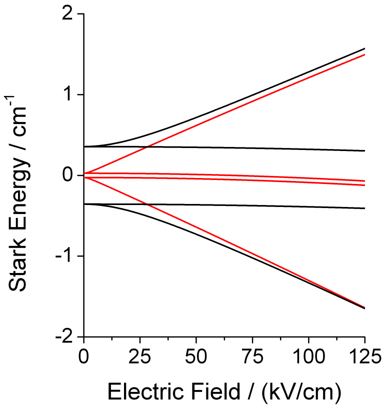

Figure A.2: Calculated Stark effect for ND_3 (red) and NH_3 (black) molecules in the $|J, K\rangle = |1, 1\rangle$ rotational state. ND_3 has a smaller ground-state inversion splitting and exhibits a stronger Stark effect than NH_3 (0.053 cm^{-1} and 0.79 cm^{-1}, respectively [146]).

Non-adiabatic 'Majorana' transitions

When a molecule with a large Stark shift is placed in an inhomogeneous electric field, its Stark energy will depend on its quantum state and location within the field. For example, a molecule in a low-field seeking quantum state will experience a force pushing it toward regions of lower electric field. The magnitude of the force will depend on the gradient of the electric field and the effective dipole moment of the molecule, which is quantum-state dependent. Molecular motion must be adiabatic (molecules must remain in their initial quantum state) with respect to changing electric fields in order for the force calculations to be valid.

Non-adiabatic transitions are more likely to occur when the electric field is switched rapidly because the dipole moment of the molecule cannot evolve quickly enough to maintain its original orientation relative to the electric-field vector. However, the effective translational temperature must be less than 1 mK for this loss mechanism to be significant in electrostatic guiding experiments [218]. Non-adiabatic transitions are also more likely to occur in regions of weak electric field when the Stark energy shifts become small compared to other perturbations. For example, a molecule may be transferred into a hyperfine state with a different projection quantum number (different orientation relative to the electric field) in a weak field due to hyperfine structure couplings [219]. Both types of non-adiabatic transitions are referred to as ‘Majorana’ transitions. Where possible, applying a weak bias field to ensure the electric field is always greater than zero often suppresses these Majorana transitions [220].

One of the reasons that ND_3 is often used in electrostatic guiding experiments rather than the more readily available NH_3 is because it is less likely to undergo Majorana transitions. The Stark shift of ND_3 increases more quickly at lower electric fields compared to NH_3, as seen in Figure A.2. This means there is a smaller range of electric fields in which non-adiabatic transitions are likely to occur, which leads to fewer molecules undergoing a non-adiabatic transition from a low-field seeking to a non-guidable, or weakly guided, state.

A.2 Asymmetric top molecules

Unlike a symmetric top molecule in which two of the principal moments of inertia are equal ($I_\mathrm{C} > I_\mathrm{B} = I_\mathrm{A}$ for oblate symmetric tops, and $I_\mathrm{C} = I_\mathrm{B} > I_\mathrm{A}$ for prolate symmetric tops), an asymmetric molecule has different moments of inertia about each molecular axis ($I_\mathrm{C} > I_\mathrm{B} > I_\mathrm{A}$). This leads to a variation in the projection of the angular momentum on the body-fixed axis as an asymmetric molecule rotates, and means that K is no longer a good quantum number to describe molecular rotation. Instead, the pseudo-quantum number $\tau = K_\mathrm{A} - K_\mathrm{C}$ is used, where K_A and K_C refer to the quantum numbers in the limiting case of a prolate and oblate orientation of the molecule, respectively [126]. To ensure the energy levels increase continuously as τ changes from $-J$ to J, the quantum numbers K_A and K_C are alternately increased and decreased from 0 to J and from J to 0. The rotational eigenstates are therefore labelled as $|J\tau M\rangle$ instead of $|JKM\rangle$.

Additionally, the asymmetric top rotational Hamiltonian has off-diagonal matrix elements that must be included when calculating the zero-field energy levels and wavefunctions. The spherical tensor representation of the rotational Hamiltonian operator is given in Equation A.4, with the three distinct, non-zero components, $T^k_q(B)$, given by in Equations A.5, A.6, and A.7 [221].

$$H_{rot} = \sum_{i\in(a,b,c)} B_i J_i^2 = \sum_{k=0}^{2} T^k(B) \cdot T^k(J,J) \tag{A.4}$$

$$T^0_0(B) = \frac{-1}{\sqrt{3}}(A+B+C) \tag{A.5}$$

$$T^2_0(B) = \frac{1}{\sqrt{6}}(2A-B-C) \tag{A.6}$$

$$T^2_2(B) = T^2_{-2}(B) = \frac{1}{2}(B-C) \tag{A.7}$$

This representation enables the rotational Hamiltonian matrix to be built in the symmetric top basis using standard angular momentum algebra [221], as shown in Equation A.8.

$$\begin{aligned}\langle J'M'K'|H_{rot}|JMK\rangle &= \delta_{M',M}\delta_{J',J} \\ &\times \sum_{k=0}^{2}\sum_{q}(-1)^{J-K'}T_q^k(B)\begin{pmatrix} J & k & J \\ -K' & q & K \end{pmatrix}\langle J||T^k(\mathbf{J},\mathbf{J})||J\rangle \end{aligned} \tag{A.8}$$

The reduced matrix elements can be evaluated using Equation A.9.

$$\langle J||T^k(\mathbf{J},\mathbf{J})||J\rangle = (-1)^k\sqrt{2k+1}(2J+1)J(J+1)\begin{pmatrix} J & J & 1 \\ k & 1 & J \end{pmatrix} \tag{A.9}$$

The rotational Hamiltonian matrix can be diagonalised more efficiently by breaking the matrix into four sub-blocks, which is possible because the inertia tensor exhibits D_2 point group symmetry [157]. Unlike symmetric molecules in which only the $T_0^1(\vec{\mu})$ component of the dipole moment is non-zero (Eq. 2.26), all three terms must be included for asymmetric top molecules because the dipole moment can have components along more than one of the principal axes.

Appendix B

Velocity Distribution Analysis

High frequency noise in the TOF signal makes it difficult to calculate velocity distributions directly from the signal. Instead, a sigmoidal function is used to model the signal, and the velocity distribution is computed from the modelled signal. The Gompertz function (Equation B.1), often used to model population growth, is also commonly used to model TOF signals because the initial growth is more rapid than the approach to the future asymptote. The modelled signal is denoted by S, t is the arrival time of the molecules at the detector, and the other parameters a, t_{c}, and k correspond to the amplitude, centre, and growth coefficient, respectively.

$$S = a \exp\Big(-\exp\big(-k(t - t_{\mathrm{c}})\big)\Big) \tag{B.1}$$

However, comparison of the Gompertz function fit to several other sigmoidal functions reveals that a better fit of the data is obtained using a logistic function, which is based on a dose response curve frequently used in pharmacology (Equation B.2). Again, S is the modelled signal, t is the arrival time, while the parameters a_1, a_2, t_{c}, and p correspond to initial asymptotic value, final asymptotic value, centre, and power.

$$S = \frac{a_1 - a_2}{1 + (t/t_{\mathrm{c}})^p} + a_2 \tag{B.2}$$

A TOF trace obtained for ND_3 with a flow rate of 2.0 sccm and a helium buffer gas inlet pressure of 0.6 mbar for a 6 K cell is used to compare the Gompertz function and logistic function fits of the signal. The fits were done using OriginPro 8.5.1 (Academic), and the calculated parameters with corresponding errors are given in Table B.1. The raw data and both the modelled Gompertz and Logistic functions are shown in Figure B.1, along with their respective residuals from the fit. The sum of the residual squares was 185.48173 (145.8375) with an adjusted R^2 value of 0.97756 (0.98199) for the Gompertz function (logistic function) fit.

Table B.1: Typical values and their standard deviations for parameters used to fit the TOF traces, shown for both a Gompertz function (left) and logistic function (right). The experimental trace and modelled fits are shown in Figure B.1.

Gompertz function			Logistic function		
Parameter	Value	Error	Parameter	Value	Error
a	0.98787	1.26187×10^{-4}	a_1	-0.03516	5.46547×10^{-4}
t_c	20.58703	0.01217	a_2	0.99707	1.30293×10^{-4}
k	0.09358	1.30137×10^{-4}	t_c	23.41808	1.547×10^{-2}
			p	3.01924	4.39×10^{-3}

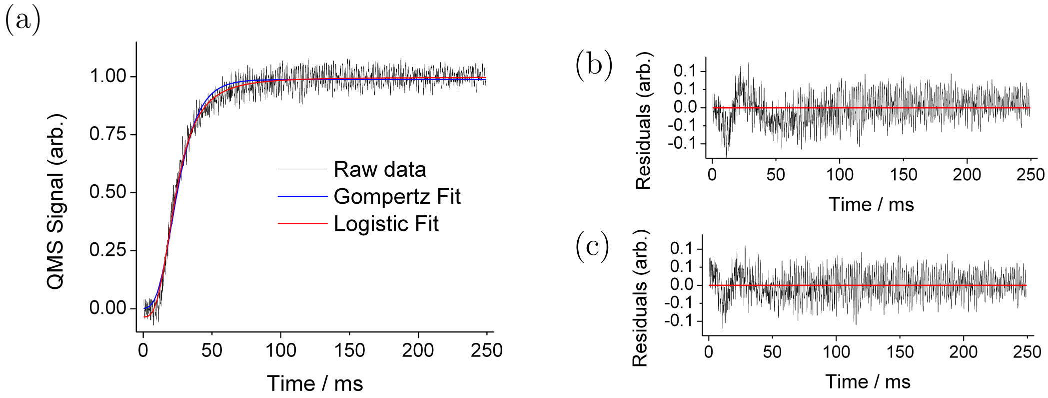

Figure B.1: (a) A representative TOF trace (black) is shown with a Gompertz function (blue) and a logistic function (red) fit to the experimental data. The residuals of the fits are shown in (b) for the Gompertz function and (c) for the logistic function.

Both functions yield good fits of the data at the later time period, which corresponds to the low velocity molecules arriving at the detector. The fit deviates from the signal at early time periods for the Gompertz fit, corresponding to the fast molecules arriving at the detector. This is less pronounced in the Logistic function fit. The velocity distribution of the molecular beam can be determined from the arrival time of the molecules at the detector, as described in Section 4.2. Figure B.2 shows the velocity distribution calculated directly from the raw data and from the modelled signal using the Gompertz and logistic function. It supports the conclusion that the logistic function provides a very good fit of the data, and is a better fit than the Gompertz function.

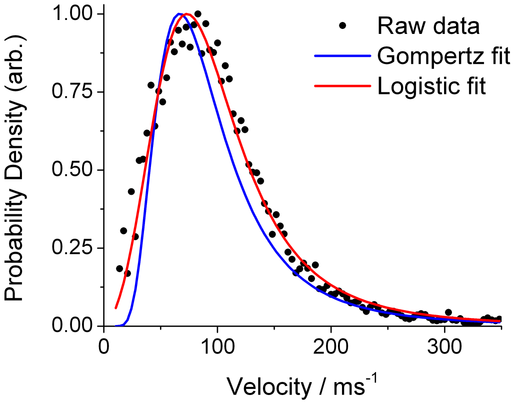

Figure B.2: The ND_3 velocity distribution calculated directly from the experimental data (black dots), or calculated from a Gompertz function (blue) and logistic function (red) fit of the experimental data.

Appendix C

TOF-Mass Spectrometry

In the Wiley McLaren type time-of-flight mass spectrometer (TOF-MS) used in this work, ions are formed in the ionisation region and then accelerated toward the ion detector by a series of constant electric fields. The charge to mass ratio, q/m, of the ions determines the velocity of the ions in the field free drift tube located after the acceleration region, and consequently the arrival time of the ions at the detector (Figure C.1). For ions with the same charge, lighter species will reach the detector first.

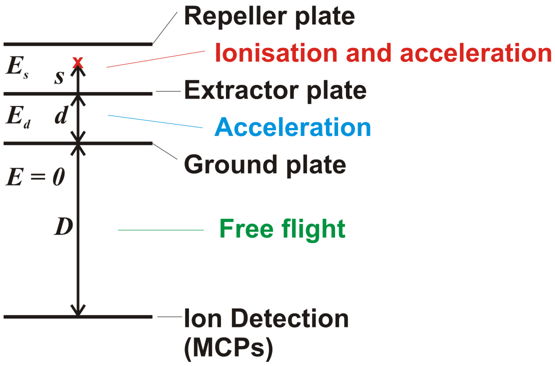

Figure C.1: Schematic showing the geometry of a Wiley McLaren type of time-of-flight mass spectrometer. Of particular note is the double-field source with two accelerating regions that significantly improves the resolution of this non-magnetic spectrometer.

The entire mass spectrum can be recorded every few microseconds using this type of TOF-MS. The resolution of this design of TOF spectrometer is limited by the initial spatial and kinetic energy distribution of the ions, which results in a spread in their arrival time at the detector. Generally, a compromise must be made between space and energy resolution, since adjustment of the system parameters often improves the space resolution at the expense of energy resolution (and vice versa). Use of a double-field source with two accelerating regions minimises the compromises that must be made and significantly improves the resolution.

The total flight time $t(U_0, s)$ of the molecules from ionisation to detection is shown in Equation C.1, with the parameters defined in Figure C.1. In the TOF-MS used experimentally, $d = 25.6$ mm and $D = 193.58$ mm, while the distance s ranges between about 3 mm and 8 mm, depending on laser alignment and optimisation of the signal. Typical voltage settings for the TOF-MS are given in Table C.1.

$$\begin{aligned}
t(U_0, s) &= t_s + t_d + t_D && \text{(C.1)}\\
t_s &= 1.02\frac{(2m)^{1/2}}{qE_s}[(U_0 + qsE_s)^{1/2} \pm (U_0)^{1/2}] && \text{(C.2)}\\
t_d &= 1.02\frac{(2m)^{1/2}}{qE_d}[U^{1/2} - (U_0 + qsE_s)^{1/2}] && \text{(C.3)}\\
t_D &= 1.02\frac{(2m)^{1/2}D}{2U^{1/2}} && \text{(C.4)}
\end{aligned}$$

Table C.1: Typical voltage settings for the various components of the time-of-flight-mass spectrometer used to detect the molecular ions.

Component	Voltage / V
Repeller plate	+300
Extractor plate	+217
Ground plate	0
Front MCP	-1900
Back MCP	0
Anode (signal output)	+100

References

[1] T. Hänsch and A. Schawlow, *Opt. Commun.*, **13**, 68 (1975).

[2] D. Wineland and H. Dehmelt, *Bull. Am. Phys. Soc.*, **20**, 637 (1975).

[3] S. Chu, L. Hollberg, J.E. Bjorkholm, A. Cable and A. Ashkin, *Phys. Rev. Lett.*, **55**, 48 (1985).

[4] C. J. Foot, *Atomic Physics*, Oxford, 2005.

[5] E.S. Schuman, J.F. Barry and D. DeMille, *Nature*, **467**, 820 (2010).

[6] A. Fioretti, D. Comparat, A. Crubellier, O. Dulieu, F. Masnou-Seeuws and P. Pillet, *Phys. Rev. Lett.*, **80**, 4402 (1998).

[7] J. Weinstein, R. deCarvalho, T. Guillet, B. Friedrich and J. Doyle, *Nature*, **395**, 148 (1998).

[8] L. Carr, D. DeMille, R. Krems and J. Ye, *New J. Phys.*, **11**, 055049 (2009).

[9] D. Herschbach, *Faraday Disscus.*, **142**, 9 (2009).

[10] O. Dulieu, R. Krems, M. Weidemüller and S. Willitsch, *Phys. Chem. Chem. Phys.*, **13**, 18703 (2011).

[11] G. Quéméner and P. Julienne, *Chem. Rev.*, **112**, 4949 (2012).

[12] O. Dulieu and C. Gabbanini, *Rep. Prog. Phys.*, **72**, 086401 (2009).

[13] P. W. Atkins, *Molecular Quantum Mechanics*, Oxford, 1970.

[14] D. Skouteris, D. E. Manolopoulos, W. S. Bian, H. J. Werner, L. H. Lai and K. P. Liu, *Science*, **286** 1713 (1999).

[15] N. Balakrishnan, *J. Chem. Phys.*, **121**, 5563 (2004).

[16] R. Krems, B. Friedrich and W. C. Stwalley, *Cold Molecules: Theory, Experiment, Applications*, CRC Press, 2009.

[17] R. V. Krems, *Int. Rev. Phys. Chem.*, **24**, 99 (2005).

[18] J. van Veldhoven, J. Küpper, H. L. Bethlem, B. Sartakov, A. J. A. van Roij and G. Meijer, *Eur. Phys. J. D*, **31**, 337 (2004).

[19] M. Quack, *Angew. Chem.*, **114**, 4812 (2002).

[20] M. Quack and J. Stohner, *Chirality*, **13**, 745 (2001).

[21] P. Schwerdtfeger and R. Bast, *J. Am. Chem. Soc.*, **126**, 1652 (2004).

[22] J. Crassous, C. Chardonnet, T. Saue and P. Schwerdtfeger, *Org. Biomol. Chem.*, **3**, 2218 (2005).

[23] J. J. Hudson, B. E. Sauer, M. R. Tarbutt and E. A. Hinds, *Phys. Rev. Lett.*, **89**, 023003 (2002).

[24] J. K. Webb, M. T. Murphy, V. V. Flambaum, V. A. Dzuba, J. D. Barrow, C. W. Churchill, J. X. Prochaska and A. M. Wolfe, *Phys.Rev. Lett.*, **87**, 091301 (2001).

[25] R. Srianand, H. Chand, P. Petitjean and B. Aracil, *Phys. Rev. Lett.*, **92**, 121302 (2004).

[26] E. Reinhold, R. Buning, U. Hollenstein, A. Ivanchik, P. Petitjean and W. Ubachs, *Phys. Rev. Lett.*, **96**, 151101 (2006).

[27] A. Shelkovnikov, R. J. Butcher, C. Chardonnet and A. Amy-Klein, *Phys. Rev. Lett.*, **100**, 150801 (2008).

[28] A. Micheli, G. K. Brennen and P. Zoller, *Nat. Phys.*, **2**, 341 (2006).

[29] D. DeMille, *Phys. Rev. Lett.*, **88**, 067901 (2002).

[30] S. Ospelkaus,K.-K. Ni, D. Wang, M. H. G. de Miranda, B. Neyenhuis, G. Quemener, P. S. Julienne, J. L. Bohn, D. S. Jin, and J. Ye, *Science*, **327**, 853 (2010).

[31] K.-K. Ni, S. Ospelkaus, D. Wang, G. Quemener, B. Neyenhuis, M. H. G. de Miranda, J. L. Bohn, D. S. Jin, J. Ye, *Nature*, **464**, 1324 (2010).

[32] R. V. Krems, *Phys. Chem. Chem. Phys.*, **10** 4079 (2008).

[33] P. F. Weck and N. Balakrishnan, *Int. Rev. Phys. Chem.*, **25**, 283 (2006).

[34] J. M. Hutson and P. Soldan, *Int. Rev. Phys. Chem.*, **25** 497 (2006).

[35] P. Staanum, S. D. Kraft, J. Lange, R. Wester and M. Weidemüller, *Phys. Rev. Lett.*, **96**, 023201 (2006).

[36] N. Zahzam, T. Vogt, M. Mudrich, D. Comparat, P. Pillet, *Phys. Rev. Lett.* **96**, 023202 (2006).

[37] J. Turner, P. Anderson, T. Lachlan-Cope, S. Colwell, T. Phillips, A. Kirchgaessner, G. J. Marshall, J. C. King, T. Bracegirdle, D. G. Vaughan, V. Lagun and A. Orr, *J. Geophys. Res.*, **114**, D24102 (2009).

[38] E. Herbst and T. J. Millar, *The chemistry of cold interstellar cloud cores*, World Scientific Publishing, 2008.

[39] R. Sahai and L. A. Nyman, *Astrophys. J.*, **487**, L155L159 (1997).

[40] D.E. Woon, *The Astrochymist*, www.astrochymist.org/astrochymist_ism.html, (2010).

[41] S. Iglesias Groth, A. Manchado, D.A. García-Hernández, J.I. Gonzlez-Hernández and D.L. Lambert, *Astrophys. J. Lett.*, **685**, L55 (2008).

[42] E. Herbst and W. Klemperer, *Astrophys. J.*, **185**, 505 (1973).

[43] J. Woodall, M. Agúndez, A. J. Markwick-Kemper, and T. J. Millar, *Astrnom. Astrophys.*, **466**, 1197 (2007).

[44] The Ohio State University, *Astrophysical Chemistry Group*, http://www.physics.ohio-state.edu/eric/research.html

[45] T. Su and W. J. Chesnavich, *J. Chem. Phys.*, **76**, 5183 (1982).

[46] A. Canosa, *EPJ Conf.*, **18**, 02003 (2010).

[47] V. Wakelam, I. W. M. Smith, E. Herbst, J. Troe, W. Geppert, H. Linnartz, K. Ö berg, E. Roueff, M. Agundez, P. Pernot, H. M. Cuppen, J. C. Loison and D. Talbi, *Space Sci. Rev.*, **156**, 13 (2010).

[48] M.J. Frost, P. Sharkey and I.W.M. Smith, *J. Phys. Chem.*, **97**, 12254 (1993).

[49] M.A. Smith, *Ion Molecule Reaction Dynamics at very low Temperatures*, John Wiley & Sons Ltd, New York, 1994.

[50] D. Gerlich and M. Smith, *Phys. Scripta*, **73**, C25 (2006).

[51] S.E. Barlow, G.H. Dunn and M. Schauer, *Phys. Rev. Lett.*, **52**, 902 (1984).

[52] G. Scoles, *Atomic and molecular beam methods*, Oxford University Press, 1988.

[53] M. Hawley, T.L. Mazely, L.K. Randeniya, R.S. Smith, X.K. Zeng and M.A. Smith, *Int. J. Mass Spectrom. Ion Processes*, **97**, 55 (1990).

[54] S. R. Mackenzie and T. P. Softley, *J. Chem. Phys.*, **101**, 10609 (1994).

[55] C. W. Hsu and C. Y. Ng, *J. Chem. Phys.*, **101**, 5596 (1994).

[56] M.A. Smith and M. Hawley, *Adv. Gas Phase Ion. Chem.*, **1**, 167 (1992).

[57] C. Naulin and M. Costes, *Chem. Phys. Lett.*, **310**, 231 (1999).

[58] C. Berteloite, M. Lara, A. Bergeat, S.D. Le Picard, F. Dayou, K.M. Hickson, A. Canosa, C. Naulin, J.M. Launay, I.R. Sims and M. Costes, *Phys. Rev. Lett.*, **105**, 203201 (2010).

[59] R.A. Phaneuf, C.C. Havener, G.H. Dunn and A. Muller, *Reports on Progress in Physics*, **62**, 1143 (1999).

[60] D. Gerlich, *J. Chem. Soc. Faraday Trans.*, **89**, 2199 (1993).

[61] A. B. Henson, S. Gersten, Y. Shagam, J. Narevicius and E. Narevicius, *Science*, **338**, 234 (2012).

[62] G. Dupeyrat, J.B. Marquette and B.R. Rowe, *Phys. Fl.*, **28**, 1273 (1985).

[63] I.R. Sims, J.L. Queffelec, A. Defrance, C. Rebrion-Rowe, D. Travers, P. Bocherel, B.R. Rowe and I.W.M. Smith, *J. Chem. Phys.*, **100**, 4229 (1994).

[64] D.B. Atkinson and M.A. Smith, *Rev. Sci. Instrum.*, **66**, 4434 (1995).

[65] A. Canosa, F. Goulay, I.R. Sims and B.R. Rowe, *Gas Phase Reactive Collisions at very Low Temperature: Recent Experimental Advances and Perspectives*, Imperial College Press, 2008.

[66] K. M. Jones, E. Tiesinga, P. D. Lett and P. S. Julienne *Rev. Mod. Phys.*, **78**, 483 (2006).

[67] H. J. Metcalf and P. van der Straten, *J. Opt. Soc. Am. B*, **20**, 887 (2003).

[68] M. Schnell and G. Meijer, *Angew. Chem. Int. Ed.*, **48**, 6010 (2009).

[69] M. Viteau, A. Chotia, M. Allegrini, N. Bouloufa, O. Dulieu, D. Comparat and P. Pillet, *Science* **321**, 232 (2008).

[70] J. Deiglmayr, A. Grochola, M. Repp, K. Mörtlbauer, C. Glück, J. Lange, O. Dulieu, R. Wester and M. Weidemüller, *Phys. Rev. Lett.*, **101**, 133004 (2008).

[71] J. Weiner, V. S. Bagnato, S. Zilio and P. S. Julienne, *Rev. Mod. Phys.*, **71**, 1 (1999).

[72] F. Masnou-Seeuws and P. Pillet, *Adv. Atom. Mol. Opt. Phys.*, **47**, 53 (2001).

[73] W. C. Stwalley and H.Wang, *J. Mol. Spectrosc.*, **195**, 194 (1999).

[74] T. Köhler, K. Góral and P. S. Julienne, *Rev. Mod. Phys.*, **78**, 1311 (2006).

[75] C. Chin, R. Grimm, P. Julienne and E. Tiesinga, *Atomic Physics*, arXiv:0812.1496 (2009).

[76] S. Thompson, E. Hodby and C. Wieman, *Phys. Rev. Lett.*, **95**, 190404 (2005).

[77] K. Winkler, F. Lang, G. Thalhammer, P. v. d. Straten, R. Grimm and J. Hecker Denschlag, *Phys. Rev. Lett.*, **98**, 043201 (2007).

[78] J. G. Danzl, E. Haller, M. Gustavsson, M. J. Mark, R. Hart, N. Bouloufa, O. Dulieu, H. Ritsch and H.-C. Nägerl, *Science*, **321**, 1062 (2008).

[79] K.-K. Ni, S. Ospelkaus, M. H. G. de Miranda, A. Pe'er, B. Neyenhuis, J. J. Zirbel, S. Kotochigova, P. S. Julienne, D. S. Jin and J. Ye, *Science*, **322**, 231 (2008).

[80] W. D. Phillips, *Rev. Mod. Phys.*, **70**, 721 (1998).

[81] E.S. Schuman, J.F. Barry, D.R. Glenn and D. DeMille, *Phys. Rev. Lett.*, **103**, 223001 (2009).

[82] J. M. Hollas, *Modern Spectroscopy*, Wiley, 2004.

[83] D. J. Berkeland and M. G. Boshier, *Phys. Rev. A*, **65**, 033413 (2002).

[84] B. K. Stuhl, M. T. Hummon, M. Yeo, G. Quéméner, J. L. Bohn and J. Ye, *Nature*, **492**, 398 (2012).

[85] J. Kim, B. Friedrich, D.P. Katz, D. Patterson, J.D. Weinstein, R. deCarvalho and J.M. Doyle, *Phys. Rev. Lett.*, **78**, 3665 (1997).

[86] R. deCarvalho, J.M. Doyle, B. Friedrich, T. Guillet, J. Kim, D. Patterson and J. Weinstein, *Eur. Phys. J. D*, **7**, 289 (1999).

[87] D.R. Willey, D.N. Bittner and F.C. Delucia, *Mol. Phys.*, **67**, 455 (1989).

[88] D. Egorov, W. C. Campbell, B. Friedrich, S. E. Maxwell, E. Tsikata, L. D. van Buuren and J. M. Doyle, *Eur. Phys. J. D*, **31**, 307 (2004).

[89] W. C. Campbell, E. Tsikata, H. I. Lu, L. D. van Buuren and J. M. Doyle, *Phys. Rev. Lett.*, **98**, 213001 (2007).

[90] D. Patterson, Ph.D. Thesis, Harvard University (2010).

[91] C. Sommer, L.D. vanBuuren, M.Motsch, S.Pohle, J.Bayerl, P.W.H.Pinkse and G.Rempe, *Faraday Disscus.*, **142**, 203 (2009).

[92] J. Doyle, B. Friedrich, R. Krems and F. Masnou-Seeuws, *Eur. Phys. J. D*, **31**, 149 (2004).

[93] M. S. Elioff, J. J. Valentini and D.W. Chandler, *Science*, **302**, 1940 (2003).

[94] N.-N. Liu and H. Loesch, *Phys. Rev. Lett.*, **98**, 103002 (2007).

[95] N.-N. Liu and H. Loesch, *J. Phys. Chem. A 2010*, **114**, 3247 (2009).

[96] D. Levy, *Science*, **214** 263 (1981).

[97] E. Narevicius, A. Libson, M. F. Riedel, C. G. Parthey, I. Chavez, U. Even and M. G. Raizen, *Phys. Rev. Lett.*, **98**, 103201 (2007).

[98] S. van de Meerakker, H. Bethlem, N. Vanhaecke and G. Meijer, *Chem. Rev.*, **112**, 4828 (2012).

[99] S.A. Meek, H. Conrad and G. Meijer, *New J. Phys.*, **110**, 1829 (2012).

[100] A. Osterwalder, S. A. Meek, G. Hammer, H. Haak and G. Meijer, *Phys. Rev. A*, **81**, 051401 (2010).

[101] S. D. Hogan, Ch. Seiler and F. Merkt, *Phys. Rev. Lett.*, **103** 123001 (2009).

[102] H. L. Bethlem, G. Berden and G. Meijer, *Phys. Rev. Lett.*, **83**, 1558 (1999).

[103] N. Vanhaecke, U. Meier, M. Andrist, B. H. Meier and F. Merkt, *Phys. Rev. A*, **75**, 031402 (2007).

[104] E. Narevicius, A. Libson, C. G. Parthey, I. Chavez, J. Narevicius, U. Even, M. G. Raizen, *Phys. Rev. Lett.*, **100**, 093003 (2008).

[105] E. Narevicius, A. Libson, C. G. Parthey, I. Chavez, J. Narevicius, U. Even and Mark G. Raizen, *Phys. Rev. A*, **77**, 051401 (2008).

[106] B. Friedrich and D. Herschbach, *Phys. Rev. Lett.*, **74**, 4623 (1995).

[107] R. Fulton, A. I. Bishop and P. F. Barker, *Phys. Rev. Lett.*, **93**, 243004 (2004).

[108] P. F. Barker and M. N. Shneider, *Phys. Rev. A*, **66**, 065402 (2002).

[109] A. Trimeche, M. N. Bera, J. P. Cromières, J. Robert and N. Vanhaecke, *Euro. Phys. J. D*, **65**, 263 (2011).

[110] S. A. Rangwala, T. Junglen, T. Rieger, P. W. H. Pinkse and G. Rempe, *Phys. Rev. A*, **67**, 043406 (2003).

[111] A.D. Gingell, M.T. Bell, J.M. Oldham and T.P. Softley, *J. Chem. Phys.*, **133**, 194302 (2010).

[112] B. Ghaffari, J. M. Gerton, W. I. McAlexander, K. E. Strecker, D. M. Homan and R. G. Hulet, *Phys. Rev. A*, **60**, 3878 (1999).

[113] E. Nikitin, E. Dashevskaya, J. Alnis, M. Auzinsh, E. R. I. Abraham, B. R. Furneaux, M. Keil, C. McRaven, N. Shafer-Ray and R. Waskowsky, *Phys. Rev. A*, **68**, 023403 (2003).

[114] M. Zeppenfeld, M. Motsch, P. W. H. Pinkse and G. Rempe, *Phys. Rev. A*, **80**, 041401 (2009).

[115] M. Zeppenfeld, B. G. U. Englert, R. Glöckner, A. Prehn, M. Mielenz, C. Sommer, L. D. van Buuren, M. Motsch and G. Rempe, *Nature*, **491**, 570 (2012).

[116] J. Kpper and J. M. Merritt, *Int. Rev. Phys. Chem.*, **26**, 249 (2007).

[117] M. Y. Choi, G. E. Douberly, T. M. Falconer, W. K. Lewis, C. M. Lindsay, J. M. Merritt, P. L. Stiles and R. E. Miller, *Int. Rev. Phys. Chem.*, **25**, 15 (2006).

[118] S. Goyal, D.L. Schutt and G. Scoles, *Phys. Rev. Lett.*, **69**, 933 (1992).

[119] J. Higgins, C. Callegari, J. Reho, F. Stienkemeier, W.E. Ernst, M. Gutowski and G. Scoles, *J. Phys. Chem. A*, **102**, 4952 (1998).

[120] M. Mudrich, O. Bünermann, F. Stienkemeier, O. Dulieu and M. Weidemüller, *Eur. Phys. J. D*, **31**, 291 (2004).

[121] C.J. Burnham, S.S. Xantheas, M.A. Miller, B.E. Applegate and R.E. Miller, *J. Chem. Phys.*, **117**, 1109 (2002).

[122] P. B. Moon, C. T. Rettner and J. P. Simons, *J. Chem. Soc. Faraday Trans.*, **74**, 630 (1978).

[123] M. Gupta and D. Herschbach, *J. Phys. Chem. A*, **103**, 10670 (1999).

[124] M. Gupta and D. Herschbach, *J. Phys. Chem. A*, **105**, 1626 (2001).

[125] S. Deachapunya, P. J. Fagan, A. G. Major, E. Reiger, H. Ritsch, A. Stefanov, H. Ulbricht and M. Arndt, *Eur. Phys. J. D*, **46**, 307 (2008).

[126] C. Sommer, Ph.D. Dissertation, Max-Planck-Institut für Quantenoptik, Garching and Technische Universität München (2011).

[127] X. Wu, S. Chervenkov, C. Sommer, J. Bayerl, A. Rohlfes, M. Zeppenfeld and G. Rempe, *Conference on Cold and Ultracold Molecules*, Centrifuge deceleration of electrically guided continuous supersonic beams of cold polar molecules, Obergurgl, 2012.

[128] W.D. Geppert, D. Reignier, T. Stoecklin, C. Naulin, M. Costes, D. Chastaing, S.D. LePicard, I.R. Sims and I.W.M. Smith, *Phys. Chem. Chem. Phys.*, **2**, 2873 (2000).

[129] J.P. Toennies, A.F. Vilesov and K.B. Whaley, *Phys. Today*, **54**, 31 (2001).

[130] S. Y. T. van de Meerakker, N. Vanhaecke and G. Meijer, *Annu. Rev. Phys. Chem.*, **57**, 159 (2006).

[131] S. D. Hogan, A.W. Wiederkehr, H. Schmutz and F. Merkt, *Phys. Rev. Lett.*, **101**, 143001 (2008).

[132] I. W. Smith, *Low Temperature and Cold Molecules*, Imperial College Press, 2008.

[133] D. Jin and J. Ye, *Chem. Rev.*, **112**, 4801 (2012).

[134] M.T. Bell and T.P. Softley, *Molecular Physics*, **107**, 99 (2009).

[135] C. Sommer, M. Motsch, S. Chervenkov, L.D. van Buuren, M. Zeppenfeld, P.W.H. Pinkse, and G. Rempe, *Phys. Chem*, (2010).

[136] D. Patterson and J.M. Doyle, *J. Chem. Phys.*, **126**, 154307 (2007).

[137] W. C. Campbell and J. M. Doyle, *Cold molecules: Theory, experiment, applications*, CRC Press (2009).

[138] S. E. Maxwell, N. Brahms, R. DeCarvalho, D. R. Glenn, J. S Helton, S. V. Nguyen, D. Patterson, J. Petricka, D. DeMille and J. M. Doyle, *Phys. Rev. Lett.*, **95**, 173201 (2005).

[139] M.R. Hutzler, M. F. Parsons, Y. V. Gurevich, P. W. Hess, S. B. Petrik, A. C. Vutha, D. DeMille, G. Gabrielse and J. M. Doyle, *Phys. Chem. Chem. Phys.*, **13**, 18976 (2011).

[140] S. M. Skoff, R. J. Henricks, C. D. J. Sinclair, J. J. Hudson, D. M. Segal, B. E. Sauer, E. A. Hinds and M. R. Tarbutt, *Phys. Rev. A*, **83**, 023418 (2011).

[141] N. Hutzler, H. Lu, and J. Doyle, *Chem. Rev.*, **112**, 4803 (2012).

[142] J. M. Lafferty, *Foundations of Vacuum Science and Technology*, John Wiley and Sons Ltd., New York, 1998.

[143] J. B. Hasted, *Physics of Atomic Collisions*, Elsevier, 1972.

[144] R. C. Forrey, V. Kharchenko, N. Balakrishnan and A. Dalgarno, *Phys. Rev. A.*, **59**, 2146 (1999).

[145] S.V. Khristenko, A.I. Maslov and V.P. Shevelko, *Molecules and Their Spectroscopic Properties*, Springer, 1998.

[146] C. H. Townes and A. L. Schawlow, *Microwave Spectroscopy*, Dover Publications, New York, 1975.

[147] G. Danby, D.R. Flower, E. Kochanski, L. Kurdi, P. Valiron, G.H.F. Diercksen, *J. Phys. B: At. Mol. Opt. Phys.*, **19**, 2891 (1986).

[148] K. Tanaka, H. Ito and T. Tanaka, *J. Chem. Phys.*, **87**, 1557 (1987).

[149] D. Papousek, Z. Papouskova and D. P. Chong, *J. Phys. Chem.*, **99**, 15387 (1995).

[150] H. Akagia, K. Yokoyamaa, A. Yokoyamaa and A. Wadab, *J. Mol. Spectrosc.*, **231**, 37 (2005).

[151] E. W. Vanstryland and R. L. Shoemaker, *J. Chem. Phys.*, **64**, 4968 (1976).

[152] A. Sushkov and D. Budker, *Phys. Rev. A*, **77**, 042707 (2008).

[153] R. K. Pathria, *Statistical Mechanics*, Butterworth-Heinemann, 1996.

[154] H. Lu, J. Rasmussen, M. J. Wright, D. Patterson and J. M. Doyle, *Phys. Chem. Chem. Phys.*, **13**, 18986 (2011).

[155] J. F. Barry, E. S. Shuman and D. DeMille, *Phys. Chem. Chem. Phys.*, **13**, 18976 (2011).

[156] L. D. van Buuren, C. Sommer, M. Motsch, S. Pohle, M. Schenk, J. Bayerl, P. W. H. Pinkse and G. Rempe, *Phys. Rev. Lett.*, **102**, 033001 (2009).

[157] R. N. Zare, *Angular Momentum: Understanding Spatial Aspects in Chemistry and Physics*, Wiley, 1988.

[158] M.T. Bell, DPhil. Thesis, University of Oxford (2008).

[159] S. Choi and B. Bernstein, *J. Chem. Phys.*, **85**, 150 (1986).

[160] B. Friedrich and D. R. Herschbach, *Nature*, **353**, 412 (1991).

[161] T. Junglen, T. Rieger, S. A. Rangwala, P. W. H. Pinkse and G. Rempe, *Eur. Phys. J. D*, **31**, 365 (2004).

[162] D. C. Clary, *Annu. Rev. Phys. Chem.*, **41**, 61 (1990).

[163] M. Motsch, C. Sommer, M. Zeppenfeld, L. D. van Buuren, G. Rempe and P. W. H. Pinkse, *New J. Phys.*, **11**, 055030, (2009).

[164] H.M. Cave, K.-C. Tseng, J.-S. Wu, M.C. Jermy, Y.-Y Lian, S.P. Krumdieck,T.-C. Kuo and M.-Z. Wu, *16th Australasian Fluid Mechanics Conference*, Modelling Unsteady Processes with the Direct Simulation Monte Carlo Technique,Gold Coast, Australia, 2007.

[165] H. Tsuji, T. Sekiguchi, T. Mori, T. Momose, and H. Kanamori, *J. Phys. B: At. Mol. Opt. Phys.*, **43**, 095202 (2010).

[166] T. Junglen, Ph.D. Dissertation, Max-Planck-Institut für Quantenoptik, Garching and Technische Universität München (2005).

[167] F.M.H. Crompvoets, Ph.D. Thesis, Radboud Universiteit Nijmegen (2004).

[168] J. L. Pittman and P.B. O'Connor, *J Am Soc Mass Spectrom*, **16**, 441 (2005).

[169] B. Bertsche and A. Osterwalder, *Phys. Chem. Chem. Phys.*, **13**, 18954 (2011).

[170] F. Pobell, *Matter and Methods at Low Temperatures*, Second Edition, Springer, 1996.

[171] J. W. Ekin, *Experimental Techniques for Low Temperature Measurements*, Oxford, 2006.

[172] G. W. Swift, *J. Acoustic Soc. Amer.*, **84**, 1145 (1988).

[173] R. Radebaugh M. Lewis, E. Luo, J. M. Pfotenhauer, G. F. Nellis et al., *AIP Conf. Proc.*, **823**, 59 (2006).

[174] A. C. Ruffin, *Fatigue and Fracture*, Vol. 19, ASM International Handbook (1996).

[175] Lake Shore Cryotronics, *Temperature Sensors*, Product Specifications (2010).

[176] A. G. Tobin and D. W. Sedgley, *J. Vac. Sci. Technol. A*, **5**, 101 (1987).

[177] C. Day, *Basics and applications of cryopumps*, CERN Accelerator School and ALBA Synchrotron Light Facility, 2007.

[178] L. D. van Buuren, *Private communication*, (2010).

[179] Valley Design, *Thermal-Mechanical Properties of Glass*, Product Specifications (2012).

[180] K. J. Åström and R. M. Murray, *Feedback Systems: An Introduction for Scientists and Engineers*, Princeton, 2008.

[181] Bronkhorst, *Digital Mass Flow Controller*, Operating Manual (2009).

[182] R.V. Latham,*Phys. Technol.*, **9**, 20 (1978).

[183] J. A. Eldridge, *Phys. Rev.*, **30**, 931 (1927).

[184] Pfieffer Vacuum, *Prisma 80 - QMS 200*, Operating Instructions (2001).

[185] T. Junglen, T. Rieger, S. A. Rangwala, P. W. H. Pinkse and G.Rempe, *Phys. Rev. Lett.*, **92**, 223001 (2004).

[186] K. Okada, T. Suganuma, T. Furukawa, T. Takayanagi, M. Wada and H. A. Schuessler, *Phys. Rev. A*, **87**, 043427 (2013).

[187] D. Patterson, J. Rasmussen and J. M. Doyle, *New J. Phys.*, **11**, 55018 (2009).

[188] M. N. R. Ashfold and J. D. Howe, *Annu. Rev. Phys. Chem.*, **45**, 57 (1994).

[189] A. E. Douglas, *Discuss. Faraday Soc.*, **35**, 158 (1963).

[190] M. N. R. Ashfold, R. N. Dixon, R. J. Stickland and C. M. Western, *Chem. Phys. Lett.*, **138**, 201 (1987).

[191] M. N. R. Ashfold, R. N. Dixon, N. Little, R. J. Stickland and C. M. Western, *J. Chem. Phys.*, **89**, 754 (1988).

[192] M. N. R. Ashfold, C. L. Bennett and R. N. Dixon, *Chem. Phys.*, **93**, 293 (1985).

[193] M. N. R. Ashfold, C. L. Bennett, R. N Dixon, P. Fielden, H. Rieley, and R. J. Stickland, *J. Mol. Spectrosc.*, **117**, 216 (1986).

[194] B. Bertsche and A. Osterwalder, *Phys. Rev. A*, **82**, 033418 (2010).

[195] W. C. Wiley and I. H. McLaren, *Rev. Sci. Instr.*, **26**, 12 (1955).

[196] C. M. Western, *PGOPHER, a Program for Simulating Rotational Structure*, University of Bristol, http://pgopher.chm.bris.ac.uk

[197] *Š*. Urban, D. Papoušek, M. Bester, K. Yomada, G Winnewisser and A. Guarnieri, *J. Mol. Spectrosc.*, **106**, 29 (1984).

[198] J. Bentley, B.J. Cotterell, A. Langham and R.J. Stickland, *Chem. Phys. Lett.*, **323**, 85 (2000).

[199] X. Wu, *Private communication*, (2012).

[200] D. C. Lis, M. Gerin, E. Roueff, C. Vastel and T. G. Phillips, *Astrophys. J.*, **636**, 916 (2006).

[201] M. Nolde, K. M. Weitzel and C. M. Western, *Phys. Chem. Chem. Phys.*, **7**, 1527 (2005).

[202] M. N. R. Ashfold, R. N. Dixon and R. J. Stickland, *Chem. Phys.*, **88**, 463 (1984).

[203] S. A. Henck, M.S. Mason, W. B. Yan and K. K. Lehmann, *J. Chem. Phys.*, **102**, 4772 (1995).

[204] S. A. Henck, M.S. Mason, W. B. Yan, K. K. Lehmann and S. L. Coy, *J. Chem. Phys.*, **102**, 4783 (1995).

[205] C.-H. Yang, G. Sarma, A. K. Saha, D. H. Parker and C. M. Western, *Phys. Chem. Chem. Phys.*, **15**, 6390 (2013).

[206] J. M. Allen, M. N. R. Ashfold, R. J. Stickland and C. M. Western, *Mol. Phys.*, **74**, 49 (1991).

[207] L. L. Pollum, K. S. Twyman, M. T. Bell and T. P. Softley, *Progress toward studying cold ion-molecule reactions:trap design and cold beam characterisation*, poster presented at IOTA Conferance, Siegen, April 2012.

[208] G. J. Dick, J. D. Prestage and L. Maleki, *J. Appl. Phys.*, **66**, 10131017 (1989).

[209] A. D. Gingell, DPhil. Thesis, University of Oxford (2010).

[210] W. M. Itano, J. J. Bollinger, D. J. Wineland, J. C. Bergquist and C. H. Manney, *Phys. Rev. Lett.*, **59**, 2935 (1987).

[211] J. M. Chen, W. Quint, F. Diedrich, E. Peik and H.Walther, *Phys. Rev. Lett.*, **59**, 2931 (1987).

[212] S. Willitsch, M. T. Bell, A. D. Gingell, S. R. Procter and T.P. Softley, *Phys. Rev. Lett.*, **100**, 043203 (2008).

[213] S. Willitsch, M. T. Bell, A. D. Gingell and T.P. Softley, *Phys. Chem. Chem. Phys.*, **10**, 7200 (2008).

[214] S. Willitsch, *Int. Rev. Phys. Chem.*, **31**, 175 (2012).

[215] M. Schwarz, O. Versolato, A. Windberger, F. Brunner, T. Ballance, S. Eberle, J. Ullrich, P. Schmidt, A. Hansen, A. Gingell, M. Drewsen and J. Crespo Lpez-Urrutia, *Rev. Sci. Instrum.*, **83**, 083115 (2012).

[216] D. C. Clary, *J. Chem. Soc., Faraday Trans. 2*, **83**, 139 (1987).

[217] P. R. Bunker and P. Jensen, *Molecular Symmetry and Spectroscopy*, 2nd ed., NRC Research Press, Canada, 2006.

[218] M. Lara, B. L. Lev and J. L. Bohn, *Phys. Rev. A*, **78**, 11 (2008).

[219] P. W. Harland, W. P. Hu, C. Vallance and P. R. Brooks, *Phys. Rev. A*, **60**, 3138 (1999).

[220] J. van Veldhoven, H. L. Bethlem, M. Schnell and G. Meijer, *Phys. Rev. A*, **73**, 063408 (2006).

[221] I. C. Bowater, J. M. Brown and A. Carrington, *Proc. R. Soc. Lond. A*, **333** 265 (1973).